

Chapter 2

At Least a Higgs Boson

On July 4th, 2012 the ATLAS and CMS collaborations at CERN's Large Hadronic Collider reported the observation of a new particle with properties consistent with those expected from the SM Higgs [1, 2]. This discovery is truly remarkable, first because the Higgs boson was the last elementary particle predicted by the SM remaining to be observed after many years of unsuccessful searches. But most of all, it is the key role of the Higgs field in the SM—triggering the breaking of the electroweak symmetry and giving masses to the elementary particles, as explained in Sect. 1.1—that makes the discovery of the Higgs boson so special. This has been rewarded in 2013 with the Nobel Prize in physics for François Englert and Peter Higgs for the “theoretical discovery” of what is now called the Higgs (or Brout–Englert–Higgs) mechanism [3–8].

This new particle certainly represents the ultimate triumph of the SM. In the difficult quest for new physics beyond the SM, motivated by several problems for which I give a short and personal review in Sect. 1.2, we, particle physicists, sometimes forget to look back and admire the fact that such a simple theory, based on symmetry considerations, suffices to describe all observed phenomena in the microscopic world with an excellent precision, to say the least. This being said, the LHC would not have been built only to fix the last free parameter of the SM. Its *raison d'être* is the search for new physics, hence the discovery of this Higgs boson should also be viewed as an opportunity to discover—or at least corner—new physics. Hopefully, the first observation of a Higgs boson will later be seen as the opening of a new chapter in particle physics and not only as the closing of the SM one.

Indeed, the measurements of the properties of the Higgs boson (starting from its mass) are of immediate relevance for models aiming at solving the hierarchy problem, and in general for any model predicting a modified or extended Higgs sector and/or new particles coupling to the Higgs field. As we will see in several examples, the information that is obtained is complementary to the direct searches for new particles at the LHC, or even to direct searches for dark matter. For that reason, the discovery of a Higgs-like boson and the subsequent measurement of its properties at the LHC

have generated an intense activity in the theory community—to which I started to participate in mid-2012, shortly after the discovery.

This chapter will be divided as follows. In Sect. 2.1, I will start by the pre-LHC constraints on an SM(-like) Higgs boson, before turning in Sect. 2.2 to a brief review of the properties of the Higgs boson, as predicted in the SM. I will then list and discuss the various measurements performed at the LHC in Sect. 2.3. The way this experimental information is used to constrain new physics scenarios is described in Sect. 2.4. I will then present the various works I have been involved in. The physics studies are separated into two categories: the model-independent studies in which new physics is constrained from an effective approach are presented in Sects. 2.5, 2.6 and 2.7, while the complete study of the constraints on a specific new physics scenario, the phenomenological MSSM (pMSSM), will be presented in Sect. 2.8. In Sect. 2.9, I will present `Lilith`, a new public tool that provides an approximation to the Higgs likelihood in order to constrain generic BSM scenarios. Finally, the future of Higgs constraints on new physics will be discussed in Sect. 2.10.

For all of this, I would like to acknowledge collaboration with Geneviève Bélanger, Jérémy Bernon, Ulrich Ellwanger, Sylvain Fichet, Gero von Gersdorff, John F. Gunion, Sabine Kraml, and Sezen Sekmen as well as useful discussions with, in particular, Guillaume Drieu La Rochelle.

2.1 Pre-LHC Constraints on the Higgs Boson

While being crucial, it should be noted that the discovery of a Higgs boson at the LHC did not come as a surprise. Mass terms for the W^\pm and Z^0 bosons—as well as mass terms for the fermions—break the $SU(2)_L \times U(1)_Y$ symmetry that successfully describes the electroweak interactions. Ignoring aesthetic considerations and breaking explicitly this symmetry, i.e. putting directly a mass term $M_W^2 W^\mu W_\mu$ in the Lagrangian, leads to the violation of unitarity in the $W_L W_L$ scattering process (W_L being the longitudinal component of the W^\pm bosons) at center-of-mass energies $\sqrt{s} \gtrsim 1$ TeV, which would be a clear indication of the presence of a new particle at or below the TeV scale, see e.g. [9] and references therein. Fortunately, all these problems can be solved at once if the electroweak symmetry is *spontaneously broken* via the Higgs mechanism, as explained in Sect. 1.1. The simplest solution involves only one elementary scalar field, the Higgs field. This is what is done in the SM.

This picture is strengthened by the precision tests of the electroweak sector. In particular, the precise measurements performed on the Z^0 resonance at the LEP experiment [10] constitute a stringent test of the SM. From these data, a fit to a relevant subset of the SM parameters that enters the loop corrections to the observables (listed in the left panel of Fig. 2.1) was performed by the collaborations at LEP, thus making it

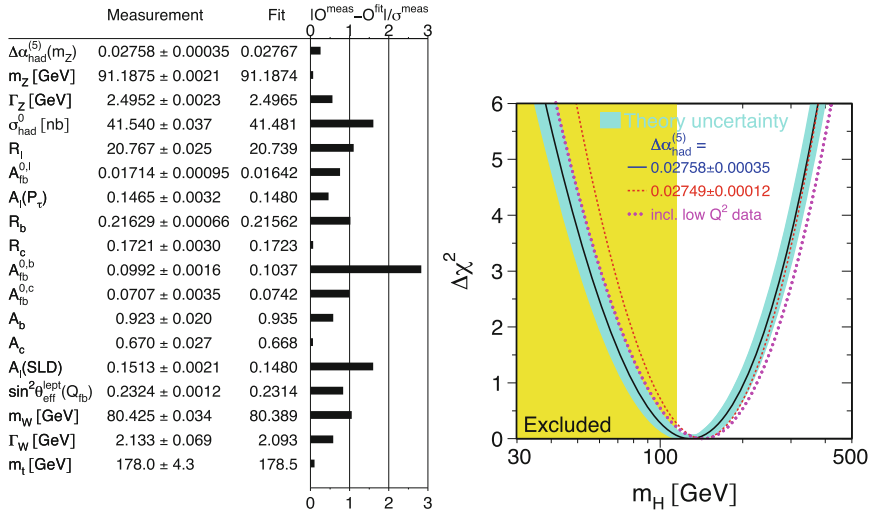


Fig. 2.1 Electroweak fit using mostly observables at the Z^0 pole, as was performed by the LEP collaborations in 2005 [10]. *Left* pull comparison of the fit results with the measurements of the observables. *Right* fit of the Higgs boson mass from the observables shown in the left panel

possible to check the consistency of the SM with high accuracy.¹ An overall excellent agreement is found, as can be seen in the left panel of Fig. 2.1. The largest deviation with respect to SM expectations comes from the forward-backward asymmetry in b -quark production, $A_{\text{FB}}^{0,b}$, and is at the level of 2.8 standard deviations. From this SM fit, a prediction on the Higgs boson mass can be made since it enters (however, only logarithmically) in the loop corrections. The result is shown in the right panel of Fig. 2.1. This corresponds to an imprecise yet relevant information on the Higgs mass in the SM, being $m_H = 129_{-49}^{+74}$ GeV at 68 % confidence level (CL). Note that, in addition to the LEP I results at the Z^0 resonance, some results from LEP II and from Tevatron Run I were used in this fit. This electroweak fit has been regularly updated by the LEP electroweak working group [11], and the Gfitter group is also performing electroweak fits using all publicly available data [12], also including the Higgs mass since its discovery [13, 14]. The latest update still shows a very good agreement with the SM predictions, while the determination of the Higgs boson mass (not including LHC data) is significantly improved: $m_H = 94_{-22}^{+25}$ GeV. This is mostly coming from the precise measurement of the top mass and of the W mass using the full statistics collected in the $p\bar{p}$ collisions at Tevatron.

Electroweak fits show the perfect consistency of the SM and give the expected range for the Higgs boson mass. However, and even if all other searches for BSM physics only produced negative results so far, there were very good reasons to search

¹The five relevant SM parameters for the calculation of Z^0 -pole observables were identified to be the QED and QCD coupling constants $\alpha_s(m_Z^2)$ and $\alpha(m_Z^2)$, the masses of the Z^0 and Higgs bosons m_Z and m_H , and the top mass m_t .

for the Higgs boson itself, beyond the simple determination of its mass. The hierarchy problem, which is one of the most pressing issues of the SM as explained in Sect. 1.2.1, is believed to be most naturally solved by TeV-scale new physics. First of all, the value of the Higgs mass can have substantial implications on these models, and in particular supersymmetry, since it is no longer a free parameter but rather comes as a prediction. Moreover, the new, BSM particles couple to or mix with the Higgs boson, and can dramatically change its properties compared to the SM predictions. Therefore the study of the properties of the Higgs boson gives an additional insight on the electroweak symmetry breaking, complementary to the direct searches for these new TeV-scale particles at colliders. The Higgs boson can also have profound implications on cosmology since if dark matter is made of WIMPs, the observed relic density of dark matter is likely to be explained from the interactions with the Higgs.

Before the LHC, direct searches for the Higgs boson were performed at LEP [15] and at Tevatron [16]. Searches performed at LEP, being an e^+e^- collider, are sensitive to the production of a Higgs boson in association with a Z^0 , with the decay $H \rightarrow b\bar{b}$ or $H \rightarrow \tau^+\tau^-$. Tevatron searches involve many different categories sensitive to different final states and production modes, but in the light region ($m_H \lesssim 140$ GeV) the results are mostly driven by the production of a Higgs boson in association with a vector boson (W^\pm or Z^0), with the decay $H \rightarrow b\bar{b}$, subsequently denoted as $VH \rightarrow b\bar{b}$. The final results from the two experiments are shown in Fig. 2.2. In both cases the 95% CL upper bounds on the ratio of production cross sections $\sigma/\sigma^{\text{SM}}$ are given as a function of the Higgs mass. From LEP results, a lower bound of 114.4 GeV is set on the SM Higgs mass, while 2012 Tevatron results moreover excludes the [149, 182] GeV range and observes an excess of events between 115 and 140 GeV, with a local significance of 3σ at $m_H = 125$ GeV. As can be seen,

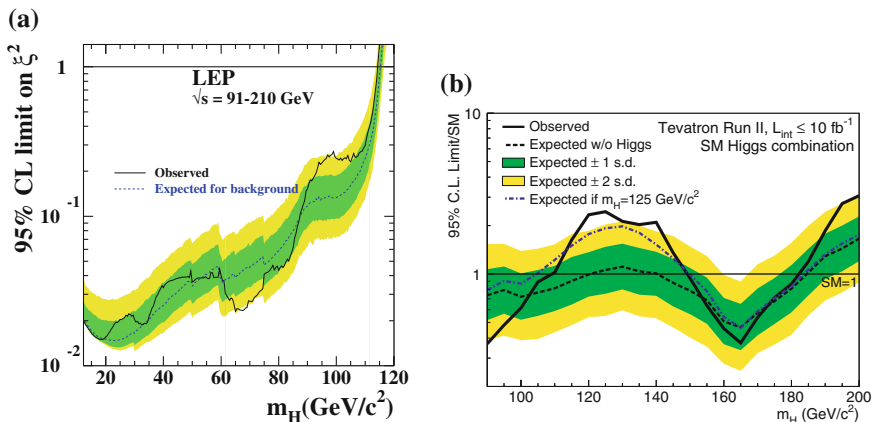


Fig. 2.2 Final results in the search for the Higgs boson at LEP [15] (left) and at Tevatron [16] (right). In the left panel, ξ is defined as a reduced HZZ coupling, $g_{HZZ}/g_{HZZ}^{\text{SM}}$

the situation before the LHC was quite undecided and a large range of the possible Higgs masses remained unexplored.

Before turning to the properties of the SM Higgs that will be necessary to understand and interpret the results from the LHC, it is worth mentioning that there are other, theoretical constraints on the SM Higgs boson mass coming from the requirement of validity up to a certain physical scale (that can be pushed up to the Planck scale, $M_{\text{Pl}} \approx 10^{19}$ GeV). Indeed, 2-loop calculations of the RG running of the λ parameter in the Higgs potential show that λ can become negative (leading to instability of the potential) or non-perturbative at a certain scale. The maximum validity scale Λ as a function of the Higgs mass, as derived in Ref. [17], is shown in the left panel of Fig. 2.3. It shows that a heavy Higgs boson, which is already disfavored from the electroweak fit of the SM, must come with new physics at a relatively low scale, and that light Higgses, just above the LEP bound, may suffer from the stability bound. These has been updated with 3-loop results and a better precision on the SM input parameters in Refs. [18, 19]. The result is given in the right panel of Fig. 2.3, showing in addition a meta-stability region, in which the potential is unstable but has a very small probability of quantum tunneling such that the lifetime of the electroweak vacuum exceeds the one of the Universe. The currently favored region after the discovery at the LHC is inside the black rectangle, and is close to the stable region but seems to lie in the meta-stable region (depending however on the top quark mass, see also Ref. [20]).

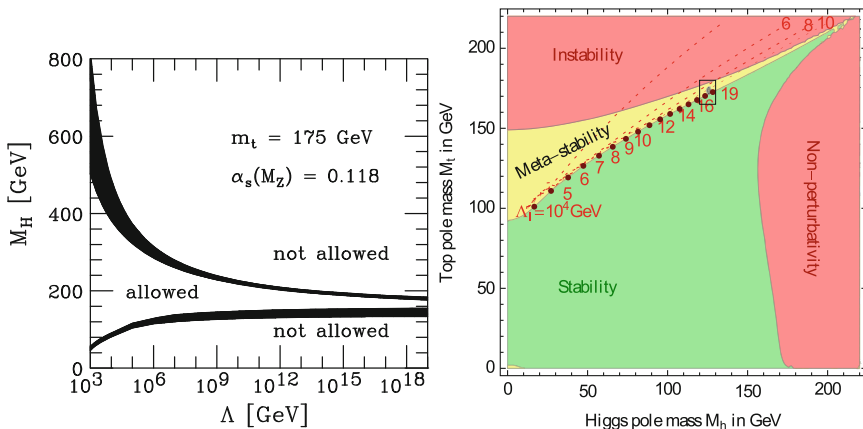


Fig. 2.3 *Left* the maximum validity of the SM as a function of the Higgs mass, from Ref. [17]. The lower curve is the stability bound, while the upper one is the triviality bound. *Right* regions of absolute stability, meta-stability and instability of the SM vacuum in the m_t versus m_H plane, from Ref. [19]. The dashed red lines show the instability scale, denoted as Λ_I

2.2 Production and Decay of the SM Higgs Boson at the LHC

Searches for the Higgs boson at LEP turned out unsuccessful, while the Tevatron final results only exhibit a 3σ evidence around $m_H = 125 \text{ GeV}$ but no discovery. Since almost all results that will be used to constrain new physics from the properties of the observed Higgs boson come from LHC searches, it is interesting to first look in detail at the various production mechanisms at a 8 TeV pp collider (corresponding to most of the data collected during Run I of the LHC) and at the accessible decay modes. A comprehensive introduction to the production and decay modes of the SM Higgs boson can be found in Ref. [21], while a summary of the latest SM predictions is provided by the LHC Higgs Cross Section Working Group [22] (see also [23]) and shown here in Fig. 2.4.

First of all, it should be noted that searches for the Higgs boson at a hadron collider such as the LHC are notoriously difficult due to the small cross sections, which are at most several dozens of pb in the low-mass region. This is in strong contrast with W and Z production, where the cross sections are of several dozens of nb, i.e. three orders of magnitude larger. This can be understood because the couplings of the SM Higgs boson to particles inside the proton are either tiny or simply absent at tree-level. Indeed, the Higgs boson couples to fermions as $g_{Hff} = m_f/v$, which is very small for the light quarks constituting the proton, while gluons only couple to the Higgs boson at loop level because it is a color-neutral particle. The two remaining possibilities for a sizable production of Higgs bosons at the LHC are (i) via the coupling of the Higgs to W and Z vector bosons, or (ii) via indirect or loop-induced processes originating from gluons. The latter possibility turns out to be the dominant production mechanism at the LHC, because of the strong, $\mathcal{O}(1)$ coupling of the Higgs

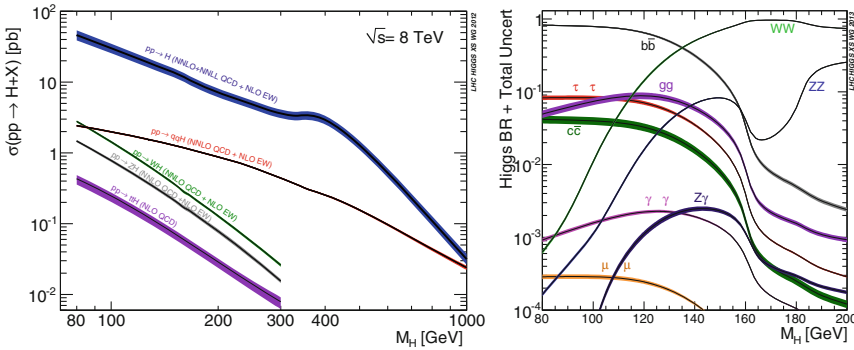


Fig. 2.4 *Left* Production modes and associated cross sections for the SM Higgs boson at the LHC for $\sqrt{s} = 8 \text{ TeV}$. *Right* decay branching fractions of the SM Higgs boson. These results are given as a function of the Higgs mass, and are provided by the LHC Higgs Cross Section Working Group [22]. In both cases, the width of the band around each line gives an estimate of the theoretical uncertainty

to top quarks running in a one-loop (“triangle”) diagram originating from two gluons. This process will be subsequently denoted as gluon fusion (ggF), and constitute the dominant contribution to the blue, $pp \rightarrow H$ curve in the left panel on Fig. 2.4.

Production of the Higgs boson via W and Z can be separated into two categories, leading to experimentally distinct signatures. First of all two vector bosons emitted from two distinct quarks can fuse into a Higgs boson, via its relatively large couplings to vector bosons, being $g_{HVV} = 2m_V^2/v$. This is known as vector boson fusion (VBF), and corresponds to a $pp \rightarrow qqH$ final state, where two quarks are emitted in the forward directions of the detector, allowing for a discrimination against the QCD background. The second possibility is to produce a Higgs boson in association with a W or Z vector boson, via an off-shell vector boson produced from quarks. The (possibly leptonic) decay of the vector boson can then be used to trigger the event and/or discriminate it against the background or other Higgs production modes. This will be further referred to as WH and ZH, commonly denoted as VH. Finally, the production mechanism with the lowest cross section at the LHC, while still being accessible, involves the fusion of two top quarks into a Higgs boson, with the top quarks coming from the splitting of two gluons into a pair of top-antitop. This is denoted as ttH, production of the Higgs boson in association with a top quark pair. This rare production mechanism is however crucial to access directly the coupling of the Higgs to top quarks, as relatively light Higgs bosons can not decay into top quarks.

Turning to the possible decays of the Higgs, as shown in the right panel of Fig. 2.4, two distinct regions can be seen. For $m_H \lesssim 160$ GeV, decays into fermions and gluons constitute a sizable or dominant part of the decay width, while above this threshold the decays into WW and ZZ completely dominate. This comes from the transition to the on-shell decay into vector bosons, with $\Gamma(H \rightarrow VV) \propto m_H^3$ at high mass while the decay width into fermions always scales as m_H . In order to constrain the properties of the Higgs boson, the most interesting region is at low-mass, $m_H \lesssim 160$ GeV, where complementary measurements can be made in many different final states. It is thus fortunate that an SM-like Higgs with a mass of about 125 GeV was found at the LHC, as we will see in Sect. 2.3.

In spite of a relatively large $\sigma \times \text{BR}$, some of the production \times decay modes are difficult or impossible to access at the LHC because of the very large QCD background. In contrast, some rare decays were already observed with a good accuracy from the data collected during Run I of the LHC since they correspond to “clean” final state, i.e. easy to distinguish from the SM background. For a 125 GeV SM-like Higgs boson, we expect $N = \sigma_{\text{tot}} \times \mathcal{L} \approx 20 \text{ pb} \times 20 \text{ fb}^{-1} = 400,000$ Higgs bosons to be produced with the 20 fb^{-1} of data collected at $\sqrt{s} = 8 \text{ TeV}$ at the LHC. It is interesting to note that about 50% of these events correspond to $gg \rightarrow H \rightarrow b\bar{b}$, which cannot be distinguished from the overwhelming QCD background. At the LHC, the decay of Higgs bosons into a pair of b -quarks can only be probed when the Higgs boson is produced in association with other particles which can be triggered. A prime candidate is VH with leptonic decays of the massive vector bosons, i.e. $W^\pm \rightarrow \ell^\pm \nu$ or $Z^0 \rightarrow \ell^+ \ell^-$, with $\ell \equiv e, \mu$.

The observation of $H \rightarrow gg$, loop-induced decay of the Higgs into gluons, and $H \rightarrow c\bar{c}$ processes at LHC is much more difficult. The large QCD background already mentioned for $H \rightarrow b\bar{b}$ remain as a problem, but in addition (i) branching fractions, hence signal over background ratios, are much smaller, and (ii) from the tagging of b -jets a discrimination can be made between $H \rightarrow b\bar{b}$ and most of the QCD background, while the tagging of c -jets and, even worse, gluon jets is extremely challenging. For these reasons, the expected sensitivity to these channels is very low at the LHC, even in association with a vector boson.² Finally, $H \rightarrow \mu\mu$ has a small, $\mathcal{O}(10^{-4})$ branching fraction hence its observation will require a lot of statistics at the LHC [25, 26]. As a consequence, for an SM-like Higgs only the couplings to the 3rd generation of quarks and leptons are accessible on the middle term.

2.3 Discovery and Measurements at the LHC

ATLAS and CMS are the two main, multi-purpose detectors at the LHC. The physics operations at the LHC started in 2010, but most of the data was accumulated in 2011 ($\sim 4.7 \text{ fb}^{-1}$ at $\sqrt{s} = 7 \text{ TeV}$) and in 2012 ($\sim 20.3 \text{ fb}^{-1}$ at $\sqrt{s} = 8 \text{ TeV}$). The observation of a new particle in the search for the Higgs boson was announced jointly by the ATLAS and CMS collaborations on July 4th, 2012, and published shortly after [1, 2, 27]. This was based on the full statistics collected at 7 TeV plus about 5.5 fb^{-1} of data at 8 TeV, and resulted for each experiment from the combination of searches for the following five final states: $H \rightarrow \gamma\gamma$, $H \rightarrow ZZ^{(*)} \rightarrow 4\ell$, $H \rightarrow WW^{(*)} \rightarrow 2\ell 2\nu$, $H \rightarrow \tau\tau$ and $VH \rightarrow b\bar{b}$.

In high energy physics, the statistical significance of a new phenomenon is expressed as a p -value, corresponding to the degree to which a given null hypothesis (in this case, SM with no Higgs boson) is incompatible with the data. More precisely, it quantifies the probability of obtaining a result at least as extreme as the one that was actually observed, assuming that the null hypothesis is true [28]. The p -value is commonly expressed in units of standard deviation of a normal distribution, or “number of sigmas”. From the p -value, this equivalent significance Z is given by $Z = \Phi^{-1}(1 - p)$, where Φ^{-1} is the inverse of the cumulative distribution function of the normal distribution. The commonly accepted criteria to declare discovery is five-sigma, $Z = 5$, which corresponds to an extremely small p -value of 3×10^{-7} . As can be seen in Fig. 2.5, this local significance of 5σ was observed by the ATLAS and CMS collaborations, at around the same mass of $\sim 125 \text{ GeV}$. One can directly see that the CMS discovery was mostly driven by the $H \rightarrow \gamma\gamma$ and $H \rightarrow ZZ^* \rightarrow 4\ell$ channels, which is also true for ATLAS but not explicitly shown here. This is an interesting observation because, at 125 GeV, $\text{BR}(H \rightarrow \gamma\gamma) = 2.3 \times 10^{-3}$ and $\text{BR}(H \rightarrow ZZ^* \rightarrow 4\ell) = 1.3 \times 10^{-4}$ [22, 29, 30], meaning that the Higgs boson was discovered from rare decays. This latter decay mode was often called the “gold

²Modifications of the Higgs coupling to charm quarks were discussed recently in Ref. [24].

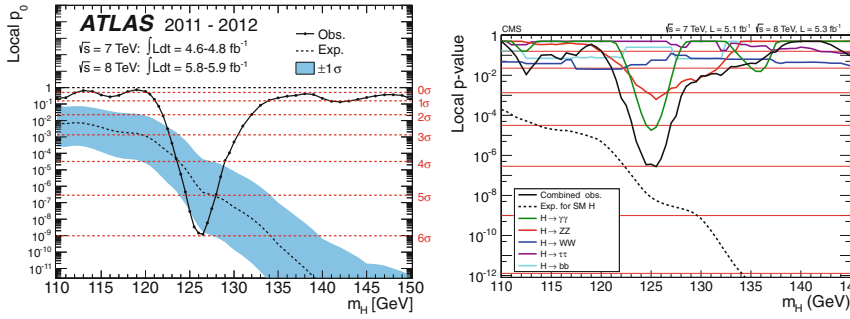


Fig. 2.5 Observed and expected p -value as a function of the Higgs mass in the search for the Higgs boson with the ATLAS (*left*) and CMS (*right*) detectors in July 2012. In both cases the *black line* corresponds to the combination of the search for the Higgs boson in different final states, which is shown explicitly for CMS

plated mode” for the discovery of the Higgs boson as it gives a very clear signature with a low background.

Turning to results using the full luminosity collected during Run I of the LHC, let us first look at the mass measurement. This is done using the two “high-resolution” channels, $H \rightarrow \gamma\gamma$ and $H \rightarrow ZZ^* \rightarrow 4\ell$. Indeed, the estimate from $H \rightarrow WW^* \rightarrow 2\ell 2\nu$ is very imprecise due to the presence of neutrinos in the final state, while mass measurements from $H \rightarrow b\bar{b}$ are affected by larger uncertainties due to the showering and hadronization of b quarks. Finally, $H \rightarrow \tau\tau$ suffers from one or both problems, depending on the leptonic or hadronic nature of the τ decays. The latest results on the measurement of the Higgs mass from $H \rightarrow \gamma\gamma$ and $H \rightarrow ZZ^* \rightarrow 4\ell$ in ATLAS and CMS are shown in Fig. 2.6. ATLAS results are taken from the final Run I mass measurement [31], while CMS results are a preliminary

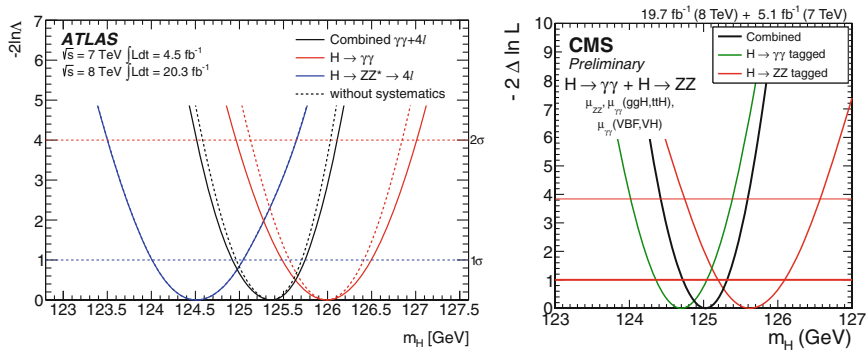


Fig. 2.6 Constraints on the Higgs mass from the measurements in the $H \rightarrow \gamma\gamma$ and $H \rightarrow ZZ^* \rightarrow 4\ell$ channels, as was performed by the ATLAS collaboration (*left*) and by the CMS collaboration (*right*). The y-axis is $-2 \Delta \log L$, where L is the likelihood profiled over all parameters except m_H

combination of the $H \rightarrow \gamma\gamma$ and $H \rightarrow ZZ^*$ results [32]. The combination of these two channels in ATLAS gives a mass of 125.36 ± 0.37 (stat.) ± 0.18 (sys.) GeV, in perfect agreement with the CMS result of $125.03^{+0.26}_{-0.27}$ (stat.) $^{+0.13}_{-0.15}$ (sys.) GeV [33]. The discrepancy between the two channels is at the level of 2.0σ in ATLAS, which is a reduced tension compared to the 2.4σ discrepancy found in a previous mass estimate [34]. Both ATLAS and CMS measurements are dominated by statistical uncertainties and should improve significantly during Run II of the LHC. Finally, note that $H \rightarrow Z\gamma$ (with $Z \rightarrow \ell^+\ell^-$) is also a high-resolution channel, but it is not yet accessible at the LHC (the current limit on $H \rightarrow Z\gamma$ at $m_H = 125.5$ GeV is of about 10 times the SM expectation [35, 36]).

Beyond the mass of the observed state, the various searches at the LHC—thanks to the many decay modes accessible for a 125 GeV Higgs boson—open up the possibility to test in detail the properties of the Higgs boson and its couplings to other particles. This is crucial information to constrain new physics, as we will see in concrete examples in Sects. 2.5–2.8. The results of the Higgs searches at the LHC are given in terms of signal strengths, μ , which scale the number of signal events expected for the SM Higgs, n_s . For a given set of selection criteria (or “cuts”), the expected number of events is therefore $\mu \cdot n_s + n_b$, where n_b is the expected number of background events, so that $\mu = 0$ corresponds to the no-Higgs scenario and $\mu = 1$ to an SM-like Higgs. Equivalently, signal strengths can be expressed as

$$\mu = \frac{\sigma \times A \times \varepsilon}{[\sigma \times A \times \varepsilon]_{\text{SM}}}, \quad (2.1)$$

i.e. the “visible cross section” $\sigma_{\text{vis}} = \sigma \times A \times \varepsilon$ divided by its SM expectation. Here, A is the (geometrical) acceptance factor, i.e. the fraction of produced events that will cross the detector, while ε is the efficiency of the cuts.

The presentation of the results in terms of signal strengths has non-trivial implications when using these results to constrain new physics affecting (or possibly faking) the Higgs boson. We will discuss that shortly after, in Sect. 2.4; here we first focus on the status of the Higgs measurements with the full statistics collected during Run I of the LHC. Experimental results on the Higgs boson are usually divided into publications presenting searches targeting one decay mode. This is well justified because in most cases the experimental signatures are clearly distinct, i.e. no or little contamination is expected between searches. For a given decay mode, there are usually several “categories” (or “subchannels” or “signal regions”), corresponding to a set of cuts and for which results are given in terms of observed signal strengths as shown in Eq. (2.1). These categories can be defined according to the nature of the final state particles produced from the decay of the Higgs (e.g. $H \rightarrow ZZ^* \rightarrow 4\ell$ gives $4e$, 4μ or $2e2\mu$), or categories can be defined in order to improve sensitivity to given production modes (among ggF, VBF, WH, ZH and ttH) or from other properties of the final state objects (e.g. which part of the detector is involved).

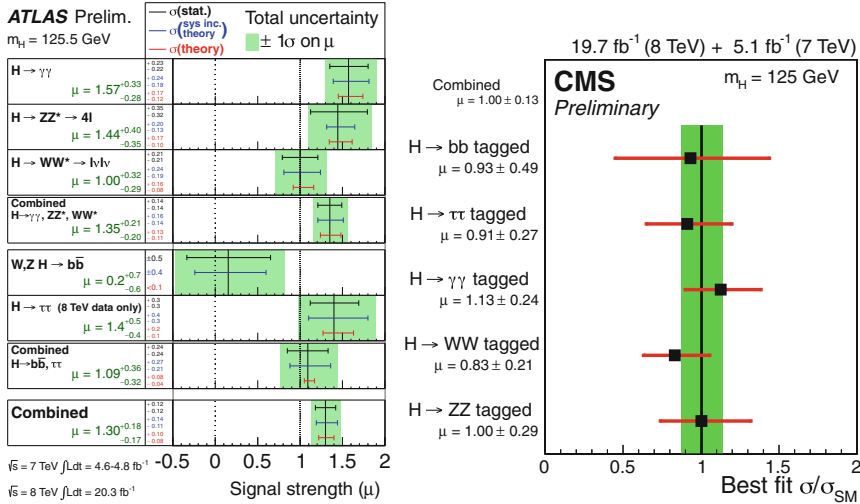


Fig. 2.7 Results in the search for the Higgs boson from ATLAS [37] (left) and CMS [32] (right), given in terms of combined signal strengths (denoted as μ) for the main decay modes of the Higgs boson: $\gamma\gamma$, ZZ^* , WW^* , $b\bar{b}$, $\tau\tau$. Also shown is the combination of several or all decay modes into one signal strength

For each individual decay mode a combination of the categories can be made, but only *under the assumption of a universal rescaling of the production cross sections*. The results then corresponds to “combined” signal strengths. Due to this underlying assumption, it should be stressed that while a significant deviation of these combined μ from 1 must indicate the presence of new physics, a value of $\mu = 1$ could result from new physics enhancing the signal in some channels while reducing it in others. As we will see in Sect. 2.4, this is the reason why we do not use this information to constrain new physics. However, these combined signal strengths give useful information on the current precision with which Higgs properties are measured. This information is shown in Fig. 2.7 for the latest ATLAS and CMS Higgs results [32, 37]. All the combined signal strengths show a very good consistency with the SM prediction. This leaves very little doubt that the observed state really is the Higgs boson from the scalar field³ mostly responsible for the breaking of the electroweak symmetry. As can be seen, the diboson final states ($\gamma\gamma$, ZZ^* and WW^*) are measured with a much better precision than the fermionic ($b\bar{b}$, $\tau\tau$) ones. Each of these three diboson final states are observed with a significance of more than 3σ by ATLAS or CMS alone, and uncertainties in the $\gamma\gamma$ and WW^* channels start to be dominated by systematic uncertainties (in which theory uncertainties have a large part) while the ZZ^* channel is still dominated by statistical uncertainties [40–43]. Turning to

³The spin-parity of the observed state induces significant changes in the kinematic distributions and has been constrained at the LHC in the diboson final states [33, 38–41]. The SM value of $J^P = 0^+$ is favored against all other tested hypotheses.

the fermionic channels, while the decay of the Higgs into $\tau\tau$ has been observed with more than 3σ significance in both experiments [44, 45], measurements on $H \rightarrow b\bar{b}$ remain very imprecise [46, 47]. Fortunately, Tevatron final result exhibit a 3σ excess around 125 GeV in the $VH \rightarrow b\bar{b}$ channel [48], leading to $\mu = 1.59^{+0.69}_{-0.72}$ at $m_H = 125$ GeV [16] and to a constraint complementary to the LHC ones in this channel. Finally, as can be seen in Fig. 2.7, combination of several (or all) decay modes is also performed by the collaborations. This however carries little information and is not expected to be useful in constraining new physics because a completely universal rescaling of all number of signal events has to be assumed.

As mentioned, the information given in Fig. 2.7 is not sufficient to constrain new physics. Indeed, as we will see even simple extensions of the SM make it possible, for instance, to reduce VBF and VH production modes while having enhanced or SM-like gluon fusion. Given the various categories defined for each decay mode, experiments have sensitivity to various production channels. In order to capture these effects with a few numbers, one can define new scale factors with respect to the SM Higgs as

$$\mu(X, Y) \equiv \frac{\sigma(X)\text{BR}(H \rightarrow Y)}{\sigma(X_{\text{SM}})\text{BR}(H_{\text{SM}} \rightarrow Y)}, \quad (2.2)$$

where X are the production modes (ggF, VBF, WH, ZH, ttH) and Y are the decay modes (mainly $\gamma\gamma$, ZZ^* , WW^* , $b\bar{b}$, $\tau\tau$) of the SM Higgs boson. As discussed in the next Section, the $\sigma(X)$ and $\text{BR}(H \rightarrow Y)$ are assumed to be simple rescalings of the SM value. For all accessible decay modes, the ATLAS and CMS collaborations are showing results in terms of these “signal strengths in the theory plane”. The five production modes of the SM are usually combined to form just two effective X modes, VBF + VH (both of which depend on the HVV coupling at tree-level) and ggF + ttH. The relevance of this combination will be discussed in the next Section. The likelihood can then be shown in the $(\mu(\text{ggF} + \text{ttH}, Y), \mu(\text{VBF} + \text{VH}, Y))$ plane for each decay mode Y .

The latest results from the LHC in this 2D plane [32, 37] are shown in Fig. 2.8. The excellent agreement with the SM predictions, already discussed from Fig. 2.7, is even more manifest here. It is important to keep in mind that in these results, $\mu(\text{ggF} + \text{ttH}, Y)$ always reduces to a very good approximation to $\mu(\text{ggF}, Y)$, except for $Y = b\bar{b}$ (only shown for CMS), where the (very weak) constraint comes from ttH alone because ggF is not accessible. The current experimental results on ttH are imprecise (see, in particular [49–51]) and never compete with the constraints from ggF, when available. Production of the Higgs boson in association with a pair of top quarks is experimentally challenging, as was discussed in Sect. 2.2, because of its small cross section, being 150 times lower than ggF for $m_H = 125$ GeV at $\sqrt{s} = 8$ TeV. Besides, note that there is a clear correlation between $\mu(\text{ggF} + \text{ttH}, Y)$ and $\mu(\text{VBF} + \text{VH}, Y)$ in almost all contours. This is because the categories designed to improve sensitivity to a given production mode within a given search will always contain some (often large) contamination from the other production modes. For

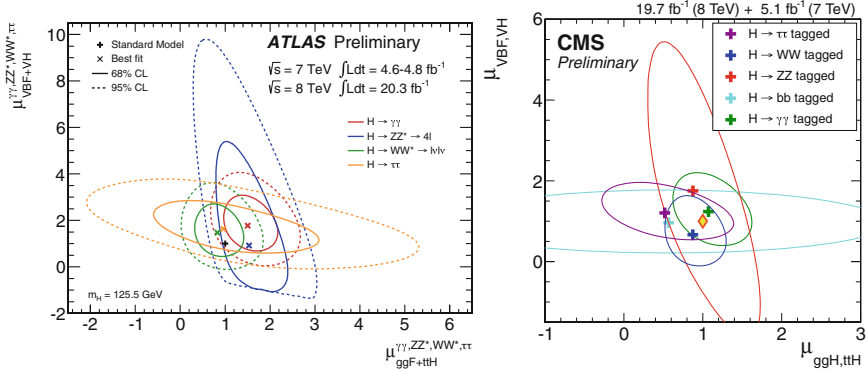


Fig. 2.8 Summary of the searches for the Higgs boson using the full luminosity collected during Run I of the LHC with the ATLAS [37] (*left*) and CMS [32] (*right*) detectors, in the plane $(\mu(\text{ggF} + \text{ttH}, Y), \mu(\text{VBF} + \text{VH}, Y))$ where $Y = \gamma\gamma, ZZ^*, WW^*, \tau\tau$, and (for CMS only) $b\bar{b}$. Contours of constant likelihood are shown, with the *solid line* corresponding to 68% CL and the *dashed line* (for ATLAS only) to 95% CL

example, requiring two additional forward jets in the $H \rightarrow \gamma\gamma$ analysis clearly improves the sensitivity to VBF production, but also has contamination from ggF (through $gg \rightarrow H + 2 \text{ jets}$) and from VH (when the vector boson decays hadronically).

A comment on the $H \rightarrow ZZ^*$ decay mode can also be made. This decay is clearly mostly constrained through ggF and not via VBF and VH. This is a direct consequence of the lack of statistics in this channel (only 32 events in the [120, 130] GeV window in ATLAS [42], 25 events in the [121.5, 130.5] GeV window in CMS [40]), thus efficiently constraining only the dominant production mode, gluon fusion. (The sharp cut seen at $\mu(\text{VBF} + \text{VH}, ZZ^*) \approx -1$ in the ATLAS results comes from the impossibility to test a total number of events, $n_{\text{tot}} = \mu \cdot n_s + n_b$, that is negative.)

2.4 Constraining New Physics with the LHC Higgs Results

Since all results are expressed in terms of signal strengths, it is interesting to go back to the general expression given in Eq. (2.1) and ask ourselves how we can constrain new physics from it. As reminder, we have

$$\mu = \frac{\sigma \times A \times \varepsilon}{[\sigma \times A \times \varepsilon]_{\text{SM}}}, \quad (2.3)$$

where, in general, $A \times \varepsilon$ and $[A \times \varepsilon]_{\text{SM}}$ will not be the same. Indeed, in most experimental categories several production modes contribute to the expected Higgs signal, and new physics typically affect these production modes in a different way. For instance, suppressing gluon fusion while enhancing vector boson fusion may lead to the SM cross section while having $\mu \neq 1$ because of the change in the total fraction of events passing the cuts. Moreover, as we will see in Sect. 2.7, new physics could lead to modifications in the structure of the Higgs couplings to SM particles that lead to a change in the kinematic distributions, hence to a modification in $A \times \varepsilon$. However, an SM-like structure for the Higgs couplings happens to be an excellent approximation in most of the new physics models. In this case, i.e. modification of the strengths of the couplings only, the general expression for the signal strengths is

$$\mu = \frac{\sum_{X,Y} (A \times \varepsilon)_{XY} \sigma_X \text{BR}_Y}{\sum_{X,Y} (A \times \varepsilon)_{XY} \sigma_X^{\text{SM}} \text{BR}_Y^{\text{SM}}}. \quad (2.4)$$

We recall that X are the production modes (ggF, VBF, WH, ZH, ttH) and Y are the decay modes (mainly $\gamma\gamma$, ZZ^* , WW^* , $b\bar{b}$, $\tau\tau$) of the SM Higgs boson. In most cases, experimental categories are only sensitive to one decay mode of the Higgs, and Eq. (2.4) reduces to

$$\begin{aligned} \mu &= \frac{\sum_X (A \times \varepsilon)_X \sigma_X}{\sum_X (A \times \varepsilon)_X \sigma_X^{\text{SM}}} \times \frac{\text{BR}_Y}{\text{BR}_Y^{\text{SM}}} = \frac{\sum_X (A \times \varepsilon)_X \sigma_X^{\text{SM}} C_X^2}{\sum_X (A \times \varepsilon)_X \sigma_X^{\text{SM}}} \times \frac{\text{BR}_Y}{\text{BR}_Y^{\text{SM}}} \\ &= \sum_X \text{eff}_X C_X^2 \times \frac{\text{BR}_Y}{\text{BR}_Y^{\text{SM}}}, \end{aligned} \quad (2.5)$$

where the C_X^2 are factors scaling the cross sections compared to the SM expectation for each process X , and eff_X are “reduced efficiencies” that add up to 1. In the case of an inclusive search (i.e. $\forall X, (A \times \varepsilon)_X = (A \times \varepsilon)$), the eff_X are equal to the ratio of SM cross sections, $\sigma_X^{\text{SM}} / (\sum_X \sigma_X^{\text{SM}})$.

While the LHC is constraining $\sigma \times \text{BR}$, new physics affecting the decays of the Higgs correspond to a modification of the partial decays widths. In the approximation of an SM-like structure, the partial widths simply are simply scaled as $\Gamma_Y = \Gamma_Y^{\text{SM}} C_Y^2$. Defining Γ_H as the total decay width of the Higgs, signal strengths can then be expressed as

$$\begin{aligned} \mu &= \sum_X \text{eff}_X C_X^2 \times \frac{\text{BR}_Y}{\text{BR}_Y^{\text{SM}}} = \sum_X \text{eff}_X C_X^2 \times \frac{\Gamma_Y}{\Gamma_Y^{\text{SM}}} \times \frac{\Gamma_H^{\text{SM}}}{\Gamma_H} \\ &= \sum_X \text{eff}_X C_X^2 \times \frac{\Gamma_Y^{\text{SM}} C_Y^2}{\Gamma_Y^{\text{SM}}} \times \frac{\Gamma_H^{\text{SM}}}{\sum_Y \Gamma_Y^{\text{SM}} C_Y^2} \\ &= \frac{1}{\sum_Y \text{BR}_Y^{\text{SM}} C_Y^2} \sum_X \text{eff}_X C_X^2 C_Y^2. \end{aligned} \quad (2.6)$$

This means that a modification of a single decay width will impact all channels. This is particularly significant for $H \rightarrow b\bar{b}$, as we will see in several examples, because it has the largest branching fraction (57 % at $m_H = 125.5 \text{ GeV}$).

We now have the general procedure for matching new physics modifications to the Higgs couplings—assuming SM-like coupling structure—with the measurement of a signal strength in a given channel. In order to assess the compatibility of a given set of (C_X, C_Y) with a single experimental result, we need to define a likelihood function $L(\mu, \mathbf{v})$, where \mathbf{v} are the nuisance parameters, whose values are known with a limited accuracy from auxiliary or control measurements. The nuisance parameters model detector effects (affecting the identification and reconstruction of the particles) but also theoretical uncertainties, coming from uncertainties in the parton distribution functions (PDF), from the imperfect knowledge of the value of the SM parameters and from the missing higher-order corrections in the calculation of the SM cross sections and branching fractions. In the latter case, the auxiliary measurements do not truly exist but are introduced in the likelihood for convenience. The full likelihood function depends on the internal modeling of all these effects and is almost never provided by the experimental collaborations. It is however possible to reconstruct a simple likelihood, $L(\mu)$, from two information given in the experimental publications: the best fit to the data, denoted as $\hat{\mu}$, and the uncertainty at 68 % CL (or 1σ , also called the standard error), $\Delta\mu$. Assuming that the measurements are Gaussian, $-2 \log L(\mu)$ follows a χ^2 law, which is expressed as

$$-2 \log L(\mu) = \chi^2(\mu) = \left(\frac{\mu - \hat{\mu}}{\Delta\mu} \right)^2. \quad (2.7)$$

While this is often a valid approximation, it needs to be pointed out that measurements are not necessarily Gaussian, depending on the size of the sample (which is currently a problem for $H \rightarrow ZZ^*$) and on the modeling of the systematic uncertainties. For example, it can be seen from the category results of $H \rightarrow \gamma\gamma$ from both experiments [43, 52] that the error bars are not necessarily symmetric around the best fit point, which indicates non-Gaussianities. Furthermore, even if the Gaussian approximation holds around the best fit point it may be inaccurate when testing signal strengths well beyond the standard error. It is also worth noting that this likelihood is only a function of μ and not of the nuisance parameters. It comes from the presentation of the experimental result, in which nuisance parameters have been removed from the full likelihood by constructing a profile likelihood,

$$L(\mu) = L(\mu, \hat{\mathbf{v}}(\mu)), \quad (2.8)$$

where $\hat{\mathbf{v}}(\mu)$ is given by the \mathbf{v} that maximizes the likelihood for fixed μ [28]. Working with an approximation of the likelihood profiled over the nuisance parameters is not an issue, but it removes some freedom a theorist would like to have when using the Higgs data. In particular, there is no universal agreement on the treatment of theoretical uncertainties at the LHC and one might want to change it. Moreover,

theoretical uncertainties will reduce in the future with more precise calculations of the Higgs production and decay processes and with the inclusion of new data into the PDF sets. Having only the likelihood profiled over all parameters except μ makes it very difficult to take into account these future improvements or simply to test an alternative treatment of the theoretical uncertainties. Finally, there should also be a dependence on the Higgs mass, while these individual results are usually only given for a single choice of Higgs mass.

Barring these limitations, Eq. (2.7) can be used to constrain new physics. However, it requires that at least $\hat{\mu}$, $\Delta\mu$, and also the reduced efficiencies eff_X [see Eq. (2.5)] be provided by the experimental collaborations for every individual category. This is unfortunately not always the case. Categories are sometimes defined without giving the corresponding signal efficiencies (i.e. the ATLAS $H \rightarrow WW^*$ analysis [53]), and/or the result is given as a (set of) “combined” signal strength(s) but not in terms of signal strengths category per category (i.e. the ATLAS ZZ^* analysis [54] and the CMS $\tau\tau$ analysis [45]). Such combined μ should in general not be used because they have been obtained under the assumption of SM-like production of the Higgs boson. Whenever the eff_X are not given in the experimental publications it is in principle possible to obtain estimates from a reproduction of the analysis cuts applied on signal samples generated by Monte Carlo (MC) simulation. However, this turns out to be a very difficult or impossible task. Indeed, the discovery of the Higgs boson and the measurement of its properties were a top priority of the LHC physics program, hence experimentalists prepared complex search strategies to optimize the sensitivity. They often rely on multivariate analyses (MVA) techniques that are impossible to reproduce in practice. Whenever the information on reduced efficiencies is not available we are left to guesswork, with a natural default choice being that $\text{eff}_X = \sigma_X^{\text{SM}} / (\sum_X \sigma_X^{\text{SM}})$, corresponding to an inclusive analysis.

We have just discussed the constraints on new physics from one LHC Higgs channel. While this is already a non-trivial task, complications arise when using several categories/searches at the same time, which is our goal ultimately. The simplest solution is to define the full likelihood as the product of the individual likelihoods,

$$L(\boldsymbol{\mu}) = \prod_{i=1}^n L(\mu_i) \Rightarrow \chi^2(\boldsymbol{\mu}) = \sum_{i=1}^n \chi^2(\mu_i) = \sum_{i=1}^n \left(\frac{\mu_i - \hat{\mu}_i}{\Delta\mu_i} \right)^2. \quad (2.9)$$

However, this assumes that all the measurements are completely independent. We know that this is not the case and that the various individual measurement share common systematic uncertainties. They are divided into two categories: the shared experimental uncertainties, coming from the presence of the same final state objects and from the estimation of the luminosity, and the shared theoretical uncertainties, dominated by the contributions from identical production and/or decay modes to the expected Higgs signal in different categories. The estimation of the experimental uncertainties in ATLAS should be largely independent from the one in CMS, hence these correlations can be treated separately for measurements performed by one

collaboration or the other. Conversely, the estimation of the theoretical uncertainties are the same in ATLAS and CMS and should be correlated between all measurements.

In the case where all measurements are Gaussian, it is possible to take these correlations into account in a simple way, defining our likelihood as

$$-2 \log L(\boldsymbol{\mu}) = \chi^2(\boldsymbol{\mu}) = (\boldsymbol{\mu} - \hat{\boldsymbol{\mu}})^T V^{-1} (\boldsymbol{\mu} - \hat{\boldsymbol{\mu}}), \quad (2.10)$$

where V^{-1} is the inverse of the $n \times n$ covariance matrix [28], with $V_{ij} = \text{cov}[\hat{\mu}_i, \hat{\mu}_j]$ (leading to $V_{ii} = \sigma_i^2$). Unfortunately, the off-diagonal elements of this matrix are not given by the experimental collaborations and are very difficult to estimate from outside the collaboration. This remarkably simple and compact expression for the likelihood (a $n \times n$ matrix) is only valid under the Gaussian approximation; beyond that the expression and the communication of the likelihood become more complicated.

In spite of the various caveats and difficulties due to missing information from the experiments, this simple procedure typically gives an acceptable approximation to the experimental likelihood with the current data (as can be seen, i.e., in Fig. 2.10 below in cases where all the information on reduced efficiencies is available) and has been used in countless papers to fit the couplings of the Higgs and apply constraints on new physics models. There is however an alternative experimental input one can use to constrain new physics: the signal strengths in the theory plane, previously defined as

$$\mu(X, Y) \equiv \frac{\sigma(X) \text{BR}(H \rightarrow Y)}{\sigma(X_{\text{SM}}) \text{BR}(H_{\text{SM}} \rightarrow Y)}. \quad (2.11)$$

Results in terms of theoretical signal strengths are (most of the time) shown in the plane $(\mu(\text{ggF} + \text{ttH}, Y), \mu(\text{VBF} + \text{VH}, Y))$, as can be seen in Fig. 2.8. The combination of the VBF, WH and ZH production modes is well justified from the theory point of view. Indeed, one can generate different scaling factors ($C_{\text{VBF}} \neq C_{\text{WH}} \neq C_{\text{ZH}}$) from

$$\left[C_Z \frac{m_Z^2}{v} (Z_\mu)^2 + C_W \frac{2m_W^2}{v} W_\mu^+ W_\mu^- \right] H \quad (2.12)$$

terms in the Lagrangian, with $C_W \neq C_Z$, which can be induced from the dimension-6 operator $\mathcal{O}'_{D^2} = |H^\dagger D_\mu H|^2$, as we will see in Sect. 2.7. This corresponds to a violation of the custodial symmetry which leads to large corrections to the Peskin–Takeuchi T parameter [55, 56], which is constrained to be very small from the electroweak precision measurements at LEP [10] (see Ref. [14] for the latest results from a global electroweak fit). While there are ways to generate $C_{\text{VBF}} \neq C_{\text{WH}} \neq C_{\text{ZH}}$ without violating the custodial symmetry in an effective approach (see Sect. 2.7), these effects are usually small and therefore grouping together VBF, WH and ZH is not a problem for testing the vast majority of the new physics models.

The combination of the ggF and ttH production modes might be more problematic. In the SM, gluon fusion is dominated by the top quark contribution [21]. We have $C_{\text{ggF}} \approx C_{\text{ttH}}$ in models of new physics where it is still the case, but (i) this is only an approximation where the contributions from the bottom quark are neglected, and (ii) this can be drastically modified with new physics affecting the Higgs boson. For instance, in the Two-Higgs-doublet-model (2HDM) of Type II, tree-level couplings of the Higgs to top quarks and to bottom quarks are rescaled independently. Moreover, new particles could enter the gluon fusion loop (such as the stops in SUSY, the superpartners of the top quark) and change the ggF scaling factor independently from the ttH one. “Fortunately”, as already discussed in Sect. 2.3, for all decay modes except $H \rightarrow b\bar{b}$ (where gluon fusion initiated production of the Higgs is not accessible) the ttH production mode is currently constrained with much poorer precision than ggF because of its small cross section. Therefore, with the current data it is justified to take $\mu(\text{ggF} + \text{ttH}, Y) = \mu(\text{ggF}, Y)$ for all channels except $H \rightarrow b\bar{b}$, and $\mu(\text{ggF} + \text{ttH}, Y) = \mu(\text{ttH}, Y)$ for $Y = b\bar{b}$.

The information presented in Fig. 2.8 consists in 68 % CL contours in the 2D plane $(\mu(\text{ggF} + \text{ttH}, Y), \mu(\text{VBF} + \text{VH}, Y))$ (supplemented by the corresponding 95 % CL contours in the case of ATLAS). At this point, a comment is in order. In order to obtain this result for each decay mode Y , the experiments have defined as test statistic the profile likelihood ratio, defined as

$$\Lambda(\boldsymbol{\mu}) = \frac{L(\boldsymbol{\mu}, \hat{\hat{\mathbf{v}}}(\boldsymbol{\mu}))}{L(\hat{\boldsymbol{\mu}}, \hat{\mathbf{v}})}, \quad (2.13)$$

where $\boldsymbol{\mu} = \left(\mu(\text{ggF} + \text{ttH}, Y), \mu(\text{VBF} + \text{VH}, Y) \right)$ and $L(\hat{\boldsymbol{\mu}}, \hat{\mathbf{v}})$ corresponds to the (global) maximum of the full likelihood [28, 32, 37]. All other parameters are treated as nuisance parameters. According to asymptotic properties of the profile likelihood ratio, $-2 \log \Lambda(\boldsymbol{\mu})$ is supposed to be distributed as a χ^2 distribution with n degrees of freedom, with $n = \dim(\boldsymbol{\mu}) = 2$ in our case. It is thus possible to directly match a value of $-2 \log \Lambda(\boldsymbol{\mu})$ with a confidence level from the cumulative distribution function of the χ^2 distribution. The most common values are tabulated, and for $n = 2$, the 68 and 95 % CL contours correspond to $-2 \log \Lambda(\boldsymbol{\mu}) = 2.3$ and 6.0, respectively.

In order to constrain new physics, we need for each experiment and for each decay mode the full information in this 2D plane and not only one (or two) contours. Hopefully, this information will be released systematically by the experimental collaborations. At the moment it is available for the $H \rightarrow \gamma\gamma$, $H \rightarrow ZZ^*$ and $H \rightarrow WW^*$ final states in ATLAS under a convenient format available on HepData [57–59], and a “temperature plot” in this 2D plane (with the color indicating the value of the likelihood) is given for the CMS $H \rightarrow \gamma\gamma$ results [43]. Whenever this information is not available the way out is to fit the 68 % CL contour, corresponding to

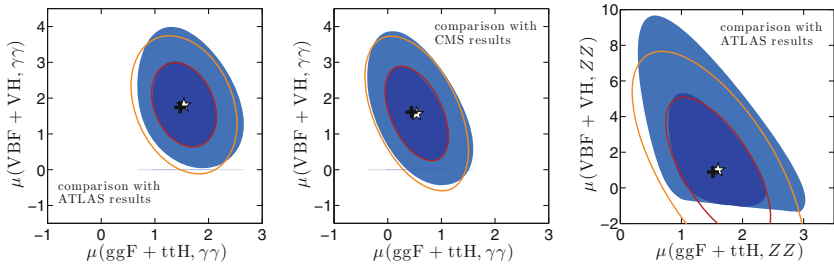


Fig. 2.9 Gaussian fit to signal strengths in the $(\mu(\text{ggF} + \text{ttH}, Y), \mu(\text{VBF} + \text{VH}, Y))$ plane, from left to right for the ATLAS $H \rightarrow \gamma\gamma$ [42], CMS $H \rightarrow \gamma\gamma$ (preliminary) [60], and ATLAS $H \rightarrow ZZ^*$ [42] channels. The dark and light blue filled areas are the 68 and 95 % CL regions given by the experiments, the red and orange lines show the fitted ones. In all three cases, we approximately reconstruct the likelihood by fitting a bivariate normal distribution to the 68 % CL contour given by the collaboration. The black crosses are the experimental best fit points, while the white stars are the mean values from the fit

$-2 \log \Lambda(\boldsymbol{\mu}) = 2.3$, with a bivariate normal distribution. Using the shorthand ggF for ggF+ttH, and VBF for VBF+VH, the likelihood for a given decay mode Y can be expressed as

$$-2 \log \Lambda(\boldsymbol{\mu}) = (\boldsymbol{\mu} - \hat{\boldsymbol{\mu}})^T \begin{pmatrix} \sigma_{\text{ggF}}^2 & \rho \sigma_{\text{ggF}} \sigma_{\text{VBF}} \\ \rho \sigma_{\text{ggF}} \sigma_{\text{VBF}} & \sigma_{\text{VBF}}^2 \end{pmatrix}^{-1} (\boldsymbol{\mu} - \hat{\boldsymbol{\mu}}), \quad (2.14)$$

which is equal to 2.3 for the points $\boldsymbol{\mu} = \begin{pmatrix} \mu_{\text{ggF}} \\ \mu_{\text{VBF}} \end{pmatrix}$ sitting on the 68 % CL contour. From this expression, and using a digitized version of the contour, one can fit the five parameters $\hat{\mu}_{\text{ggF}}$, $\hat{\mu}_{\text{VBF}}$, σ_{ggF} , σ_{VBF} , and ρ (the correlation between the measurements). Several checks can then be made: $(\hat{\mu}_{\text{ggF}}, \hat{\mu}_{\text{VBF}})$ has to be close to the position of the true best fit point, agreement between the fitted 68 % CL contour and the one from ATLAS or CMS should be good, and if a 95 % CL contour is available one can evaluate the importance of non-Gaussianities further away from the best fit region. This is shown for the ATLAS $H \rightarrow \gamma\gamma$ [42], CMS $H \rightarrow \gamma\gamma$ (preliminary) [60], and ATLAS $H \rightarrow ZZ^*$ [42] results in Fig. 2.9. The agreement is excellent except for ATLAS $H \rightarrow ZZ^*$, as could be expected given the small number of events. However, the discrepancy is significant only in extreme regions ($\mu \gg 1$) that are likely to be excluded from other measurements (and first of all from the results in $H \rightarrow WW^*$); also for this channel the full likelihood is now available [58].

This procedure can be applied to all accessible final state in each experiment, and the final likelihood can be expressed as

$$\begin{aligned}
-2 \log L &= \sum_{i=1}^n (-2 \log \Lambda(\boldsymbol{\mu}_i)) + \sum_{j=1}^m (-2 \log L_{\text{full}}(\boldsymbol{\mu}_j)) \\
&= \sum_{i=1}^n (\boldsymbol{\mu}_i - \hat{\boldsymbol{\mu}}_i)^T \left(\begin{array}{cc} \sigma_{\text{ggF},i}^2 & \rho_i \sigma_{\text{ggF},i} \sigma_{\text{VBF},i} \\ \rho_i \sigma_{\text{ggF},i} \sigma_{\text{VBF},i} & \sigma_{\text{VBF},i}^2 \end{array} \right)^{-1} (\boldsymbol{\mu}_i - \hat{\boldsymbol{\mu}}_i) + \sum_{j=1}^m (-2 \log L_{\text{full}}(\boldsymbol{\mu}_j)),
\end{aligned} \tag{2.15}$$

where the index i runs over the n 2D measurements taken into account in the Gaussian approximation, while the index j runs over the m 2D measurements for which the full likelihood is available and taken into account. In order to constrain new physics, taking the results in the $(\mu(\text{ggF} + \text{ttH}, Y), \mu(\text{VBF} + \text{VH}, Y))$ plane has several advantages compared to using the signal strength information from each category. First of all, the problems related to missing information from the experimental side are largely solved: in this approach, the reduced efficiencies eff_X are not needed and there is no concern related to the use of signal strengths before any combination. But the main reason for the likelihood defined in Eq. (2.15) to be a better approximation to the full likelihood than the one in Eq. (2.9) is the complete treatment of the correlations between all systematic uncertainties—for a given decay mode Y in a given experiment. Last but not least, this approach depends less on the Gaussian approximation. This is obvious when the full likelihood in this 2D plane is available, but it generally remains true even when the 2D likelihood is reconstructed from the 68 % CL contour under the (bivariate) Gaussian approximation. Typically, we are losing less information on non-Gaussianities from a single 2D measurement than when using several measurements (if more than two) under the Gaussian approximation.

The results in the $(\mu(\text{ggF} + \text{ttH}, Y), \mu(\text{VBF} + \text{VH}, Y))$ plane can be reconstructed from the information in the individual categories, thus allowing us to check against the results from ATLAS or CMS in the same plane. This is shown in Fig. 2.10, in three example cases (ATLAS $H \rightarrow \gamma\gamma$ [52], CMS $H \rightarrow \gamma\gamma$ (preliminary) [60], and CMS $H \rightarrow ZZ^*$ (preliminary) [61]) where the information on the efficiencies is clearly given. While the ATLAS $H \rightarrow \gamma\gamma$ results are reproduced reasonably well, large discrepancies appear in the two other examples. It should be said that, being closer to the experimental selections, the use of signal strengths from categories should offer more flexibility in testing models, beyond a simple scaling of the SM production and decay modes. However, it would require to reproduce the cuts of the analysis in order to estimate the acceptance \times efficiency factor, $A \times \varepsilon$, that appears in Eq. (2.1). In most cases this is impossible given the complexity of the current analyses.

In Sects. 2.5, 2.6, 2.7 and 2.8, the impact of the LHC Higgs results on new physics will be studied in an effective approach and on explicit new physics scenario. In all cases, the experimental input will be taken from the $(\mu(\text{ggF} + \text{ttH}, Y), \mu(\text{VBF} + \text{VH}, Y))$ plane whenever available. However, this approximation to the full Higgs likelihood can and should be improved in the future. This is in particular crucial for a complete treatment of the theoretical uncertainties and of their correlations. This will be discussed when presenting the public tool `Lilith` in Sect. 2.9. Possible future improvements will be discussed in Sect. 2.10.

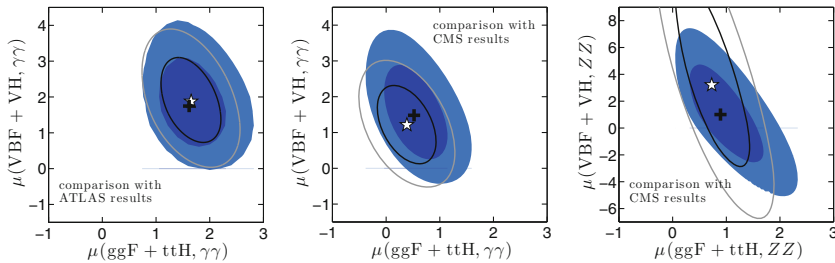


Fig. 2.10 Reconstructing the likelihood from subchannel information. The *black* and *gray lines* show the 68 and 95 % CL contours in the $(\mu(\text{ggF} + \text{ttH}, Y), \mu(\text{VBF} + \text{VH}, Y))$ plane, reconstructed from signal strengths and efficiencies for the experimental categories *I* in each final state; from left to right for the ATLAS $H \rightarrow \gamma\gamma$ [52], CMS $H \rightarrow \gamma\gamma$ [60], and CMS $H \rightarrow ZZ^*$ (preliminary) [61] channels. For comparison, the *dark* and *light blue filled areas* show the 68 and 95 % CL regions directly given by the collaborations. The *black crosses* are the experimental best fit points, the *white stars* are the reconstructed ones

2.5 The Excitement About an Excess in the Diphoton Channel in 2012

In the latest LHC Higgs results presented in Sect. 2.3, no significant deviation from the SM value $\mu = 1$ can be seen. The situation was certainly different at the end of 2012 and at the beginning of 2013. Indeed, the preliminary results from ATLAS and CMS, using the full statistics collected at $\sqrt{s} = 7$ TeV and 5–13 fb^{-1} of data at $\sqrt{s} = 8$ TeV (over the 20 fb^{-1} collected in total in 2012) suggested the presence of an excess in the diphoton channel compared to SM expectations. The experimental situation at the end of 2012 in the $(\mu(\text{ggF} + \text{ttH}, \gamma\gamma), \mu(\text{VBF} + \text{VH}, \gamma\gamma))$ plane is shown in Fig. 2.11. The ATLAS results were updated with 13 fb^{-1} of data at 8 TeV [62] at the Open Session of the CERN Council in December 2012 [63], while CMS results [64] were presented in this plane at the Hadron Collider Physics Symposium in Nov. 2012 (HCP2012) [65], but correspond to the analysis presented in Refs. [2, 66] for 7 TeV data and 5.3 fb^{-1} at 8 TeV. A more than 2σ excess can be seen in Fig. 2.11, and is mostly driven by the ATLAS results. (The excess in the ATLAS data was already present at the time of the discovery [1] and was slightly strengthen with the update presented in December.)

At the end of the summer 2012, Geneviève Bélanger, Ulrich Ellwanger, John F. Gunion, Sabine Kraml and myself started working on possible implications of the LHC Higgs results on new physics—including the $H \rightarrow \gamma\gamma$ results in addition to all other available results—in an effective approach and in the 2HDM. This lead to the paper “Higgs Couplings at the End of 2012”, Ref. [67], that was submitted to arXiv on December 20, 2012 and published in JHEP in February 2013. In the rest of the Section the methodology and the main results presented in Ref. [67] will be given. In 2012 and 2013, there has been a lot of activity from many different groups in fitting the Higgs couplings to the LHC data, using various parametrizations. An

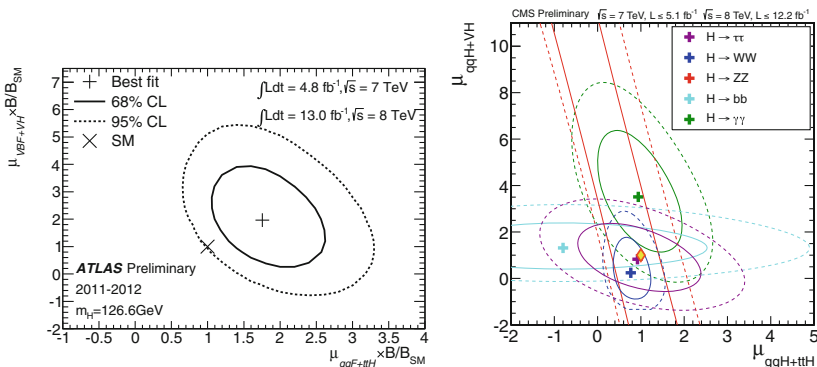


Fig. 2.11 Results from the searches of the Higgs boson decaying into two photons in 2012, from the ATLAS [62] (*left*) and CMS [2, 64, 66] (*right*) collaborations, given in the plane $(\mu(\text{ggF} + \text{ttH}), \mu(\text{VBF} + \text{VH}))$. In addition to the full luminosity at 7 TeV, 13.0 fb⁻¹ (ATLAS) and 5.3 fb⁻¹ (CMS) of data at 8 TeV are used. Shown are contours of constant likelihood, with the *solid line* corresponding to 68 % CL and the *dashed line* to 95 % CL

extensive (yet probably incomplete) list of work on this topic up to now can be found in [68–102]; theoretical uncertainties were also discussed in [103].

The section is organized as follows. The framework that is used is presented in Sect. 2.5.1, while the experimental inputs and the fitting procedure are described in Sect. 2.5.2. The results of three generic fits are presented in Sect. 2.5.3 together with the results of a fit in Two-Higgs-Doublet models in Sect. 2.5.4. Section 2.5.5 contains our conclusions.

2.5.1 Framework

With the measurements in various channels, a comprehensive study of the properties of the Higgs-like state becomes possible and has the potential for revealing whether or not the Higgs sector is as simple as envisioned in the SM. In particular it is crucial to determine the Higgs couplings to gauge bosons and to fermions as defined by the Lagrangian

$$\mathcal{L} = g \left[C_W m_W W_\mu W^\mu + C_Z \frac{m_Z}{\cos \theta_W} Z_\mu Z^\mu - \sum_F C_F \frac{m_F}{2m_W} \bar{F} F \right] H, \quad (2.16)$$

where the C_I are scaling factors for the couplings relative to their SM values, introduced to test possible deviations in the data from SM expectations. In principle all the C_I are independent, in particular the C_F can be different for up- and down-type quarks and/or leptons. A significant deviation of any C_I from unity would imply new physics beyond the SM.

While fits to various combinations of C_I 's are performed by the experimental collaborations themselves [64, 104], we find it important to develop our own scheme in order to bring all results from ATLAS, CMS and the Tevatron experiments together and test not only the SM but also specific models beyond. In the present study, we include all publicly available data as of the end of 2012. In particular we take into account the updates presented at HCP2012 in Nov. 2012 [65] and at the Open Session of the CERN Council in Dec. 2012 [63].

Our parametrization is as follows. We treat the couplings to up-type and down-type fermions, C_U and C_D , as independent parameters (but we only consider the case $C_L = C_D$, and we assume that the C_F are family universal). Moreover, we assume a custodial symmetry in employing a single $C_W = C_Z \equiv C_V$ in Eq. (2.16). The structure we are testing thus becomes

$$\mathcal{L} = g \left[C_V \left(m_W W_\mu W^\mu + \frac{m_Z}{\cos \theta_W} Z_\mu Z^\mu \right) - C_U \frac{m_t}{2m_W} \bar{t}t - C_D \frac{m_b}{2m_W} \bar{b}b - C_D \frac{m_\tau}{2m_W} \bar{\tau}\tau \right] H. \quad (2.17)$$

In general, the C_I can take on negative as well as positive values; there is one overall sign ambiguity which we fix by taking $C_V > 0$. Even in this restricted context, various types of deviations of these three C_I from unity are possible in extended theories such as 2HDMs, models with singlet-doublet mixing, and supersymmetric models such as the MSSM and the Next-to-MSSM (NMSSM).

In addition to the tree-level couplings given above, the H has couplings to gg and $\gamma\gamma$ that are first induced at one loop and are completely computable in terms of C_U , C_D and C_V if only loops containing SM particles are present. We define \overline{C}_g and \overline{C}_γ to be the ratio of these couplings so computed to the SM (i.e. $C_U = C_D = C_V = 1$) values. However, in some of our fits we will also allow for additional loop contributions ΔC_g and ΔC_γ from new particles; in this case $C_g = \overline{C}_g + \Delta C_g$ and $C_\gamma = \overline{C}_\gamma + \Delta C_\gamma$. The largest set of independent parameters in our fits is thus

$$C_U, C_D, C_V, \Delta C_g, \Delta C_\gamma. \quad (2.18)$$

In this study, we focus on models in which the Higgs decays only to SM particles, in particular not allowing for invisible (i.e. $H \rightarrow \tilde{\chi}_1^0 \tilde{\chi}_1^0$, where $\tilde{\chi}_1^0$ is the lightest SUSY particle) or undetected decays (such as $H \rightarrow aa$, where a is a light CP-odd, perhaps singlet scalar). This approach, when we allow in the most general case for the C_U , C_D , C_V , C_γ and C_g couplings to be fully independent, encompasses a very broad range of models, including in particular those in which the Higgs sector consists of any number of doublets + singlets, the only proviso being the absence of decays of the observed ~ 125 GeV state to non-SM final states. (A fit for invisible Higgs decays was performed early on in [105].) This approach however does not cover models such as composite models and Higgs-radion mixing models for which the VVH coupling has a more complicated tensor structure than that given in Eq. (2.17). Our procedure will also be inadequate should the observed signal at ~ 125 GeV actually arise from two or more degenerate Higgs bosons (see i.e. [106, 107]). Although the

success of our fits implies that there is no need for such extra states, the explicit tests for degenerate states developed in [108] should be kept in mind as a means to test directly for two or more Higgs bosons contributing to the signal at 125 GeV. Note that the presence of two near mass-degenerate states has already been tested by the CMS collaboration in the $H \rightarrow \gamma\gamma$ channel [109].

2.5.2 Experimental Inputs and Fitting Procedure

We perform fits employing all production/decay channels for which results are available from the ATLAS and CMS collaborations at the LHC, as well as the Tevatron CDF+D0 Higgs results. The values for the signal strengths in the various (sub)channels as reported by the experiments and used in this analysis, together with the estimated decompositions into production channels are given in Tables 2.1, 2.2 and 2.3. Note that all measurements are only given in the Gaussian approximation; a χ^2 is computed using the method explained in Sect. 2.4. Measurements in the $(\mu(\text{ggF} + \text{ttH}, Y), \mu(\text{VBF} + \text{VH}, Y))$ plane were not yet systematically available and have not always been favored over the category results. For the computation of the various $\mu(X, Y)$ from the reduced couplings including next-to-leading order (NLO) corrections we follow the procedure recommended by the LHC Higgs Cross Section Working Group in [110]. In particular we include all the available QCD

Table 2.1 ATLAS results as employed in this analysis. The correlations included in the fits are $\rho = -0.37$ for the $\gamma\gamma$ and $\rho = -0.50$ for the $\tau\tau$ channels

Channel	Signal strength μ	m_H (GeV)	Reduced efficiencies			
			ggF (%)	VBF (%)	VH (%)	ttH (%)
$H \rightarrow \gamma\gamma$ (4.8 fb ⁻¹ at 7 TeV + 13.0 fb ⁻¹ at 8 TeV) [62]						
$\mu(\text{ggF} + \text{ttH}, \gamma\gamma)$	1.85 ± 0.52	126.6	100	–	–	–
$\mu(\text{VBF} + \text{VH}, \gamma\gamma)$	2.01 ± 1.23	126.6	–	60	40	–
$H \rightarrow ZZ$ (4.6 fb ⁻¹ at 7 TeV + 13.0 fb ⁻¹ at 8 TeV) [113, 114]						
Inclusive	$1.01^{+0.45}_{-0.40}$	125	87	7	5	1
$H \rightarrow WW$ (13.0 fb ⁻¹ at 8 TeV) [114, 115]						
$e\nu\mu\nu$	$1.42^{+0.58}_{-0.54}$	125.5	95	3	2	–
$H \rightarrow b\bar{b}$ (4.7 fb ⁻¹ at 7 TeV + 13.0 fb ⁻¹ at 8 TeV) [114, 116]						
VH tag	-0.39 ± 1.02	125.5	–	–	100	–
$H \rightarrow \tau\tau$ (4.6 fb ⁻¹ at 7 TeV + 13.0 fb ⁻¹ at 8 TeV) [117]						
$\mu(\text{ggF}, \tau\tau)$	2.41 ± 1.57	125	100	–	–	–
$\mu(\text{VBF} + \text{VH}, \tau\tau)$	-0.26 ± 1.02	125	–	60	40	–

Table 2.2 CMS results as employed in this analysis. The correlation included for the $\gamma\gamma$ channel is $\rho = -0.54$

Channel	Signal strength μ	m_H (GeV)	Reduced efficiencies			
			ggF (%)	VBF (%)	VH (%)	ttH (%)
$H \rightarrow \gamma\gamma$ (5.1 fb $^{-1}$ at 7 TeV + 5.3 fb $^{-1}$ at 8 TeV) [2, 64, 66]						
$\mu(\text{ggF} + \text{ttH}, \gamma\gamma)$	0.95 ± 0.65	125.8	100	–	–	–
$\mu(\text{VBF} + \text{VH}, \gamma\gamma)$	3.77 ± 1.75	125.8	–	60	40	–
$H \rightarrow ZZ$ (5.1 fb $^{-1}$ at 7 TeV + 12.2 fb $^{-1}$ at 8 TeV) [64, 118]						
Inclusive	$0.81^{+0.35}_{-0.28}$	125.8	87	7	5	1
$H \rightarrow WW$ (up to 4.9 fb $^{-1}$ at 7 TeV + 12.1 fb $^{-1}$ at 8 TeV) [64, 119, 120]						
0/1 jet	$0.77^{+0.27}_{-0.25}$	125.8	97	3	–	–
VBF tag	$-0.05^{+0.74}_{-0.55}$	125.8	17	83	–	–
VH tag	$-0.31^{+2.22}_{-1.94}$	125.8	–	–	100	–
$H \rightarrow b\bar{b}$ (up to 5.0 fb $^{-1}$ at 7 TeV + 12.1 fb $^{-1}$ at 8 TeV) [64, 121, 122]						
VH tag	$1.31^{+0.65}_{-0.60}$	125.8	–	–	100	–
ttH tag	$-0.80^{+2.10}_{-1.84}$	125.8	–	–	–	100
$H \rightarrow \tau\tau$ (up to 5.0 fb $^{-1}$ at 7 TeV + 12.1 fb $^{-1}$ at 8 TeV) [64, 123, 124]						
0/1 jet	$0.85^{+0.68}_{-0.66}$	125.8	76	16	7	1
VBF tag	$0.82^{+0.82}_{-0.75}$	125.8	19	81	–	–
VH tag	$0.86^{+1.92}_{-1.68}$	125.8	–	–	100	–

Table 2.3 Tevatron results for up to 10 fb $^{-1}$ at $\sqrt{s} = 1.96$ TeV, as employed in this analysis

Channel	Signal strength μ	m_H (GeV)	Reduced efficiencies			
			ggF (%)	VBF (%)	VH (%)	ttH (%)
$H \rightarrow \gamma\gamma$ [125]						
Combined	$6.14^{+3.25}_{-3.19}$	125	78	5	17	–
$H \rightarrow WW$ [125]						
Combined	$0.85^{+0.88}_{-0.81}$	125	78	5	17	–
$H \rightarrow b\bar{b}$ [126]						
VH tag	$1.56^{+0.72}_{-0.73}$	125	–	–	100	–

corrections for C_g using HIGLU [29, 111, 112] and for C_γ using HDECAY [29, 30], and we switch off the electroweak corrections. The reduced efficiencies eff_X are specific to every analysis and hence differ from experiment to experiment. Whenever these are not given, we assume that the search is inclusive.

With this framework programmed, our fitting procedure is as follows. We first scan over a fine grid of the free parameters of the scenario considered, for example, C_U, C_D, C_V with $C_g, C_\gamma = \overline{C}_g, \overline{C}_\gamma$ as computed from the SM-particle loops (this

will be Fit II below). We obtain the value of χ^2 associated with each point in the grid and thus determine the values of the parameters associated with the approximate minimum (or minima). To get the true minimum χ^2 , χ_{\min}^2 , and the associated “best-fit” values and the one-standard deviation (1σ) errors on them we employ MINUIT [127]. (The errors on parameters which are not input, i.e. C_g and C_γ , are determined from the grid data.) For plotting distributions of χ^2 as a function of any one variable, we use the above grid data together with the best fit value, to profile the minimal χ^2 value with respect to the remaining unconstrained parameters. The 68, 95 and 99.7% CL intervals are then given by $\chi^2 = \chi_{\min}^2 + 1, +4$ and $+9$, respectively. Two-dimensional χ^2 distributions are obtained analogously from a grid in the two parameters of interest, profiling over the other, unseen parameters; in this case, we show contours of χ^2 corresponding to the 68% ($\chi^2 = \chi_{\min}^2 + 2.30$), 95% ($\chi^2 = \chi_{\min}^2 + 6.18$) and 99.7% ($\chi^2 = \chi_{\min}^2 + 11.83$) confidence levels for 2 parameters treated jointly. Note that it corresponds to a profile likelihood ratio and that the same procedure is used by the experimental collaborations to perform coupling fits and also derive the results in the $(\mu(\text{ggF} + \text{ttH}, Y), \mu(\text{VBF} + \text{VH}, Y))$ plane, as was explained in Eq. (2.13) in Sect. 2.4.

Before presenting our results, a couple of comments are in order. First of all, we stress that in models of new physics beyond-the-SM (BSM), both the branching fractions and the production cross sections and distributions (and indeed the number of Higgs particles) may differ from SM expectations. For any BSM interpretation of the Higgs search results it is absolutely crucial to have as precise and complete channel-by-channel information as possible [128]. Unfortunately, not all the experimental analyses give all the necessary details. Below we comment on how we use the currently available information from the experiments.

ATLAS

- $H \rightarrow \gamma\gamma$: we fit the 68% CL contour in the $(\mu(\text{ggF} + \text{ttH}, Y), \mu(\text{VBF} + \text{VH}, Y))$ plane from Fig. 4 of [62] as explained around Eq. (2.14) in Sect. 2.4. We note that while Fig. 4 of [62] is for 126.6 GeV, Fig. 12 (right) in the same paper shows that there is a broad “plateau” as a function of the mass when the energy scale uncertainty is taken into account, implying that the results should not depend too much on the mass.
- $H \rightarrow ZZ$: the signal strength in this channel reported by ATLAS [113, 114] is $\mu = 1.3^{+0.53}_{-0.48}$ with a best fit mass of $m_H = 123.5 \pm 0.9$ (stat.) ± 0.3 (sys.) GeV. At $m_H = 125$ GeV, the signal strength is $\mu = 1.01^{+0.45}_{-0.40}$, see Fig. 10 in [114]. Assuming that the discrepancy in the Higgs mass determined from the $\gamma\gamma$ and the 4 lepton final states is due to a statistical fluctuation (rather than unknown systematics) we use the inclusive $\mu(H \rightarrow ZZ)$ results at $m_H = 125$ GeV, i.e. close to the combined best fit mass from ATLAS, in our fits. Alternatively, one could rescale the value of $\mu = 1.3^{+0.53}_{-0.48}$ at $m_H = 123.5$ GeV for a Higgs mass of 125 GeV. This would give $\mu(H \rightarrow ZZ) = 1.15^{+0.53}_{-0.48}$ at $m_H = 125$ GeV (or $\mu(H \rightarrow ZZ) = 1.11^{+0.53}_{-0.48}$ at $m_H = 125.5$ GeV). We checked that taking this alternative approach has only marginal influence on our results. Regarding the

decomposition in production modes, no statement is made in the conference note or paper. However, as it is an inclusive analysis, we take the relative ratios of production cross sections for an SM Higgs as a reasonable approximation. To this end, we use the ratios given by the LHC Higgs Cross Section Working Group [129].

- $H \rightarrow WW$: we adopt relative contributions of 95 % ggF and 5 % VBF [115]. We do not include any result for 7 TeV because the update presented at HCP is a combination of 7 and 8 TeV.

CMS

- $H \rightarrow \gamma\gamma$: we follow the same procedure as for ATLAS $H \rightarrow \gamma\gamma$, using Fig. 11 from [64]. The correlation is $\rho = -0.54$.
- $H \rightarrow ZZ$: no decomposition with respect to production modes is given in the conference note or paper. As it is a fully inclusive analysis, we use the relative ratios of production cross sections given by the LHC Higgs Cross Section Working Group [129] as a good approximation [130].
- $H \rightarrow WW$: the information provided in the conference note and papers is incomplete; our decomposition into production modes is based on [130]. Our combination (weighted mean) agrees within 9 % with that given by CMS ($\mu_{\text{comb}} = 0.64 \pm 0.24$ instead of $0.70^{+0.24}_{-0.23}$).
- $H \rightarrow b\bar{b}$: as there is no information on possible contaminations by other production modes, we assume 100 % VH or 100 % tH production for the respective categories.
- $H \rightarrow \tau\tau$: for the 0/1 jet and VBF tag categories we extract the decomposition into production modes from [123], assuming that there is no significant change in the efficiencies between $m_H = 125 \text{ GeV}$ and $m_H = 125.8 \text{ GeV}$. We use the efficiencies from the first three categories ($\mu\tau_h + X$, $e\tau_h + X$ and $e\mu + X$) because they are the most sensitive ones; they lead to very similar decompositions which we use in our analysis. Our combination (weighted mean) agrees within 6 % with that given by CMS ($\mu_{\text{comb}} = 0.83 \pm 0.49$ instead of $0.88^{+0.51}_{-0.48}$).

Tevatron

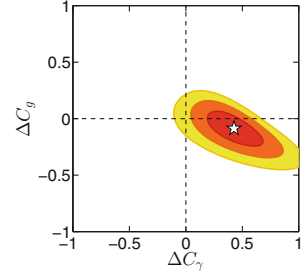
- $H \rightarrow \gamma\gamma$ and $H \rightarrow WW$: no decomposition into production modes is given by the experiments. We assume that the analyses are inclusive and we thus employ the ratios of the theoretical predictions for the (SM) Higgs production cross sections.
- $H \rightarrow b\bar{b}$: we use the results presented at HCP2012 [126] assuming 100 % VH.

2.5.3 Fits to Reduced Higgs Couplings

Fit I: $C_U = C_D = C_V = 1$, ΔC_g and ΔC_γ Free

For a first test of the SM nature of the observed Higgs boson, we take $C_U = C_D = C_V = 1$ (i.e. quark, lepton and W , Z vector boson couplings to the Higgs are required to be SM-like) but we allow for additional new physics contributions to the $\gamma\gamma$ and

Fig. 2.12 Two parameter fit of ΔC_γ and ΔC_g , assuming $C_U = C_D = C_V = 1$ (Fit **I**). The red, orange and yellow ellipses show the 68, 95 and 99.7 % CL regions, respectively. The white star marks the best-fit point $\Delta C_\gamma = 0.426$, $\Delta C_g = -0.086$



gg couplings, parameterized by ΔC_g and ΔC_γ , coming from loops involving non-SM particles. This fit, which we refer to as Fit **I**, is designed to determine if the case where all tree-level Higgs couplings are equal to their SM values can be consistent with the data. For example, such a fit is relevant in the context of UED models where the tree-level couplings of the Higgs are SM-like [131, 132].

Figure 2.12 displays the results of this fit in the ΔC_g versus ΔC_γ plane. The best fit is obtained for $\Delta C_\gamma \simeq 0.43$, $\Delta C_g \simeq -0.09$, and has $\chi^2_{\min} = 12.31$ for 19 degrees of freedom (d.o.f.), giving a p -value of 0.87. The results of this fit are summarized in Table 2.4, together with the results of the other fits of this section.

We note that the SM (i.e. $C_U = C_D = C_V = 1$, $\Delta C_g = \Delta C_\gamma = 0$) has $\chi^2 = 20.2$ and is hence more than 2σ away from the best fit in Fig. 2.12. The number of degrees of freedom for the SM fit is 21, implying a p -value of 0.51. The largest χ^2 contributions come from the $H \rightarrow \gamma\gamma$ channels from ATLAS ($\Delta\chi^2 = 5.06$), CMS ($\Delta\chi^2 = 3.36$) and Tevatron ($\Delta\chi^2 = 2.60$), followed by the VBF result for $H \rightarrow WW$ from CMS with $\Delta\chi^2 = 2.01$.

Fit II: Varying C_U , C_V and C_V ($\Delta C_\gamma = \Delta C_g = 0$)

Next, we let C_U , C_D , C_V vary, assuming there are no new particles contributing to the effective Higgs couplings to gluons and photons, i.e. we take $\Delta C_\gamma = \Delta C_g = 0$

Table 2.4 Summary of results for Fits **I–III**. For Fit **II**, the tabulated results are from the best fit, cf. column 1 of Table 2.5

Fit	I	II	III , 1st min.	III , 2nd min.
C_U	1	$-0.86^{+0.14}_{-0.16}$	-0.06 ± 1.30	0.06 ± 1.30
C_D	1	$0.99^{+0.28}_{-0.26}$	$1.00^{+0.28}_{-0.26}$	$-1.00^{+0.26}_{-0.28}$
C_V	1	$0.95^{+0.12}_{-0.13}$	$0.93^{+0.12}_{-0.14}$	$0.93^{+0.12}_{-0.14}$
ΔC_γ	$0.43^{+0.17}_{-0.16}$	–	$0.16^{+0.38}_{-0.36}$	$0.21^{+0.37}_{-0.39}$
ΔC_g	-0.09 ± 0.10	–	$0.83^{+0.24}_{-1.17}$	$0.83^{+0.24}_{-1.17}$
C_γ	$1.43^{+0.17}_{-0.16}$	1.43 ± 0.17	$1.36^{+0.26}_{-0.23}$	$1.36^{+0.26}_{-0.23}$
C_g	0.91 ± 0.10	$0.92^{+0.17}_{-0.15}$	$0.95^{+0.26}_{-0.23}$	$0.95^{+0.26}_{-0.23}$
χ^2_{\min}	12.31	11.95	11.46	11.46
$\chi^2_{\min}/\text{d.o.f.}$	0.65	0.66	0.72	0.72

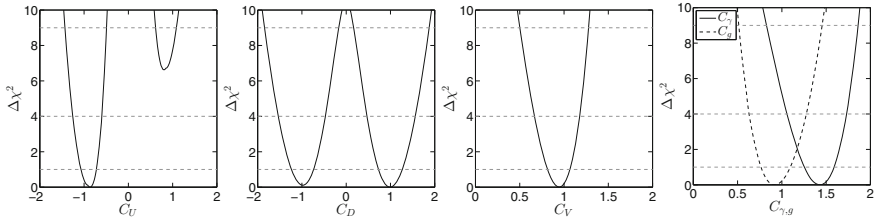


Fig. 2.13 One-dimensional χ^2 distributions for the three parameter fit, Fit II, of C_U, C_D, C_V with $C_\gamma = \overline{C_\gamma}$ and $C_g = \overline{C_g}$ as computed in terms of C_U, C_D, C_V .

implying $C_g = \overline{C_g}$, $C_\gamma = \overline{C_\gamma}$ as computed from the SM-particle loops. The results for the one-dimensional and two-dimensional χ^2 distributions are shown in Figs. 2.13 and 2.14. The value of C_V is rather well determined to be close to unity. It is intriguing that the best fit of C_V is indeed just slightly below 1, as any model with only Higgs doublets or singlets requires $C_V \leq 1$. The best fit values for C_D and C_U are SM-like in that they have magnitudes that are close to one. However, the best fit C_U value is opposite in sign to the SM Higgs case. The preference for $C_U < 0$ is at the level of 2.6σ —see the first plot in Fig. 2.13. This results from the fact that an enhanced $\gamma\gamma$ rate (as observed in the experimental data) is obtained by changing the sign of the top-loop contribution so that it adds, rather than subtracts, from the

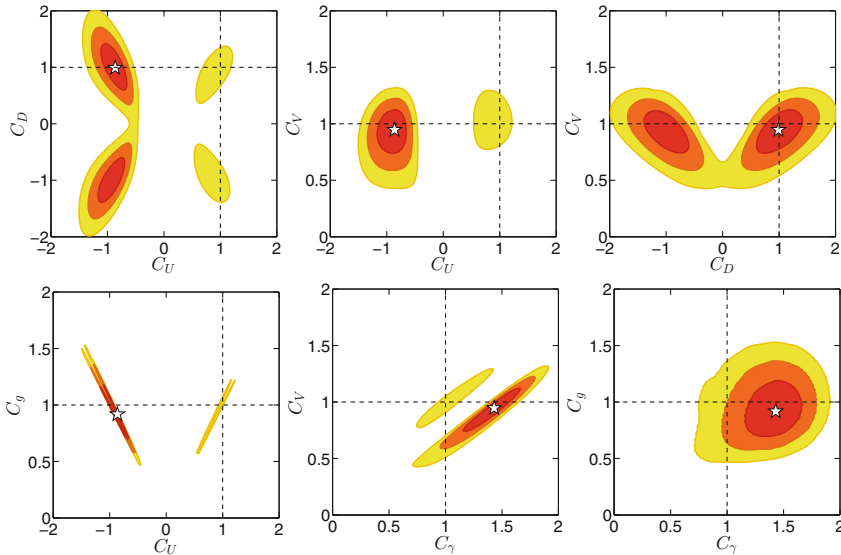


Fig. 2.14 Two-dimensional χ^2 distributions for the three parameter fit, Fit II, of C_U, C_D, C_V with $C_\gamma = \overline{C_\gamma}$ and $C_g = \overline{C_g}$ as computed in terms of C_U, C_D, C_V . The red, orange and yellow ellipses show the 68, 95 and 99.7 % CL regions, respectively. The white star marks the best-fit point. Details on the minima in different sectors of the (C_U, C_D) plane can be found in Table 2.5.

Table 2.5 Results for Fit II in different sectors of the (C_U, C_D) plane

Sector	$C_U < 0, C_D > 0$	$C_U, C_D < 0$	$C_U, C_D > 0$
C_U	$-0.86^{+0.14}_{-0.16}$	$-0.91^{+0.15}_{-0.17}$	$0.85^{+0.15}_{-0.13}$
C_D	$0.99^{+0.28}_{-0.26}$	$-0.98^{+0.26}_{-0.27}$	$0.85^{+0.22}_{-0.21}$
C_V	$0.95^{+0.12}_{-0.13}$	$0.94^{+0.12}_{-0.13}$	$1.06^{+0.11}_{-0.12}$
C_γ	1.43 ± 0.17	$1.43^{+0.16}_{-0.17}$	$1.11^{+0.15}_{-0.16}$
C_g	$0.92^{+0.17}_{-0.15}$	$0.91^{+0.17}_{-0.15}$	$0.85^{+0.16}_{-0.13}$
χ^2_{\min}	11.95	12.06	18.66
$\chi^2_{\min}/\text{d.o.f.}$	0.66	0.67	1.04

W loop. In contrast, in the case of C_D almost equally good minima are found with $C_D < 0$ and $C_D > 0$. Details on the minima in different sectors of the (C_U, C_D) plane are given in Table 2.5. Note that, for the best fit point, the resulting C_γ and C_g are in good agreement with the result of Fit I above, for which $C_\gamma = 1.43$ and $C_g = 0.91$. Here, however, the enhanced C_γ value derives from $C_U < 0$ rather than from $\Delta C_\gamma \neq 0$. The best fit results are again tabulated in Table 2.4.

A negative sign of C_U —while maintaining a positive sign of m_t —is actually not easy to achieve. (A sign change of both C_U and m_t would have no impact on the top quark induced loop amplitudes.) It would require that m_t is induced dominantly by the vev of a Higgs boson which is *not* the Higgs boson considered here. Hence, we have $C_U > 0$ in most models, implying that it is important to study the impact of this constraint on our fits. The fit results when requiring $C_U, C_D > 0$ are shown in the left two plots of Fig. 2.15 and the top row of Fig. 2.16; see also Table 2.5. We observe that for this quadrant the results are consistent with SM expectations (i.e. within $\sim 1\sigma$). Interestingly the fit is not better than the SM itself: $\chi^2_{\min} = 18.66$ for $21 - 3 = 18$ d.o.f., corresponding to $p = 0.41$.

Another possible model constraint is to require $C_V \leq 1$ (recall that $C_V > 0$ by convention). This constraint applies to any model containing only Higgs doublets and singlets. The 1d results for the combined requirement of $C_U, C_D > 0$ and $C_V \leq 1$ are shown in the right two plots of Fig. 2.15, and in the bottom-row plots of Fig. 2.16. We

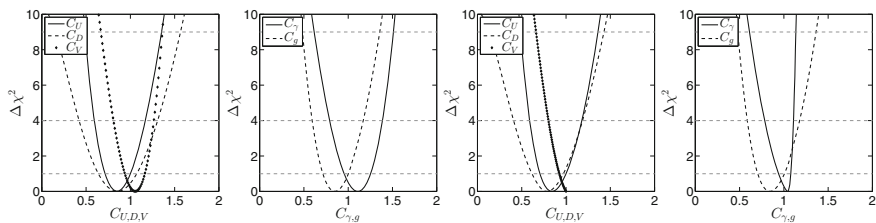


Fig. 2.15 One-dimensional χ^2 distributions for the three parameter fit, Fit II, but imposing $C_U > 0, C_D > 0$; the *left two plots* allow for $C_V > 1$ ($\chi^2_{\min} = 18.66$), while in the *right two plots* $C_V \leq 1$ ($\chi^2_{\min} = 18.89$)

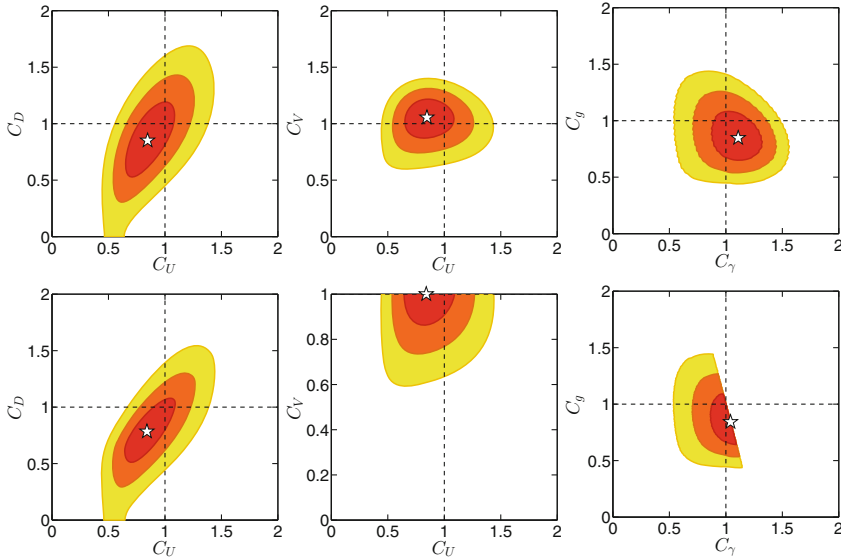


Fig. 2.16 Two-dimensional χ^2 distributions for the three parameter fit, Fit II, as in Fig. 2.14 but with $C_U > 0$, $C_D > 0$, $C_V > 0$. The *upper row* of plots allows for $C_V > 1$, while in the *lower row* of plots $C_V \leq 1$ is imposed

observe that the best fit values for C_U and C_D are only slightly shifted relative those found without constraining C_V , and that accordingly the $C_\gamma = \overline{C}_\gamma$ and $C_g = \overline{C}_g$ at the best fit point are only slightly shifted. However, the $C_V \leq 1$ constraint does severely change the upper bound on C_γ , which for $C_U > 0$ and $\Delta C_\gamma = 0$ mostly depends on the W -boson loop contribution. The apparent sharpness of the boundary in the C_g versus C_γ plane is a result of the fact that these two quantities really only depend on C_U for $C_V = 1$.

Finally note that it has been shown in [133, 134] that single top production in association with a Higgs is greatly enhanced when C_U , C_V have opposite signs. Thus, the possibility of $C_U < 0$ should be further scrutinized by precision measurements of the single top production cross section at the LHC.

Fit III: Varying C_U , C_D , C_V , ΔC_γ and ΔC_g

Finally, in Fit III, we allow the ΔC_g and ΔC_γ additions to \overline{C}_g and \overline{C}_γ , fitting therefore to five free parameters: C_U , C_D , C_V , ΔC_g , and ΔC_γ . The associated 1d and 2d plots are given in Figs. 2.17 and 2.18. There are two main differences as compared to Fit II. On the one hand, the preference for $C_\gamma > 1$ does not necessarily imply a negative value for C_U , since a positive value for ΔC_γ can contribute to an increase in C_γ even when the top-quark loop interferes destructively with the W loop. (This is obviously already expected from Fit I.) On the other hand, both C_U and ΔC_g feed into the effective C_g , and if one of them is large the other one has to be small to result in a near SM-like $gg \rightarrow H$ cross section. This anti-correlation between $|C_U|$ and ΔC_g

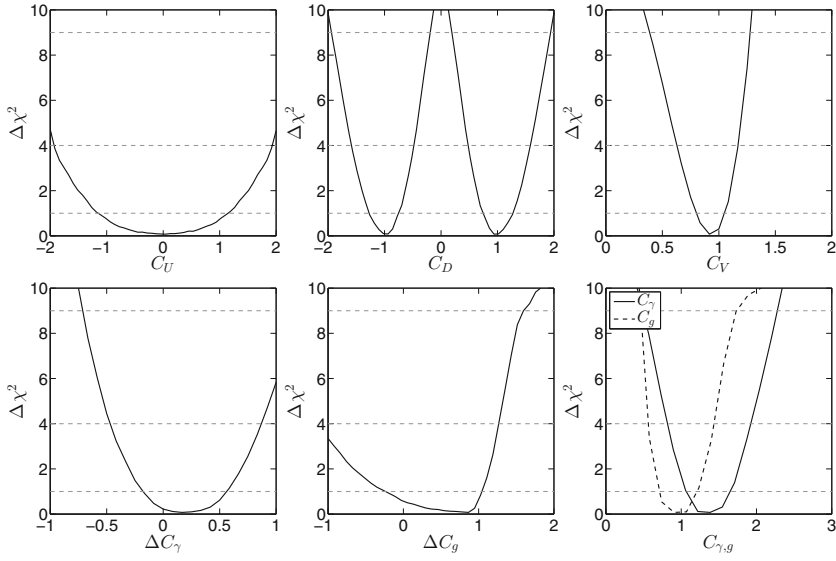


Fig. 2.17 One-dimensional χ^2 distributions for the five parameter fit of C_U , C_D , C_V , ΔC_γ and ΔC_g (Fit III). Details regarding the best fit point are given in Table 2.4

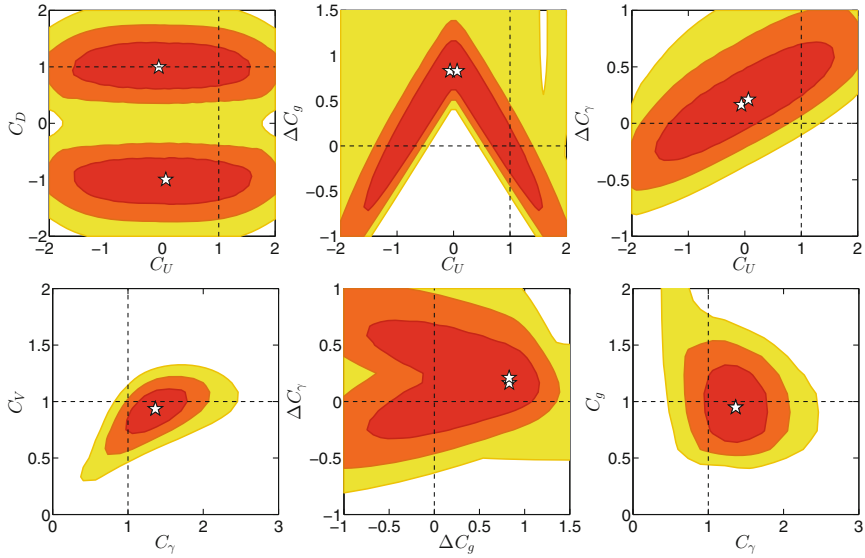
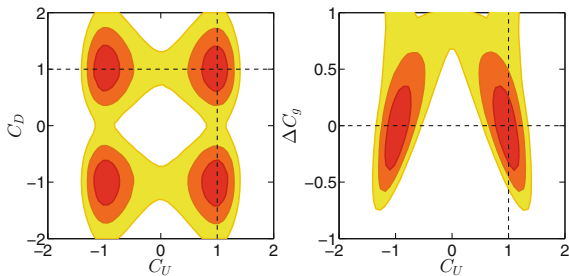


Fig. 2.18 Two-dimensional distributions for the five parameter fit of C_U , C_D , C_V , ΔC_γ and ΔC_g (Fit III). Details regarding the best fit point are given in Table 2.4

Fig. 2.19 Lifting of the degeneracy in C_U and ΔC_g in Fit **III** when $t\bar{t}H$ is measured to 30% accuracy ($\mu(t\bar{t}H) = 1 \pm 0.3$). These two plots should be compared to the *top left* and *top middle* plots of Fig. 2.18. See text for details



can be seen in the center-top plot in Fig. 2.18. The best fit is actually obtained for $C_U \approx 0$, with $\Delta C_g \approx 1$ in order to compensate for the very suppressed top-loop contribution to ggF. However, it is also apparent that the minimum at $C_U = 0$ is quite shallow (cf. the top left plot in Fig. 2.17) and that a fit with $C_U \approx 1$ with small ΔC_g is well within the 68% contour (as should indeed be the case for consistency with Fits **I** and **II**).

We also note that at the best fit, i.e. that with $C_U \approx 0$, one finds $C_\gamma \sim \overline{C}_\gamma > 1$ by virtue of the fact that the W loop is not partially canceled by the top loop and only a small $\Delta C_\gamma \sim 0.16\text{--}0.21$ is needed to further enhance the $\gamma\gamma$ final state and bring $\mu(\gamma\gamma)$ into agreement with observations; see top-right and bottom-right plots of Fig. 2.18. If we move to the SM value of $C_U = 1$ then $\Delta C_\gamma \sim 0.45$ is needed to fit the $\gamma\gamma$ rate. The best fit results are tabulated in Table 2.4.

A way to lift the degeneracy in C_U and ΔC_g would be to have an independent determination of C_U . This might be achieved by an accurate measurement of the $t\bar{t}H$ channel, as illustrated in Fig. 2.19. This figure assumes that $\mu(t\bar{t}H)$ will eventually be measured with 30% accuracy—more concretely, the figure assumes $\mu(t\bar{t}H) = 1 \pm 0.3$. This is certainly a very challenging task. For comparison, CMS currently gives $\mu(t\bar{t}H) \approx -0.8^{+2.2}_{-1.8}$ [64]. Finally, as mentioned above, C_U may also be constrained by the associated production of a single top and a Higgs [133, 134].

2.5.4 Application to Two-Higgs-Doublet Models

So far our fits have been model-independent, relying only on the Lagrangian structure of Eq. (2.17). Let us now turn to the concrete examples of Two-Higgs-Doublet Models (2HDMs) of Type I and Type II. In both cases, the basic parameters describing the coupling of either the light h or heavy H CP-even Higgs boson are only two: α (the CP-even Higgs mixing angle) and $\tan \beta = v_u/v_d$, where v_u and v_d are the vacuum expectation values of the Higgs field that couples to up-type quarks and down-type quarks, respectively. The Type I and Type II models are distinguished by the pattern of their fermionic couplings as given in Table 2.6. The SM limit for the h (H) in the case of both Type I and Type II models corresponds to $\alpha = \beta - \pi/2$ ($\alpha = \beta$). In our

Table 2.6 Tree-level vector boson couplings $C_V^{h_i}$ ($V = W, Z$) and fermionic couplings $C_F^{h_i}$ normalized to their SM values for the Type I and Type II two-Higgs-doublet models

	Type I and II	Type I		Type II	
Higgs	VV	Up quarks	Down quarks & leptons	Up quarks	Down quarks & leptons
h	$\sin(\beta - \alpha)$	$\cos \alpha / \sin \beta$	$\cos \alpha / \sin \beta$	$\cos \alpha / \sin \beta$	$-\sin \alpha / \cos \beta$
H	$\cos(\beta - \alpha)$	$\sin \alpha / \sin \beta$	$\sin \alpha / \sin \beta$	$\sin \alpha / \sin \beta$	$\cos \alpha / \cos \beta$
A	0	$\cot \beta$	$-\cot \beta$	$\cot \beta$	$\tan \beta$

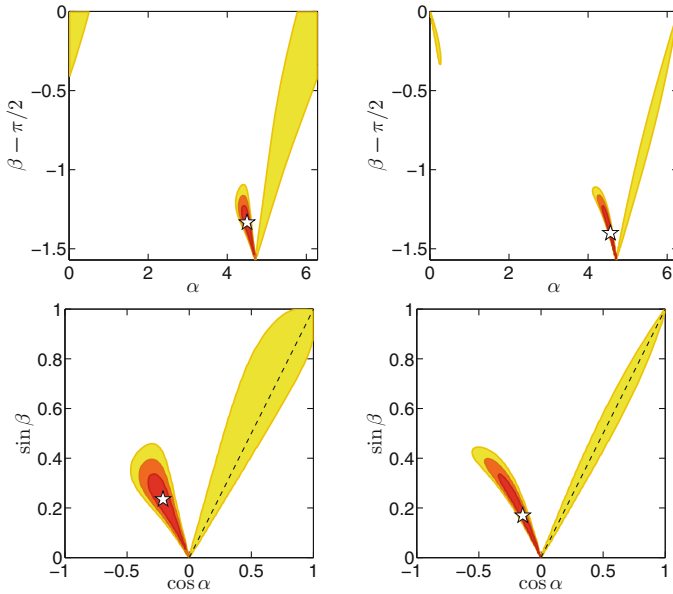


Fig. 2.20 2HDM fits for the h in the Type I (left) and Type II (right) models. The *upper row* shows the fit results in the $\beta - \pi/2$ versus α plane, while the *lower row* shows the $\sin \beta$ versus $\cos \alpha$ plane. The *dashed lines* indicate the SM limit. The same results are obtained for the heavier H with the replacements $\beta - \pi/2 \rightarrow \beta$ and $\alpha \rightarrow \alpha + \pi/2$ ($\sin \beta \rightarrow -\cos \beta$, $\cos \alpha \rightarrow \sin \alpha$)

discussion below, we implicitly assume that there are no contributions from non-SM particles to the loop diagrams for C_γ and C_g . In particular, this means our results correspond to the case where the charged Higgs boson, whose loop might contribute to C_γ , is heavy.

The results of the 2HDM fits are shown in Fig. 2.20 for the case that the state near 125 GeV is the lighter CP-even h . The figure also applies for the case of the heavier H being identified with the ~ 125 GeV state with the replacement rules given in the

Table 2.7 Summary of fit results for the h in 2HDMs of Type I and Type II

Fit	2HDM-I	2HDM-II	2HDM-I, $\tan \beta > 1$	2HDM-II, $\tan \beta > 1$
α [rad]	$4.50^{+0.09}_{-0.08}$	$4.56^{+0.15}_{-0.14}$	$5.37^{+1.11}_{-0.13}$	$6.28^{+0.17}_{-0.83}$
β [rad]	$0.24^{+0.07}_{-0.10}$	$0.17^{+0.12}_{-0.17}$	$[\pi/4, \pi/2]$	$1.56^{+0.01}_{-0.78}$
$\cos \alpha$	$-0.21^{+0.09}_{-0.08}$	$-0.15^{+0.15}_{-0.13}$	$0.61^{+0.39}_{-0.11}$	$1.00_{-0.67}$
$\tan \beta$	$0.24^{+0.08}_{-0.10}$	$0.17^{+0.13}_{-0.17}$	$[1, +\infty[$	$[1, +\infty[$
C_U	$-0.90^{+0.17}_{-0.19}$	$-0.87^{+0.12}_{-0.13}$	$0.87^{+0.17}_{-0.15}$	$1.02^{+0.05}_{-0.07}$
C_D	$-0.90^{+0.17}_{-0.19}$	$1.00_{-0.01}$	$0.87^{+0.17}_{-0.15}$	$0.94^{+0.13}_{-0.11}$
C_V	0.90 ± 0.07	$0.95^{+0.05}_{-0.12}$	$0.99^{+0.01}_{-0.04}$	$1.00_{-0.05}$
C_γ	$1.37^{+0.09}_{-0.10}$	$1.44^{+0.08}_{-0.13}$	$1.03_{-0.06}$	$1.01^{+0.01}_{-0.09}$
C_g	$0.90^{+0.19}_{-0.16}$	$0.92^{+0.13}_{-0.11}$	$0.87^{+0.16}_{-0.15}$	$0.99^{+0.08}_{-0.04}$
χ^2_{\min}	12.20	11.95	19.43	19.88

figure caption.⁴ Note that the convention $C_V > 0$ implies $\sin(\beta - \alpha) > 0$ for the h and $\cos(\beta - \alpha) > 0$ for the H . Moreover, the requirement $\tan \beta > 0$ restricts $\beta \in [0, \pi/2]$. The best fit values and 1σ ranges for α and β , together with the corresponding values for C_U , C_D , C_V , C_g and C_γ , are listed in Table 2.7. These numbers are again for the case of h being the state near 125 GeV. Replacing h by H amounts to a shift in $\alpha \rightarrow \alpha + \pi/2$; thus we find $\alpha = 6.07^{+0.09}_{-0.08}$ ($\cos \alpha = 0.98 \pm 0.02$) for the 2HDM-I and $\alpha = 6.14^{+0.15}_{-0.14}$ ($\cos \alpha = 0.99^{+0.01}_{-0.03}$) for the 2HDM-II, while the values for $\tan \beta$, C_U , C_D , C_V , etc. do not change.

Note that for both the Type I and the Type II model, the best fits are quite far from the SM limit in parameter space. In particular, since we do not include any extra loop contributions to C_γ , we end up with negative C_U close to -1 as in Fit II. Demanding $C_U > 0$ (i.e. $\cos \alpha > 0$ for h , $\sin \alpha > 0$ for H), one ends up in a long ‘valley’ along the decoupling limit where the Higgs couplings are SM like, see Fig. 2.20; this is however always more than 2σ away from the best fit. Furthermore, solutions with very small $\tan \beta < 1$ are preferred at more than 2σ . Since such small values of $\tan \beta$ are rather problematic (in particular $\tan \beta < 0.5$ is problematical for maintaining a perturbative magnitude for the top-quark Yukawa coupling) we also give in Table 2.7 the corresponding fit results requiring $\tan \beta > 1$. These results come quite close to the SM limit, and accordingly have a χ^2_{\min} of about 19–20 (recall that for the SM we find $\chi^2 \simeq 20.2$). 2HDMs with $\tan \beta > 1$ hence do not provide a better fit than the SM itself.

A couple of more comments are in order. First, an important question that we leave for future work is whether other—i.e. stability, unitarity, perturbativity (SUP) and precision electroweak (PEW)—constraints are obeyed at the best-fit points, or

⁴Since the ~ 125 GeV state clearly couples to WW , ZZ we do not consider the case where the A is the only state at ~ 125 GeV. We also do not consider the cases where the ~ 125 GeV peak comprises degenerate (h, H) , (h, A) or (H, A) pairs.

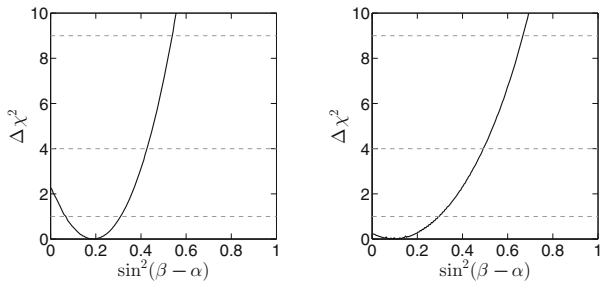


Fig. 2.21 $\Delta\chi^2$ distribution of $\sin^2(\beta - \alpha)$ in the Type I (left) and Type II (right) models for the case that H is the observed state near 125 GeV

the 68 % CL regions. Here we just note that according to Fig. 1 of [135], the SUP and PEW constraints do not seem problematic for Type II, but may play a role for Type I models at low $\tan\beta$.

Second, the best fits correspond to very small $\tan\beta$ (small β) values that are potentially constrained by limits from B-physics, in particular from ΔM_{B_s} and $Z \rightarrow b\bar{b}$. The B-physics constraints are summarized in Figs. 15 and 18 of [136] for Type II and Type I, respectively. Figure 18 for Type I places a lower bound on $\tan\beta$ as a function of the charged Higgs mass which excludes small $\tan\beta < 1$ unless the charged Higgs is *very* heavy, something that is possible but somewhat unnatural. Figure 15 for Type II places a substantial lower bound on the charged Higgs mass for all $\tan\beta$, but such a constraint does not exclude the 68 % CL region.

Third, we remind the reader that in the 2HDMs, the soft Z_2 -symmetry-breaking m_{12}^2 and the other Higgs masses (m_h , m_H and M_A) are independent parameters. It is thus possible to have either m_h or $m_H \sim 125$ GeV without violating constraints from direct searches for the charged Higgs whose mass is related to m_A . However, in the case of $m_H \sim 125$ GeV, one has to avoid the LEP limits for the lighter h , which severely constrain the h coupling to ZZ in case of $m_h < 114$ GeV [137]. So either $m_h \gtrsim 114$ GeV for $m_H \approx 125$ GeV, or $\sin^2(\beta - \alpha)$ needs to be small (i.e. $\sin^2(\beta - \alpha) \lesssim 0.3$ for $m_h \approx 100$ GeV, or $\sin^2(\beta - \alpha) \lesssim 0.1$ for $m_h < 90$ GeV). The $\Delta\chi^2$ distributions of $\sin^2(\beta - \alpha)$ for Type I and Type II with $m_H \sim 125$ GeV are shown in Fig. 2.21. Interestingly, around the best fit the h coupling to ZZ is sufficiently suppressed to allow for m_h of the order of 100 GeV (or lower in Type II).

2.5.5 Conclusions

We assessed to which extent the available data on the Higgs-like scalar at the end of 2012 constrain the Higgs couplings. To this end we performed fits to all public data from the LHC and the Tevatron experiments.

First, we employed a general parametrization of the Higgs couplings based on an SM-like Lagrangian, but allowing for extra contributions to the loop-induced couplings of the Higgs-like scalar to gluons and photons. While the SM does not provide a bad fit ($\chi^2/\text{d.o.f.} = 0.96$), it is more than 2σ away from our best fit solutions. The main pull comes from the enhanced $H \rightarrow \gamma\gamma$ rates observed by ATLAS and CMS, as well as from the Tevatron experiments. The best fits are thus obtained when either $C_U \sim -1$ (i.e. opposite in sign to the SM expectation) or there is a large BSM contribution to the $\gamma\gamma$ coupling of the Higgs. In short, significant deviations from the SM values are preferred by the currently available data and should certainly be considered viable. Since having $C_U \sim -1$ (in the $C_V > 0$ convention) is not easy to achieve in a realistic model context, and leads to unitarity violation in $WW \rightarrow t\bar{t}$ scattering at scales that can be as low as 5 TeV [138, 139], it would seem that new physics contributions to the effective couplings of the Higgs to gluons and photons are the preferred option. (The possibility of a second, degenerate Higgs boson contributing to the observed signal remains another interesting option, not considered here.)

Second, we examined how well 2HDM models of Type I and Type II fit the data. We found that it is possible to obtain a good fit in these models with $\sin(\beta - \alpha)$ ($\cos(\beta - \alpha)$), in the h (H) cases, respectively, not far from 1. However, the best fit values for the individual C_U , C_D , C_V and C_g parameters lie far from their SM values. Further, the best fits give $\tan \beta < 1$, which is disfavored from the theoretical point of view if we want perturbativity up to the GUT scale. Requiring $\tan \beta > 1$ (or simply $C_U > 0$) pushes the fit into the SM ‘valley’ and no improvement over the pure SM solution is obtained. In particular the χ^2 obtained in this region is substantially larger than that for the best fit, and not far from the χ^2 found for the SM.

We once again refer the reader to Tables 2.4, 2.5 and 2.7 which summarize the best fit values and 1σ errors for the parameters for the various cases considered. In Fig. 2.22 we show some of these results graphically. Moreover, in order to assess the physics associated with our best fit points, we give in Table 2.8 the values of the derived (theory level) signal strengths $\mu(\text{ggF}, \gamma\gamma)$, $\mu(\text{ggF}, ZZ)$, $\mu(\text{ggF}, b\bar{b})$, $\mu(\text{VBF}, \gamma\gamma)$, $\mu(\text{VBF}, ZZ)$, and $\mu(\text{VBF}, b\bar{b})$ for the best fit point in the various

Fig. 2.22 Graphical representation of the best fit values for C_U , C_D , C_V , ΔC_γ and ΔC_g of Table 2.4. The labels refer to the fits discussed in the text. The dashed lines indicate the SM value for the given quantity. The \times 's indicate cases where the parameter in question was fixed to its SM value

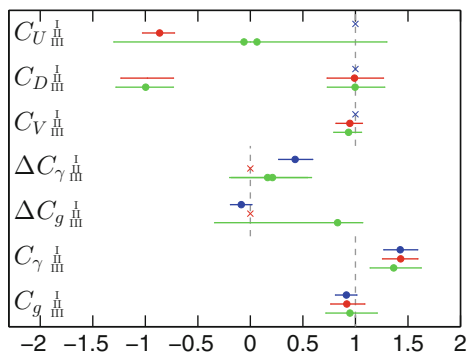


Table 2.8 Summary of μ results for Fits I–III. For Fit II, the tabulated results are for the best fit with $C_U < 0$, column 1 of Table 2.5, and for the case $C_U, C_D > 0$, column 3 of Table 2.5

Fit	I	II, $C_U < 0$	II, $C_U > 0$	III
$\mu(\text{ggF}, \gamma\gamma)$	$1.71^{+0.33}_{-0.32}$	$1.81^{+0.43}_{-0.41}$	1.07 ± 0.18	$1.79^{+0.36}_{-0.34}$
$\mu(\text{ggF}, ZZ)$	$0.84^{+0.18}_{-0.17}$	0.79 ± 0.15	0.97 ± 0.20	$0.84^{+0.21}_{-0.18}$
$\mu(\text{ggF}, b\bar{b})$	$0.84^{+0.18}_{-0.17}$	$0.87^{+0.57}_{-0.40}$	$0.63^{+0.36}_{-0.26}$	$0.96^{+0.59}_{-0.43}$
$\mu(\text{VBF}, \gamma\gamma)$	$2.05^{+0.54}_{-0.44}$	$1.92^{+0.78}_{-0.68}$	$1.66^{+0.70}_{-0.63}$	$1.74^{+0.84}_{-0.73}$
$\mu(\text{VBF}, ZZ)$	1.00 ± 0.02	$0.84^{+0.42}_{-0.36}$	$1.50^{+0.50}_{-0.46}$	$0.82^{+0.38}_{-0.35}$
$\mu(\text{VBF}, b\bar{b})$	1.00 ± 0.02	0.92 ± 0.30	0.98 ± 0.32	$0.93^{+0.25}_{-0.29}$

coupling fits we have considered. (These are a complete set since for the models we consider $\mu(X, \tau\tau) = \mu(X, b\bar{b})$, $\mu(X, WW) = \mu(X, ZZ)$ and $\mu(\text{VBF}, Y) = \mu(\text{VH}, Y)$.) We see that in the general case both $\mu(\text{ggF}, \gamma\gamma)$ and $\mu(\text{VBF}, \gamma\gamma)$ are enhanced by factors 1.7–2.1, while the other signal strengths tend to be $\lesssim 1$. When demanding $C_U > 0$ without allowing for extra contributions from new particles, then only very small enhancements of $\mu(\text{VBF}, \gamma\gamma)$ and $\mu(\text{VBF}, ZZ)$ of the order of 1.2–1.3 are found.

Using the same framework, our group also investigated the extent to which 2012 data constrain invisible (or undetected) decays of the Higgs boson. This results were presented in the letter “Status of invisible Higgs decays”, Ref. [140] that was submitted to arXiv on February 22, 2013 and published in PLB in June 2013. We found in particular the limit $\text{BR}(H \rightarrow \text{invisible}) < 0.23$ at 95 % CL for SM-like Higgs couplings, but up to 60 % invisible/undetected decays of the Higgs were allowed at 95 % CL in Fit I. These results have been obtained without taking account any direct search for $H \rightarrow \text{invisible}$, for which no result was available in 2012.

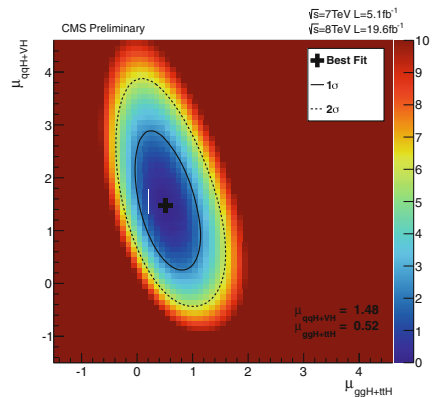
2.6 The Status of Higgs Couplings After Moriond 2013

At the 48th Rencontres de Moriond in March 2013 [141, 142], preliminary results using the full statistics collected at $\sqrt{s} = 7$ and 8 TeV were given for various channels. This includes the search for $H \rightarrow \gamma\gamma$ in CMS [60], for which in addition to the main analysis, using MVA techniques, a cut-based version of the analysis was given. The result of the MVA analysis in the $(\mu(\text{ggF} + \text{ttH}, \gamma\gamma), \mu(\text{VBF} + \text{VH}, \gamma\gamma))$ plane is shown in Fig. 2.23. The best fit point in this 2D plane is at (0.52, 1.48), which is in strong contrast with the 2012 results shown in Fig. 2.11, where the best fit point was located at (0.95, 3.77). The new physics interpretations using 2012 data, presented in the previous section, were mostly driven by the excess in $H \rightarrow \gamma\gamma$. This new CMS result is thus expected to have a large impact on the determination of the couplings of the Higgs boson and on the favored regions in new physics scenarios.

Fig. 2.23 Preliminary CMS

results for $H \rightarrow \gamma\gamma$ [60] (MVA), using the full statistics collected during Run I of the LHC and given in the plane

$(\mu(\text{ggF} + \text{ttH}, \gamma\gamma), \mu(\text{VBF} + \text{VH}, \gamma\gamma))$. The color code gives the value of $-2 \log L$. Contours of constant likelihood are shown, with the *solid line* corresponding to 68 % CL and the *dashed line* to 95 % CL



After Moriond 2013, the same team involved in Refs. [67, 140] (Geneviève Bélanger, Ulrich Ellwanger, John F. Gunion, Sabine Kraml and myself) worked on updating the fits previously presented with the latest results using the full luminosity at 8 TeV. We went beyond our previous works in several ways. First, we found it interesting to show results in terms of combined signal strengths in the $(\mu(\text{ggF} + \text{ttH}, Y), \mu(\text{VBF} + \text{VH}, Y))$ plane, for $Y = \gamma\gamma, VV, b\bar{b}$, and $\tau\tau$. From these results we obtained a simple χ^2 formula that can easily be used to constrain a large class of new physics models. Second, we studied the implications for various new physics scenarios with extended Higgs sectors: in addition to the 2HDM of Type I and Type II, we studied the Inert Doublet model (IDM), and the Georgi–Machacek triplet Higgs model. The paper “Global fit to Higgs signal strengths and couplings and implications for extended Higgs sectors”, Ref. [143], was submitted to arXiv on June 12, 2013 and published in PRD in October 2013. In addition, I made a contribution to the proceedings of the 2013 Moriond conference based on this work [144].

The rest of this section is largely based on [143]. Section 2.6.1 explains our procedure for deriving the combined signal strengths in the $(\mu(\text{ggF} + \text{ttH}, Y), \mu(\text{VBF} + \text{VH}, Y))$ plane and give the updated experimental results we use compared to the end of 2012. We parametrize the signal strengths μ_i in terms of various sets of Higgs couplings and show results in Sect. 2.6.2. The implications for dark matter of the limits on invisible decays of the Higgs (originally presented in Ref. [140]) will be discussed in Sect. 2.6.3. The impact of Higgs searches will then be discussed in the context of the 2HDM in Sect. 2.6.4 and of the IDM in Sect. 2.6.5 (constraints on triplet Higgs models, presented in [143], will not be reproduced here). Finally, our conclusions are given in Sect. 2.6.6.

2.6.1 Methodology and Combined Signal Strengths Ellipses

Our first purpose is to combine the information provided by ATLAS, CMS and the Tevatron experiments on the $\gamma\gamma$, $ZZ^{(*)}$, $WW^{(*)}$, $b\bar{b}$ and $\tau\tau$ final states including the error correlations among the (VBF+VH) and (ggF+ttH) production modes. Using a Gaussian approximation, we derive for each final state a combined likelihood in the $\mu(\text{ggF} + \text{ttH})$ versus $\mu(\text{VBF} + \text{VH})$ plane, which can then simply be expressed as a χ^2 . From the general expression of the likelihood given in Eq. (2.15), we obtain

$$\begin{aligned}\chi_i^2 &= (\mu_i - \hat{\mu}_i)^T \begin{pmatrix} \sigma_{\text{ggF},i}^2 & \rho_i \sigma_{\text{ggF},i} \sigma_{\text{VBF},i} \\ \rho_i \sigma_{\text{ggF},i} \sigma_{\text{VBF},i} & \sigma_{\text{VBF},i}^2 \end{pmatrix}^{-1} (\mu_i - \hat{\mu}_i) \\ &= (\mu_i - \hat{\mu}_i)^T \begin{pmatrix} a_i & b_i \\ b_i & c_i \end{pmatrix} (\mu_i - \hat{\mu}_i) \\ &= a_i (\mu_{\text{ggF},i} - \hat{\mu}_{\text{ggF},i})^2 + 2b_i (\mu_{\text{ggF},i} - \hat{\mu}_{\text{ggF},i}) (\mu_{\text{VBF},i} - \hat{\mu}_{\text{VBF},i}) + c_i (\mu_{\text{VBF},i} - \hat{\mu}_{\text{VBF},i})^2,\end{aligned}\tag{2.19}$$

where the indices ggF and VBF stand for (ggF+ttH) and (VBF+VH), respectively, and the index i stands for $\gamma\gamma$, $VV^{(*)}$, $b\bar{b}$ and $\tau\tau$ (or $b\bar{b} = \tau\tau$), and $\hat{\mu}_{\text{ggF},i}$ and $\hat{\mu}_{\text{VBF},i}$ denote the best-fit points obtained from the measurements. We thus obtain “combined likelihood ellipses”, which can be used in a simple, generic way to constrain non-standard Higgs sectors and new contributions to the loop-induced processes, provided they have the same Lagrangian structure as the SM. In particular, these likelihoods can be used to derive constraints on a model-dependent choice of generalized Higgs couplings, the implications of which we study subsequently for several well-motivated models. The choice of models is far from exhaustive, but we present our results for the likelihoods as a function of the independent signal strengths μ_i in such a manner that these can easily be applied to other models.

As was mentioned in Sect. 2.4, in this approach we do not account for correlations between different final states (but identical production modes) which originate from common theoretical errors on the production cross sections [96, 145], nor for correlations between systematic errors due to common detector components (like EM calorimeters) sensitive to different final states (such as $\gamma\gamma$ and e^- from $ZZ^{(*)}$ and $WW^{(*)}$). A discussion on the precise treatment of these ‘2nd order’ corrections to our likelihood will be made in Sect. 2.10. It is however possible to estimate their importance, i.e., by reproducing the results of coupling fits performed by ATLAS and CMS using all available results up to the Moriond 2013 conference [33, 146]. For the aim of comparison, we have performed fits to the (C_F, C_V) and (C_g, C_γ) couplings, using separately only ATLAS or CMS data up to the Moriond 2013 conference. Figure 2.24 compares our results to those published by ATLAS [146] and CMS [33]. We obtain good agreement in all four cases. The ATLAS (CMS) best fit points are at distances of $\sqrt{(\Delta C_V)^2 + (\Delta C_F)^2} = 0.03$ (0.07) and $\sqrt{(\Delta C_\gamma)^2 + (\Delta C_g)^2} = 0.04$ (0.05) from the reconstructed best fit points, and good coverage of the 68 and 95 % CL regions is observed.

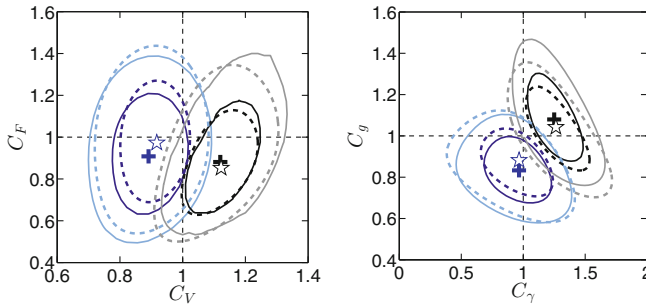


Fig. 2.24 Fit to the couplings (C_F, C_V) (left) and (C_g, C_γ) (right) using separately results from ATLAS and CMS up to the Moriond 2013 conference. The black and gray (dark blue and light blue) contours show the 68 and 95 % CL regions for ATLAS (CMS), respectively. The solid contours correspond to the results published by the experimental collaborations, while dashed contours have been obtained using the fitted signal strength ellipses as determined using the separate data for ATLAS (CMS) in the manner described in this section

Once the expressions for the various χ_i^2 are given in the form of Eq. (2.19), it becomes straightforward to evaluate the numerical value of $\chi^2 = \sum_i \chi_i^2$ in any theoretical model with SM-like Lagrangian structure, in which predictions for the Higgs branching fractions and the (VBF+VH) and (ggF+ttH) production modes (relative to the SM) can be made. From the corresponding information provided by the experimental collaborations one finds that the Gaussian approximation is justified in the neighborhood (68 % CL contours) of the best fit points. Hence we parametrize these 68 % CL contours, separately for each experiment, as in Eq. (2.19), using the procedure explained in Sect. 2.4 around Eq. (2.14). Occasionally, only a single signal rate including error bars for a specific final state is given. Using the relative contributions from the various production modes, this kind of information can still be represented in the form of Eq. (2.19), leading to an “ellipse” which reduces to a strip in the plane of the (VBF+VH) and (ggF+ttH) production modes. Subsequently these expressions can easily be combined and be represented again in the form of Eq. (2.19). We expect that the result is reliable up to $\chi_i^2 \lesssim 6$ (making it possible to derive 95 % CL contours), but its extrapolation to (much) larger values of χ_i^2 should be handled with care.

Starting with the $H \rightarrow \gamma\gamma$ final state, we treat in this way the 68 % CL contours given by ATLAS in [34, 52, 146], by CMS in [33, 60, 147]⁵ and the Tevatron in [16]. (In the case of the Tevatron, for all final states only a strip in the plane of the (VBF+VH) and (ggF+ttH) production modes is defined.) For the combination of the ZZ and WW final states, we use the 68 % CL contours given by ATLAS for

⁵Note that we are using the MVA analysis for CMS $H \rightarrow \gamma\gamma$. The cut-based analysis (CiC) also presented by CMS [60]—that leads to higher but compatible signal strengths—is unfortunately not available in the form of contours in the plane of the (VBF+VH) and (ggF+ttH) production modes. Moreover, no information is given on the sub-channel decomposition, so in fact the CMS CiC analysis cannot be used for our purpose.

Table 2.9 Combined best-fit signal strengths $\hat{\mu}_{\text{ggF}}$, $\hat{\mu}_{\text{VBF}}$ and correlation coefficient ρ for various final states, as well as the coefficients a , b and c for the χ^2 in Eq. (2.19)

	$\hat{\mu}_{\text{ggF}}$	$\hat{\mu}_{\text{VBF}}$	ρ	a	b	c
$\gamma\gamma$	0.98 ± 0.28	1.72 ± 0.59	-0.38	14.94	2.69	3.34
VV	0.91 ± 0.16	1.01 ± 0.49	-0.30	44.59	4.24	4.58
$b\bar{b}/\tau\tau$	0.98 ± 0.63	0.97 ± 0.32	-0.25	2.67	1.31	10.12
$b\bar{b}$	-0.23 ± 2.86	0.97 ± 0.38	0	0.12	0	7.06
$\tau\tau$	1.07 ± 0.71	0.94 ± 0.65	-0.47	2.55	1.31	3.07

ZZ in [34, 54, 146], by CMS for ZZ in [33, 61], by ATLAS for WW in [53, 146], by CMS for WW in [33, 148, 149] and by the Tevatron for WW in [16]. For the combination of the $b\bar{b}$ and $\tau\tau$ final states, we use the “strip” defined by the ATLAS result for $b\bar{b}$ in associated VH production from [116], the 68 % CL contour given by CMS for $b\bar{b}$ in [150], the Tevatron result for $b\bar{b}$ from [16] and combine them with the ATLAS 68 % CL contour for $\tau\tau$ from [117, 146] and the CMS 68 % CL contours for $\tau\tau$ from [33, 151]. We also use the ATLAS search for $ZH \rightarrow \ell^+\ell^- + \text{invisible}$, extracting the likelihood from Fig. 10b of [152]. All the above 68 % CL likelihood contours are parametrized by ellipses (or strips) in χ^2 as in Eq. (2.19), which can subsequently be combined. (The analytical expressions are given in Appendix A of Ref. [143].) While ATLAS searches for $H \rightarrow b\bar{b}$ and $H \rightarrow \tau\tau$ still correspond to only 13 fb^{-1} at $\sqrt{s} = 8 \text{ TeV}$, almost all of other results correspond to the full luminosity collected during Run I of the LHC. Therefore, and while notable changes can be seen between the preliminary and the published results, the results that will be shown in the rest of the Section are expected to remain largely valid until the first results from Run II of the LHC.

The resulting parameters $\hat{\mu}_{\text{ggF}}$, $\hat{\mu}_{\text{VBF}}$, a , b and c for Eq. (2.19) (and, for completeness, the correlation coefficient ρ) for the different final states are listed in Table 2.9. The corresponding 68, 95 and 99.7 % CL ellipses are represented graphically in Fig. 2.25. We see that, after combining different experiments, the best fit signal strengths are astonishingly close to their SM values, the only exception being the $\gamma\gamma$ final state produced via (VBF+VH) for which the SM is, nonetheless, still within the 68 % CL contour. Therefore, these results serve mainly to constrain BSM contributions to the properties of the Higgs boson.

The combination of the $b\bar{b}$ and $\tau\tau$ final states is justified, in principle, in models where one specific Higgs doublet has the same reduced couplings (with respect to the SM) to down-type quarks and leptons. However, even in this case QCD corrections and so-called Δ_b corrections (from radiative corrections, notably at large $\tan\beta$, inducing couplings of another Higgs doublet to b quarks, see i.e. [153, 154]) can lead to deviations of the reduced $Hb\bar{b}$ and $H\tau\tau$ couplings from a common value. Therefore, for completeness we show the result for the $b\bar{b}$ final state only (combining ATLAS, CMS and Tevatron results as given in the previous paragraph) in the fourth line of Table 2.9, and the resulting 68, 95 and 99.7 % CL contours in the left plot in

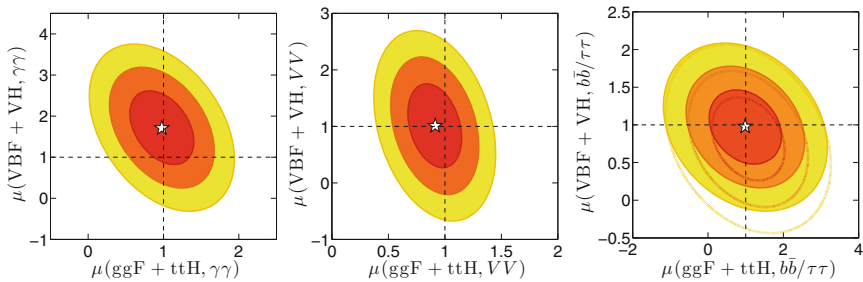


Fig. 2.25 Combined signal strength ellipses for the $\gamma\gamma$, $VV = ZZ, WW$ and $b\bar{b} = \tau\tau$ channels. The filled red, orange and yellow ellipses show the 68, 95 and 99.7 % CL regions, respectively, derived by combining the ATLAS, CMS and Tevatron results. The red, orange and yellow line contours in the right-most plot show how these ellipses change when neglecting the Tevatron results. The white stars mark the best-fit points

Fig. 2.26 Combined signal strength ellipses as in Fig. 2.25 but treating the couplings to $b\bar{b}$ and $\tau\tau$ separately

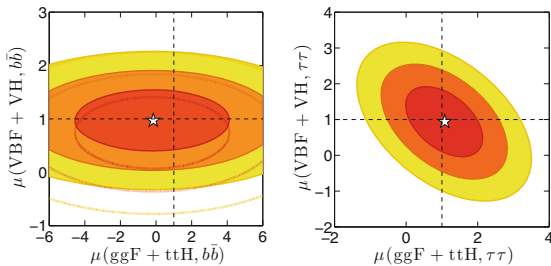


Fig. 2.26. The result for the $\tau\tau$ final state only (combining ATLAS and CMS results as given in the previous paragraph) is shown in the fifth line of Table 2.9, and the resulting 68, 95 and 99.7 % CL contours in the right plot in Fig. 2.26. Before proceeding, a comment is in order regarding the impact of the Tevatron results. While for the $\gamma\gamma$ and VV final states, our combined likelihoods are completely dominated by the LHC measurements, to the extent that they are the same with or without including the Tevatron results, this is not the case for the $b\bar{b}$ final state. For illustration, in the plots for the $b\bar{b}$ final state in Figs. 2.25 and 2.26 we also show what would be the result neglecting the Tevatron measurements.

2.6.2 Fits to Reduced Higgs Couplings

Using the results of the previous section, it is straightforward to determine constraints on the couplings of the observed Higgs boson to various particle pairs, assuming only an SM-like Lagrangian structure. As in Sect. 2.5, we define C_U , C_D and C_V to be ratios of the H coupling to up-type quarks, down-type quarks and leptons, and vector boson pairs, respectively, relative to that predicted in the case of the SM Higgs boson

(with $C_V > 0$ by convention). In addition to these tree-level couplings there are also the one-loop induced couplings of the H to gg and $\gamma\gamma$. Given values for C_U , C_D and C_V the contributions of SM particles to the gg and $\gamma\gamma$ couplings, denoted $\overline{C_g}$ and $\overline{C_\gamma}$ respectively, can be computed. We take into account NLO corrections to $\overline{C_g}$ and $\overline{C_\gamma}$ as recommended by the LHC Higgs Cross Section Working Group [110]. In particular we include all the available QCD corrections for C_g using HIGLU [29, 111, 112] and for C_γ using HDECAY [29, 30], and we switch off the electroweak corrections. In some of the fits below, we will also allow for additional new physics contributions to C_g and C_γ by writing $C_g = \overline{C_g} + \Delta C_g$ and $C_\gamma = \overline{C_\gamma} + \Delta C_\gamma$.

We note that in presenting one- (1D) and two-dimensional (2D) distributions of $\Delta\chi^2$, those quantities among C_U , C_D , C_V , ΔC_g and ΔC_γ not plotted, but that are treated as variables, are being profiled over. The fits presented below will be performed with and without allowing for invisible decays of the Higgs boson. In the latter case, only SM decay modes are present. In the former case, the new decay modes are assumed to produce invisible or undetected particles that would be detected as missing transverse energy at the LHC. A direct search for invisible decays of the Higgs boson has been performed by ATLAS in the $ZH \rightarrow \ell^+\ell^- + E_T^{\text{miss}}$ channel [152] and is implemented in the analysis. Thus, the total width is fully calculable from the set of C_i and $\mathcal{B}(H \rightarrow \text{invisible})$ in all the cases we consider. (We will come back to this at the end of this section.)

We begin by taking SM values for the tree-level couplings to fermions and vector bosons, i.e. $C_U = C_D = C_V = 1$, but allow for new physics contributions to the couplings to gg and $\gamma\gamma$. The fit results with and without allowing for invisible/unseen Higgs decays are shown in Fig. 2.27. We observe that the SM point of $\Delta C_g = \Delta C_\gamma = 0$ is well within the 68% contour with the best fit points favoring a slightly positive (negative) value for ΔC_γ (ΔC_g). Allowing for invisible/unseen decays expands the 68, 95 and 99.7% CL regions by only a modest amount. This is in contrast to the situation at the end of 2012 (see Sect. 2.5 and Ref. [140]), where some new physics contribution to both ΔC_g and ΔC_γ was preferred, and allowing for invisible decays had a large effect; with the higher statistics and with the reduced $\gamma\gamma$ signal strength from CMS [60], ΔC_g and ΔC_γ are now much more constrained. The best fit is obtained for $\Delta C_g = -0.06$, $\Delta C_\gamma = 0.13$, $\mathcal{B}_{\text{inv}} \equiv \mathcal{B}(H \rightarrow \text{invisible}) = 0$ and has $\chi_{\text{min}}^2 = 17.71$ for 21 d.o.f. (degrees of freedom),⁶ as compared to $\chi^2 = 18.95$ with 23 d.o.f. for the SM, so allowing for additional loop contributions does not improve the fit.

Next, we allow C_U , C_D and C_V to vary but assume that there is no new physics in the gg and $\gamma\gamma$ loops, i.e. we take $\Delta C_g = \Delta C_\gamma = 0$. Results for this case are shown in Fig. 2.28. We observe that, contrary to the situation at the end of 2012, the latest data prefer a positive value of C_U close to 1. This is good news, as a negative sign of C_U —in the convention where m_t is positive—is quite problematic in the

⁶There are in total 23 measurements entering our fit, and we adopt the simple definition of the number of d.o.f. as number of measurements minus number of parameters.

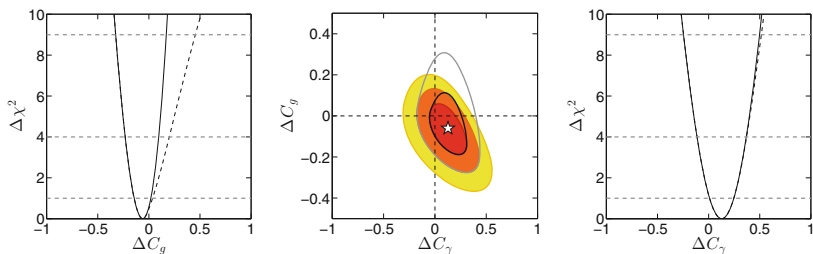
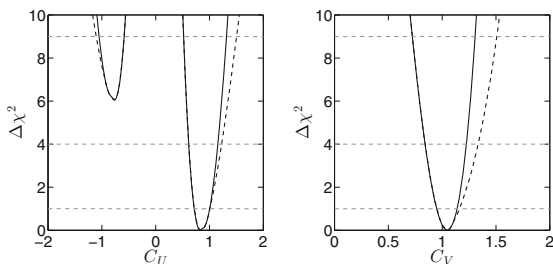


Fig. 2.27 $\Delta\chi^2$ distributions in 1D and 2D for the fit of ΔC_g and ΔC_γ for $C_U = C_D = C_V = 1$. In the 1D plots, the *solid (dashed) lines* are for the case that invisible/unseen decays are absent (allowed). In the 2D plot, the *red, orange and yellow areas* are the 68, 95 and 99.7 % CL regions, respectively, assuming invisible decays are absent. The *white star* marks the best-fit point. The *black and gray lines* show the 68 and 95 % CL contours when allowing for invisible decays

Fig. 2.28 Fit of C_U, C_D, C_V for $\Delta C_g = \Delta C_\gamma = 0$. The plots show the 1D $\Delta\chi^2$ distribution as a function of C_U (left) and C_V (right). The *solid (dashed) lines* are for the case that invisible/unseen decays are absent (allowed)



context of most theoretical models.⁷ (We do not show the distribution for C_D here but just remark that $|C_D| \simeq 1 \pm 0.2$ with a sign ambiguity following from the weak dependence of the gg and $\gamma\gamma$ loops on the bottom-quark coupling.) For C_V , we find a best-fit value slightly above 1, at $C_V = 1.07$, but with the SM-like value of $C_V = 1$ lying well within one standard deviation.

Since $C_U < 0$ is now disfavored and the sign of C_D is irrelevant, we confine ourselves subsequently to $C_U, C_D > 0$. In Fig. 2.29 we show $\Delta\chi^2$ distributions in 2D planes confined to this range, still assuming $\Delta C_g = \Delta C_\gamma = 0$. The mild correlation between C_U and C_D in the leftmost plot of Fig. 2.29 follows from the very SM-like signal rates in the VV and $\gamma\gamma$ final states in ggF: varying C_D implies a variation of the partial width $\Gamma(H \rightarrow bb)$ which dominates the total width. Hence, the branching fractions $\mathcal{B}(H \rightarrow VV)$ and $\mathcal{B}(H \rightarrow \gamma\gamma)$ change in the opposite direction, decreasing with increasing total width (i.e. with increasing C_D) and vice versa. In order to keep the signal rates close to 1, the ggF production cross section, which is roughly proportional to C_U^2 , has to vary in the same direction as C_D . The best fit is obtained for $C_U = 0.88$, $C_D = 0.94$, $C_V = 1.04$, $C_\gamma = 1.09$, $C_g = 0.88$

⁷If the top quark and Higgs bosons are considered as fundamental fields, it would require that the top quark mass is induced dominantly by the vev of at least one additional Higgs boson which is not the Higgs boson considered here, and typically leads to various consistency problems as discussed, i.e., in [138].

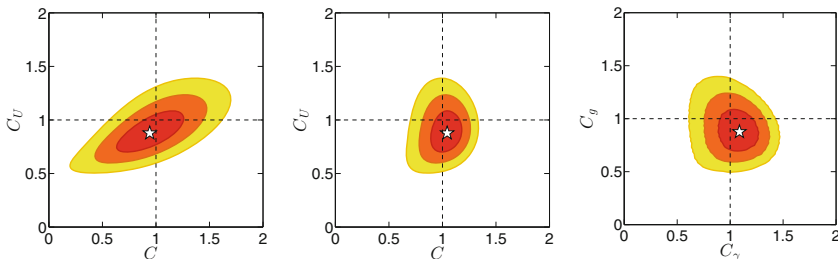


Fig. 2.29 Fit of $C_U > 0$, $C_D > 0$ and C_V for $\Delta C_g = \Delta C_\gamma = 0$. The red, orange and yellow areas are the 68, 95 and 99.7 % CL regions, respectively, assuming invisible decays are absent. The white star marks the best-fit point

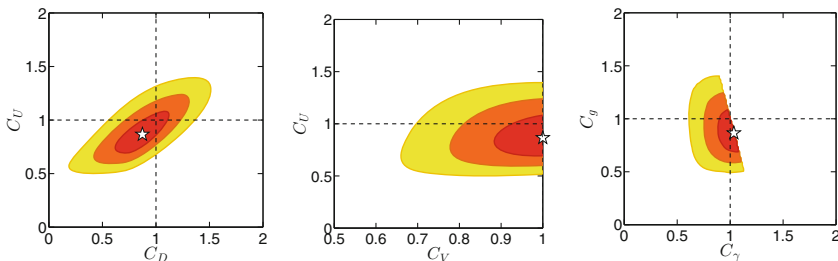


Fig. 2.30 As in Fig. 2.29 but for $C_V \leq 1$

(and, in fact, $\mathcal{B}_{\text{inv}} = 0$). Note that if $C_V > 1$ were confirmed, this would imply that the observed Higgs boson must have a significant triplet (or higher representation) component [155, 156]. Currently the coupling fits are, however, perfectly consistent with SM values. Again, with a $\chi^2_{\text{min}} = 17.79$ (for 20 d.o.f.) as compared to $\chi^2 = 18.95$ for the SM, allowing for deviations from the SM does not significantly improve the fit.

In models where the Higgs sector consists of doublets+singlets only one always obtains $C_V \leq 1$. Results for this case are shown in Fig. 2.30. Given the slight preference for $C_V > 1$ in the previous free- C_V plots, it is no surprise the $C_V = 1$ provides the best fit along with $C_U = C_g = 0.87$, $C_D = 0.88$ and $C_\gamma = 1.03$. Of course, the SM is again well within the 68 % CL zone. The general case of free parameters C_U , C_D , C_V , ΔC_g and ΔC_γ is illustrated in Fig. 2.31, where we show the 1D $\Delta\chi^2$ distributions for these five parameters (each time profiling over the other four parameters). As before, the solid (dashed) lines indicate results not allowing for (allowing for) invisible/unseen decay modes of the Higgs. Allowing for invisible/unseen decay modes again relaxes the $\Delta\chi^2$ behavior only modestly. The best fit point always corresponds to $\mathcal{B}_{\text{inv}} = 0$.

An overview of the current status of invisible decays is given in Fig. 2.32, which shows the behavior of $\Delta\chi^2$ as a function of \mathcal{B}_{inv} for various different cases of interest:

- (a) SM Higgs with allowance for invisible decays—one finds $\mathcal{B}_{\text{inv}} < 0.09$ (0.19);
- (b) $C_U = C_D = C_V = 1$ but ΔC_γ , ΔC_g allowed for— $\mathcal{B}_{\text{inv}} < 0.11$ (0.29);

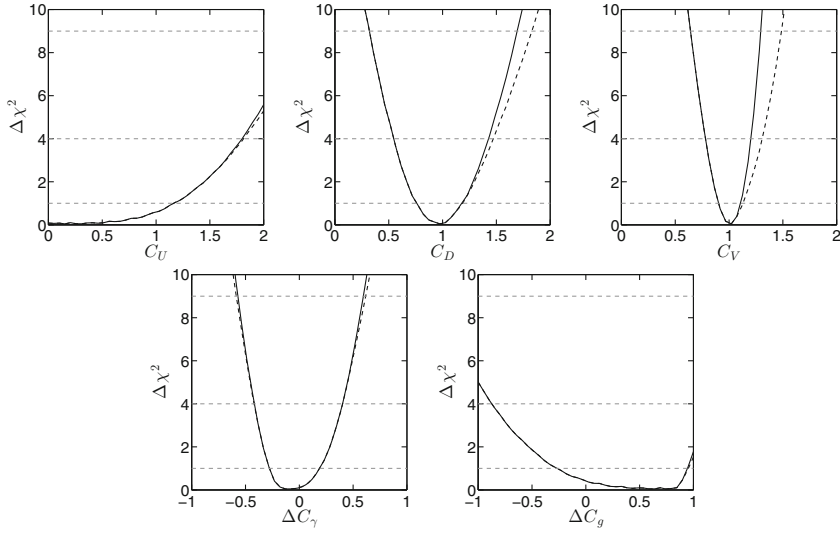


Fig. 2.31 Five (six) parameter fit of C_U , C_D , C_V , ΔC_g and ΔC_γ ; the *solid* (*dashed*) curves are those obtained when invisible/unseen decay modes are not allowed (allowed) for

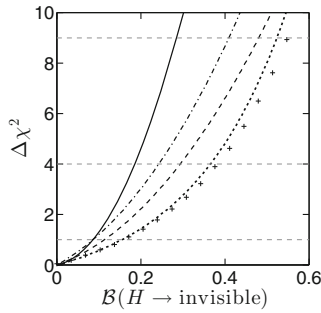


Fig. 2.32 $\Delta\chi^2$ distributions for the branching fraction of invisible Higgs decays for various cases. *Solid* SM+invisible. *Dashed* varying ΔC_g and ΔC_γ for $C_U = C_D = C_V = 1$. *Dotted* varying C_U , C_D and C_V for $\Delta C_g = \Delta C_\gamma = 0$. *Dot-dashed* varying C_U , C_D and $C_V \leq 1$ for $\Delta C_g = \Delta C_\gamma = 0$. *Crosses* varying C_U , C_D , C_V , ΔC_g and ΔC_γ

- (c) C_U , C_D , C_V free, $\Delta C_\gamma = \Delta C_g = 0$, $-\mathcal{B}_{\text{inv}} < 0.15$ (0.36);
- (d) C_U , C_D free, $C_V \leq 1$, $\Delta C_\gamma = \Delta C_g = 0$ $-\mathcal{B}_{\text{inv}} < 0.09$ (0.24);
- (e) C_U , C_D , C_V , ΔC_g , ΔC_γ free $-\mathcal{B}_{\text{inv}} < 0.16$ (0.38).

(All \mathcal{B}_{inv} limits are given at 68 % (95 %) CL.) Thus, while \mathcal{B}_{inv} is certainly significantly limited by the current data set, there remains ample room for invisible/unseen decays. At 95 % CL, \mathcal{B}_{inv} as large as ~ 0.38 is possible. Here, we remind the reader that the above results are obtained after fitting the 125.5 GeV data *and* inputting the experimental results for the $(Z \rightarrow \ell^+ \ell^-) + \text{invisible}$ direct searches. When $C_V \leq 1$, $H \rightarrow$

invisible is much more constrained by the global fits to the H properties than by the direct searches for invisible decays, cf. the solid, dashed and dash-dotted lines in Fig. 2.32. For unconstrained C_U , C_D and C_V , on the other hand, cf. dotted line and crosses in Fig. 2.32, the limit comes from the direct search for invisible decays in the ZH channel.

A comment is in order here. In principle there is a flat direction in the unconstrained LHC Higgs coupling fit when unobserved decay modes are present: setting $C_U = C_D = C_V \equiv C$, so that ratios of rates remain fixed, all the Higgs production \times decay rates can be kept fixed to the SM ones by scaling up C while adding a new, unseen decay mode with branching fraction \mathcal{B}_{new} according to $C^2 = 1/(1 - \mathcal{B}_{\text{new}})$ [157, 158], see also [159]. In [140] we found that it is mainly C_V which is critical here, because of the rather well measured $\text{VBF} \rightarrow H \rightarrow VV$ channel. Therefore limiting $C_V \leq 1$ gives a strong constraint on \mathcal{B}_{new} , similar to the case of truly invisible decays. Concretely we find at 95 % CL: (i) $\mathcal{B}_{\text{new}} < 0.21$ for an SM Higgs with allowance for unseen decays; (ii) $\mathcal{B}_{\text{new}} < 0.39$ for $C_U = C_D = C_V = 1$ but $\Delta C_\gamma, \Delta C_g$ allowed for; and (iii) $\mathcal{B}_{\text{new}} < 0.31$ for C_U, C_D free, $C_V \leq 1$ and $\Delta C_\gamma = \Delta C_g = 0$. For unconstrained C_U, C_D and C_V , however, there is no limit on \mathcal{B}_{new} .

With this in mind, the global fit we perform here also makes it possible to constrain the Higgs boson's total decay width, Γ_{tot} , a quantity which is not directly measurable at the LHC. For SM + invisible decays, we find $\Gamma_{\text{tot}}/\Gamma_{\text{tot}}^{\text{SM}} < 1.11$ (1.25) at 68 % (95 %) CL. Figure 2.33 shows the $\Delta\chi^2$ as function of $\Gamma_{\text{tot}}/\Gamma_{\text{tot}}^{\text{SM}}$ for the fits of: C_U, C_D , and $C_V \leq 1$; C_U, C_D , and C_V free; and $C_U, C_D, C_V, \Delta C_g, \Delta C_\gamma$. The case of $\Delta C_g, \Delta C_\gamma$ with $C_U = C_D = C_V = 1$ is not shown; without invisible decays we find $\Gamma_{\text{tot}}/\Gamma_{\text{tot}}^{\text{SM}} = [0.98, 1.0]$ ([0.97, 1.02]) at 68 % (95 %) CL in this case. Allowing for invisible decays this changes to $\Gamma_{\text{tot}}/\Gamma_{\text{tot}}^{\text{SM}} = [0.97, 1.14]$, ([0.96, 1.46]), i.e. it is very close to the line for $C_U, C_D, C_V \leq 1$ in the right plot of Fig. 2.33.

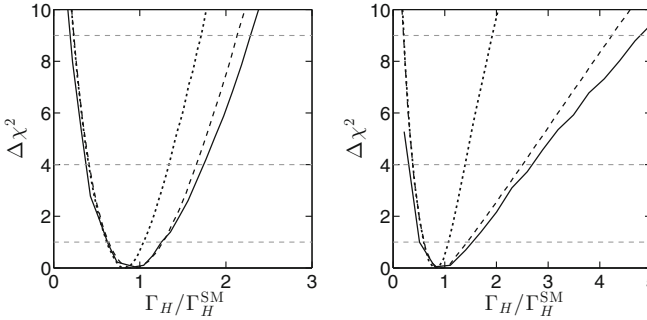


Fig. 2.33 $\Delta\chi^2$ distributions for the total Higgs decay width relative to SM, $\Gamma_{\text{tot}}/\Gamma_{\text{tot}}^{\text{SM}}$, in the *left panel* without invisible decays, in the *right panel* including \mathcal{B}_{inv} as a free parameter in the fit. The *lines* are for: C_U, C_D and $C_V \leq 1$ (*dotted*); C_U, C_D and free C_V (*dashed*); and C_U, C_D , free $C_V, \Delta C_g, \Delta C_\gamma$ (*solid*)

2.6.3 Interplay with Direct Dark Matter Searches

Assuming that the invisible particle which the Higgs potentially decays into is the dark matter of the Universe, the LHC bounds on \mathcal{B}_{inv} can be turned into bounds on the DM scattering off nucleons, mediated by Higgs exchange, cf. [160–166]. These bounds are often much stronger than the current limits from XENON100 [167] and LUX [168] for $m_{\text{DM}} < 62 \text{ GeV}$ (i.e., $m_H/2$). Both the invisible width of the Higgs and the spin-independent cross section for scattering on protons depend on the square of the Higgs–DM–DM coupling C_{DM} . If the DM is a Majorana fermion, χ , the invisible width arising from $H \rightarrow \chi\chi$ decays is given by

$$\Gamma_{\text{inv}} = \Gamma(H \rightarrow \chi\chi) = \frac{g^2}{16\pi} m_H C_\chi^2 \beta^3, \quad (2.20)$$

where $\beta = (1 - 4m_\chi^2/m_H^2)^{1/2}$ and C_χ is defined by $\mathcal{L} = gC_\chi \bar{\chi}\chi H$. In case of the DM being a real scalar, ϕ , we have $\mathcal{L} = gm_\phi C_\phi \phi\phi H$ and

$$\Gamma_{\text{inv}} = \Gamma(H \rightarrow \phi\phi) = \frac{g^2}{32\pi} \frac{m_\phi^2 C_\phi^2}{m_H} \beta. \quad (2.21)$$

The spin-independent cross section for scattering on a nucleon, considering only the Higgs exchange diagram, can then be directly related to the invisible width of the Higgs:

$$\sigma_{\text{SI}} = \eta \mu_r^2 m_p^2 \frac{g^2}{M_W^2} \Gamma_{\text{inv}} \left[C_U (f_u^N + f_c^N + f_t^N) + C_D (f_d^N + f_s^N + f_b^N) + \frac{\Delta C_g}{\bar{C}_g} f_g^N \right]^2, \quad (2.22)$$

with $\eta = 4/(m_H^5 \beta^3)$ for a Majorana fermion and $\eta = 2/(m_H^3 m_\phi^2 \beta)$ for a real scalar; μ_r is the reduced mass and f_q^N (f_g^N) are the quark (gluon) coefficients in the nucleon. We take the values $f_s^P = 0.0447$, $f_u^P = 0.0135$, and $f_d^P = 0.0203$ from an average of recent lattice results [169, 170]. The gluon and heavy quark ($Q = c, b, t$) coefficients are related to those of light quarks, and $f_Q^P = 2/27 f_g^P = 2/27(1 - \sum_{q=u,d,s} f_q^P)$ at leading order. Since the contribution of heavy quarks to the scattering amplitude originates from their contribution to the Hgg coupling, we write the effect of ΔC_g , the last term in Eq. (2.22), in terms of an additional top quark contributing to the Hgg coupling; numerically $\hat{C}_g = \bar{C}_g = 1.052$ with only the SM top-quark contribution taken into account for computing \bar{C}_g .

For the numerical evaluation of σ_{SI} , we use micrOMEGAS [170, 171] in which the relation between the heavy quark coefficients and the light ones are modified by QCD corrections. This amounts to taking

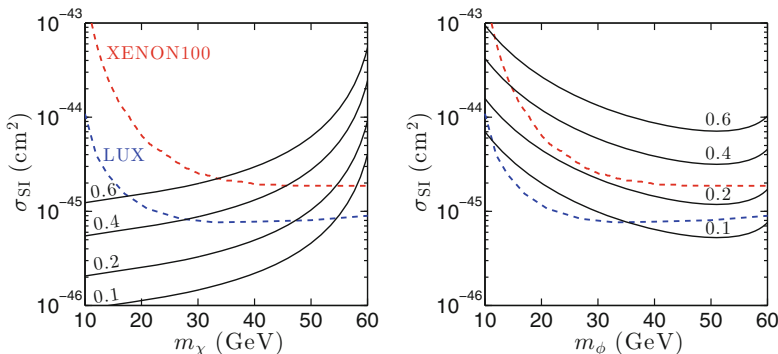


Fig. 2.34 σ_{SI} as a function of the mass of the DM particle, for $\mathcal{B}_{\text{inv}} = 0.1, 0.2, 0.4, 0.6$ (from bottom to top) for the case of a Majorana χ (left panel) or a real scalar ϕ (right panel) when $C_U = C_D = C_V = 1$ and $\Delta C_g = \Delta C_\gamma = 0$, i.e. an SM Higgs plus invisible decays. The red (blue) dashed curves show the XENON100 (LUX) exclusion limit at 90 % CL

$$C_Q f_Q^p \rightarrow C_Q \left(1 + \frac{35\alpha_s(m_Q)}{36\pi} \right) f_Q^p, \quad \Delta C_g f_g^p \rightarrow \Delta C_g \left(1 - \frac{16\alpha_s(m_t)}{9\pi} \right) f_g^p. \quad (2.23)$$

The results for σ_{SI} versus the DM mass and for different \mathcal{B}_{inv} are displayed in Fig. 2.34 for a Majorana fermion (left panel)⁸ and a real scalar (right panel) assuming SM-like couplings of the Higgs boson. As can be seen, for a Majorana fermion the current LUX limits [168] exclude, for example, $\mathcal{B}_{\text{inv}} > 0.4$ when $28 \text{ GeV} < m_\chi < m_H/2$. For scalar DM, the cross sections are larger, and LUX excludes $\mathcal{B}_{\text{inv}} > 0.2$ for any m_ϕ in the $[10 \text{ GeV}, m_H/2]$ range. These limits become much stronger when C_U and/or C_D are large provided they have the same sign. Further, these limits become stronger when we include a non-zero value of ΔC_g . For example, for $\Delta C_g = 1$ we find that σ_{SI} increases by a factor 1.8 as compared to the case $\Delta C_g = 0$ for any given value of \mathcal{B}_{inv} . This increase is due in part to the new contribution in Eq. (2.22) and in part because a larger coupling of the DM to the Higgs is necessary to maintain a constant value of \mathcal{B}_{inv} . Note that imposing universality of quark couplings to the Higgs has an impact on our predictions for σ_{SI} since all quark flavors contribute to this observable, whereas universality plays basically no role for Higgs decays as only the third generation is important.

When $C_U < 0$ and $C_D > 0$, there is a destructive interference between the u -type and d -type quark contributions such that σ_{SI} is much below the current limit. Note however that this is clearly disfavored by the latest data. When the DM candidate is a Dirac fermion and one assumes the same amount of matter and anti-matter in the early Universe, the results for σ_{SI} are simply a factor 1/2 lower than those obtained in the Majorana case. However if this fermion also couples to the Z , this gives an additional positive contribution to σ_{SI} , thus leading to stronger constraints from direct detection experiments. Similar arguments hold for the case of a complex scalar, as compared to a real scalar.

⁸For a Dirac fermion, the cross sections are a factor 1/2 smaller.

2.6.4 Application to Two-Higgs-Doublet Models

So far our fits have been largely model-independent, relying only on assuming the Lagrangian structure of the SM. Let us now apply our fits to some concrete examples of specific models in which there are relations between some of the coupling factors C_I . As a first example, we consider Two-Higgs-Doublet Models (2HDMs) of Type I and Type II (see also [87, 89, 172–179] for other 2HDM analyses in the light of recent LHC data). In both cases, the basic parameters describing the coupling of either the light h or heavy H CP-even Higgs boson are only two: α (the CP-even Higgs mixing angle) and $\tan\beta = v_2/v_1$, where v_2 and v_1 are the two vacuum expectation values. The Type I and Type II models are distinguished by the pattern of their fermionic couplings as given in Table 2.6. The SM limit for the h (H) in the case of both Type I and Type II models corresponds to $\alpha = \beta - \pi/2$ ($\alpha = \beta$). We implicitly assume that there are no contributions from non-SM particles to the loop diagrams for C_γ and C_g . In particular, this means our results correspond to the case where the charged Higgs boson, whose loop might contribute to C_γ , is heavy.

The results of the 2HDM fits are shown in Fig. 2.35 for the case that the state near 125 GeV is the lighter CP-even h . To be precise, the top row shows $\Delta\chi^2$ contours in the β versus $\cos(\beta - \alpha)$ plane while the bottom row shows the 1D projection of

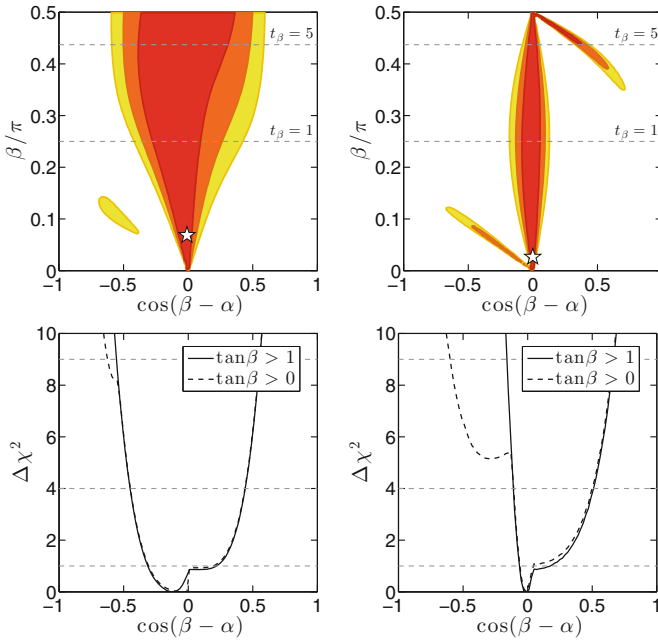


Fig. 2.35 Fits for the 2HDM Type I (*left*) and type II (*right*) models for $m_h = 125.5$ GeV. See text for details

$\Delta\chi^2$ onto $\cos(\beta - \alpha)$ with β profiled over. For identifying the heavier H with the state near 125 GeV, replace $\cos(\beta - \alpha)$ by $\sin(\beta - \alpha)$ in the 1D plots. (Since the ~ 125 GeV state clearly couples to WW , ZZ we do not consider the case where the A is the only state at ~ 125 GeV.)

In the case of the Type I model, we note a rather broad valley along the SM limit of $\cos(\beta - \alpha) = 0$, which is rather flat in $\tan\beta$; the 68 % (95 %) CL region extends to $\cos(\beta - \alpha) = [-0.31, 0.19]$ ($[-0.45, 0.44]$). The best fit point lies at $\beta \simeq 0.02\pi$ and $\alpha \simeq 1.52\pi$ with $\chi_{\min}^2 = 18.01$ for 21 d.o.f. (to be compared to the SM $\chi_{\min}^2 = 18.95$). Requiring $\tan\beta > 1$, this moves to $\beta \simeq 0.25\pi$, i.e. $\tan\beta$ just above 1, with $\alpha \simeq 1.71\pi$ and $\chi_{\min}^2 = 18.08$. At 99.7 % CL, there is also a small island at $\cos(\beta - \alpha) \approx -0.5$ and $\tan\beta < 1$, which corresponds to the $C_U < 0$ solution. (This is responsible for the splitting of the two lines at $\cos(\beta - \alpha) \lesssim -0.5$ in the 1D plot.)

In contrast, for the Type II model, we observe two narrow 68 % CL valleys in the β versus $\cos(\beta - \alpha)$ plane, one along the SM solution with the minimum again very close to $\beta \approx 0$ and a second banana-shaped one with $\tan\beta \gtrsim 5$ (3) and $\cos(\beta - \alpha) \lesssim 0.4$ (0.6) at 68 % (95 %) CL. This second valley is the degenerate solution with $C_D \approx -1$; it does not appear in Fig. 3 of [178] because there $C_U, C_D > 0$ was implicitly assumed. The best fit point is very similar to that for Type I: $\beta \simeq 0.01\pi$ (0.25π) and $\alpha \simeq 1.5\pi$ (1.75π) with $\chi_{\min}^2 = 18.68$ (18.86) for 21 d.o.f. for arbitrary $\tan\beta$ ($\tan\beta > 1$). Again, there is an additional valley very close to $\beta \sim 0$, extending into the negative $\cos(\beta - \alpha)$ direction, which however does not have a 68 % CL region. In 1D, we find $\cos(\beta - \alpha) = [-0.11, 0.50]$ at 95 % CL.

Let us end the 2HDM discussion with some comments regarding the “other” scalar and/or the pseudoscalar A . To simplify the discussion, we will focus on the $m_h = 125.5$ GeV case. First, we note that if the H and A are heavy enough (having masses greater than roughly 600 GeV) then their properties are unconstrained by LHC data and the global fits for the h will be unaffected. If they are lighter then it becomes interesting to consider constraints that might arise from not having observed them. Such constraints will, of course, depend upon their postulated masses, both of which are independent parameters in the general 2HDM. For purposes of discussion, let us neglect the possibly very important decays into the 125.5 GeV Higgs boson (such as $H \rightarrow hh$). The most relevant final states are then $H \rightarrow VV$ and $H, A \rightarrow \tau\tau$.

With regard to observing the heavy Higgs in the $H \rightarrow VV$ channels, we note that for the H our fits predict the VV coupling to be very much suppressed in a large part (but not all) of the 95 % CL allowed region. While this implies suppression of the VBF production mode for the H it does not affect the ggF production mode and except for very small VV coupling the branching fraction of the H to VV final states declines only modestly. As a result, the limits in the $ZZ \rightarrow 4\ell$ channel [54], which already extend down to about $0.1 \times \text{SM}$ in the mass range $m_H \approx 180\text{--}400$ GeV, and to about $0.8 \times \text{SM}$ at $m_H \approx 600$ GeV, can be quite relevant. For instance, for a heavy scalar H of mass $m_H = 300$ GeV, in the 95 % CL region of our fits the signal strength in the $gg \rightarrow H \rightarrow ZZ$ channel ranges from 0 to 5.4 in Type I and from 0 to 33 in Type II. For $m_H = 600$ GeV, we find $\mu(gg \rightarrow H \rightarrow ZZ) \lesssim 1.1$ (0.6) in Type I (II). Further, at the best-fit point for $\tan\beta > 1$, $\mu(gg \rightarrow H \rightarrow ZZ) = 1.10$ (0.08)

at $m_H = 300$ (600) GeV in Type I and $\mu(gg \rightarrow H \rightarrow ZZ) = 0.12$ (0.001) at $m_H = 300$ (600) GeV in Type II, which violate the nominal limits at $m_H = 300$ GeV in both models. Note, however, that it is possible to completely evade the 4ℓ bounds if $H \rightarrow hh$ decays are dominant.

Moreover, both the H and the A , which has no tree-level couplings to VV , may show up in the $\tau\tau$ final state through ggF. Limits from ATLAS [180] range (roughly) from $\mu(gg \rightarrow H, A \rightarrow \tau\tau) < 2500$ at $m_{H,A} = 300$ GeV to $< 21,000$ at $m_{H,A} = 500$ GeV. These may seem rather weak limits, but in fact the signal strengths for $H \rightarrow \tau\tau$ and $A \rightarrow \tau\tau$ (relative to H_{SM}) can be extremely large. In the case of the A , this is because the $A \rightarrow \tau\tau$ branching fraction is generically much larger than the $H_{\text{SM}} \rightarrow \tau\tau$ branching fraction, the latter being dominated by VV final states at high mass. In the case of the H , the same statement applies whenever its VV coupling is greatly suppressed. We find that only the Type I model with $\tan\beta > 1$ completely evades the $\tau\tau$ bounds throughout the 95 % CL region of the h fit since both the fermionic couplings of H and A are suppressed by large $\tan\beta$. In the Type II model, $gg \rightarrow A \rightarrow \tau\tau$ satisfies the $\tau\tau$ bounds at 95 % CL, but $gg \rightarrow H \rightarrow \tau\tau$ can give a very large signal. However, the best fit h point for $\tan\beta > 1$ in Type II predicts $\mu(gg \rightarrow H \rightarrow \tau\tau)$ values of 674 and 6.4 at 300 and 500 GeV, both of which satisfy the earlier-stated bounds. We also stress that no bounds are available in the $\tau\tau$ channel above 500 GeV.

Clearly, a full study is needed to ascertain the extent to which limits in the $H \rightarrow ZZ$ and $H, A \rightarrow \tau\tau$ channels will impact the portion of the α — β plane allowed at 95 % CL after taking into account Higgs-to-Higgs decays, which are typically substantial. This is beyond the scope of this section and will be presented elsewhere [181].

2.6.5 Application to the Inert Doublet Model

In the Inert Doublet Model (IDM) [182], a Higgs doublet \tilde{H}_2 which is odd under a Z_2 symmetry is added to the SM leading to four new particles: a scalar \tilde{H} , a pseudoscalar \tilde{A} , and two charged states \tilde{H}^\pm in addition to the SM-like Higgs h .⁹ All other fields being even, this discrete symmetry not only guarantees that the lightest inert Higgs particle is stable, and thus a suitable dark matter candidate [183–186], but also prevents the coupling of any of the inert doublet particles to pairs of SM particles. Therefore, the only modification to the SM-like Higgs couplings is through the charged Higgs contribution to ΔC_γ . The scalar potential of the IDM is given by

$$V = \mu_1^2 |H_1|^2 + \mu_2^2 |\tilde{H}_2|^2 + \lambda_1 |H_1|^4 + \lambda_2 |\tilde{H}_2|^4 + \lambda_3 |H_1|^2 |\tilde{H}_2|^2 + \lambda_4 |H_1^\dagger \tilde{H}_2|^2 + \frac{\lambda_5}{2} \left[\left(H_1^\dagger \tilde{H}_2 \right)^2 + \text{h.c.} \right], \quad (2.24)$$

⁹For distinction with the 2HDM, we denote all IDM particles odd under Z_2 with a tilde.

where $\mu_2^2 > -\lambda_3 v^2/2$ is required in order that \tilde{H}_2^0 not acquire a non-zero vev (which would violate the symmetry needed for \tilde{H} to be a dark matter particle). The crucial interactions implied by this potential are those coupling the light Higgs h associated with the H_1 field to pairs of Higgs bosons coming from the \tilde{H}_2 field. These are given by: $-(2m_W/g)\lambda_3 h \tilde{H}^+ \tilde{H}^-$, $-(2m_W/g)\lambda_L h \tilde{H} \tilde{H}$ and $-(2m_W/g)\lambda_S h \tilde{A} \tilde{A}$ for the charged, scalar and pseudo scalar, respectively, where

$$\lambda_{L,S} = \frac{1}{2} (\lambda_3 + \lambda_4 \pm \lambda_5). \quad (2.25)$$

With these abbreviations, the Higgs masses at tree-level can be written as

$$m_h^2 = \mu_1^2 + 3\lambda_1 v^2, \quad m_{\tilde{H},(\tilde{A})}^2 = \mu_2^2 + \lambda_{L(S)} v^2, \quad m_{\tilde{H}^\pm}^2 = \mu_2^2 + \frac{1}{2}\lambda_3 v^2. \quad (2.26)$$

Moreover, the couplings to the inert charged and neutral Higgses are related by

$$\frac{\lambda_3}{2} = \frac{1}{v^2} (m_{\tilde{H}^+}^2 - m_{\tilde{H}}^2) + \lambda_L. \quad (2.27)$$

It is important to note that a priori $m_{\tilde{H},\tilde{A},\tilde{H}^\pm}^2$ are each free parameters and could be small enough that h decays to a pair of the dark sector states would be present and possibly very important. The $h \rightarrow \tilde{H} \tilde{H}$ and $h \rightarrow \tilde{A} \tilde{A}$ decays would be invisible and contribute to \mathcal{B}_{inv} for the h ; $h \rightarrow \tilde{H}^+ \tilde{H}^-$ decays would generally be visible so long as the \tilde{H}^+ was not closely degenerate with the \tilde{H} .

Theoretical constraints impose some conditions on the couplings. Concretely, we assume a generic perturbativity upper bound $|\lambda_i| < 4\pi$, which, when coupled with the vacuum stability and perturbative unitarity conditions on the potential, leads to $\lambda_3 > -1.5$ and $\mu_2^2 \gtrsim -4.5 \times 10^4 \text{ GeV}^2$ [186, 187]. We also adopt a lower bound of $m_{\tilde{H}^\pm} > 70 \text{ GeV}$, as derived from chargino limits at LEP [188, 189]. Note however that LHC exclusions for the SM Higgs do not apply to members of the inert doublet because (i) they do not couple to fermions and (ii) trilinear and quartic couplings to gauge bosons involve two inert Higgses.

Let us now turn to the fit results.¹⁰ First, we consider the case where $m_{\tilde{H}}, m_{\tilde{A}} > m_h/2$ —the only deviation from the SM then arises from the charged Higgs contribution to ΔC_γ parametrized by λ_3 and $m_{\tilde{H}^\pm}$. The general one-parameter fit to the Higgs couplings leads to the bounds -0.02 (-0.13) $< \Delta C_\gamma < 0.17$ (0.26) at 1σ (2σ). The corresponding contours in the $m_{\tilde{H}^\pm}$ versus λ_3 plane are shown in Fig. 2.36. Note that the 3rd equality of Eq. (2.26) and the lower bound of $\mu_2^2 \gtrsim -4.5 \times 10^4 \text{ GeV}^2$ imply an upper bound on λ_3 for any given $m_{\tilde{H}^\pm}$. This excludes the large- λ_3 region when $m_{\tilde{H}^+} \gtrsim 130 \text{ GeV}$. The impact of the global fit is confined to the region $m_{\tilde{H}^+} \lesssim 130 \text{ GeV}$ and $|\lambda_3| \lesssim 2$ (at 95 % CL). The best fit point lies at $m_{\tilde{H}^+} = 170 \text{ GeV}$ and $\lambda_3 = -1.47$.

¹⁰In our IDM fits, the $h\gamma\gamma$ coupling is computed with micrOMEGAS 3 [170].

Fig. 2.36 Contours of 68, 95, 99.7 % CL in the $m_{\tilde{H}^\pm}$ versus λ_3 plane for the IDM assuming that there are no invisible decays of the SM-like Higgs h

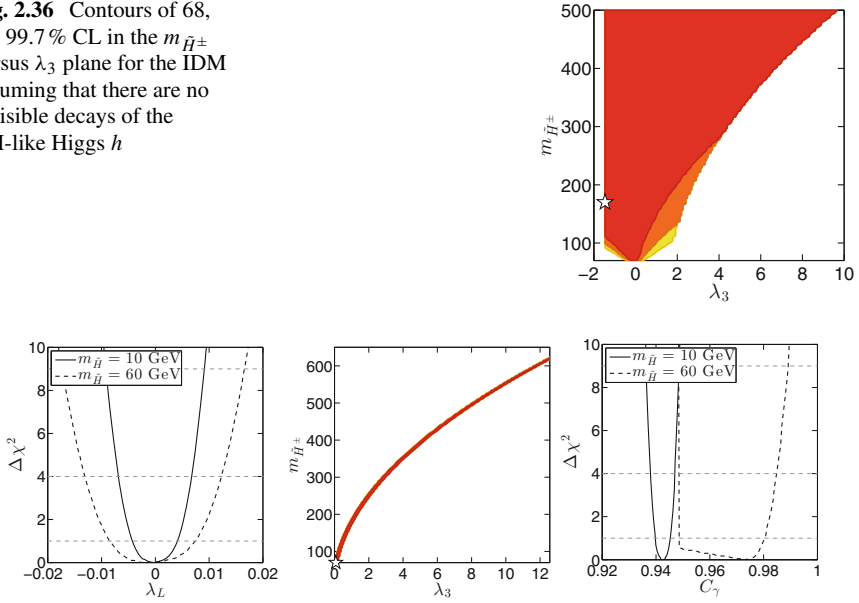


Fig. 2.37 Left panel $\Delta\chi^2$ distribution of λ_L for $m_{\tilde{H}} = 10$ GeV (full line) and 60 GeV (dashed line) with $m_{\tilde{H}^\pm}$ profiled over its whole allowed range. Middle panel relation between $m_{\tilde{H}^\pm}$ and λ_3 with $m_{\tilde{H}}$ profiled over from 1 to 60 GeV. Right panel: $\Delta\chi^2$ as function of C_γ for $m_{\tilde{H}} = 10$ GeV (full line) and 60 GeV (dashed line) with $m_{\tilde{H}^\pm}$ profiled over

Second, we consider the case where the inert scalar is light and examine how invisible $h \rightarrow \tilde{H}\tilde{H}$ decays further constrain the parameters. The bounds on the invisible width actually lead to a strong constraint on the coupling λ_L . The 1σ (2σ) allowed range is roughly $\lambda_L \times 10^3 = \pm 4$ (± 7) for $m_{\tilde{H}} = 10$ GeV. This bound weakens only when the invisible decay is suppressed by kinematics; for $m_{\tilde{H}} = 60$ GeV, we find $\lambda_L \times 10^3 = [-9, 7]$ ($[-13, 12]$) at 1σ (2σ). The $\Delta\chi^2$ distributions of λ_L for $m_{\tilde{H}} = 10$ and 60 GeV are shown in the left panel in Fig. 2.37, with $m_{\tilde{H}^\pm}$ profiled over from 70 GeV to about 650 GeV (the concrete upper limit being determined by the perturbativity constraint). This strong constraint on λ_L implies that it can be neglected in Eq. (2.27) and that the charged Higgs coupling λ_3 is directly related to $m_{\tilde{H}^\pm}$ for a given $m_{\tilde{H}}$, as illustrated in the middle panel of Fig. 2.37 (here, the mass of the inert scalar is profiled over in the range $m_{\tilde{H}} \in [1, 60]$ GeV). As a result the value of C_γ is also strongly constrained from the upper bound on the invisible width. For example for $m_{\tilde{H}} = 10$ GeV, we find that $C_\gamma = [0.940, 0.945]$ at 68 % CL. Note that because $m_{\tilde{H}^\pm} > m_{\tilde{H}}$ is needed in order to have a neutral dark matter candidate, λ_3 is always positive and therefore $C_\gamma < 1$. To approach $C_\gamma \simeq 1$, the inert Higgs mass has to be close to the kinematic threshold, $m_{\tilde{H}} \rightarrow m_h/2$ so that the constraint on λ_L is relaxed. For illustration, see the right panel in Fig. 2.37. These results imply that with an improved accuracy on the measurements of the Higgs

coupling, for example showing that $C_\gamma > 0.95$, it would be possible to exclude light dark matter ($m_{\tilde{H}} < 10 \text{ GeV}$) in the IDM. Another consequence is that for a given $m_{\tilde{H}}$ the perturbativity limit $\lambda_3 < 4\pi$ implies an upper bound on the charged Higgs mass. For $m_{\tilde{H}} \in [1, 60] \text{ GeV}$ we obtain $m_{\tilde{H}^\pm} < 620 \text{ GeV}$.

Finally note that the case where \tilde{A} is the lightest neutral state and $m_{\tilde{A}} < m_h/2$ is analogous to the \tilde{H} case just discussed, with $m_{\tilde{H}} \rightarrow m_{\tilde{A}}$ and $\lambda_L \rightarrow \lambda_S$ and leads to analogous conclusions. Analyses of the Higgs sector of the Inert Doublet Model were also performed recently in [186, 190–193].

2.6.6 Conclusions

The most general fits considered were those in which $C_U, C_D, C_V, \Delta C_g, \Delta C_\gamma$ were all allowed to vary freely. If there are no unseen (as opposed to truly invisible) decay modes of the Higgs, one finds that the observed 125.5 GeV state prefers to have quite SM-like couplings whether or not $\mathcal{B}_{\text{inv}} = 0$ is imposed—more constrained fits, for example taking $\Delta C_g = \Delta C_\gamma = 0$ while allowing C_U, C_D, C_V to vary, inevitably imply that the other parameters must lie even closer to their SM values.

Allowing for invisible decays of the 125.5 GeV state through $\mathcal{B}_{\text{inv}} > 0$ does not change the best-fit parameter values but does widen the $\Delta\chi^2$ distributions somewhat leading to important implications, i.e., for decays into dark matter particles. In particular, we found that at 95% CL there is still considerable room for such Higgs decays, up to $\mathcal{B}_{\text{inv}} \sim 0.38$ when $C_U, C_D, C_V, \Delta C_g, \Delta C_\gamma$ are all allowed to vary independently of one another. In comparison, a fit for which C_U, C_D are allowed to vary freely, but $C_V \leq 1$ is required (as appropriate for any doublets+singlets model) and $\Delta C_g = \Delta C_\gamma = 0$ is imposed, yields $\mathcal{B}_{\text{inv}} \lesssim 0.24$ at 95% CL. Even requiring completely SM couplings for the Higgs ($C_U = C_D = C_V = 1, \Delta C_g = \Delta C_\gamma = 0$) still allows $\mathcal{B}_{\text{inv}} \leq 0.19$ at 95% CL. It is worthwhile noting that for $C_V \leq 1$, the limits on \mathcal{B}_{inv} from global coupling fits are currently more constraining than those from direct searches for invisible decays, i.e., in the $ZH \rightarrow \ell^+\ell^- + E_T^{\text{miss}}$ mode; thus for $C_V \leq 1$ the limits on merely unseen (i.e. not strictly invisible) decays are similar to the ones on \mathcal{B}_{inv} .

As part of the fitting procedure, the total width of the Higgs relative to the SM prediction is computed as a function of the parameters and a $\Delta\chi^2$ distribution for $\Gamma_{\text{tot}}/\Gamma_{\text{tot}}^{\text{SM}}$ is obtained. Assuming no unseen, but potentially visible, decays, we found $\Gamma_{\text{tot}}/\Gamma_{\text{tot}}^{\text{SM}} \in [0.5, 2]$ at 95% CL for the case where $C_U, C_D, C_V, \Delta C_g, \Delta C_\gamma$ and \mathcal{B}_{inv} are all allowed to vary freely, while $\Gamma_{\text{tot}}/\Gamma_{\text{tot}}^{\text{SM}} \in [1, 1.25]$ at 95% CL if $C_U = C_D = C_V = 1, \Delta C_g = \Delta C_\gamma = 0$ are imposed and only $\mathcal{B}_{\text{inv}} \geq 0$ is allowed for. These are useful limits given the inability to directly measure Γ_{tot} at the LHC. Of course, if there are unseen (but not invisible) decays, there is a flat direction that would prevent setting limits on the total width.

Finally, we have also shown that if $\mathcal{B}_{\text{inv}} \neq 0$ is due to H decays to a pair of DM particles, there are significant constraints on the size of \mathcal{B}_{inv} from the non-observation

of spin-independent DM scattering on nucleons, the most important such limits currently being those from the LUX experiment. These constraints are much stronger for scalar DM than for Majorana or Dirac fermions. Overall, our results suggest a continued competition between limits on σ_{SI} and those on \mathcal{B}_{inv} as direct detection experiments achieve improved sensitivity and increasingly accurate measurements of the properties of the H become available with future LHC running.

In the second part of the section, we then examined implications of these results in the context of some simple concrete models with an extended Higgs sector: the Type I and Type II Two-Higgs-doublet models, and the Inert Doublet Model, using the combined likelihood ellipses to constrain the parameter spaces. In the 2HDM, enhancement of the signal strength for a 2nd neutral (scalar or pseudoscalar) Higgs boson with mass above 125.5 GeV can occur in both the 4ℓ and $\tau\tau$ channels. Therefore additional constraints on α and β can be set unless the decay of the heavier Higgs to a pair of the 125.5 GeV states dominates. Generally the signals in both channels can be at a level of interest for future LHC runs. In the Inert Doublet Model, the inert Higgs states can only be pair-produced and therefore are not currently constrained. However, we showed that the bound on the invisible decay of the 125.5 GeV SM-like Higgs, relevant when one inert Higgs is lighter than ≈ 60 GeV, constrains the allowed range for the two-photon width. Thus, a precise determination of C_γ could rule out light inert Higgs dark matter.

2.7 A Bayesian View of the Higgs Sector with Higher Dimensional Operators

So far, constraints on new physics have been parametrized in the context of the Lagrangian shown in Eq. (2.16), which introduced reduced couplings to vector bosons (C_W, C_Z) and to fermions (C_F). In addition, there are (i) effective contributions to the $\gamma\gamma$ and gg loop-induced couplings, entering the Lagrangian as $H(F_{\mu\nu})^2$ and $H(G_{\mu\nu})^2$, respectively, and (ii) generic invisible/undetected decays of the Higgs boson. This framework is fully justified and applicable to a very wide class of new physics models. It is however possible to take a different perspective in light of the negative LEP, Tevatron and LHC results in the search for new physics at or close to the electroweak scale. If new physics is indeed present and is somehow separated from the electroweak scale, the couplings of the Higgs boson will be close to those of the SM and will only be modified by the effect of a few higher dimensional operators (HDOs). In this section, we will explore an effective field theory (EFT) with only relatively few new parameters. As we will see, most higher dimensional operators will not only have an effect on the Higgs phenomenology but also on measured quantities related to the electroweak sector, such as the Peskin–Takeuchi S and T parameters [55, 56]. This will be taken into account and the interplay between the different observables will be discussed.

The statistical procedure is another difference with the work presented in Sects. 2.5 and 2.6, where we considered a fully frequentist approach and derived confidence intervals for the parameters of interest after profiling over the other, unseen

parameters. In this section, we will adopt the statistical framework of Bayesian inference, which allows us to assign probabilities to our parameters and to deal with partially constrained problems. Another interesting property is that the unnatural (i.e. fine-tuned) character of precise cancellations which may occur between HDO contributions is built-in in this framework. Indeed, regions of the parameter space in which precise cancellations occur have by construction a weak statistical weight.

The work presented in this section has been conducted in collaboration with Sylvain Fichet and Gero von Gersdorff at the end of 2012 and at the beginning of 2013, in parallel to work presented in Sects. 2.5 and 2.6. This led to the paper “A Bayesian view of the Higgs sector with higher dimensional operators”, Ref. [194], that was submitted to arXiv on April 11, 2013 and published in JHEP in July 2013.

The outline of the Section is as follows. In Sect. 2.7.1, we lay out the formalism for higher-dimension operators in the electroweak sector. In Sect. 2.7.2, we present the dataset used for the analysis and the measurements entering the likelihood functions. The peculiar case of observables sensitive to tensorial couplings relating Higgs and weak bosons is investigated in Sect. 2.7.3. In Sect. 2.7.4, we derive the observable deviations from the SM induced by the higher dimensional operators, taking into account leading NLO QCD effects. Section 2.7.5 presents the setup of our Bayesian analysis. Section 2.7.6 is devoted to our results. Our conclusions are given in Sect. 2.7.7.

2.7.1 *Electroweak Higher-Dimension Operators*

We consider that new states appear at a typical scale Λ substantially larger than the electroweak scale. For physical processes involving an energy scale smaller than Λ , new physics can be integrated out. As a consequence of this hypothesis, the resulting low-energy effective theory consists in the Standard Model, supplemented by infinite series of local operators with higher dimension, which involves negative powers of Λ ,

$$\mathcal{L}_{\text{eff}} = \mathcal{L}_{\text{SM}} + \sum_i \frac{\alpha_i}{\Lambda^{n_i}} \mathcal{O}_i. \quad (2.28)$$

The effects of such higher dimensional operators have been investigated in many contexts such as flavor physics, or the study of the properties of the electroweak gauge bosons through LEP precision measurements. The purpose of this work is to study the electroweak sector again, which now includes new Higgs observables. For our analysis, we only have to consider the leading HDOs. The only operator with $n_i = 1$ is the one giving a Majorana mass to the neutrino, and is not relevant for our study. We will thus be exclusively interested in the $n_i = 2$ terms, i.e. dimension-6 operators.

In this section, we define the basis of dimension-6 operators supplementing the renormalizable electroweak sector of the SM Lagrangian. We refer to [195, 196] for further details on the Standard Model HDOs. A basis of CP-even operators not

involving fermions can be chosen as¹¹

$$\mathcal{O}_6 = |H|^6, \quad \mathcal{O}_{D^2} = |H|^2 |D_\mu H|^2, \quad \mathcal{O}'_{D^2} = |H^\dagger D_\mu H|^2, \quad (2.29)$$

$$\mathcal{O}_{WW} = H^\dagger H (W_{\mu\nu}^a)^2, \quad \mathcal{O}_{BB} = H^\dagger H (B_{\mu\nu})^2, \quad \mathcal{O}_{WB} = H^\dagger W_{\mu\nu} H B_{\mu\nu}, \quad (2.30)$$

$$\mathcal{O}_{GG} = H^\dagger H (G_{\mu\nu}^a)^2. \quad (2.31)$$

Any other operator can be reduced to these via integration by parts and the use of the SM equations of motion for the Higgs and gauge fields, possibly generating operators involving fermions. Amongst the latter, only a limited set will be relevant for our purpose. Operators of the form $J_H \cdot J_f$, where J_H and J_f are $SU(2)$ or $U(1)_Y$ currents involving Higgs field and fermion f respectively, will in general contribute to FCNC as well as electroweak non-oblique corrections (i.e., non-universal couplings of fermions to gauge bosons).¹² However, the operators

$$\mathcal{O}_D = J_{H\mu}^a J_\mu^a, \quad \mathcal{O}'_D = J_{H\mu}^Y J_\mu^Y, \quad (2.32)$$

where $J = \sum_f J_f$ are the SM fermion currents coupling to B_μ and W_μ , are flavor diagonal and only result in universal corrections to gauge couplings and should hence be viewed as contributing to S and T .¹³ We will also need to consider Yukawa corrections of the form

$$\mathcal{O}_f = 2y_f |H|^2 H \bar{f}_L f_R, \quad (2.33)$$

where $f_R = t_R, b_R, \tau_R$ and f_L the corresponding doublet ($\bar{f}_L^a = \epsilon^{ab} \bar{q}_L^{b,3}, \bar{q}_L^{a,3}, \bar{\ell}_L^{a,3}$) and y_f the Yukawa coupling.

Note that the operators \mathcal{O}_D and \mathcal{O}'_D could be traded for the operators

$$\mathcal{O}_W = (D_\mu H)^\dagger W_{\mu\nu} D_\nu H, \quad \mathcal{O}_B = (D_\mu H)^\dagger D_\nu H B_{\mu\nu}, \quad (2.34)$$

by use of the SM equations of motion for B and W . While \mathcal{O}_D and \mathcal{O}'_D contribute to S and T but not to the modified Higgs couplings, for \mathcal{O}_B and \mathcal{O}_W it is the other way around. Both choices of basis are physically equivalent. Before passing from a general redundant set of operators to a convenient irreducible basis via the equations of motion, it is useful to first identify the operators that cannot be generated at

¹¹The operator \mathcal{O}_6 plays no role in what follows and is listed here only for completeness.

¹²The non-universal corrections to the weak bosons couplings of the top quark are only very mildly constrained by EW data, and it is a priori not justified to set them to zero. However the only effect to Higgs observables at leading order is a modification of the top loop contribution to the $h \rightarrow Z\gamma$ decay due to the anomalous Ztt vertex. The top contribution is however about one order of magnitude smaller than the leading contribution from the W loop [21]. We will therefore only consider universal (oblique) corrections to EW data.

¹³In fact this is the way how contributions to S and T can arise in theories with new spin-1 states, such as in warped extra dimensions [197, 198].

tree-level.¹⁴ This is valuable information and we would like to avoid it to be lost in the course of the reduction. However this is what would happen if we eliminated \mathcal{O}_D and \mathcal{O}'_D in favor of \mathcal{O}_W and \mathcal{O}_B . Indeed, this would cause the coefficient of i.e. \mathcal{O}_{WB} (which cannot be generated at tree-level) to be shifted by the coefficient of \mathcal{O}_D (which can be generated at the tree-level via exchange of spin-one states). This is why we choose this basis.

The only remaining two-fermion operators are of the dipole type. These operators are tightly constrained by FCNC as well as by their contributions to electric and magnetic dipole moments. Moreover, they are necessarily generated at the loop-level, and only affect Higgs couplings to gauge bosons by modifying existing SM loops. They will not have any impact on our results, therefore we can neglect them entirely.

We do not take into account CP-violating HDOs. These operators are constrained by observables such as electric dipole moments. If we choosed to include these CP-odd HDOs in our analysis, we would also need to consider the whole set of data sensitive to CP violation. Although there is no fundamental problem with such extended analysis, that is beyond the scope of the present work. Moreover, the effects induced by CP-violating HDOs are often subleading with respect to the effects of CP-even operators, unless the latter are sufficiently suppressed. This is the case for Higgs decays, because CP-violating amplitudes do not interfere with SM amplitudes, whereas CP-conserving amplitudes do interfere with SM amplitudes [200]. In the following we will derive observable deviations from the Standard Model using the full set of HDOs, and perform the analysis presented in Sect. 2.7.5 taking into account only operators that respect custodial symmetry.

We could also rigorously take into account the running of the HDO coefficients α_i from the scale Λ to the low scale (m_h or \sqrt{s} , depending on the process considered), see for example [201]. However, the consequences of this running are rather mild so we will neglect them in this study. Notice that the strong effect of the operator \mathcal{O}_{WB} on the $h\gamma\gamma$ vertex found in [201] requires large enhancement of α_{WB} with respect to $s_w^2 \alpha_{WW} + c_w^2 \alpha_{BB} - \frac{1}{2}s_w c_w \alpha_{WB}$ (the coefficient of $h F_{\mu\nu} F^{\mu\nu}$, see Eq. (2.43)). As is evident in our basis, this cannot be explained by a relative loop factor as none of these operators receive contributions at tree-level. Moreover, it has been shown in Ref. [202] that operators that can be generated at tree-level (such as \mathcal{O}_D) do not mix with the loop-suppressed operators such as \mathcal{O}_{VV} in the renormalization group flow. In the absence of large hierarchies in the couplings of new physics states, we conclude that operator mixing does not lead to a large enhancement of the $h \rightarrow \gamma\gamma$ rate.

¹⁴A detailed study about perturbative generation of HDOs can be found in [199].

Effective Lagrangian

In this section we will present the effect of the HDOs on the SM tree-level couplings. Loops involving SM particles are considered in Sect. 2.7.1. We define the physical Higgs field h as

$$H = \begin{pmatrix} 0 \\ \frac{1}{\sqrt{2}}(\tilde{v} + h) \end{pmatrix}, \quad (2.35)$$

and parameterize the couplings of h to gauge bosons and fermions as¹⁵

$$\mathcal{L}_{v,f}^{\text{tree}} = \lambda_Z h (Z_\mu)^2 + \lambda_W h W_\mu^+ W_\mu^- + \sum_f \lambda_f h \bar{f}_L f_R. \quad (2.36)$$

The SM tree-level predictions for these quantities are given in terms of the SM input parameters \tilde{g} , \tilde{v} and $\tilde{s}_w^2 \equiv \tilde{g}^2/(\tilde{g}^2 + \tilde{g}'^2)$:

$$\lambda_Z = \frac{\tilde{g}^2 \tilde{v}}{4 \tilde{c}_w^2} \equiv \frac{\tilde{m}_Z^2}{\tilde{v}}, \quad \lambda_W = \frac{\tilde{g}^2 \tilde{v}}{2} \equiv \frac{2 \tilde{m}_W^2}{\tilde{v}}, \quad \lambda_f = -\frac{\tilde{y}_f}{\sqrt{2}} \equiv -\frac{\tilde{m}_f}{\tilde{v}}, \quad (2.37)$$

where the quantities with a tilde are the ones that appear in the SM part of the Lagrangian. For instance, \tilde{g} and \tilde{g}' are the couplings appearing in the covariant derivatives. However, these couplings do not take the same values as in the SM, since there are corrections from HDOs. There are distinct effects, as follows (see Ref. [203] for an analogous discussion on fermion couplings).

- Operators such as \mathcal{O}_{D^2} correct directly the tree-level SM vertices.
- Some operators (i.e. \mathcal{O}_{D^2} , \mathcal{O}_{WW}) modify the kinetic terms of Higgs and gauge fields and thus indirectly lead to the rescaling of some couplings.
- Finally, there can be indirect effects from input parameters. They are taken to be the fine-structure constant α , the Z boson mass m_Z and the Fermi constant G_F , as well as the physical fermion masses m_f and the strong coupling constant α_s . These quantities receive corrections from HDOs but must be held fixed in the analysis. Yet, this causes the SM parameters \tilde{g} , \tilde{v} and \tilde{s}_w to become functions of the HDO coefficients.

The last point is sometimes not taken into account in the literature. Let us focus on it and *define* the quantities v , g and s_w via

$$4\pi\alpha \equiv s_w^2 g^2, \quad m_Z^2 \equiv \frac{v^2 g^2}{4 c_w^2}, \quad G_F \equiv \frac{1}{\sqrt{2} v^2}. \quad (2.38)$$

These quantities can be viewed as the “familiar” numbers from the SM (i.e. $v = 246\text{GeV}$). Like the input parameters they stay fixed in our analysis. On the other hand, the parameters \tilde{g} , \tilde{s}_w and \tilde{v} are the gauge couplings appearing in the covariant

¹⁵For the hVV couplings with different tensor structure see below.

derivatives and the vacuum expectation value (vev) of the Higgs field, and must be expressed in terms of the HDO coefficients. The details of this procedure are presented in Appendix A of [194]. Taking into account all the above effects, we obtain

$$\lambda_Z = a_Z \frac{m_Z^2}{v}, \quad \lambda_W = a_W \frac{2m_W^2}{v}, \quad \lambda_f = -c_f \frac{m_f}{v}, \quad (2.39)$$

where m_f and m_W are the *physical* masses. In particular, m_W is given by¹⁶

$$\begin{aligned} m_W^2 &= \frac{g^2 v^2}{4} \left(1 + \left(\frac{1}{2} \alpha_D - \frac{c_w^2}{2(c_w^2 - s_w^2)} [\alpha'_{D^2} + \alpha_D] - \frac{c_w s_w}{c_w^2 - s_w^2} \alpha_{WB} \right) \frac{v^2}{\Lambda^2} \right) \\ &= \frac{g^2 v^2}{4} \left(1 - \frac{\alpha S}{2(c_w^2 - s_w^2)} + \frac{c_w^2 \alpha T}{c_w^2 - s_w^2} \right). \end{aligned} \quad (2.40)$$

In the last row we have used Eqs. (2.78) and (2.79) in order to compare our derivation of m_W with the one in [203]. The SM prediction of m_W is thus only corrected by the oblique parameters. In this parametrization, the rescaling factors a_Z , a_W and c_f are given by

$$\begin{aligned} a_Z &= 1 + \left(\frac{1}{2} \alpha_{D^2} - \frac{1}{4} \alpha_D + \frac{1}{4} \alpha'_{D^2} \right) \frac{v^2}{\Lambda^2}, \\ a_W &= 1 + \left(\frac{1}{2} \alpha_{D^2} - \frac{1}{4} \alpha_D - \frac{1}{4} \alpha'_{D^2} \right) \frac{v^2}{\Lambda^2}, \\ c_f &= 1 - \left(\frac{1}{4} \alpha'_{D^2} - \frac{1}{4} \alpha_D - \alpha_f \right) \frac{v^2}{\Lambda^2}. \end{aligned} \quad (2.41)$$

As a non-trivial consistency check, note that the vector anomalous couplings are rescaled in a custodially symmetric way ($a_Z = a_W$) once the custodial-symmetry violating operator \mathcal{O}'_{D^2} is turned off.

To conclude this subsection we compute the direct tree-level HDO contribution to the tensor couplings,

$$\mathcal{L}_t^{\text{tree}} = \zeta_\gamma h (F_{\mu\nu})^2 + \zeta_g h (G_{\mu\nu})^2 + \zeta_{Z\gamma} h F_{\mu\nu} Z_{\mu\nu} + \zeta_Z h (Z_{\mu\nu})^2 + \zeta_W h W_{\mu\nu}^+ W_{\mu\nu}^-, \quad (2.42)$$

which are all zero in the SM at tree-level. One finds

$$\zeta_\gamma = \left(s_w^2 \alpha_{WW} + c_w^2 \alpha_{BB} - \frac{1}{2} s_w c_w \alpha_{WB} \right) \frac{v}{\Lambda^2}, \quad \zeta_g = \alpha_{GG} \frac{v}{\Lambda^2}, \quad (2.43)$$

$$\zeta_{Z\gamma} = \left(2c_w s_w \alpha_{WW} - 2c_w s_w \alpha_{BB} - \frac{1}{2} (c_w^2 - s_w^2) \alpha_{WB} \right) \frac{v}{\Lambda^2}, \quad (2.44)$$

¹⁶Unlike m_Z and m_f , which are input parameters, the W mass is a prediction in terms of input parameters and HDO coefficients.

$$\zeta_Z = \left(c_w^2 \alpha_{WW} + s_w^2 \alpha_{BB} + \frac{1}{2} c_w s_w \alpha_{WB} \right) \frac{v}{\Lambda^2}, \quad \zeta_W = 2 \alpha_{WW} \frac{v}{\Lambda^2}. \quad (2.45)$$

The first two quantities constitute important corrections to the production and decay of the Higgs boson. The last two corrections modify the tensorial structure of the SM Higgs–weak bosons coupling in a non-trivial way, which is discussed in detail in Sect. 2.7.3.

Standard Model Loop-Induced HDOs

In this section we compute the Standard Model loop-induced operators relevant for Higgs physics. These operators contain indirect modifications due to couplings modified by the HDOs considered in the previous subsection. We want to make sure that we do not double-count possible new physics contribution to the Higgs couplings. In order to have a well-defined HDO framework at loop-level, we should consider that the HDOs we present in Eqs. (2.29)–(2.33) are generated exclusively through new physics states at leading order, and enclose higher-order SM corrections only from irreducible loops.¹⁷ Hence, the modified SM loops are not included in the tree-level contributions computed in the previous subsection. Our strategy is thus to compute the one-loop corrections to $\mathcal{L}^{\text{tree}}$ using the couplings shown in Eq. (2.41).

The one-loop Lagrangian is parametrized as

$$\mathcal{L}^{1\text{-loop}} = \lambda_\gamma h (F_{\mu\nu})^2 + \lambda_g h (G_{\mu\nu})^2 + \lambda_{Z\gamma} h F_{\mu\nu} Z_{\mu\nu}. \quad (2.46)$$

Let us decompose these couplings according to the particle in the loop, $\lambda_i = \sum_X \lambda_i^X$. We find¹⁸

$$\lambda_\gamma^W = a_W \lambda_\gamma^{W,\text{SM}} = \frac{7}{2} \frac{g^2 s_w^2}{16\pi^2} \frac{a_W}{v} A_v(\tau_W), \quad (2.47)$$

$$\lambda_\gamma^f = c_f \lambda_\gamma^{f,\text{SM}} = -\frac{2}{3} N_f^c e_f^2 \frac{g^2 s_w^2}{16\pi^2} \frac{c_f}{v} A_f(\tau_f), \quad \lambda_g^f = c_f \lambda_g^{f,\text{SM}} = -\frac{1}{3} \frac{g_s^2}{16\pi^2} \frac{c_f}{v} A_f(\tau_f), \quad (2.48)$$

$$\begin{aligned} \lambda_{Z\gamma}^W &= a_W \lambda_{Z\gamma}^{W,\text{SM}} = \frac{e^2}{16\pi^2} \frac{a_W}{v} t_w^{-1} \left(2 [t_w^2 - 3] A_{Z\gamma}(\tau_W, \kappa_W) \right. \\ &\quad \left. + \left[\frac{5 - t_w^2}{2} + \frac{1 - t_w^2}{\tau_W} \right] B_{Z\gamma}(\tau_W, \kappa_W) \right), \end{aligned} \quad (2.49)$$

¹⁷This last point is important for NLO QCD corrections, see Sect. 2.7.4.

¹⁸Note that in Eqs. (2.47)–(2.50) only the quantities with a tilde appear. Besides the modified Higgs couplings, the HDOs we consider only affect the couplings of the fermions to the W and Z bosons, precisely via the oblique parameters S and T . The latter would in fact only show up in $\lambda_{Z\gamma}^f$. However these corrections are subleading and rather small (few percents at most), so that it is safe to neglect them.

$$\lambda_{Z\gamma}^f = -c_f \lambda_{Z\gamma}^{f,\text{SM}} = \frac{e^2}{16\pi^2} \frac{c_f}{v} N_f^c \frac{e_f^2 (T_f^{3L} - 2e_f s_w^2)}{s_w c_w} (B_{Z\gamma}(\tau_f, \kappa_f) - A_{Z\gamma}(\tau_f, \kappa_f)). \quad (2.50)$$

where N_f^c and e_f are the number of colors and the fraction of electric charge of the fermion running in the loop, respectively. We define $\tau_i = 4m_i^2/m_h^2$, $\kappa_i = 4m_i^2/m_Z^2$. The form factors A_i , B are given in Appendix B of [194]. They are defined so that in the decoupling limit, $A_{f,v} \rightarrow 1$ when $\tau \rightarrow \infty$, and $A_{Z\gamma} \rightarrow 1$, $B_{Z\gamma} \rightarrow 0$ when $\tau, \kappa \rightarrow \infty$.

Trilinear Gauge Boson Vertices

The higher dimensional operators that we are considering also affect charged triple gauge boson vertices (TGV). In the parametrization of Ref. [204],

$$\mathcal{L}_{\text{TGV}} = -i e \kappa_\gamma F_{\mu\nu} W_\mu^- W_\nu^+ - i g c_w \kappa_Z Z_{\mu\nu} W_\mu^- W_\nu^+ - i g c_w g_1^Z [W_{\mu\nu}^+ W_\nu^- - W_{\mu\nu}^- W_\nu^+] Z_\mu, \quad (2.51)$$

the deviations from the Standard Model can be expressed in terms of the HDO coefficients as follows:

$$\begin{aligned} \kappa_\gamma &= 1 + \frac{\alpha_{WB}}{2t_w} \frac{v^2}{\Lambda^2}, \\ \kappa_Z &= 1 - \left(\frac{s_w c_w}{(c_w^2 - s_w^2)} \alpha_{WB} + \frac{1}{4(c_w^2 - s_w^2)} [\alpha'_{D^2} + \alpha_D] \right) \frac{v^2}{\Lambda^2}, \\ g_1^Z &= 1 - \left(\frac{s_w}{2c_w(c_w^2 - s_w^2)} \alpha_{WB} + \frac{1}{4(c_w^2 - s_w^2)} [\alpha'_{D^2} + \alpha_D] \right) \frac{v^2}{\Lambda^2}, \end{aligned} \quad (2.52)$$

where again some indirect effects from fixing input parameters were taken into account. Gauge invariance implies the relation $\kappa_Z = g_1^Z - (\kappa_\gamma - 1)t_w^2$ and one can check that it is indeed fulfilled. We then choose κ_γ and g_1^Z as independent couplings.

2.7.2 Data Treatment

We exploit the results from Higgs searches at the LHC and at Tevatron as well as electroweak precision observables and trilinear gauge couplings. Starting from the Higgs searches, as in Sect. 2.6 we use the results given in the $(\mu(\text{ggF} + \text{ttH}), Y)$, $\mu(\text{VBF} + \text{VH}), Y)$ plane when available. The values for the signal strengths in the various (sub)channels as reported by the experiments and used in this analysis, together with the estimated decompositions into production channels are given in Tables 2.10, 2.11 and 2.12. Some of the decompositions into production channels are taken from [67]. In case of missing information, we take the relative ratios of production cross sections for an SM Higgs as a reasonable approximation, i.e. we

Table 2.10 ATLAS results, as employed in this analysis. The following correlations are included in the fit: $\rho_{\gamma\gamma} = -0.27$, $\rho_{ZZ} = -0.50$, $\rho_{WW} = -0.18$, $\rho_{\tau\tau} = -0.49$

Channel	Signal strength μ	m_h (GeV)	Reduced efficiencies				
		ggF (%)	VBF (%)	WH (%)	ZH (%)	ttH (%)	
$h \rightarrow \gamma\gamma$ (4.8 fb $^{-1}$ at 7 TeV + 20.7 fb $^{-1}$ at 8 TeV) [34, 52]							
$\mu(\text{ggF} + \text{ttH}, \gamma\gamma)$	1.60 ± 0.41	125.5	100	–	–	–	–
$\mu(\text{VBF} + \text{VH}, \gamma\gamma)$	1.94 ± 0.82	125.5	–	60	26	14	–
$h \rightarrow ZZ$ (4.6 fb $^{-1}$ at 7 TeV + 20.7 fb $^{-1}$ at 8 TeV) [34, 54]							
$\mu(\text{ggF} + \text{ttH}, ZZ)$	1.51 ± 0.52	125.5	100	–	–	–	–
$\mu(\text{VBF} + \text{VH}, ZZ)$	1.99 ± 2.12	125.5	–	60	26	14	–
$h \rightarrow WW$ (4.6 fb $^{-1}$ at 7 TeV + 20.7 fb $^{-1}$ at 8 TeV) [53, 146]							
$\mu(\text{ggF} + \text{ttH}, WW)$	0.79 ± 0.35	125.5	100	–	–	–	–
$\mu(\text{VBF} + \text{VH}, WW)$	1.71 ± 0.76	125.5	–	60	26	14	–
$h \rightarrow b\bar{b}$ (4.7 fb $^{-1}$ at 7 TeV + 13.0 fb $^{-1}$ at 8 TeV) [34, 116]							
VH tag	-0.39 ± 1.02	125.5	–	–	64	36	–
$h \rightarrow \tau\tau$ (4.6 fb $^{-1}$ at 7 TeV + 13.0 fb $^{-1}$ at 8 TeV) [34]							
$\mu(\text{ggF} + \text{ttH}, \tau\tau)$	2.31 ± 1.61	125.5	100	–	–	–	–
$\mu(\text{VBF} + \text{VH}, \tau\tau)$	-0.20 ± 1.06	125.5	–	60	26	14	–

assume that the experimental search is fully inclusive and compute the signal strength modified by HDOs accordingly. To this end, we use the latest predictions of the cross sections at the LHC [129] and at Tevatron [205]. In our analysis, the Higgs mass is set to $m_h = 125.5$ GeV (close to the combined mass measurement from the two experiments) since it is not yet possible to take it as a nuisance parameter without losing the correlations between production channels. We consider experimental measurements of the signal strengths as close as possible to this value.

We take into account the electroweak precision observables using the Peskin–Takeuchi S and T parameters [55, 56]. Beyond S and T , the W and Y parameters [207] should be used in the HDO framework. However we find that constraints arising from these parameters are by far subleading with respect to our other constraints. Experimental values of S and T are taken from the latest electroweak fit of the SM done by the Gfitter Group [13]: $S = 0.05 \pm 0.09$ and $T = 0.08 \pm 0.07$ with a correlation coefficient of 0.91. Regarding constraints on TGV, we take into account the LEP measurements [208]:

$$\begin{aligned} \kappa_\gamma &= 0.973^{+0.044}_{-0.045}, \\ g_1^Z &= 0.984^{+0.022}_{-0.019}. \end{aligned} \quad (2.53)$$

Table 2.11 CMS results, as employed in this analysis. The following correlations are included in the fit: $\rho_{\gamma\gamma} = -0.50$, $\rho_{ZZ} = -0.73$

Channel	Signal strength μ	m_h (GeV)	Reduced efficiencies				
		ggF (%)	VBF (%)	WH (%)	ZH (%)	ttH (%)	
$h \rightarrow \gamma\gamma$ (5.1 fb $^{-1}$ at 7 TeV + 19.6 fb $^{-1}$ at 8 TeV) [60]							
$\mu(\text{ggF} + \text{ttH}, \gamma\gamma)$	0.49 ± 0.39	125	100	–	–	–	–
$\mu(\text{VBF} + \text{VH}, \gamma\gamma)$	1.65 ± 0.87	125	–	60	26	14	–
$h \rightarrow ZZ$ (5.1 fb $^{-1}$ at 7 TeV + 19.6 fb $^{-1}$ at 8 TeV) [61]							
$\mu(\text{ggF} + \text{ttH}, ZZ)$	0.99 ± 0.46	125.8	100	–	–	–	–
$\mu(\text{VBF} + \text{VH}, ZZ)$	1.05 ± 2.38	125.8	–	60	26	14	–
$h \rightarrow WW$ (up to 4.9 fb $^{-1}$ at 7 TeV + 19.5 fb $^{-1}$ at 8 TeV) [64, 119, 120, 148]							
0/1 jet	0.76 ± 0.21	125	97	3	–	–	–
VBF tag	$-0.05^{+0.74}_{-0.55}$	125.8	17	83	–	–	–
VH tag	$-0.31^{+2.22}_{-1.94}$	125.8	–	–	64	36	–
$h \rightarrow b\bar{b}$ (up to 5.0 fb $^{-1}$ at 7 TeV + 12.1 fb $^{-1}$ at 8 TeV) [64, 121, 122]							
$Z(\ell^-\ell^+)h$	$1.55^{+1.20}_{-1.07}$	125	–	–	–	100	–
$Z(\nu\bar{\nu})h$	$1.79^{+1.11}_{-1.02}$	125	–	–	–	100	–
$W(\ell\nu)h$	$0.69^{+0.91}_{-0.88}$	125	–	–	100	–	–
ttH tag	$-0.80^{+2.10}_{-1.84}$	125.8	–	–	–	–	100
$h \rightarrow \tau\tau$ (4.9 fb $^{-1}$ at 7 TeV + 19.4 fb $^{-1}$ at 8 TeV) [151]							
0/1 jet	$0.76^{+0.49}_{-0.52}$	125	76	16	4	3	1
VBF tag	$1.40^{+0.60}_{-0.57}$	125	19	81	–	–	–
VH tag	$0.77^{+1.48}_{-1.43}$	125	–	–	64	36	–
$h \rightarrow Z\gamma$ (5.0 fb $^{-1}$ at 7 TeV + 19.6 fb $^{-1}$ at 8 TeV) [206]							
Inclusive	< 9.3 at 95 CL	125.5	87	7	3	2	1

The global likelihood function is defined as the product of the likelihoods associated to the various observables,

$$L = L_{\text{Higgs}} \times L_{S,T} \times L_{\text{TGV}}, \quad (2.54)$$

where L_{Higgs} is the likelihood as given in Eq. (2.15). The likelihood associated to the measurement of an observable \hat{O} , given as a central value O and a symmetric uncertainty σ , is modeled by a normal law,

$$L_O \propto e^{-(O-\hat{O})^2/2\sigma^2}. \quad (2.55)$$

Table 2.12 Tevatron results for up to 10 fb^{-1} at $\sqrt{s} = 1.96 \text{ TeV}$, as employed in this analysis

Channel	Signal strength μ	m_h (GeV)	Reduced efficiencies				
		ggF (%)	VBF (%)	WH (%)	ZH (%)	ttH (%)	
$h \rightarrow \gamma\gamma$ [125]							
Combined	$6.14^{+3.25}_{-3.19}$	125	78	5	11	6	–
$h \rightarrow WW$ [125]							
Combined	$0.85^{+0.88}_{-0.81}$	125	78	5	11	6	–
$h \rightarrow b\bar{b}$ [126]							
VH tag	$1.56^{+0.72}_{-0.73}$	125	–	–	62	38	–

When uncertainties are asymmetric, we use the positive error bar if $(\hat{O} - O) > 0$, whereas we use the negative error bar if $(\hat{O} - O) < 0$. Finally, the CMS bound on the decay channel $h \rightarrow Z\gamma$ is implemented as a step function,

$$L_{\mu_{Z\gamma}} \propto \begin{cases} 1 & \text{if } \hat{\mu}_{Z\gamma} < 9.3, \\ 0 & \text{otherwise.} \end{cases} \quad (2.56)$$

We will now derive the deviations induced by the HDOs to the observables presented in Sect. 2.7.2. We first discuss the particular treatment of tensorial couplings. All formulas are given in the following section.

2.7.3 On Weak Bosons Tensorial Couplings

Because of electroweak symmetry breaking, the $W, Z \equiv V$ bosons generally couple to the Higgs through two different Lorentz structures. The coupling can be vectorial, $\propto g^{\mu\nu}$, or it can be tensorial with a vertex $\propto (g^{\mu\nu} - \frac{q_1^\mu q_2^\nu}{q_1 \cdot q_2})$, where q_1, q_2 are the momenta of the two gauge bosons. The leading SM couplings λ_W, λ_Z given in Eqs. (2.36) and (2.37) are vectorial. Tensorial couplings are generated only at one-loop and are $\mathcal{O}(\alpha) \sim 10^{-2}$.

Once HDOs are taken into account, the relative importance of the vectorial and tensorial terms is modified. On one hand vectorial couplings are rescaled by the coefficients $a_{W,Z}$. On the other hand new tensorial contributions ζ_W, ζ_Z are generated following Eq. (2.45). The amplitude associated to a hVV vertex (with the V 's possibly off-shell) is in general

$$\mathcal{M}(hVV)^{\lambda_1, \lambda_2} = e_{\lambda_1}^{\mu(*)} e_{\lambda_2}^{\nu(*)} \left(i a_V \lambda_V^{\text{SM}} g^{\mu\nu} - i 2 \zeta_V q_1 \cdot q_2 \left[g^{\mu\nu} - \frac{q_1^\mu q_2^\nu}{q_1 \cdot q_2} \right] \right), \quad (2.57)$$

where $\mathcal{M}^{0,0}$ and $\mathcal{M}^{\pm,\pm}$ are the longitudinal and transverse helicities amplitudes, respectively. Interferences among helicity amplitudes then determine angular distributions (see i.e. [209]). In this work, we consider that the SM contribution to the tensorial coupling is small with respect to the one induced by new physics. The relative magnitude of the longitudinal and transverse amplitudes in case of a vectorial coupling is given by

$$r_v = \left| \frac{\mathcal{M}_v^{0,0}}{\mathcal{M}_v^{\pm,\pm}} \right| = \frac{|m_h^2 - q_1^2 - q_2^2|}{2|q_1||q_2|}, \quad (2.58)$$

while it is the inverse in case of a tensorial coupling,

$$r_t = \left| \frac{\mathcal{M}_t^{0,0}}{\mathcal{M}_t^{\pm,\pm}} \right| = \frac{2|q_1||q_2|}{|m_h^2 - q_1^2 - q_2^2|}. \quad (2.59)$$

The two vector bosons can be off-shell in the above expression, while the Higgs is on-shell.

As $r_v \neq r_t$, the two Lorentz structures imply generally different angular distributions. Moreover, even for unpolarized processes, the energy dependence in Eq. (2.57) is different for both contributions, such that also energy distributions are modified. Because of this different energy dependence, kinematic cuts prepared for the SM are generally unadapted to such a non-trivial modification. That is, in Eq. (2.1), $A \times \varepsilon \neq [A \times \varepsilon]_{\text{SM}}$. The consequences may be an incorrect estimation of the signal strength and of the Higgs mass. To perform an exact analysis, one should redo the fits to LHC data taking into account the modified Lorentz structure in the expected signal. Such work is clearly beyond the scope of our present study. Instead we will show that under reasonable approximations we can use $A \times \varepsilon = [A \times \varepsilon]_{\text{SM}}$ in the present analysis.

There are three processes sensitive to the ζ_V tensorial couplings in the context of the searches for the Higgs boson at around 125 GeV: the leading decay to weak bosons $h \rightarrow VV^*$, and the VBF and VH production modes. We now discuss how we treat these three tensorial contributions.

Decay into Vector Bosons

In the case of a light Higgs boson, the leading decay occurs with one of the V off the mass shell. The weak bosons then decay into fermions. For massless fermions, the kinematic bounds on the on-shell boson energy E_V are $m_V < E_V < (m_h^2 + m_V^2)/2m_h$ in the rest frame of the Higgs. Because of the V^* propagator, the lower bound $E_V = m_V$ is favored, implying that both weak bosons are preferentially produced at rest. Longitudinal and transverse amplitudes are then equally populated, $r_v = 1$. Therefore, one has $r_t = 1$ as well, such that one can see qualitatively that a tensorial contribution cannot radically modify angular distributions. This is confirmed with the exact angular and invariant mass distributions among leptons induced by pure

vectorial and pure tensorial couplings [210, 211].¹⁹ In our study, the tensorial contributions are constrained to be subleading with respect to the vectorial contributions, such that the deviations induced on angular and invariant mass distributions can easily be smaller than the current statistical uncertainty. In addition, they could also be misidentified with the background. For example, in $h \rightarrow VV^*$, the distribution of the most discriminant observable, “lepton-opposite Z momentum angle”, is very similar to the distribution of the irreducible background $q\bar{q} \rightarrow ZZ^*$ (see Fig. 3 in [212]).

Following what discussed above, we can reasonably assume that angular and invariant mass distributions are not affected by the presence of tensorial couplings given the current level of precision. Polarization of the on-shell V can thus be averaged, and we are left with a matrix element scaling as

$$|\mathcal{M}|^2 = |\mathcal{M}_v + \mathcal{M}_t|^2 \propto |a_V \lambda_V^{\text{SM}} - 2\zeta_V q_1 \cdot q_2|^2, \quad (2.60)$$

where q_1, q_2 are the momenta of the two vector bosons. In the Higgs rest frame, one has $q_1 \cdot q_2 = m_h E_V - m_V^2$, which is bounded as

$$m_V(m_h - m_V) < q_1 \cdot q_2 < \frac{m_h^2 - m_V^2}{2}. \quad (2.61)$$

The exact tensorial contributions to the total decay widths are given in Appendix C of [194]. We introduce the dimensionless positive quantity

$$v_{VV} = q_1 \cdot q_2 / m_h^2, \quad (2.62)$$

with $V \equiv W, Z$. Defining

$$\langle v_{VV} \rangle = \frac{\int v_{VV} \mathcal{M}_v \mathcal{M}_t^* dPS}{\int \mathcal{M}_v \mathcal{M}_t^* dPS}, \quad \langle v_{VV}^2 \rangle = \frac{\int v_{VV}^2 |\mathcal{M}_t|^2 dPS}{\int |\mathcal{M}_t|^2 dPS}, \quad (2.63)$$

the vector-tensor interference term will be $\propto \zeta_V \langle v_{VV} \rangle$ and the pure tensor contribution will be $\propto |\zeta_V|^2 \langle v_{VV}^2 \rangle$. For $m_h = 125.5 \text{ GeV}$, $m_Z = 91 \text{ GeV}$, $m_W = 80 \text{ GeV}$, one gets $\langle v_{ZZ} \rangle = 0.2209$, $\langle v_{ZZ}^2 \rangle^{\frac{1}{2}} = 0.2211$, $\langle v_{WW} \rangle = 0.2653$, $\langle v_{WW}^2 \rangle^{\frac{1}{2}} = 0.2659$. In the following we will make the approximation $\langle v_{VV}^2 \rangle \approx \langle v_{VV} \rangle^2$.

VBF Production Mode

For the VBF process, both ATLAS and CMS apply hard cuts on the outgoing jets rapidities and their difference. The rapidity distributions of the two jets are similar in presence of a tensorial coupling, just like in the decay into two photons or in the production via gluon-gluon fusion, such that one can assume that cut efficiency is the same. The crucial change lies in the azimuthal angle ϕ_{jj} between the two tagging

¹⁹ Overall, the situation is much less striking than for a CP-violating contribution, which forbids the decay to the longitudinal polarization state.

jets (see i.e. [209] and references therein). Indeed, both weak bosons are space-like, with virtualities considerably smaller than m_h^2 . Such values are favored to balance the space-like V and the outgoing jets virtualities. As a result one has typically $r_v \gg 1$, $r_t \ll 1$ i.e. vectorial and tensorial amplitudes are mostly longitudinal and transverse, respectively. Consequently, the ϕ_{jj} distribution is almost flat for a pure vectorial coupling, and strongly peaked at $\pi/2$ for a pure tensorial coupling. For a large enough HDO contribution to the tensorial coupling, an anomalous ϕ_{jj} distribution could thus be observed. However, this variable is not used for the selection of the events in the experimental analyses we consider. Therefore, the selection efficiencies are also suitable in the case of large tensorial contributions, and one has $\varepsilon_{\text{SM}} = \varepsilon_{\text{SM}+\text{HDO}}$. One can average over the polarizations, and the squared amplitude is then simply rescaled by a factor $|a_V \lambda_{VBF}^{\text{SM}} - 2\zeta_V q_1 \cdot q_2|^2$.

We still have to determine the magnitude of the tensorial contribution. In this process, the scalar product of the weak boson momenta $q_1 \cdot q_2$ is related to the incoming and outgoing quarks as $q_1 \cdot q_2 = m_h^2/2 + p_1 \cdot p_3 + p_2 \cdot p_4$. The outgoing quarks are highly energetic with respect to the amount of p_T they receive from the V fusion, such that one has $|\mathbf{p}_1| \simeq |\mathbf{p}_3|$ and $|\mathbf{p}_2| \simeq |\mathbf{p}_4|$. In terms of the p_T and rapidities of the outgoing quarks we have then

$$q_1 \cdot q_2 = \frac{m_h^2}{2} + |p_{T,3}|^2 \frac{1 + e^{-\eta_3}}{2} + |p_{T,4}|^2 \frac{1 + e^{-\eta_4}}{2}. \quad (2.64)$$

Without the tensorial contribution, the p_T distribution peaks typically at values smaller than m_V . The tails of the p_T distributions drop quickly for higher energies [213], with typically one jet at a time getting a large p_T [21]. One can thus assume $q_1 \cdot q_2 \approx m_h^2/2$ to a good approximation. Once the tensorial coupling is taken into account, a deviation from the expected SM distributions might be present in the high- p_T tails, as $q_1 \cdot q_2$ is enhanced at large p_T . However, as long as one counts the total number of events, i.e. the integral of the distribution, this enhancement of $q_1 \cdot q_2$ has a small weight and can be safely neglected. Finally, defining the dimensionless positive quantity

$$\nu_{\text{VBF}} = q_1 \cdot q_2 / m_h^2, \quad (2.65)$$

with $V = W, Z$, we have thus $\nu_{\text{VBF}} \approx 1/2$ after phase space integration.

VH Production Mode

In the case of the associated production with an electroweak gauge boson, the scalar product of the momenta of the weak bosons is given by

$$q_1 \cdot q_2 = \frac{s + m_V^2 - m_h^2}{2}, \quad (2.66)$$

where \sqrt{s} is the partonic center-of-mass energy, which can much larger than $m_V + m_h$ at the LHC. Therefore, contrary to the two other processes, the product $q_1 \cdot q_2$ can be

large. The tensorial contribution can then be substantially enhanced in this process, and lead to modifications of the angular distributions.

However, it turns out that for both polar and angular distributions, the angular effects can be neglected. We refer to [214] and references therein for the expressions. Although results are given for e^+e^- collisions, they can be trivially generalized in the case of the LHC. For the distribution of the polar angle of the vector boson in the laboratory frame, it is the longitudinal component of V which enters mainly, such that the tensorial contribution to the distribution is suppressed by an additional factor $\mathcal{O}(m_V^2/s)$. For the azimuthal distributions, the tensorial contributions can be sizable, but the whole distribution tends to be flat for $s \gg m_V^2$, with non-flat terms suppressed by powers of m_V/\sqrt{s} . As a result, although various pieces of angular information are used in event selection for this mode of production, we can safely neglect the angular effects of the tensorial coupling.

Concerning the magnitude of the tensorial contribution, it appears that it reduces to a simple rescaling $\propto \lambda_V^{\text{SM}} + 12\zeta_V m_V^2$ in the limit $s \gg m_V^2$. The rescaling is exact up to a subleading term $\mathcal{O}(12m_V^2/s) \approx 0.1$. To include the subleading s -dependent terms, an integration over the partonic density functions would be necessary.

2.7.4 Deviations Caused by New Physics

Higgs Signal Strengths

In all generality, efficiencies in the SM with and without HDOs are not necessarily the same, i.e. $A \times \varepsilon \neq [A \times \varepsilon]_{\text{SM}}$, because kinematic distributions can be modified in a non-trivial way by HDOs. The selection criteria calibrated on the SM expectations are then unadapted in such situation, which complicates the interpretation of the signal strengths. However, we have seen in Sect. 2.7.3 that one can safely ignore these possibilities of HDOs affecting the kinematic distributions, given the current precision of the experimental searches. It is therefore a good approximation to set $\varepsilon_{\text{SM+HDO}} = \varepsilon_{\text{SM}}$. Thus, for each signal strength, one can simply incorporate the contributions coming from the tensorial couplings in the rescaling of the Standard Model signal strength.

The gluon-gluon fusion process is modified both by the tree-level HDO contribution ζ_g and the anomalous Higgs–fermion couplings c_f . Keeping only the third generation, we get

$$\sigma_{\text{ggF}} = \sigma_{\text{ggF}}^{\text{SM}} \left| \frac{c_t \lambda_g^{t,\text{SM}} + c_b \lambda_g^{b,\text{SM}} + \zeta_g}{\lambda_g^{t,\text{SM}} + \lambda_g^{b,\text{SM}}} \right|^2. \quad (2.67)$$

Vector boson fusion is modified by the anomalous vectorial couplings $a_{W,Z}$ and by $\zeta_{W,Z}$. Denoting by $\lambda_{\text{VBF}}^{\text{SM}}$ the effective SM couplings, one has

$$\sigma_{\text{VBF}} = \sigma_{\text{VBF}}^{\text{SM}} \left| \frac{a_W \lambda_W^{\text{SM}} + a_Z \lambda_Z^{\text{SM}} - 2 \nu_{\text{VBF}} m_h^2 (\zeta_W + \zeta_Z)}{\lambda_W^{\text{SM}} + \lambda_Z^{\text{SM}}} \right|^2. \quad (2.68)$$

The parameter ν_{VBF} is defined in Sect. 2.7.3. We take $\nu_{\text{VBF}} = 1/2$. The associated production with an electroweak gauge boson is modified as

$$\sigma_{\text{VH}} = \sigma_{\text{VH}}^{\text{SM}} \left| \frac{a_V \lambda_V^{\text{SM}} + 12 \zeta_V m_V^2}{\lambda_V^{\text{SM}}} \right|^2, \quad (2.69)$$

where $V = W, Z$. Finally, the associated production with a $t\bar{t}$ pair is rescaled as

$$\sigma_{t\text{H}} = |c_t|^2 \sigma_{t\text{H}}^{\text{SM}}. \quad (2.70)$$

The decays of the Higgs boson into fermions are modified as

$$\Gamma_{ff} = |c_f|^2 \Gamma_{ff}^{\text{SM}}. \quad (2.71)$$

The tree-level decays to vector bosons are modified as

$$\Gamma_{VV} = \left| \frac{a_V \lambda_V^{\text{SM}} - 2 \zeta_V m_h^2 \langle \nu_{VV} \rangle}{\lambda_V^{\text{SM}}} \right|^2 \Gamma_{VV}^{\text{SM}}, \quad (2.72)$$

where the parameter $\langle \nu_{VV} \rangle$, defined in Eq. (2.63), encodes the modification of phase space integrals. Loop-induced decays are sensitive to more deviations,

$$\Gamma_{\gamma\gamma} = \Gamma_{\gamma\gamma}^{\text{SM}} \left| \frac{a_W \lambda_\gamma^{W,\text{SM}} + c_t \lambda_\gamma^{t,\text{SM}} + c_b \lambda_\gamma^{b,\text{SM}} + c_\tau \lambda_\gamma^{\tau,\text{SM}} + \zeta_\gamma}{\lambda_\gamma^{W,\text{SM}} + \lambda_\gamma^{t,\text{SM}} + \lambda_\gamma^{b,\text{SM}} + \lambda_\gamma^{\tau,\text{SM}}} \right|^2, \quad (2.73)$$

$$\Gamma_{Z\gamma} = \Gamma_{Z\gamma}^{\text{SM}} \left| \frac{a_W \lambda_{Z\gamma}^{W,\text{SM}} + c_t \lambda_{Z\gamma}^{t,\text{SM}} + c_b \lambda_{Z\gamma}^{b,\text{SM}} + c_\tau \lambda_{Z\gamma}^{\tau,\text{SM}} + \zeta_{Z\gamma}}{\lambda_{Z\gamma}^{W,\text{SM}} + \lambda_{Z\gamma}^{t,\text{SM}} + \lambda_{Z\gamma}^{b,\text{SM}} + \lambda_{Z\gamma}^{\tau,\text{SM}}} \right|^2. \quad (2.74)$$

In such cases, the tensorial couplings can compete with the SM effective couplings.

QCD Radiative Corrections

Many of the above described processes receive leading radiative corrections from QCD loops. For all the tree-level processes, the structure of loop diagrams is not modified by the insertion of HDOs, including the tensorial couplings, such that radiative corrections factorize up to higher order corrections. It is thus straightforward to take them into account, simply using the NLO predictions of σ^{SM} and Γ^{SM} .

The situation is more involved in the case of the loop-induced processes ($h \rightarrow \gamma\gamma$, $h \rightarrow Z\gamma$, and $gg \rightarrow h$) because this time the tensorial coupling is competing with the SM loops. Hence the effects of the ζ 's may be very large in these processes, such that it is important to properly take into account the radiative corrections. As stated

in Sect. 2.7.1, the HDOs implicitly contain higher-order corrections from irreducible SM loops. These contributions therefore have to be taken into account for the SM effective couplings and not for the ζ couplings.²⁰

The processes $h \rightarrow \gamma\gamma$ and $h \rightarrow Z\gamma$ only receive virtual NLO QCD corrections. For $h \rightarrow \gamma\gamma$, we take into account the exact values of the correction factor to the quark effective couplings

$$\lambda_\gamma^{q,\text{SM}} = \lambda_\gamma^{q,\text{SM}}|_{\text{LO}} \left(1 + \frac{\alpha_s}{\pi} C_H(\tau_q) \right), \quad (2.75)$$

where the C_H function can be found in [21]. For $h \rightarrow Z\gamma$, one can take the correction in the heavy top limit as a good approximation [21],

$$\lambda_\gamma^{t,\text{SM}} = \lambda_\gamma^{t,\text{SM}}|_{\text{LO}} \left(1 - \frac{\alpha_s}{\pi} \right). \quad (2.76)$$

The situation is more subtle for the ggF process, because of the presence of important NLO real corrections. Introducing the tensorial coupling leads generally to non-trivial modifications of the integrals over parton densities for real emissions. However, in the heavy-top limit and neglecting the small bottom quark contribution, the QCD corrections to the SM loop and to the tensorial coupling ζ_g become similar and factorize. Adopting this fairly good approximation, the SM effective coupling are rescaled as

$$\lambda_g^{t,\text{SM}} = \lambda_g^{t,\text{SM}}|_{\text{LO}} \left(1 + \frac{11}{4} \frac{\alpha_s}{\pi} \right). \quad (2.77)$$

S and T Parameters

The electroweak precision observables are affected in the presence of the HDOs. At tree-level the S and T parameters are related to the HDO coefficients as follows:

$$\alpha S = \left(2 s_w c_w \alpha_{WB} + s_w^2 \alpha_D + c_w^2 \alpha'_D \right) \frac{v^2}{\Lambda^2}, \quad (2.78)$$

$$\alpha T = \left(-\frac{1}{2} \alpha'_{D^2} + \frac{1}{2} \alpha'_D \right) \frac{v^2}{\Lambda^2}. \quad (2.79)$$

Moreover, the SM loops are modified by the HDOs. The T parameter receives new divergent contributions from the modified SM couplings a_Z and a_W in Eq. (2.41). A quadratic divergence,

$$\alpha \Delta T = -\frac{\Lambda^2}{16 \pi^2 v^2} \frac{\alpha'_{D^2} v^2}{\Lambda^2}, \quad (2.80)$$

arises from custodial breaking [215]. Dropping other terms that are proportional to α'_D and α'_{D^2} (that already appear at tree-level) we can take the result from Ref. [79],

²⁰We are grateful to M. Spira for enlightening discussion on this subject.

$$\alpha \Delta T = -\frac{3e^2}{32\pi^2 c_w^2} \left(\alpha_{D^2} - \frac{1}{2} \alpha_D \right) \frac{v^2}{\Lambda^2} \log \left(\frac{m_h}{\Lambda} \right). \quad (2.81)$$

Similarly, the S parameter receives corrections due to the modified Higgs coupling α_Z [79], hence it is expected to get new contributions proportional to α_{D^2} and α'_{D^2} . Finally, the tensor couplings ζ_V can also generate new SM loop contributions which have been given in Ref. [216],

$$\alpha \Delta S = \frac{e^2}{24\pi^2} \left(\alpha_{D^2} + \frac{1}{2} \alpha'_{D^2} \right) \frac{v^2}{\Lambda^2} \log \left(\frac{m_h}{\Lambda} \right) + \frac{e^2}{2\pi^2} (\alpha_{BB} + \alpha_{WW}) \frac{v^2}{\Lambda^2} \log \left(\frac{m_h}{\Lambda} \right). \quad (2.82)$$

Finally we neglect the constraints coming from the W and Y parameters [207] as they are expected to have a small impact on our results.

2.7.5 Bayesian Setup and Low- Λ Scenario

Bayesian Inference

We are working in the framework of Bayesian statistics (see [217] for an introduction). In this approach, a probability is interpreted as a measure of the degree of belief about a proposition. Our study lies in the domain of Bayesian inference, which is based on the relation

$$p(\theta|d, \mathcal{M}) \propto p(d|\theta, \mathcal{M}) p(\theta|\mathcal{M}), \quad (2.83)$$

where $\theta \equiv \{\theta_{1\dots n}\}$ are the parameters of the model \mathcal{M} , and d denotes the experimental data. The distribution $p(\theta|d, \mathcal{M})$ is the so-called posterior probability density function (PDF), $p(d|\theta, \mathcal{M}) \equiv L(\theta)$ is the likelihood function enclosing experimental data, and $p(\theta|\mathcal{M})$ is the prior PDF, which represents our a priori degree of belief on the parameters. The model \mathcal{M} is in our case the Standard Model extended with higher dimensional operators. The likelihood is defined in Sect. 2.7.2 (see Eq. (2.54)) and the theoretical expressions for the HDO modified signal strengths are given in Sect. 2.7.4. The prior PDF is discussed in the next subsection.

The posterior PDF is the core of our results. Integrating the posterior over a subset λ of the parameter set $\theta \equiv \{\psi, \lambda\}$,

$$p(\psi|d, \mathcal{M}) \propto \int d\lambda p(\psi, \lambda|\mathcal{M}) L(\psi, \lambda), \quad (2.84)$$

leads to inference on the parameters ψ .

Also the notion of naturalness and fine-tuning are built-in [218] in the Bayesian approach. This is relevant for our study, in which precise (“fine-tuned”) cancellations between various HDO contributions can happen. Intrinsically, the regions of parameter space in which precise cancellations occur have a weak statistical weight,

such that they are flushed away after integration. The results we will present can thus be considered as generic, i.e. free of improbable cancellations.

We will consider uniform (flat) priors for the quantities

$$\beta_i \equiv \alpha_i \frac{v^2}{\Lambda^2} \quad (2.85)$$

and demand $|\beta_i| < 1$. Moreover, we will fix the cutoff scale to be $\Lambda = 4\pi v$. In the following we will justify these choices and argue that it ensures in particular convergence of the HDO expansion as well as perturbativity of the UV theory, and minimizes the dependence on the choice of the HDO basis.

Priors and Low- Λ Scenarios

The prior distributions associated to our parameters is a key feature of Bayesian inference. We follow the “principle of indifference” [219, 220] that maximizes the objectiveness of the priors. Once a transformation law $\gamma = f(\theta)$ irrelevant for a given problem is identified, this principle let us find the most objective prior by identifying $p_\Theta \equiv p_\Gamma$ in the relation $p_\Theta(\theta)d\theta = p_\Gamma(\gamma)d\gamma$.

The cutoff scale Λ is given a logarithmically uniform PDF,

$$p(\Lambda) \propto \frac{1}{\Lambda}. \quad (2.86)$$

By doing so, all order of magnitudes are given the same probability density. Regarding the dimensionless coefficients α , note that the choice of the HDO basis should be irrelevant for the conclusions of our study. Given that coefficients in different basis are related through linear transformations, the most objective prior to associate to each α_i is the uniform PDF,²¹

$$p(\alpha_i) \propto 1. \quad (2.87)$$

This choice of prior is well justified, however, one should keep in mind that other possibilities still exist.

Let us emphasize that in our general framework, the following hypotheses need to be scrutinized.

- Perturbativity of the HDO expansion, $|\alpha_i|/\Lambda^2 < \mathcal{O}(1/v^2)$,
- Perturbativity of the couplings expansions in the UV theory, $|\alpha_i| < \mathcal{O}(16\pi^2)$,
- HDO generation by loops,
- Custodial symmetry.

In the present work, we investigate scenarios of low-scale new physics, with values of Λ going up to $\mathcal{O}(4\pi v)$. We take custodial symmetry to be an exact symmetry of

²¹Here the principle of indifference sets the shape of the PDFs but does not set the bounds. One can see that ranges on α ’s are not conserved from one basis to another. In the scenario of democratic HDOs, this issue will be automatically solved, as one relies only on perturbativity of the HDO expansion to set the bounds on α ’s. In the scenario of loop suppressed \mathcal{O}_{FF} ’s, one takes advantage of a particular choice of basis, so the same argument does not apply in that case.

the theory. This forbids the presence of the operators \mathcal{O}'_{D^2} and \mathcal{O}'_D . As a consequence, one has $a_W = a_Z \equiv a_V$ and some contributions to the EW precision observables are suppressed including the potentially large quadratic divergence in T . Recall that \mathcal{O}_{WW} , \mathcal{O}_{WB} , and \mathcal{O}_{BB} are all independently custodially symmetric. This generally implies that processes involving the W and Z are not identically rescaled, for instance

$$\frac{\sigma_{\text{WH}}}{\sigma_{\text{WH}}^{\text{SM}}} \neq \frac{\sigma_{\text{ZH}}}{\sigma_{\text{ZH}}^{\text{SM}}}. \quad (2.88)$$

Our approach goes therefore beyond the fits involving pure rescalings induced by anomalous couplings.

Over this range of Λ , perturbativity of the HDO expansion is the dominant constraint as it requires $|\alpha_i| < \Lambda^2/v^2$ which automatically implies $|\alpha_i| < 16\pi^2$ and hence perturbativity of the couplings expansions in the UV theory.

When the HDOs are generated within a perturbative UV theory, none of the field strength–Higgs operators $\mathcal{O}_{FF} \equiv \mathcal{O}_{WW, WB, BB, GG}$ [see Eqs. (2.30), (2.31)] can be generated at tree-level. Because of our appropriate choice of basis, these loop-generated HDOs are exactly the ones associated with the tensorial couplings $\zeta_{g,\gamma,Z\gamma}$. We will therefore distinguish between two scenarios, depending on whether or not the \mathcal{O}_{FF} ’s are loop suppressed with respect to the other HDOs. Given that tensorial couplings can play an important role, this distinction is particularly crucial. The two scenarios, denoted by I and II, are respectively dubbed “democratic HDOs” and “loop-suppressed \mathcal{O}_{FF} ’s”. The main features are summarized in Table 2.13. These two scenarios are generic, in the sense that they encompass all known UV models in addition to the ones not yet thought of. This implies that features predicted only by specific UV models—e.g. suppression of HDOs or precise cancellations between HDOs—will get a small statistical weight, as we consider the whole set of UV realizations. Finally, we emphasize that the interpretation of Λ as a true new physics scale also depends at which order the whole set of HDOs is generated. For instance, in the R -parity conserving MSSM, the whole set of HDOs is generated only at one-loop order, such that the actual NP scale should be $\mathcal{O}(4\pi\Lambda)$.

A parameterization particularly adapted to low- Λ scenarios is as follows. Defining the parameters

$$\beta_i = \alpha_i \frac{v^2}{\Lambda^2}, \quad (2.89)$$

Table 2.13 Summary of the setup of the scan in the two scenarios we consider. The $\beta_{FF} \equiv \alpha_{FF} v^2/\Lambda^2$ coefficients (where $FF = WW, WB, BB, GG$) correspond to the field-strength–Higgs operators. In both cases we take custodial symmetry to be an unbroken symmetry

	(I) Democratic HDOs	(II) Loop-suppressed \mathcal{O}_{FF} ’s
Λ	$4\pi v$	$4\pi v$
β_{FF}	$[-1, 1]$	$[-1/16\pi^2, 1/16\pi^2]$
Other β	$[-1, 1]$	$[-1, 1]$

it follows that the β 's and Λ are independent, i.e. $p(\alpha_i, \Lambda) = p(\Lambda)p(\beta_i)$. The β 's prior is the uniform PDF over $[-1; 1]$, noted $U(\beta_i)$. The prior of Λ is $p(\Lambda) \propto \Lambda^{2n-1}$, where n is the number of β 's. In our case, $n = 9$ is large enough such that this prior is essentially peaked at Λ_{\max} , $p(\Lambda) \approx \delta(\Lambda - \Lambda_{\max})$. We have therefore

$$p(\alpha_i, \Lambda) = \delta(\Lambda - \Lambda_{\max})U(\beta_1) \dots U(\beta_n). \quad (2.90)$$

This factorization allows us to marginalize over Λ , and to present our results in terms of β 's, which contain all the relevant information. A mild dependence on Λ will remain through loop-level $\mathcal{O}(\log \Lambda)$ terms in the S and T parameters, that will be discussed below. The fact that β 's prior is uniform and spans a constant range is essential to facilitate interpretation of the posterior PDFs. The fact that $\Lambda \approx \Lambda_{\max}$ is also useful, as it renders straightforward the evaluation of the few Λ -dependent terms.

This parameterization turns out to be convenient in order to extract information about HDOs in a scale independent way, up to a mild $\mathcal{O}(\log \Lambda_{\max})$ dependence. For example, for a given Λ , one can directly read the values of α 's on the β 's plot. Similarly, for given α 's, one can deduce the allowed Λ values from the plots. This parameterization is appropriate at low Λ , up to $\Lambda = \mathcal{O}(4\pi v)$. Beyond this scale, the bound from HDO perturbative expansion competes with the bound from the perturbative expansion of the couplings. Once the latter dominates, the features of factorization no longer hold.

The MCMC Setup

We evaluate posterior PDFs by means of a Markov Chain Monte Carlo (MCMC) method. The basic idea of a MCMC is setting a random walk in the parameter space such that the density of points asymptotically reproduces the posterior PDF. Any marginalisation is then reduced to a summation over the points of the Markov chain. We refer to [217, 221] for details on MCMCs and Bayesian inference. Our MCMC method uses the Metropolis-Hastings algorithm with a symmetric, Gaussian proposal function. We run respectively 50 and 15 chains with $\mathcal{O}(10^8)$ iterations each for the democratic HDOs case and the loop-suppressed \mathcal{O}_{FF} 's case. Finally, we check the convergence of our chains using an improved Gelman and Rubin test with multiple chains [222]. The first 10^4 iterations are discarded (burn-in).

2.7.6 Inference on HDOs

In this section we present and analyze the posterior PDFs arising in our scenarios of democratic HDOs and loop-suppressed \mathcal{O}_{FF} 's, denoted by I and II, respectively. Our results will be shown in terms of the $\beta_i \equiv \alpha_i v^2 / \Lambda^2$ parameters, which encode information about the fundamental parameters. Recall that the β 's prior PDF is uniform, and that the β PDFs we show are valid for any value of the cutoff scale $\Lambda < \mathcal{O}(4\pi v)$, up to a mild $\log \Lambda$ dependence. Moreover, this parameterization sets

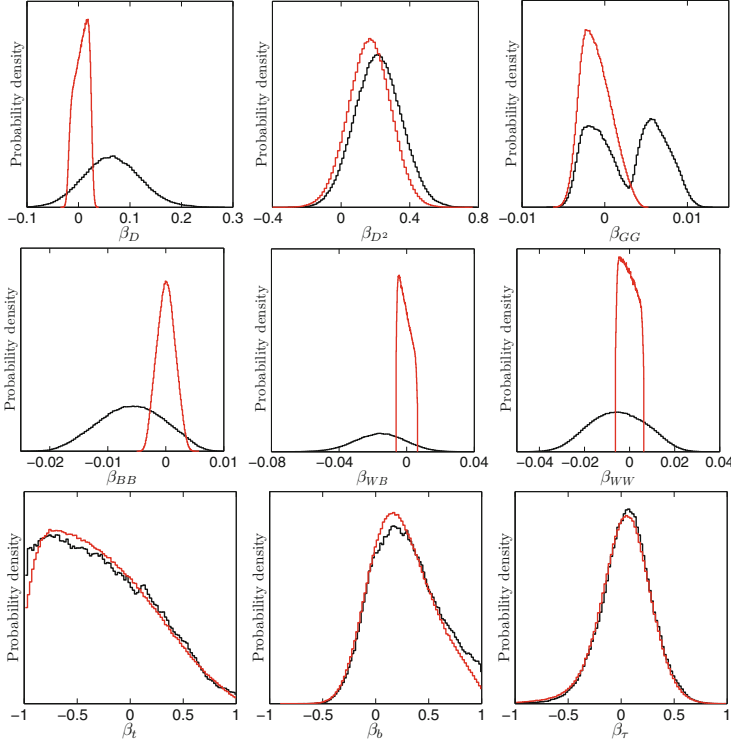


Fig. 2.38 Posterior PDFs of the 9 fundamental parameters, $\beta_i \equiv \alpha_i v^2 / \Lambda^2$, in scenario I (*black*) and scenario II (*red*)

$\Lambda \approx \Lambda_{\max}$. The posterior PDF we present is computed for $\Lambda = 4\pi v \approx 3$ TeV. For smaller Λ , we expect the $\propto \log \Lambda$ constraints from ΔS and ΔT to mildly relax. We will comment below on this effect.

We will also discuss deviations from the SM cross sections and decay widths, defining

$$R_X = \frac{\sigma_X}{\sigma_X^{\text{SM}}}, \quad R_Y = \frac{\Gamma_Y}{\Gamma_Y^{\text{SM}}}, \quad R_{\text{width}} = \frac{\Gamma_h}{\Gamma_h^{\text{SM}}}, \quad (2.91)$$

where $X = \text{ggF, VBF, WH, ZH, ttH}$, and $Y = \gamma\gamma, ZZ, Z\gamma, WW, b\bar{b}, \tau\tau$. Note that the observables are the signal strengths $\mu(X, Y)$ rather than the individual R_X and R_Y .

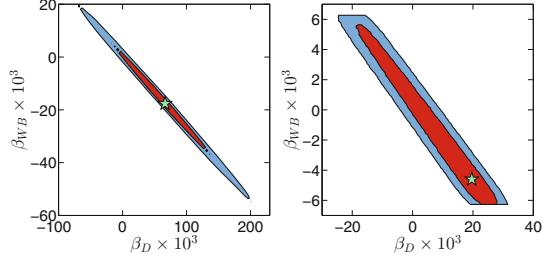
We present one-dimensional PDFs of the fundamental parameters β_i for both scenarios in Fig. 2.38. Moreover, in Table 2.14 we report the 68 and 95 % Bayesian credible intervals (BCIs) for these quantities. We also present the BCIs for the other, dependent quantities, i.e. the anomalous couplings a_V and c_f , the tensorial couplings ζ_i , and the various R 's.

Table 2.14 68 and 95 % Bayesian credible intervals (BCIs) for the democratic HDOs case (scenario I) and for the loop-suppressed \mathcal{O}_{FF} 's case (scenario II)

	Scenario I		Scenario II	
	68 % BCI	95 % BCI	68 % BCI	95 % BCI
$\beta_D \times 10^3$	[10, 120]	[−50, 180]	[−6, 23]	[−19, 26]
$\beta_{D^2} \times 10^3$	[70, 350]	[−50, 480]	[40, 290]	[−90, 400]
$\beta_t \times 10^3$	[−1000, 110]	[−1000, 610]	[−930, 10]	[−1000, 590]
$\beta_b \times 10^3$	[−10, 530]	[−220, 930]	[−110, 500]	[−280, 860]
$\beta_\tau \times 10^3$	[−170, 300]	[−420, 510]	[−190, 270]	[−450, 510]
$\beta_{GG} \times 10^3$	[−3.2, 8.0]	[−4.0, 9.6]	[−3.3, 0.6]	[−4.2, 2.7]
$\beta_{WW} \times 10^3$	[−19, 7]	[−30, 18]	[−5.6, 2.3]	[−6.0, 5.6]
$\beta_{WB} \times 10^3$	[−32, 1]	[−49, 13]	[−6.0, 1.6]	[−6.3, 5.3]
$\beta_{BB} \times 10^3$	[−12, 0]	[−17, 4]	[−1.7, 1.6]	[−2.9, 3.0]
a_V	[1.02, 1.15]	[0.96, 1.21]	[1.02, 1.14]	[0.96, 1.20]
c_t	[0.05, 1.14]	[0.03, 1.63]	[0.06, 1.01]	[0.04, 1.60]
c_b	[0.90, 1.54]	[0.79, 1.96]	[0.89, 1.50]	[0.72, 1.86]
c_τ	[0.84, 1.31]	[0.58, 1.53]	[0.81, 1.27]	[0.55, 1.51]
$\zeta_g v \times 10^3$	[−3.2, 8.0]	[−4.0, 9.6]	[−3.3, 0.6]	[−4.2, 2.7]
$\zeta_\gamma v \times 10^3$	[−5.5, 0.5]	[−6.1, 0.9]	[−0.33, 0.46]	[−0.69, 0.86]
$\zeta_{Z\gamma} v \times 10^3$	[−13, 18]	[−18, 30]	[−4.9, 4.4]	[−7.6, 7.9]
$\zeta_Z v \times 10^3$	[−20, 2]	[−31, 11]	[−3.4, 2.3]	[−5.1, 4.4]
$\zeta_W v \times 10^3$	[−39, 15]	[−59, 37]	[−11, 5]	[−12, 11]
R_{ggF}	[0.6, 1.3]	[0.5, 2.0]	[0.6, 1.3]	[0.4, 2.0]
R_{VBF}	[1.0, 1.4]	[0.9, 1.6]	[1.0, 1.3]	[0.9, 1.4]
R_{WH}	[0.7, 1.3]	[0.5, 1.7]	[1.0, 1.3]	[0.9, 1.4]
R_{ZH}	[0.7, 1.2]	[0.5, 1.5]	[1.0, 1.3]	[0.9, 1.4]
R_{tH}	[0.02, 1.0]	[0.02, 2.6]	[0, 0.9]	[0, 2.5]
$R_{\gamma\gamma}$	[1.1, 1.9]	[0.8, 2.5]	[1.1, 1.8]	[0.8, 2.3]
$R_{Z\gamma}$	[0, 5.2]	[0, 12.0]	[0, 2.2]	[0, 4.3]
R_{ZZ}	[1.0, 1.3]	[0.9, 1.5]	[1.0, 1.3]	[0.9, 1.4]
R_{WW}	[1.0, 1.3]	[0.9, 1.5]	[1.0, 1.3]	[0.9, 1.4]
$R_{b\bar{b}}$	[0.7, 2.2]	[0.5, 3.6]	[0.7, 2.1]	[0.4, 3.3]
$R_{\tau\tau}$	[0.6, 1.6]	[0.3, 2.2]	[0.6, 1.5]	[0.2, 2.1]
R_{width}	[0.8, 1.9]	[0.7, 2.7]	[0.8, 1.8]	[0.6, 2.5]

One can first remark that all of our HDO coefficients except β_t and β_b are constrained enough to stay within the bound $|\beta_i| < 1$, as required for the convergence of the HDO expansion. Furthermore, the $\beta_{FF} \equiv \beta_{WW, WB, BB, GG}$ coefficients are $\mathcal{O}(0.01)$ in both scenarios. β_D and β_{WB} are strongly correlated in both scenarios as they appear in the S parameter at tree-level, see Eq. (2.78) (we recall that

Fig. 2.39 Posterior PDFs of β_{WB} versus β_D in scenario I (left) and scenario II (right). The red and blue regions correspond to the 68 and 95 % Bayesian credible regions (BCRs). The green star indicates the maximum of our posterior PDF



we fix $\alpha'_D = \alpha'_{D^2} = 0$ in order to preserve custodial symmetry). We thus have $2c_w\beta_{WB} \approx -s_w\beta_D$ as can be seen in Fig. 2.39. The TGV observables also involve β_D and β_{WB} (see Eq. (2.52)), and thus provide an independent constraint on β_D (or equivalently β_{WB}). The slight deficit in κ_γ and g_1^Z as measured by LEP, see Eq. (2.53), tend to favor positive (negative) β_{WB} (β_D). Finally, note that in scenario II the PDF of β_{WB} is limited to the $[-1/16\pi^2, 1/16\pi^2]$ range since we consider that the operator \mathcal{O}_{WB} is loop-suppressed. This in turn fixes the allowed range for β_D .

The β_{D^2} coefficient is allowed to deviate significantly from 0 as it only appears in loop contributions to S and T and in a_V . The probability of having $\beta_{D^2} > 0$ is 94 % (90 %) in scenario I (II) and comes from T , as well as VBF and VH production modes and $h \rightarrow VV$ decays. A value for $a_V > 1$ leads to a positive contribution to T , as well as an enhancement of the VBF and VH production processes, the $h \rightarrow VV^*$ decays, and also to the loop-induced decay rates, $h \rightarrow \gamma\gamma$ and $h \rightarrow Z\gamma$.

β_{WW} and β_{BB} are mainly constrained by the searches for $h \rightarrow \gamma\gamma$ and $h \rightarrow Z\gamma$ as they contribute to the tensorial couplings ζ_γ and $\zeta_{Z\gamma}$, see Eqs. (2.43) and (2.44). Given the large allowed range for β_{WB} , a cancellation has to occur with β_{WW} and β_{BB} in order to achieve a $h \rightarrow \gamma\gamma$ rate compatible with experiment. As a result, negative values of β_{WW} and β_{BB} are favored. Moreover, β_{WW} is also constrained from VH production processes via the quantities ζ_V . In contrast β_{BB} and β_{WB} play no role for these measurements, as they are more strongly constrained by the other effects mentioned above. The contributions of β_{WW} and β_{BB} to S are up to $\mathcal{O}(0.03)$ and do not impact the PDFs. This effect is even smaller in scenario II, and is also smaller if we take $\Lambda < 4\pi v$ due to the $\log(m_h/\Lambda)$ factor in Eq. (2.82). We note that in scenario II the PDFs for β_{WW} and β_{WB} can easily reach the bounds set by the priors, while β_{BB} is more strongly constrained by the data. This is due to the fact that β_{BB} enters in ζ_γ with a coefficient roughly four times larger than the other two.

Finally, the Yukawa corrections parametrized by β_f ($f = t, b, \tau$) are much less constrained as they only contribute to the rescaling factors c_f , but account for most of the deviations of c_f from 1, such that we often have $|\beta_f| \gg |\beta_D/4|$ and thus $c_f \approx 1 + \beta_f$. It is worth noting that β_t has a fairly large probability of being close to -1 , which leads to small or vanishing c_t . The posterior PDF of c_t is shown in the left panel of Fig. 2.40.

In such case, one may wonder whether or not the preference for small c_t is due to a volume effect caused by the process of marginalization. To this end, we display

Fig. 2.40 In the *left panel*, posterior PDF of c_t in scenario I (black) and scenario II (red). In the *right panel*, profile likelihood along the c_t axis in scenario I and scenario II (same color code)

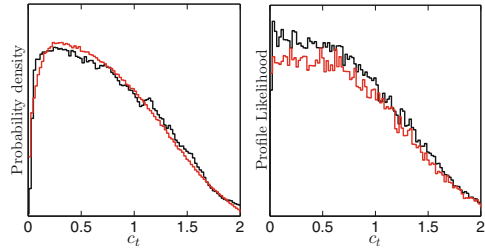
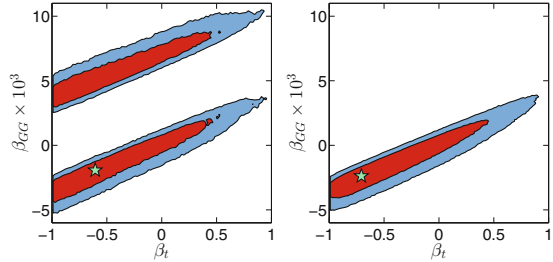


Fig. 2.41 Posterior PDF of β_{GG} versus β_t in scenario I (left) and scenario II (right). Color code as in Fig. 2.39



in the right panel of Fig. 2.40 the profile likelihood for the parameter c_t , i.e. the likelihood for given c_t , maximized over all the other parameters. We conclude that in both scenarios, the preference for small c_t originates from the likelihood and not from a volume effect.²²

The shapes of the PDF and profile likelihood for c_t in Fig. 2.40 are in fact a direct consequence of the signal strength measurement $\mu(\text{ttH}, b\bar{b})$ by CMS [122], see Table 2.11. Notice that the latter is so far the only analysis sensitive to the ttH production mode. In spite of its large error, the low central value drives c_t efficiently to small values because of the relation $R_{\text{ttH}} = c_t^2$. Although small c_t decreases (increases) the value of R_{ggF} ($R_{\gamma\gamma}$), these changes can be compensated for without decreasing the likelihood. In the case $c_t \approx 0$, the gluon-gluon fusion (ggF) process is mainly driven by the tensorial coupling $\zeta_g \equiv \beta_{GG}/v$. We show in Fig. 2.41 the correlation between β_{GG} and β_t , which is needed to reproduce the observed ggF rate. For the decay $h \rightarrow \gamma\gamma$, we observe an increased rate $R_{\gamma\gamma} > 1$, which can be seen in Fig. 2.42. Indeed, in the SM the $h \rightarrow \gamma\gamma$ process is dominated by the W loops, and there is a destructive interference between the t and W contributions. Therefore, the suppression of c_t helps increasing $R_{\gamma\gamma}$. To better understand this enhanced rate, notice that naively combining the data in Tables 2.10, 2.11 and 2.12 one obtains $\mu(\text{ggF} + \text{ttH}, \gamma\gamma) = 1.05 \pm 0.28$ and $\mu(\text{VBF} + \text{VH}, \gamma\gamma) = 1.8 \pm 0.6$. It turns out that these different values are then realized with a slightly reduced R_{ggF} and an increased $R_{\gamma\gamma}$.

²²We have also checked that no volume effects appear for any of the other posterior PDFs either.

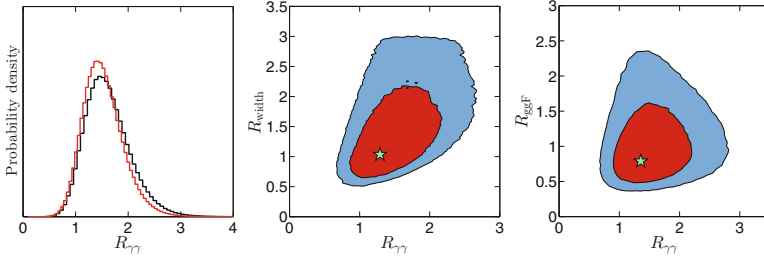


Fig. 2.42 On the *left*, posterior PDF of $R_{\gamma\gamma}$ in scenario I (*black*) and scenario II (*red*). Also shown are the 2D posterior PDFs of R_{width} versus $R_{\gamma\gamma}$ (*middle*) and R_{ggF} versus $R_{\gamma\gamma}$ (*right*) in scenario I. *Color code* as in the previous figure

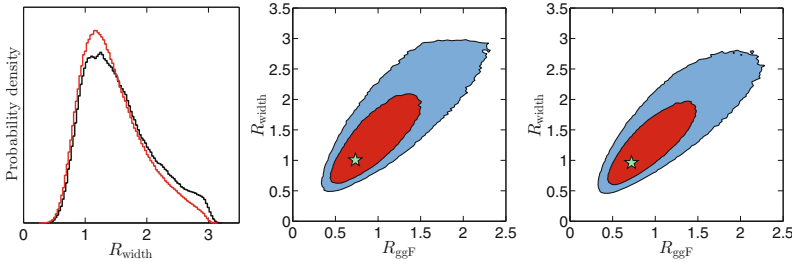


Fig. 2.43 In the *left panel*, posterior PDF of $R_{\text{width}} = \Gamma_h / \Gamma_h^{\text{SM}}$ in scenario I (*black*) and scenario II (*red*). Also shown is the 2D posterior PDF of R_{width} versus R_{ggF} in scenario I (*middle*) and scenario II (*right*). *Color code* as in the previous figures

The PDF of β_b is asymmetric with a longer right tail. β_b appears mainly in the $h \rightarrow b\bar{b}$ decay rate, i.e. in $R_{b\bar{b}}$.²³ The reason of the asymmetry is the following: as the branching fraction $\mathcal{B}(h \rightarrow b\bar{b}) = 57\%$ in the SM, a deviation of β_b from 0 (hence c_b from 1) results in a sizable modification of the total width of the Higgs. Our signal strengths are expressed as $\hat{\mu}(X, b\bar{b}) = R_X R_{b\bar{b}} / R_{\text{width}}$ and contain a strong correlation between $R_{b\bar{b}}$ and R_{width} . As R_{width} significantly increases with $R_{b\bar{b}}$, the deviations from $\mu_{b\bar{b}} = 1$ are smaller than what we could naively expect, allowing large values of $R_{b\bar{b}}$, hence β_b . This explains the tails of the PDF of β_b .

The 1D and 2D PDFs of R_{width} are shown in the left panel of Fig. 2.43. It turns out that a large increase of R_{width} is not forbidden by the measurements of other channels, in which this effect is compensated by an increase of the decay or production rates, in particular ggF. The upper bound on R_{width} , $R_{\text{width}} \lesssim 3$, comes from the requirement $\beta_b < 1$.

In Fig. 2.44, we show the PDFs of the tensorial couplings $\zeta_\gamma, \zeta_{Z\gamma}, \zeta_Z$ for scenario I. The PDF of ζ_γ is constrained to small values in order to have the correct $H \rightarrow \gamma\gamma$ rate. The PDF of $Z\gamma$ is much broader because of the weak experimental sensitivity

²³ b quark contributions in the loop-induced processes (ggF, $\gamma\gamma$, $Z\gamma$) are small and can be disregarded.

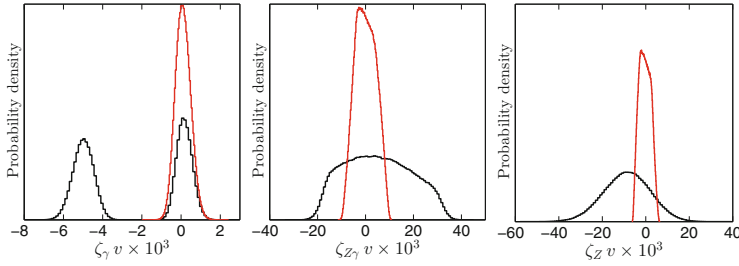
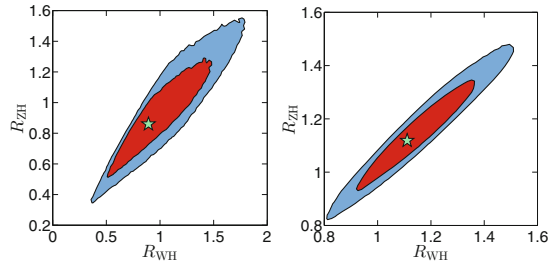


Fig. 2.44 Posterior PDFs of ζ_γ , $\zeta_{Z\gamma}$, and ζ_Z in scenario I (black) and scenario II (red)

Fig. 2.45 Posterior PDF of R_{ZH} versus R_{WH} in scenario I (left) and scenario II (right). Color code as in the previous figures



to the $Z\gamma$ rate. The distribution for ζ_Z (and similarly ζ_W) is mainly due to indirect effects on the fundamental parameters β_{VV} ($\gamma\gamma$ and $Z\gamma$ rates, as well as TGVs) rather than because of direct experimental constraints. Notice that even with the assumption of custodial symmetry (which enforces $a_W = a_Z$), Eq. (2.69) allows the rates for associated production to be different for Z and W because of the contribution of the tensorial couplings. It turns out that ζ_W and ζ_Z can be large enough in scenario I to induce a substantial deviation from $R_{WH} = R_{ZH}$. This is shown in Fig. 2.45. This effect is also present in scenario II to a lesser extent.

In scenario I, we observe two peaks of opposite signs for the tensorial couplings ζ_g and ζ_γ . These features appear because of the competition between the tree-level $\zeta_{g,\gamma}$ and the loop-level SM couplings in the ggF and diphoton amplitudes. In addition to the classical region where ζ adds up to the SM coupling and cannot be very large, regions with $\zeta = \mathcal{O}(-2\lambda^{\text{SM}})$ are also allowed. Note that ζ_γ is a linear combination of β_{WW} , β_{WB} , β_{BB} , but that the two ζ_γ peaks cannot be seen in the PDFs of these parameters. These four regions do not show up in scenario II, because the ζ_i are loop-suppressed and thus cannot be large enough to cancel the SM couplings.

A feature of the PDF of $\zeta_{Z\gamma}$ is that, in spite of the various constraints on β_{WW} , β_{WB} , and β_{BB} , the $Z\gamma$ rate can still be considerably enhanced. The shape of the $\zeta_{Z\gamma}$ PDF is mainly constrained by the CMS bound $\hat{\mu}_{Z\gamma} < 9.3$ in scenario I, while indirect constraints from the S parameter and trilinear gauge vertices dominate in scenario II. In the enhanced rate, the HDO contribution dominates, such that $R_{Z\gamma}$ is mostly proportional to $(\zeta_{Z\gamma})^2$. This happens in scenario I, but also in scenario II although the ζ_i are smaller. The PDF of the ratio $R_{Z\gamma}$ can be seen in Fig. 2.46. The 95 %

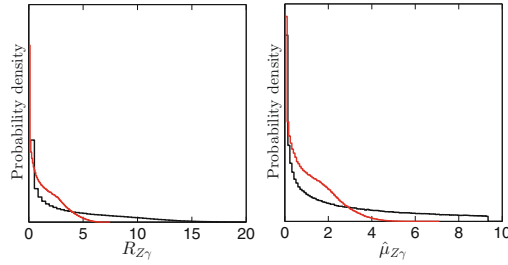


Fig. 2.46 Posterior PDFs of $R_{Z\gamma} \equiv \Gamma(h \rightarrow Z\gamma)/\Gamma^{\text{SM}}(h \rightarrow Z\gamma)$ (left) and $\hat{\mu}_{Z\gamma}$ (right) in scenario I (black) and scenario II (red)

Bayesian credible intervals are $[0, 12.0]$ for scenario I and $[0, 4.3]$ for scenario II. As large deviations are allowed in this channel within this framework, it is therefore particularly promising for the discovery of a NP signal.

In scenario I, $\zeta_{Z\gamma}$ is sufficiently large to cancel the SM coupling, such that enhancement with both signs of $\zeta_{Z\gamma}$ is realized. In contrast, for scenario II, only the branch with constructive interference $\zeta_{Z\gamma} < 0$ can enhance $R_{Z\gamma}$. In both scenarios, $\zeta_{Z\gamma}$ can cancel the SM coupling, such that having a small or vanishing $R_{Z\gamma}$ is also possible.²⁴

Finally, we compute the signal strength of $h \rightarrow Z\gamma$ in case of a fully inclusive analysis at the LHC. The PDFs are shown in the right panel of Fig. 2.46 for both scenarios. In scenario I, the distribution reaches the CMS 95 % C.L. bound $\hat{\mu}_{Z\gamma} < 9.3$, while it vanishes before in scenario II. The 68 and 95 % BCIs are $[0, 3.6]$, $[0, 8.1]$ in scenario I and $[0, 1.6]$, $[0, 3.2]$ in scenario II.

Given that the 13/14 TeV LHC has a good potential to constrain the $h \rightarrow Z\gamma$ rate, one may wonder about the impact of a more precise measurement on our results. Therefore, we investigate the possibility of having $\hat{\mu}_{Z\gamma} < 2$ at 95 % CL, and we implement this bound as a step function.²⁵ It mainly results in a better determination of β_{BB} and β_{WW} in both scenarios, as can be seen in Fig. 2.47. This new limit has an effect on the Higgs phenomenology in scenario I only. It leads to a slightly better prediction of R_{WH} : the 95 % BCI is $[0.7, 1.5]$, instead of $[0.5, 1.7]$ when we take into account the current limit on $h \rightarrow Z\gamma$.

²⁴We do not focus on this aspect as the direct searches at the LHC are still far from this level of precision. The shape of the $R_{Z\gamma}$ PDF follows the distribution of $|\zeta_{Z\gamma} + \lambda_{Z\gamma}|^2$, which presents a peak in 0. Schematically, for a uniform distribution of $\zeta_{Z\gamma}$, the peak behaves as $\zeta_{Z\gamma}^{-1/2}$. One can observe a similar behaviour for R_{tH} .

²⁵Note that the relative SM production rates $\sigma_X^{\text{SM}}/\sum_X \sigma_X^{\text{SM}}$ do not change significantly between 8 TeV and 14 TeV. Thus, assuming a fully inclusive analysis, we can take the decomposition into production channels as given in Sect. 2.7.2, Table 2.11.

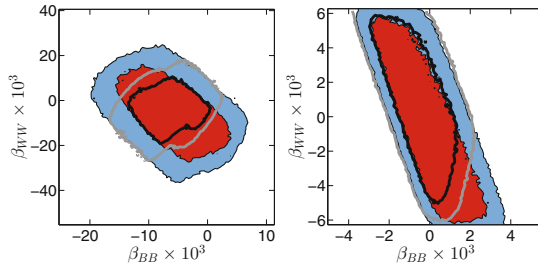


Fig. 2.47 Posterior PDF of β_{WW} versus β_{BB} in scenario I (left) and scenario II (right). The red and blue regions correspond to the 68 and 95 % BCRs from the current measurements, while the black and gray contours correspond to the 68 and 95 % BCRs assuming in addition that $\hat{\mu}_{Z\gamma} < 2$

2.7.7 Conclusions

In this section, we used a complete basis of dimension-six operators encoding NP effects in an effective Lagrangian in which all tensorial couplings are taken into account. The basis was chosen such that field-strength-Higgs operators (\mathcal{O}_{FF}) are exactly mapped into tensorial couplings. In this basis it is straightforward to study the well-motivated hypothesis of loop-suppression of these operators.

The data taken into account in our analysis are the whole set of results from ATLAS and CMS, including all available correlations, as well as Tevatron data. Trilinear gauge vertices measurements and constraints on electroweak precision observables are also included in our study.

It turns out that weak bosons tensorial couplings can in principle modify non-trivially the kinematic structure of the VBF, VH and $h \rightarrow VV$ processes, and thus the efficiency of the kinematic selections. Scrutinizing the experimental analyses, we find that one can consider unchanged kinematic cuts efficiencies for the rates of these processes to a good approximation. The effect of tensorial couplings is crucial in the ggF, $h \rightarrow \gamma\gamma$, $h \rightarrow Z\gamma$ processes, where they compete with the one-loop SM couplings. In our predicted rates, leading loop corrections are taken into account, consistently with respect to the loop-level HDO framework.

In order to put constraints on the higher dimensional operators we consider, we carry out a global analysis in the framework of Bayesian inference. We find this approach particularly appropriate as it deals with weakly constrained problems and naturally takes into account fine-tuning, such that the results we present are free of improbable, i.e. fine-tuned, cancellations. Markov Chain Monte Carlo techniques are used to perform the numerical integrations.

Our analysis is centered on new physics arising at $\lesssim 3$ TeV. It allows us to express our results in terms of $\beta_i \equiv \alpha_i v^2/\Lambda^2$, i.e. to factorize the effect of the coefficients α_i and of the scale of new physics Λ . Among other things, this parameterization is Λ -independent up to a small $\log \Lambda$ dependence. Distributions of HDO coefficients at any low Λ can be easily mapped from our results. Two general scenarios are

considered: (I) democratic HDOs, where the coefficients of all the dimension-six operators are essentially unconstrained, and (II) loop-suppressed \mathcal{O}_{FF} 's, where the field-strength-Higgs operators are loop suppressed with respect to the other HDOs.

We find overall a substantial amount of freedom in both of these scenarios. For instance, the coupling to the top quark still allows for $\mathcal{O}(1)$ deviations, while the couplings to bottom and tau are slightly more constrained. We report in both scenarios a large and natural region at small or vanishing c_t , favored by goodness of fit, which we trace back to the slight deficit observed in the $b\bar{b}$ channel with the ttH production mode, as reported by CMS. Regarding the couplings of the vector bosons, we find that only small deviations are allowed, of the order of 10–20%. Despite the fact that the inclusive rate of the $h \rightarrow \gamma\gamma$ channel is close to one, we observe a slightly enhanced $R_{\gamma\gamma} = \Gamma_{\gamma\gamma} / \Gamma_{\gamma\gamma}^{\text{SM}}$, with the 95 % Bayesian credible interval (BCI) for $R_{\gamma\gamma}$ given by [0.8, 2.5] ([0.8, 2.3]) in scenario I (II). Correlations with $R_{\text{width}} = \Gamma_h / \Gamma_h^{\text{SM}}$ as well as the deviations of the various production modes from the SM are then identified to be responsible for fitting the experimental signal strengths. We also find that an enhanced coupling to the b quark is likely, leading to a larger total width, with the 95 % BCI for R_{width} given by [0.7, 2.7] ([0.6, 2.5]) in scenario I (II). A strong correlation with R_{ggF} exists and makes the predicted signal strengths compatible with the data.

Overall, it appears that the tensorial couplings play a crucial role in the SM loop-induced processes. In particular, after taking into account all the constraints we find that the Higgs boson decay width into $Z\gamma$ can be enhanced by up to a factor 12 (4) in scenario I (II), within 95 % BCI. Conversely, future measurements in the $Z\gamma$ channel will provide important bounds on the coefficients of the higher dimensional operators we consider.

2.8 The Phenomenological MSSM in View of the 125 GeV Higgs Data

So far, in this chapter we have seen the impact of the LHC Higgs measurements on effective parameterizations of new physics. While the impact on models with extended Higgs sectors was examined in Sects. 2.5.4 and 2.6.4 for the 2HDM, and in Sect. 2.6.5 for the IDM, it remained largely restricted to the properties of the Higgs boson with mass around 125 GeV. In particular, the other physical Higgs states were ignored and other phenomenological aspects, such as the viability of possible dark matter candidates, were not explored. In this section, a complete study of the phenomenological MSSM (pMSSM), a 19-dimensional parametrization of the weak-scale Lagrangian of the MSSM (see Sect. 1.3.2), will be presented.

In the MSSM, a light Higgs mass of the order of 125 GeV requires that stops be either very heavy or near-maximally mixed (see, i.e., Refs. [223, 224]). In addition to a modification of the electroweak symmetry breaking sector by the presence of a second Higgs doublet, the MSSM predicts a wealth of new particles that couple to

the light Higgs boson. These can, depending on their masses and mixings, modify the Higgs couplings and consequently the production and decay rates of the Higgs boson in various channels. It is thus interesting to ask whether, besides the measured Higgs mass, the Higgs signal strengths provide constraints on the MSSM and may thus be used as a guide for where to look for SUSY.

Indeed, the apparent excess in the diphoton channel reported by both ATLAS and CMS in 2012 [1, 2] motivated scenarios with light status in the MSSM [225] or small $\tan\beta$ /large λ in the next-to-MSSM [226, 227] (see also [228, 229]). As we saw in Sect. 2.6, this drastically changed with the updated results presented at the Moriond 2013 conference and thereafter, which point towards a very SM-like Higgs boson, without the need of any modifications of the couplings due to new, beyond-the-SM particles.

The implications of the latest Higgs data for the MSSM were discussed recently in [230, 231]. Ref. [230] concentrated on describing (the consequences for) the heavy Higgs states in the limit of heavy SUSY particles; the best coupling fit was found at low $\tan\beta$, $\tan\beta \approx 1$, with a not too high CP-odd Higgs mass of $m_A \approx 560$ GeV. Ref. [231] analyzed the consequences of the SUSY null-searches on the one hand and of the measurements of the Higgs properties on the other hand based on flat random scans of the so-called phenomenological MSSM (pMSSM) with the conclusion that SUSY searches and Higgs boson properties are to a very good approximation orthogonal. More concretely, Ref. [231] concluded that Higgs coupling measurements at the 14 TeV LHC, and particularly at a 500 GeV International Linear Collider (ILC), will be sensitive to regions of the pMSSM space that are not accessible to direct SUSY searches.

In this section, we follow a different approach. Performing a Bayesian analysis of the pMSSM parameter space by means of a Markov Chain Monte Carlo analysis (as in Sect. 2.7), we investigate how the latest LHC results on the properties of the 125 GeV Higgs state impact the probability distributions of the pMSSM parameters, masses and other observables. In doing so, we take into account Higgs measurements as in Sect. 2.6, on top of constraints from LEP searches and low-energy observables. In addition, we explore consequences for our probability distributions from the latest dark matter constraints and discuss prospects for measurements of the Higgs signal at the next run of the LHC at 13–14 TeV. Our results are orthogonal and directly comparable to the pMSSM interpretation of the CMS SUSY Sect. [232, 233].

This work was done in collaboration with John F. Gunion, Sabine Kraml and Sezen Sekmen. The rest of the section will reproduce results from the paper “The phenomenological MSSM in view of the 125 GeV Higgs data”, Ref. [234], that was submitted to arXiv on December 25, 2013 and published in PRD in March 2014. It was also summarized in a contribution to proceedings of the DIS 2014 conference [235].

2.8.1 Analysis

Definition of the Phenomenological MSSM (pMSSM)

The purpose of this study is to assess what current Higgs data tell us, and do not tell us, about the MSSM at the weak scale, without any assumption as to the SUSY-breaking scheme. A priori, the weak-scale MSSM has 120 free parameters, assuming that R -parity is conserved (to avoid proton decay and to ensure that the lightest SUSY particle, the lightest supersymmetric particle (LSP), is stable) and assuming that the gravitino is heavy. This is clearly too much for any phenomenological study. However, most of these parameters are associated with CP-violating phases and/or flavor changing neutral currents (FCNC), which are severely constrained by experiment. A few reasonable assumptions about the flavor and CP structure therefore allow us to reduce the number of free parameters by a factor 6, without imposing any SUSY-breaking scheme. Working with parameters defined at the weak scale is indeed of great advantage for our purpose, because models of SUSY breaking always introduce relations between the soft terms that need not hold in general.

Concretely, the only generic way to satisfy very strong constraints on CP violation is to take all parameters to be real. FCNC constraints are satisfied in a generic way by taking all sfermion mass matrices and trilinear couplings to be flavor-diagonal. As a further simplification, the various independent sfermion masses for the 2nd generation are taken to be equal to their counterparts for the 1st generation. Regarding the trilinear A -terms of the first two generations, these only enter phenomenology multiplied by the associated very small Yukawa couplings and are thus not experimentally relevant unless unreasonably large. Only the 3rd generation parameters A_t , A_b and A_τ have observational impact.

This leaves us with 19 real, weak-scale SUSY Lagrangian parameters—the so-called p(henomenological) MSSM [236]. As mentioned, the pMSSM captures most of the phenomenological features of the R -parity conserving MSSM and, most importantly, encompasses and goes beyond a broad range of more constrained SUSY models. The free parameters of the pMSSM are the following:

- the gaugino mass parameters M_1 , M_2 , and M_3 ;
- the ratio of the Higgs vacuum expectation values (vevs), $\tan \beta = v_2/v_1$;
- the higgsino mass parameter μ and the pseudo-scalar Higgs mass m_A ;
- 10 sfermion mass parameters $m_{\tilde{F}}$, where $\tilde{F} = \tilde{Q}_1, \tilde{U}_1, \tilde{D}_1, \tilde{L}_1, \tilde{E}_1, \tilde{Q}_3, \tilde{U}_3, \tilde{D}_3, \tilde{L}_3, \tilde{E}_3$
(with 2nd generation sfermion masses equal to their 1st generation counterparts, i.e. $m_{\tilde{Q}_1} \equiv m_{\tilde{Q}_2}$, $m_{\tilde{L}_1} \equiv m_{\tilde{L}_2}$, etc.), and
- the trilinear couplings A_t , A_b and A_τ ,

in addition to the SM parameters. To minimize theoretical uncertainties in the Higgs sector, these parameters are conveniently defined at the scale $M_{\text{SUSY}} \equiv \sqrt{m_{\tilde{t}_1} m_{\tilde{t}_2}}$, often also referred to as the EWSB scale.

The pMSSM parameter space is constrained by a number of theoretical requirements. In particular, the Higgs potential must be bounded from below and lead to

consistent EWSB, and the sparticle spectrum must be free of tachyons. Moreover, in this study, we require that the LSP is the lightest neutralino, $\tilde{\chi}_1^0$. These requirements we refer to as theoretical constraints. Note that we do not check for charge and/or color breaking minima beyond warnings from the spectrum generator; this could be done, i.e., using *Vevacious* [237], but would require too much CPU time for this study.

Construction of the pMSSM Prior

We perform a global Bayesian analysis that yields posterior probability densities of model parameters, masses and observables. We allow the pMSSM parameters to vary within the following ranges:

$$\begin{aligned} -3 \text{ TeV} &\leq M_1, M_2, \mu \leq 3 \text{ TeV}; \\ 0 &\leq M_3, m_{\tilde{F}}, m_A \leq 3 \text{ TeV}; \\ -7 \text{ TeV} &\leq A_t, A_b, A_\tau \leq 7 \text{ TeV}; \\ 2 &\leq \tan \beta \leq 60. \end{aligned} \tag{2.92}$$

A point in this space will be denoted by θ . In addition, we treat the SM parameters $m_t, m_b(m_b)$ and $\alpha_s(M_Z)$ as nuisance parameters, constrained with a likelihood. For each pMSSM point, we use *SoftSUSY_3.3.1* [238] to compute the SUSY spectrum, *SuperIso_v3.3* [239] to compute the low-energy constraints, and *micrOMEGAs_2.4.5* [240] to compute the neutralino relic density $\Omega_{\tilde{\chi}_1^0} h^2$, direct detection cross sections and to check compatibility with various pre-LHC sparticle mass limits. Moreover, we use *SDECAY_1.3b* [241] and *HDECAY_5.11* [29, 30] to produce SUSY and Higgs decay tables. The various codes are interfaced using the SUSY Les Houches Accord (SLHA) [242, 243].

The posterior density of θ given data D is given by

$$p(\theta|D) \sim L(D|\theta) p_0(\theta), \tag{2.93}$$

where $L(D|\theta)$ is the likelihood and $p_0(\theta)$ is the prior probability density, or prior for short. Beginning with a flat distribution in the parameters within the ranges defined by Eq. (2.92), $p_0(\theta)$ is obtained by incorporating the theoretical constraints noted above. In other words, $p_0(\theta)$ is the result of sculpting the flat parameter distributions by the requirements related to theoretical consistency and $\tilde{\chi}_1^0$ being the LSP. This $p_0(\theta)$ defines the starting prior, which will be modified by actual data using Eq. (2.93). Since we consider multiple independent measurements D_i , the combined likelihood is given by $L(D|\theta) = \prod_i L(D_i|\theta)$.

We partition the data into two parts:

1. a set of constraints, listed in Table 2.15, which are independent of the Higgs measurements; these constraints are used for the MCMC sampling and are collectively referred to by the label “preHiggs”, and
2. the Higgs measurements, which include the Higgs mass window, $m_h = 123\text{--}128 \text{ GeV}$, and the signal strength likelihood as derived in Sect. 2.6.

Table 2.15 The measurements that are the basis of our pMSSM prior $p^{\text{preHiggs}}(\theta)$. All measurements were used to sample points from the pMSSM parameter space via MCMC methods. The likelihood for each point was reweighted post-MCMC based on better determinations of $\mathcal{B}(b \rightarrow s\gamma)$, $\mathcal{B}(B_s \rightarrow \mu\mu)$, $R(B_u \rightarrow \tau\nu)$, and m_t

i	Observable $\mu_j(\theta)$	Constraint D_j^{preHiggs}	Likelihood function $L(D_j^{\text{preHiggs}} \mu_j(\theta))$	MCMC/post-MCMC
1a	$\mathcal{B}(b \rightarrow s\gamma)$ [244, 245]	$(3.55 \pm 0.24^{\text{stat}} \pm 0.23^{\text{th}} \pm 0.09^{\text{sys}}) \times 10^{-4}$	Gaussian	MCMC
1b	$\mathcal{B}(b \rightarrow s\gamma)$ [246]	$(3.43 \pm 0.21^{\text{stat}} \pm 0.23^{\text{th}} \pm 0.07^{\text{sys}}) \times 10^{-4}$	Gaussian	Reweight
2a	$\mathcal{B}(B_s \rightarrow \mu\mu)$ [247, 248]	Observed CL_s curve from [247]	$d(1 - \text{CL}_s)/d(BR(B_s \rightarrow \mu\mu))$	MCMC
2b	$\mathcal{B}(B_s \rightarrow \mu\mu)$ [248, 249]	$(2.9 \pm 0.7 \pm 0.29^{\text{th}}) \times 10^{-9}$	Gaussian	Reweight
3a	$R(B_u \rightarrow \tau\nu)$ [28]	1.63 ± 0.54	Gaussian	MCMC
3b	$R(B_u \rightarrow \tau\nu)$ [246]	1.04 ± 0.34	Gaussian	Reweight
4	Δa_μ [250–252]	$(26.1 \pm 8.0^{\text{exp}} \pm 10.0^{\text{th}}) \times 10^{-10}$	Gaussian	MCMC
5a	m_t [253]	$173.3 \pm 0.5^{\text{stat}} \pm 1.3^{\text{sys}} \text{ GeV}$	Gaussian	MCMC
5b	m_t [254]	$173.20 \pm 0.87 \text{ GeV}$	Gaussian	Reweight
6	$m_b(m_b)$ [28]	$4.19^{+0.18}_{-0.06} \text{ GeV}$	Two-sided Gaussian	MCMC
7	$\alpha_s(M_Z)$ [28]	0.1184 ± 0.0007	Gaussian	MCMC
8	Sparticle	LEP [255]	1 if allowed	MCMC
	Masses	(via micrOMEGAs [240])	0 if Excluded	

With this partitioning, the posterior density becomes

$$p(\theta|D) \sim L(D^{\text{Higgs}}|\theta) L(D^{\text{preHiggs}}|\theta) p_0(\theta) = L(D^{\text{Higgs}}|\theta) p^{\text{preHiggs}}(\theta), \quad (2.94)$$

where $p_0(\theta)$ is the prior (as defined earlier) at the start of the inference chain and $p^{\text{preHiggs}}(\theta) \sim L(D^{\text{preHiggs}}|\theta) p_0(\theta)$ can be viewed as a prior that encodes the information from the preHiggs-measurements as well as the theoretical consistency requirements. This partitioning allows us to assess the impact of the Higgs results on the pMSSM parameter space while being consistent with constraints from the previous measurements. Note that at this stage we do not consider the direct limits from SUSY searches from ATLAS or CMS.

In addition to the experimental results included in our calculation of the prior $p^{\text{preHiggs}}(\theta)$, Table 2.15 lists the corresponding likelihood $L(D_j^{\text{preHiggs}}|\mu_j(\theta))$ for

each observable j , where $\mu_j(\theta)$ denotes the model prediction for the observable j , such as $\mathcal{B}(b \rightarrow s\gamma)$ for a given θ . We obtained a discrete representation of the prior $p^{\text{preHiggs}}(\theta)$ within the sub-space defined in Eq. (2.92) by sampling points from $p^{\text{preHiggs}}(\theta)$ using a MCMC method (for an introduction see, i.e., [217]). By construction, this method produces a sample of points whose density in the neighborhood of θ is $\propto p^{\text{preHiggs}}(\theta)$, i.e. the sampled points will constitute a discrete representation of the preHiggs likelihood as a function of the pMSSM parameters θ .

Our study is based on approximately 2×10^6 MCMC points, which were originally sampled for the CMS study [232] in which some of us participated. (The CMS study then used a random sub-sample of 7205 points from this data.) In the meanwhile, several experimental constraints that enter the preHiggs likelihood function have been updated. For example, first evidence for the decay $B_s \rightarrow \mu\mu$ was reported by the LHCb collaboration in [256] and recently new improved measurements have become available by CMS and LHCb [249]. We have taken the up-to-date value into account by reweighting each sampled point by the ratio of the new $\mathcal{B}(B_s \rightarrow \mu\mu)$ likelihood, 2b, to the old likelihood, 2a, in Table 2.15. Analogous reweighting was performed to take into account the updated values of $\mathcal{B}(b \rightarrow s\gamma)$, $R(B_u \rightarrow \tau\nu)$, and m_t .

Higgs Likelihood

For fitting the properties of the observed Higgs boson, we use the information presented in terms of combined ellipses in Sect. 2.6.1, as well as the preliminary ATLAS results on invisible decays from ZH associated production with $Z \rightarrow \ell^+\ell^-$ and $H \rightarrow \text{invisible}$, extracting the likelihood from Fig. 10b of [152]. All these results are combined into the “Higgs signal likelihood” $L(D^{\text{Higgs}}|\theta)$.

For the concrete calculation, we use HDECAY_5.11 and approximate $\sigma(gg \rightarrow h)/\sigma(gg \rightarrow H_{\text{SM}}) \simeq \Gamma(h \rightarrow gg)/\Gamma(H_{\text{SM}} \rightarrow gg)$. Moreover, for computing the SM results entering the calculation of signal strengths, we use the MSSM decoupling limit with m_A and the relevant SUSY masses set to 4 TeV. This ensures completely SM-like Higgs boson couplings at tree-level, as well as vanishing radiative contributions from the SUSY particles (including non-decoupling effects). We choose this procedure in order to guarantee that the radiative corrections being included are precisely the same for the numerator and denominator in Eq. (2.4).

For completeness, we also take into account the limits from the $H, A \rightarrow \tau\tau$ searches in the MSSM [257]. These limits are implemented in a binary fashion: we set the likelihood from each of these constraints to 1 when the 95 % CL limit is obeyed and to 0 when it is violated. (Including or not including this limit however has hardly any visible effect on the posterior distributions.)

Dark Matter Constraints

The calculation of the properties of the neutralino LSP as a thermal cold dark matter (DM) candidate (or one of the cold DM components) depends on a number of cosmological assumptions, like complete thermalization, no non-thermal production, no late entropy production, *etc.* In order to be independent of these assumptions, we will show results with and without requiring consistence with DM constraints.

When we do apply DM constraints, we adopt the following procedure. For the relic density, we apply an upper bound as a smoothed step function at the Planck value of $\Omega h^2 = 0.1189$ [258], accounting for a 10 % theory-dominated uncertainty. Concretely, we take

$$L = \begin{cases} 1 & \text{if } \Omega h^2 < 0.119, \\ \exp[(0.119 - \Omega h^2)/0.012]^2/2 & \text{if } \Omega h^2 > 0.119. \end{cases} \quad (2.95)$$

For the spin-independent scattering cross section off protons, we use the 90 % CL limit from LUX [168], rescaling the computed $\sigma^{\text{SI}}(\tilde{\chi}_1^0 p)$ by a factor $\xi = \Omega_{\tilde{\chi}_1^0} h^2 / 0.119$ to account for the lower local density when the neutralino is only part of the DM. (The alternative would be to assume that the missing amount of $\Omega_{\tilde{\chi}_1^0} h^2$ is substituted by non-thermal production, which would make the direct detection constraints more severe. Our approach is more conservative in the sense of not being overly restrictive.)

Prompt Chargino Requirement

Before presenting the sampled distributions, another comment is in order. Letting M_1 , M_2 and μ , vary freely over the same range implies that about 2/3 of the time M_2 or μ will be the smallest mass parameter in the neutralino mass matrix. This implies that in a considerable portion of the pMSSM parameter space the $\tilde{\chi}_1^\pm$ and $\tilde{\chi}_2^0$ are close in mass or almost degenerate with the LSP, $\tilde{\chi}_1^0$ [259]. When the $\tilde{\chi}_1^\pm - \tilde{\chi}_1^0$ mass difference becomes very small, below about 300 MeV, the charginos are long-lived and can traverse the detector before they decay. This typically occurs for wino-LSP scenarios with $|M_2| \ll |M_1|, |\mu|$. Since long-lived heavy charged particles were not considered in the SUSY searches used in [232], charginos were required to decay promptly; in practice this means a cut on the average proper lifetime of $c\tau < 10$ mm. In order to be able to directly compare our results (based on the Higgs measurements) with the CMS study (based on SUSY search results) [232] and its up-coming update [233], we also require “prompt” chargino decays, i.e. $c\tau < 10$ mm. Most of our conclusions are insensitive to this requirement. Wherever it matters, we will however also show the results obtained without imposing the $c\tau$ cut.

2.8.2 Results

Pre-Higgs Distributions and Impact of the Higgs Mass

We begin our discussion by showing in Fig. 2.48 the sampled distributions of selected parameters and masses and the effect of the model prior. All distributions except that of the pMSSM prior $p_0(\theta)$ include the prompt chargino requirement; as can be seen, this requirement substantially alters the probability distributions for the parameters M_1 , M_2 , and μ and the chargino and neutralino masses relative to the $p_0(\theta)$ distributions, but has very little impact on the other parameters or masses.

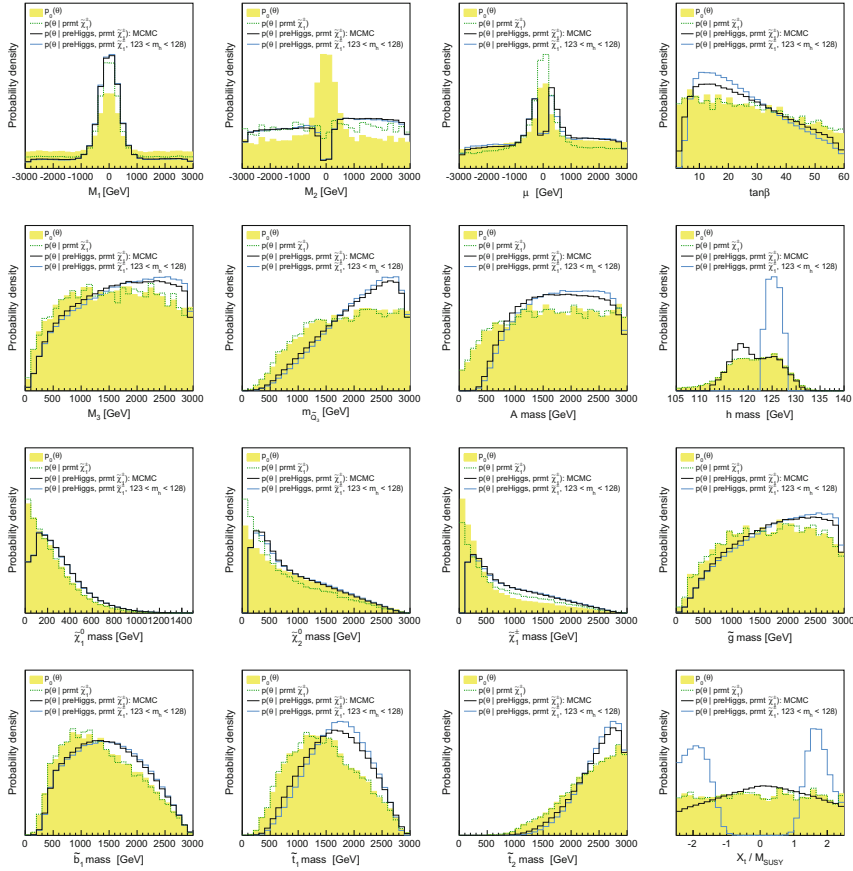


Fig. 2.48 Marginalized 1D posterior densities for selected parameters and masses. The *yellow histograms* show the sampled distributions, $p_0(\theta)$, as obtained after imposing theoretical constraints starting from a flat scan in the parameter ranges specified by Eq. (2.92). The *dashed green lines* are the distributions after requiring prompt charginos (prm t), the *full black lines* show the distributions based on the “preHiggs” measurements of Table 2.15, and the *full blue lines* are the ones when requiring $m_h = [123, 128]$ GeV in addition to “prm t” and “preHiggs” constraints. The *bottom right plot* of X_t/M_{SUSY} shows that large (but not maximal) stop mixing is favored by the $m_h = 123 - 128$ GeV requirement

Further, in all the plots we observe that the preHiggs measurements incorporated in the MCMC influence the probability distributions relative to the simple prompt-chargino-decay distributions quite significantly, in particular shifting the neutralino, chargino, gluino, and also the stop/sbottom masses to higher values.

Also shown is the impact of requiring, in addition, that the mass of the light h fall in the window $123 \text{ GeV} \leq m_h \leq 128 \text{ GeV}$. This Higgs mass constraint strongly affects the stop mixing parameter $X_t/M_{\text{SUSY}} \equiv (A_t - \mu/\tan\beta)/\sqrt{m_{\tilde{t}_1}m_{\tilde{t}_2}}$, whose distribution takes on a two-peak structure emphasizing larger absolute values.

More precisely, values around $|X_t/M_{\text{SUSY}}| \approx 2$, i.e. large but not maximal stop mixing is preferred. (Maximal stop mixing would mean $|X_t/M_{\text{SUSY}}| = \sqrt{6}$; for a detailed discussion of the relation between $|X_t/M_{\text{SUSY}}|$ and m_h see, i.e., [224, 260]). It is interesting to note here that, in view of naturalness, the optimal stop mixing is indeed somewhat shy of maximal [261]. The optimal value is actually quite close to that which has the highest probability in the pMSSM context, despite the fact that no measure of naturalness is input into the pMSSM likelihood analyses. The Higgs mass window requirement also results in a shift of the \tilde{t}_1 mass distribution to slightly larger values; however, compared to the impact of the preHiggs constraints the effect is quite small. Aside from an increased preference for values of $\tan \beta \approx 10 - 20$, the other parameters and masses are hardly affected by the Higgs mass window.

It is also interesting to consider the h signal at this level. Some relevant distributions are shown in Fig. 2.49. While generically the h signal strength can go down to zero in the MSSM, already the “preHiggs” constraints eliminate very small values below $\mu \approx 0.6$ and narrow the signal strength distributions to a range of $\mu \approx 1 \pm 0.4$. This is coming from two different effects. First, in the low- m_A region the heavier scalar H can be more SM-like than h . Second, in the region where the LSP is light ($m_{\tilde{\chi}_1^0} \lesssim 65 \text{ GeV}$) a large increase of the total width, resulting in reduced signal strengths, is possible through $h \rightarrow \tilde{\chi}_1^0 \tilde{\chi}_1^0$. The low- m_A region is mostly disfavored from flavor constraints, while a light neutralino—if mainly wino or higgsino—is excluded by the LEP bound on charginos. In both cases, requiring $m_h = 123\text{--}128 \text{ GeV}$ only has a very small additional effect.

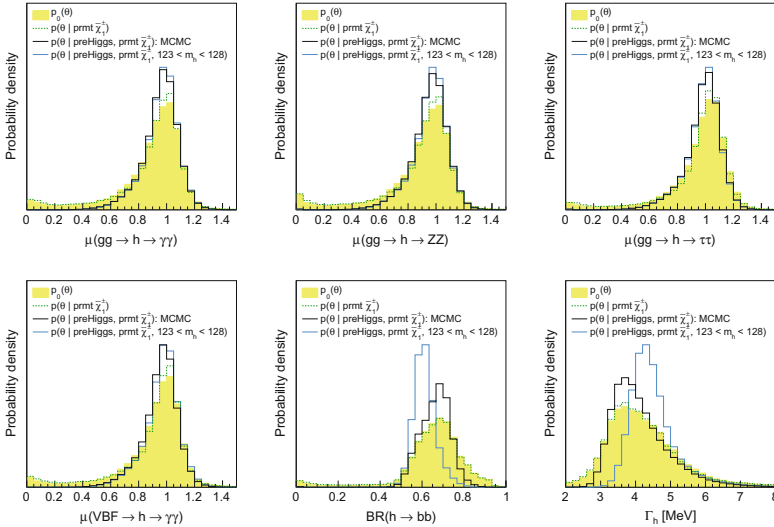


Fig. 2.49 Same as Fig. 2.48 but for selected h signal strengths, $\mathcal{B}(h \rightarrow b\bar{b})$ and the total decay width Γ_h . The VBF distributions look practically the same as the ggF distributions, as exemplified for the VBF $\rightarrow h \rightarrow \gamma\gamma$ case, though they show a slightly larger effect from requiring $m_h = 123 - 128 \text{ GeV}$ than the ggF distributions

One might expect that the influence of the Higgs mass is larger in the ggF channels than in the VBF channels (because of the negative loop contribution from maximally mixed stops affecting the former) but, in fact, the effect is very small and goes in the opposite direction, as can be seen by comparing the top-left and the bottom-left plots in Fig. 2.49. The observables which are really influenced by the Higgs mass are the branching fraction into $b\bar{b}$, which becomes centered around $\mathcal{B}(h \rightarrow b\bar{b}) \approx 0.6$, and the h total width, for which the most likely value is shifted a bit upwards to $\Gamma_h \approx 4\text{--}5$ MeV. However, this is not really a SUSY effect: the same happens for the SM Higgs when going from $m_H \lesssim 120$ GeV to $m_H \approx 125$ GeV.

Impact of Higgs Signal Strengths

As the next step, we include in addition the detailed properties of the h signal in the computation of the likelihood as outlined in Sect. 2.8.1. The effects of the Higgs observations on the pMSSM parameters and on the particle masses are shown in Fig. 2.50. In these plots, the light blue histograms show the distributions based on the “pre-Higgs” measurements of Table 2.15 plus requiring in addition $m_h \in [123, 128]$ GeV, i.e. they correspond to the blue line-histograms of Fig. 2.48. The solid red lines are the distributions when moreover taking into account the measured Higgs signal strengths in the various channels as outlined in Sect. 2. Note that the limits from the MSSM $H, A \rightarrow \tau\tau$ searches, which are also included in the red line-histograms, have a negligible effect. (For completeness, a plot of the $\tan\beta$ versus m_A plane is given in Fig. 2.53.) Finally, the dashed red lines also take into account upper limits from the DM relic density and direct DM searches, as explained in Sect. 2.8.1.

Let us first discuss the effect of the Higgs measurements, i.e. consider the solid red lines only. We observe a significant preference for small or negative μ and smaller $\tan\beta$ values when including the Higgs signal strength likelihood. The main reason is the $\mu \tan\beta$ correction to the bottom Yukawa coupling [153, 154], which for large $\tan\beta$ and large positive (negative) μ enhances (reduces) $\Gamma(h \rightarrow b\bar{b})$ and the total h width, hence reducing (increasing) all signal strengths except $\mu(Vh \rightarrow b\bar{b})$. The preference for negative μ comes from the slight excess in the VBF and VH channels of $\gamma\gamma$ (mainly seen by ATLAS). In Sect. 2.6, $\mu(\text{VBF} + \text{VH}, \gamma\gamma) = 1.72 \pm 0.59$ is found, while other combined signal strengths are fully compatible with 1 at 68 % CL. An overall excess (negative μ) is therefore preferred over a general deficit (positive μ). To a good approximation, the correction to the bottom Yukawa coupling is given by

$$\Delta_b \equiv \frac{\Delta m_b}{m_b} \simeq \left[\frac{2\alpha_s}{3\pi} \mu m_{\tilde{g}} I(m_{\tilde{g}}^2, m_{\tilde{b}_1}^2, m_{\tilde{b}_2}^2) + \frac{\lambda_t^2}{16\pi^2} A_t \mu I(\mu^2, m_{\tilde{t}_1}^2, m_{\tilde{t}_2}^2) \right] \tan\beta, \quad (2.96)$$

where $I(x, y, z)$ is of order $1/\max(x, y, z)$ [260]. The shifts to higher values of all four stops and sbottoms masses and to lower values for the gluino mass also come from Δ_b . In addition, negative values of A_t are more likely after taking into account the Higgs likelihood. This comes from the second term of Eq. (2.96): in order to compensate the first, dominant term, $\text{sgn}(A_t \mu) = -\text{sgn}(\mu)$ is required, hence a

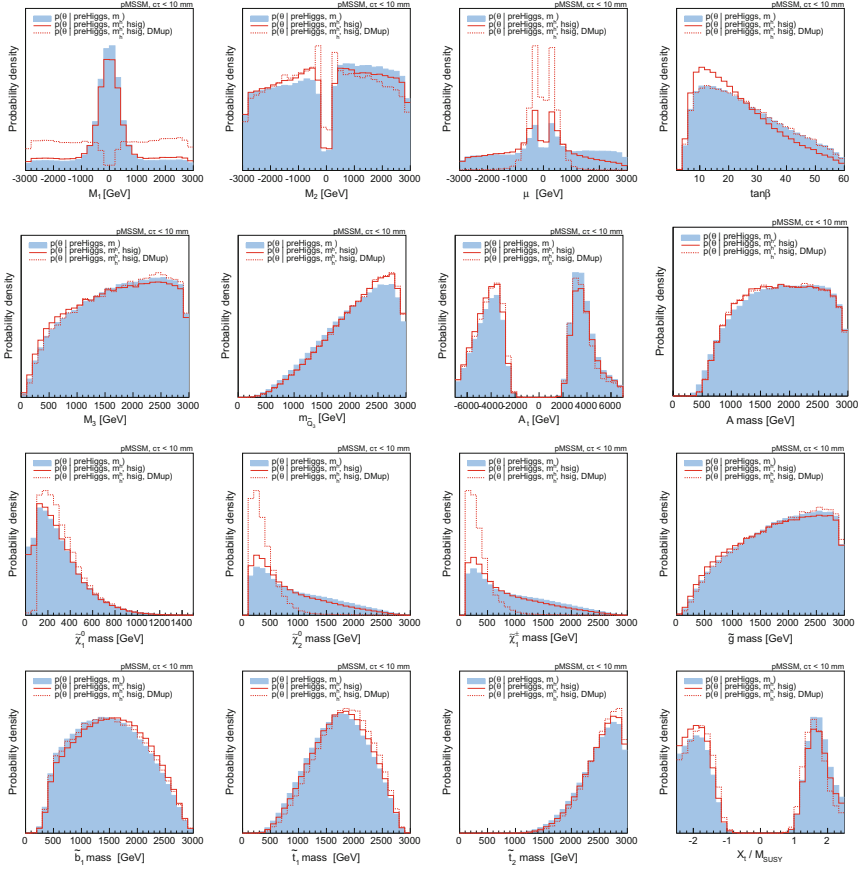


Fig. 2.50 Marginalized 1D posterior densities for selected parameters and masses, showing the effect of the Higgs signal strength measurements. The *light blue* histograms show the distributions based on the “preHiggs” measurements of Table 2.15 plus requiring in addition $m_h \in [123, 128]$ GeV. The *solid red lines*, labelled “hsig”, are the distributions when moreover taking into account the measured Higgs signal strengths in the various channels. The limits from searches for the heavy Higgses (H and A) are also included in the *red line-histograms*, but have a totally negligible effect. The *dashed red lines*, labelled “DMup”, include in addition an upper limit on the neutralino relic density and the recent direct DM detection limit from LUX as explained in the text

negative A_t . The tree-level coupling hbb also has an effect. It is given by

$$g_{hbb} \simeq 1 - \frac{M_Z^2}{2m_A^2} \sin 4\beta \tan \beta, \quad (2.97)$$

for $m_A \gg M_Z$ [260], and disfavors relatively light A and H , with masses below about 700 GeV (the effect from imposing the CMS $H, A \rightarrow \tau\tau$ limit is subdominant). Finally, M_2 shows a slight preference towards negative values. This is a direct

consequence of the asymmetry in the distribution of μ , since $\text{sgn}(\mu M_2) > 0$ is required for $\Delta a_\mu^{\text{SUSY}} > 0$ as suggested by the data.

The DM constraints, on the other hand, have a dramatic effect on the bino and higgsino mass parameters and in turn on the chargino and neutralino masses. Since a mostly bino $\tilde{\chi}_1^0$ generically leads to a large $\Omega_{\tilde{\chi}_1^0} h^2$, low values of M_1 are strongly disfavored. The preferred solutions have a relevant higgsino or wino fraction of the LSP; therefore $\tilde{\chi}_1^\pm$ and $\tilde{\chi}_2^0$ masses below about 1 TeV are strongly favored. At the same time, very light LSP masses below about 100 GeV are severely limited because of the LEP bound on the chargino mass. The preferred value of $\tan \beta$ is also affected; in fact, the preference for lower $\tan \beta$ coming from the Higgs signal strengths is removed by the DM constraints. The reason for this is an enhancement of A -funnel annihilation to comply with the upper limit on $\Omega_{\tilde{\chi}_1^0} h^2$.

The posterior distributions of the h signal strengths in the various channels are shown in Fig. 2.51. The red line-histograms correspond of course to the constraints which we used as experimental input. For the $\gamma\gamma$, ZZ and $\tau\tau$ final states, we find signal strengths of about 1 ± 0.15 after the Higgs signal requirements, and about 1 ± 0.10 after the DM requirements, at 95 % Bayesian Credibility (BC). For the $b\bar{b}$ final state, the distribution is much narrower than required by observations—we find that $\mu(Vh \rightarrow b\bar{b})$ is restricted to the 95 % BC interval $\mu(Vh \rightarrow b\bar{b}) \in [0.91, 1.09]$ after Higgs signal requirements, and $[0.94, 1.06]$ after DM requirements. This is an indirect effect of the constraint on $\mathcal{B}(h \rightarrow b\bar{b})$ and the total h width, Γ_h , in order to have large enough signal in the other channels, see Fig. 2.52. Interestingly, the constraints from the DM side narrow the signal strength distributions even more around the SM value of 1 because the higgsino mass μ tends to take on small values to fulfill the relic density requirement, leading to smaller Δ_b .

Figure 2.52 also shows posterior distributions of $r_Y \equiv \Gamma(h \rightarrow Y)/\Gamma(H_{\text{SM}} \rightarrow Y)$ for $Y = \gamma\gamma$, gg and $b\bar{b}$. These ratios are equivalent to the ratios of the coupling

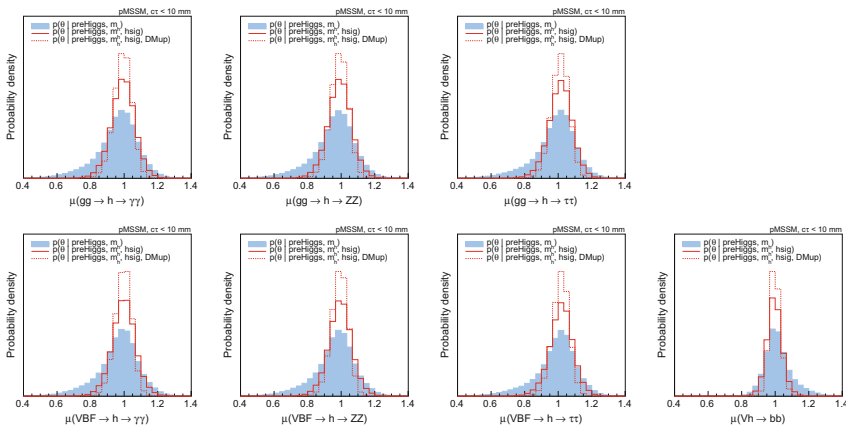


Fig. 2.51 Same as Fig. 2.50 but for the relevant h signal strengths

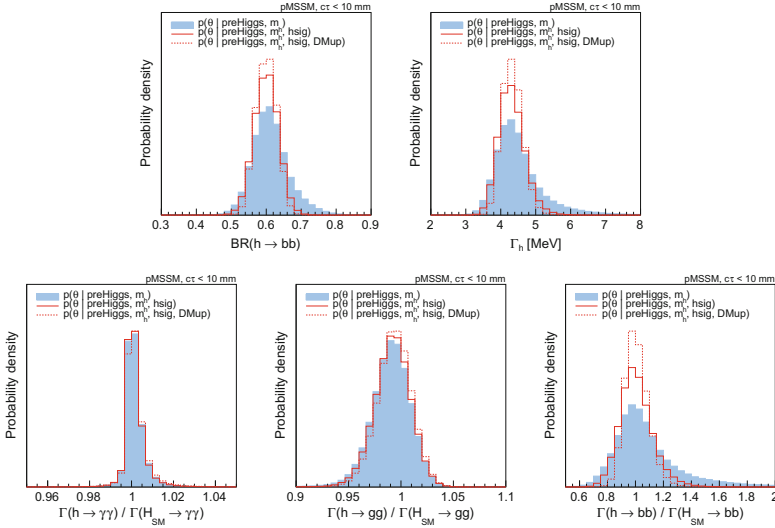


Fig. 2.52 Marginalized 1D posterior densities as in Fig. 2.50, in the *top* row for $\text{BR}(h \rightarrow b\bar{b})$ and Γ_h , in the *bottom* row for $\Gamma(h \rightarrow Y) / \Gamma(H_{\text{SM}} \rightarrow Y)$ with, from left to right, $Y = \gamma\gamma$, gg and $b\bar{b}$

strengths squared; $r_{\gamma\gamma} = C_\gamma^2$, $r_{gg} = C_g^2$, $r_{bb} = C_D^2$ in the notation of Sect. 2.6. Our results for r_γ can be compared to those for the neutralino LSP case in Ref. [231]. We observe that in our case $r_{\gamma\gamma}$ peaks sharply at 1, the 95 % BC interval being [0.99, 1.01], while r_{gg} shows a wider distribution with a 95 % BC interval of [0.96, 1.02]. (The picture does not change if we remove the $c\tau$ cut.). These features are different from those in [231], where the $r_{\gamma\gamma}$ distribution peaks within $r_{\gamma\gamma} \approx 1\text{--}1.05$, and r_{gg} exhibits an upper limit of $r_{gg} \lesssim 0.97$. Also, the r_{bb} distribution is quite different. Some differences are of course expected as the distributions in [231] come from a flat random sampling and thus do not have the statistical meaning that underlies our approach. More importantly, however, the SM calculation of HDECAY employed in [231] includes additional radiative corrections which are not present in the MSSM calculation.²⁶ In our case, we avoid this problem by taking the MSSM decoupling case as the SM limit for computing $\Gamma(H_{\text{SM}} \rightarrow Y)$, cf. Sect. 2.8.1. Of course, the r_Y are not directly measurable at the LHC. They become measurable only if it can be determined that the h has no invisible (i.e. $h \rightarrow \tilde{\chi}_1^0 \tilde{\chi}_1^0$) or unseen (i.e. $h \rightarrow 4\tau$) decay modes.

Our procedure also allows us to derive predictions for the heavier MSSM Higgs states H , A and H^\pm , as illustrated in Figs. 2.53 and 2.54. First, in the $\tan\beta$ versus m_A plane, we show that the current CMS limit [257] interpreted in the m_h^{max} scenario has a negligible effect on our distributions, since after imposing constraints from low-energy observables and from Higgs measurements the likely region corresponds to A masses above 500 GeV and moderate $\tan\beta$. (This observation remains

²⁶We thank Ahmed Ismail and Matthew Cahill–Rowley for communication on this matter.

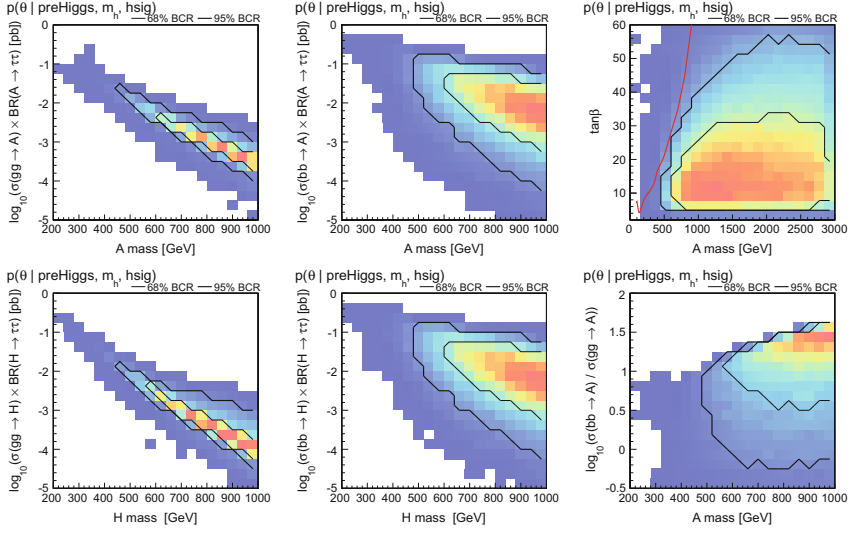


Fig. 2.53 Marginalized posterior densities in 2D for the heavy MSSM Higgses A and H . The plots on the left and in the middle show $\sigma \times B$ in the $\tau\tau$ final state, from bb and gg production at $\sqrt{s} = 14$ TeV, versus the A or H mass. The *top-right* plot shows the posterior density in the $\tan\beta$ versus m_A plane with the latest 95 % CL from the CMS search for MSSM $H, A \rightarrow \tau\tau$ [257] superimposed. The bottom-right plot compares bb to gg production as function of m_A . In all plots, the probability density is represented by *color shading*, ranging from low values in *blue* to high values in *red*. The *gray* and *black* lines are contours of 68 and 95 % Bayesian Credibility, respectively

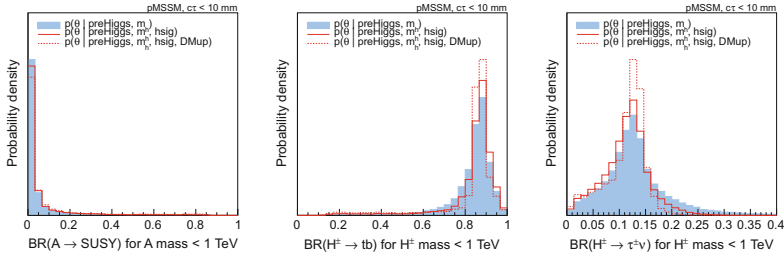


Fig. 2.54 Marginalized 1D posterior densities as in Fig. 2.50, here for the branching fractions of the heavy MSSM Higgses A and H^\pm with masses below 1 TeV

valid when dark matter requirements are taken into account; in all cases we have checked that the current limits on $H \rightarrow ZZ$ are always satisfied.) We also show $\sigma(gg, b\bar{b} \rightarrow H, A) \times \text{BR}(H, A \rightarrow \tau\tau)$ at $\sqrt{s} = 14$ TeV as a function of $m_{H,A}$, using *SusHi_1.1.1* [262] for the computation of the cross sections in the approximation of decoupled stops and sbottoms.²⁷ These plots show that the signals from

²⁷Neglecting contributions from stops and sbottoms in the computation of $gg, b\bar{b} \rightarrow H, A$ is a good approximation in most cases since the posterior densities of $m_{\tilde{t}_1}$ and $m_{\tilde{b}_1}$ peak around 2 TeV.

the CP-odd and CP-even Higgs bosons are very similar and that for high masses the dominant process is almost always $b\bar{b} \rightarrow H, A$ (see, in particular, the bottom right plot), where for a given mass $\sigma(b\bar{b} \rightarrow H, A)$ spans over about an order of magnitude due to its strong dependence on $\tan\beta$. Typical $\sigma \times \mathcal{B}$ values are of the order of 0.1 to 100 fb for $m_{H,A} < 1$ TeV and therefore most of this region should be probed during the next run of the LHC at 13–14 TeV.

Some more properties of the heavy Higgses (for masses < 1 TeV) are shown in Fig. 2.54. We see that the decay branching fraction of A into SUSY particles is often very small because most of the supersymmetric partners generally lie at the (multi-)TeV scale. Concretely, the probability for $\mathcal{B}(A \rightarrow \text{SUSY}) > 10\%$ is only 1.6% after the Higgs signal likelihood (2.1% after DM requirement). Compared to the preHiggs distributions, decays into SUSY particles are however slightly enhanced by the Higgs likelihood and dark matter requirements because μ , and hence neutralino and chargino masses, are pushed to lower values. Also shown are the dominant decay modes of the charged Higgs: $H^\pm \rightarrow tb$ and $H^\pm \rightarrow \tau^\pm \nu$. The dominance of hadronic decays over leptonic ones is strengthened when Higgs measurements are taken into account since small values of m_A and large values of $\tan\beta$ are then disfavored.

Impact of the $C\tau$ Cut

We saw from the plots in Sect. 2.8.2 that the “prompt chargino” requirement has a strong effect on some of the distributions, above all on that of the wino mass parameter M_2 . The influence on μ and M_1 is less dramatic but still quite strong. As a consequence, it is mostly the chargino and neutralino masses (and their gaugino–higgsino composition) which are affected by the $c\tau < 10$ mm requirement. To assess the impact of this cut, the relevant posterior densities *without* the $c\tau$ cut are shown in Fig. 2.55. Comparing these plots with their equivalents in Fig. 2.48 of Sect. 2.8.2, we see that, as expected, in both the “preHiggs+ m_h ” and the “preHiggs+ m_h +hsig” distributions, light charginos and neutralinos are more preferred. The effect is more pronounced for the $\tilde{\chi}_1^\pm$ and $\tilde{\chi}_2^0$ than for the $\tilde{\chi}_1^0$. Note also that the preference for smaller μ through the Higgs signal strength measurements remains. Finally, note that the DM upper limits largely overrule the effect of the $c\tau$ cut: the red dashed line histograms are almost the same with or without the $c\tau$ cut. The exception is the $\tan\beta$ distribution. (The $\tilde{\chi}_1^0, \tilde{\chi}_2^0, \tilde{\chi}_1^\pm$ mass differences can however be smaller without the $c\tau$ cut.) The posterior densities of other quantities, which do not directly depend on M_1, M_2 or μ show hardly any sensitivity to the $c\tau$ cut. In particular our conclusions about the Higgs signals remain unchanged.

It is of course also interesting to ask how likely it is at all to have a long-lived chargino. To this end we show in Fig. 2.56 the marginalized posterior density of the average $\tilde{\chi}_1^\pm$ lifetime. We find that the probability of $c\tau > 10$ mm is 28, 25 and 47% at the “preHiggs+ m_h ”, “preHiggs+ m_h +hsig”, and “preHiggs+ m_h +hsig+DMup” levels, respectively.

Interplay with Dark Matter Searches

As discussed above, the dark matter requirements (i.e., imposing upper limits on the relic density and on the spin-independent scattering cross section) have a significant

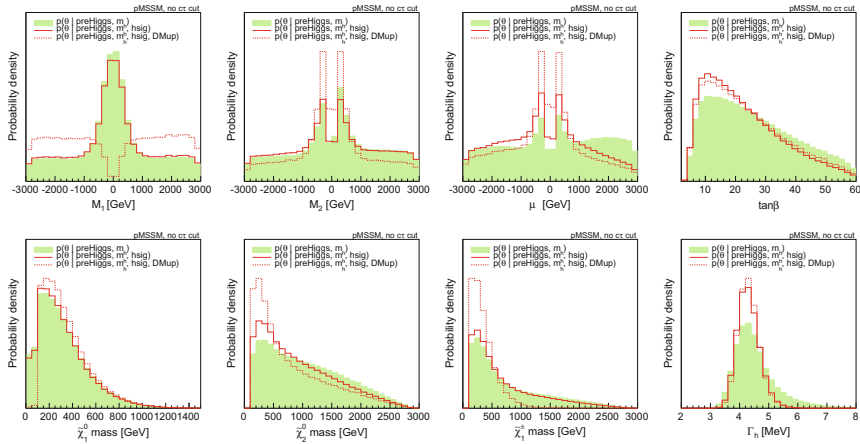
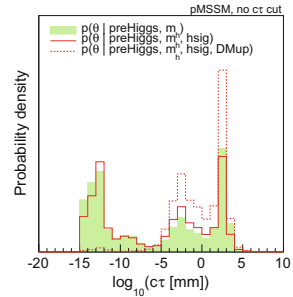


Fig. 2.55 Marginalized 1D posterior densities for selected parameters and derived quantities without the prompt chargino requirement. The *green histograms* show the distributions based on the “preHiggs” measurements of Table 2.15 plus requiring in addition $m_h \in [123, 128]$ GeV, but without the $c\tau$ cut. The *solid red lines* are the distributions when taking into account in addition the measured Higgs signal strengths in the various channels, as well as the limits from the heavy MSSM Higgs searches. The *dashed red lines* include in addition an upper limit on the neutralino relic density and the recent direct DM detection limit from LUX

Fig. 2.56 Marginalized 1D posterior density of the average $\tilde{\chi}_1^\pm$ lifetime, $c\tau$ in mm. *Color codes* as in Fig. 2.55



impact on the MSSM parameters and masses, and even on the h signal strengths. In this subsection, we now focus on dark matter observables themselves. Results for the neutralino relic density $\Omega_{\tilde{\chi}_1^0} h^2$ and the re-scaled spin-independent scattering cross section $\xi \sigma^{\text{SI}}(\tilde{\chi}_1^0 p)$ are shown in Figs. 2.57 and 2.58.

Let us start the discussion with the 1D distributions of $\log_{10}(\Omega_{\tilde{\chi}_1^0} h^2)$, shown in the upper row of plots in Fig. 2.57. Already the $p_0(\theta)$ distribution shows a two-peak structure with the minimum actually lying near the cosmologically preferred value $\Omega_{\tilde{\chi}_1^0} h^2 \approx 0.1$. This distribution is shifted to significantly higher values by the preHiggs constraints. Concretely, at preHiggs level, the probability for $\Omega_{\tilde{\chi}_1^0} h^2 < 0.14$ is 36 % (53 %) with (without) the prompt chargino requirement. This hardly changes when including also the requirement of $m_h = 123 - 128$ GeV: $p(\Omega_{\tilde{\chi}_1^0} h^2 < 0.14) \simeq$

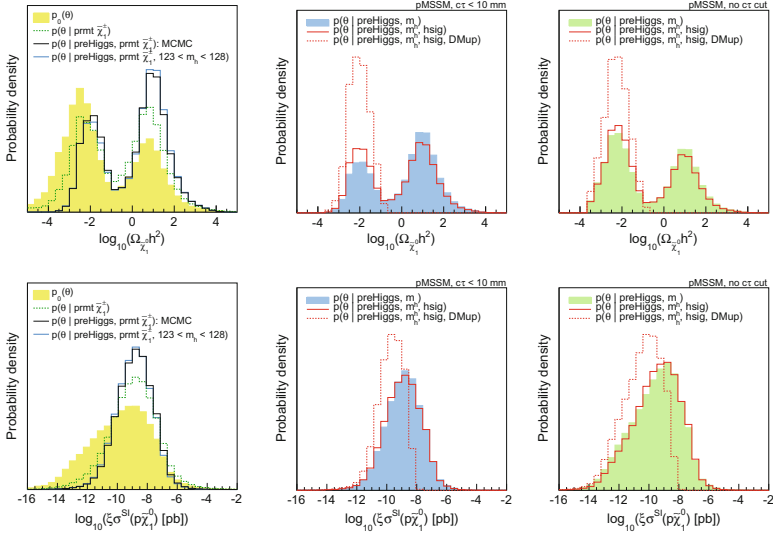


Fig. 2.57 Marginalized 1D posterior densities for dark matter quantities. *Color codes* as in Fig. 2.48 (left), Fig. 2.50 (middle) and Fig. 2.55 (right)

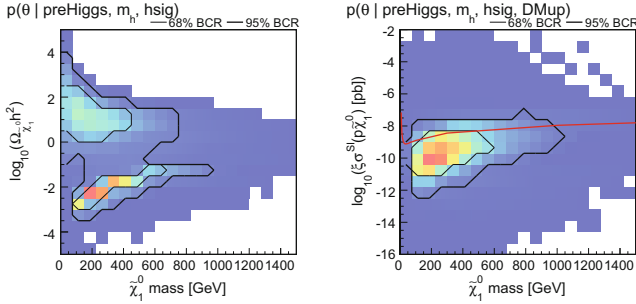


Fig. 2.58 Marginalized 2D posterior densities for dark matter quantities. The probability density is represented by *color shading*, ranging from low values in *blue* to high values in *red*. The *gray* and *black* lines are contours of 68 and 95 % Bayesian Credibility, respectively. The *red* line in the right plot is the 90 % CL limit from LUX

34 % (53 %) in this case. The Higgs signal likelihood has a larger effect, shifting the distribution towards lower $\Omega_{\tilde{\chi}_1^0} h^2$. This is mainly due to the preference for smaller μ induced by the Higgs signal likelihood. The effect is thus less pronounced without the $c\tau$ cut (RH-side plot) than with the $c\tau$ cut (middle plot). Concretely, we find $p(\Omega_{\tilde{\chi}_1^0} h^2 < 0.14) \simeq 43\%$ (57 %) with (without) the $c\tau$ cut. The peak at high $\Omega_{\tilde{\chi}_1^0} h^2$ values is of course completely removed by the DMup constraints. The probability of lying within the Planck window defined by $\Omega_{\tilde{\chi}_1^0} h^2 = 0.119 \pm 0.024$ (0.024 being the 2σ error, dominated by theory uncertainties) is, for all three of the above cases, $\sim 1.1\%$ with the $c\tau$ cut and $\sim 0.9\%$ without the $c\tau$ cut.

Turning to the predictions for direct dark matter detection, we observe that the preHiggs constraints limit the probability of having very small values of $\xi \sigma^{\text{SI}}(\tilde{\chi}_1^0 p)$. This is true with and without the $c\tau$ cut, though the effect is larger with the $c\tau$ cut. The latter is due to the fact that the prompt chargino requirement removes the pure wino-LSP scenarios which have extremely small $\Omega_{\tilde{\chi}_1^0} h^2$ and $\xi \sigma^{\text{SI}}(\tilde{\chi}_1^0 p)$ (recall that $\xi = \Omega_{\tilde{\chi}_1^0} h^2 / 0.119$). Requiring consistency with the Higgs signal strengths has only a small effect, somewhat preferring smaller values of $\xi \sigma^{\text{SI}}(\tilde{\chi}_1^0 p)$ because of the larger LSP higgsino component.

The 2D distributions of $\Omega_{\tilde{\chi}_1^0} h^2$ and $\xi \sigma^{\text{SI}}(\tilde{\chi}_1^0 p)$ versus the $\tilde{\chi}_1^0$ mass are shown in Fig. 2.58. We observe that on the one hand the neutralino LSP can have mass up to 1 TeV at 95 % BC without conflicting with the DM constraints. Very low neutralino masses, on the other hand, are severely constrained by DM requirements. Note, moreover, that the most likely values lie around $m_{\tilde{\chi}_1^0} \approx 200\text{--}300$ GeV, $\Omega_{\tilde{\chi}_1^0} h^2 \approx 10^{-2}$ and $\xi \sigma^{\text{SI}}(\tilde{\chi}_1^0 p) \approx 10^{-10}$ pb.

Consequences of Future h Signal Strength Measurements

It is also interesting to consider what happens if, with precision data at the next run of the LHC, the Higgs signal strengths have an even narrower probability distribution around unity. We estimate the precision attainable with 300 fb^{-1} at 14 TeV based on [25, 26]

$$\begin{aligned} \mu(\text{ggF} + \text{ttH}, \gamma\gamma) &= 1 \pm 0.1, & \mu(\text{VBF} + \text{VH}, \gamma\gamma) &= 1 \pm 0.3, \\ \mu(\text{ggF} + \text{ttH}, VV) &= 1 \pm 0.1, & \mu(\text{VBF} + \text{VH}, VV) &= 1 \pm 0.6, \\ \mu(\text{ggF} + \text{ttH}, b\bar{b}) &= 1 \pm 0.6, & \mu(\text{VBF} + \text{VH}, b\bar{b}) &= 1 \pm 0.2, \\ \mu(\text{ggF} + \text{ttH}, \tau\tau) &= 1 \pm 0.2, & \mu(\text{VBF} + \text{VH}, \tau\tau) &= 1 \pm 0.2. \end{aligned} \quad (2.98)$$

The effect of these hypothetical results is illustrated in Fig. 2.59. We conclude that if the Higgs signal remains SM-like (but with smaller uncertainties), the effects already observed on some SUSY parameters are only slightly strengthened by more precise measurements.

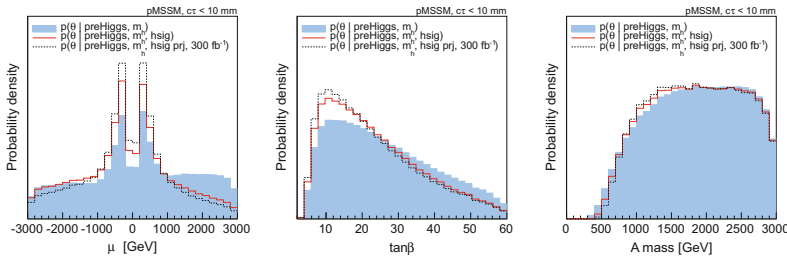


Fig. 2.59 Marginalized 1D posterior densities for some MSSM parameters, showing the effect of all h signal strengths being ≈ 1 with uncertainties as expected for 300 fb^{-1} of data at 14 TeV, cf. Eq. (2.98)

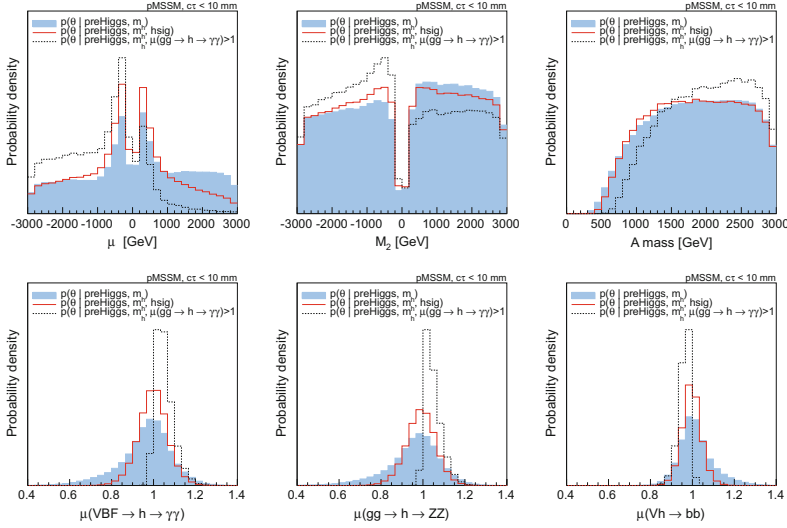


Fig. 2.60 Marginalized 1D posterior densities for selected MSSM parameters and h signal strengths, showing the effect of a hypothetical future determination of $\mu(gg \rightarrow h \rightarrow \gamma\gamma) > 1$

The picture is quite different should the signal strength finally turn out to be larger than one. For illustration, we assume $\mu(ggF, \gamma\gamma) > 1$ and show in Fig. 2.60 the impact on some other quantities. As we have seen, $\Delta_b < 0$ corresponds to a suppression of $h \rightarrow b\bar{b}$ and, hence, to the enhancement of all other signal strengths. This is how one obtains $\mu(ggF, \gamma\gamma) > 1$ in our case. This leads to a strong preference for $\mu < 0$ and to an associated asymmetry for the M_2 distribution. Moreover, strong evidence for $\mu(ggF, \gamma\gamma) > 1$ would strongly disfavor a CP-odd Higgs lying close to the current CMS bound because of the impact of m_A on the tree-level coupling hbb . Finally, $\mu(ggF, \gamma\gamma) > 1$ would also imply a preference for an enhancement of the diphoton signal in VBF production, as well as an enhancement of the ZZ mode in both ggF and VBF. This is accompanied at the same time by the expected suppression of $Vh \rightarrow b\bar{b}$. Nonetheless, signal strength values close to 1 are still the most likely ones.

2.8.3 Conclusions

We have performed a Bayesian analysis of the pMSSM taking into account the latest LHC results on the Higgs signal at 125.5 GeV in addition to relevant low-energy observables and LEP constraints. We find that the requirement of obtaining the right m_h strongly favors $|X_t/M_{\text{SUSY}}| \approx 2$, i.e. near-maximal (but not maximal) stop mixing. Coincidentally, such near-maximal mixing is also favored by naturalness arguments [261].

The constraints from the Higgs signal strengths in the various production \times decay modes, on the other hand, have an important influence on the posterior distributions of μ and $\tan \beta$, and hence on the electroweak-ino spectrum. Concretely, low values of μ and $\tan \beta \approx 10$ are favored. This is mainly due to radiative corrections to the bottom Yukawa coupling, which are proportional to $\mu \tan \beta$ and can significantly modify the total Higgs width. As a consequence, $\tilde{\chi}_2^0$ and $\tilde{\chi}_1^\pm$ masses below about 500 GeV are favored, as are LSPs with a significant higgsino fraction. While there is of course still a substantial tail at large masses, these results suggest that the Higgs data yield a certain preference for natural-SUSY-like scenarios.

Regarding the heavy Higgs states, H and A , we find that $m_{H,A} \gtrsim 500$ GeV mostly due to B-physics constraints. The 125 GeV Higgs data give only a small additional constraint; they mostly affect the heavy Higgses through their effect on $\tan \beta$. The limits from direct searches for $H, A \rightarrow \tau\tau$ at 7–8 TeV are less sensitive. If $m_A \lesssim 1$ TeV, prospects for discovery of H and A at the next LHC run are substantial. Because $\tan \beta \gtrsim 10$ is preferred, we find that $b\bar{b} \rightarrow H, A$ typically dominates (by about a factor of 30) over gluon fusion, with $\sigma(b\bar{b} \rightarrow H, A) \mathcal{B}(H, A \rightarrow \tau\tau)$ of the order of a few fb.

We have also explored the impact of DM limits associated with $\Omega_{\tilde{\chi}_1^0} h^2$ and $\xi \sigma^{\text{SI}}(\tilde{\chi}_1^0 p)$ on the Higgs bosons in the pMSSM context as well as the impact of the Higgs precision data on these same DM observables. The most probable values for $\Omega_{\tilde{\chi}_1^0} h^2$ lie in the vicinity of 10^{-2} , implying that DM would not consist entirely of the $\tilde{\chi}_1^0$ (or that the missing abundance of $\tilde{\chi}_1^0$ is substituted by non-thermal production). The probability for obtaining $\Omega_{\tilde{\chi}_1^0} h^2$ within the Planck window is only of order 1 %: to get the correct annihilation rate, the $\tilde{\chi}_1^0$ has to have a carefully balanced composition, or a mass that is fine-tuned with respect to the A or co-annihilating sparticles. Imposing the upper limit on $\Omega_{\tilde{\chi}_1^0} h^2$, we find $m_{\tilde{\chi}_1^0} \in [100, 760]$ GeV and $\xi \sigma^{\text{SI}}(\tilde{\chi}_1^0 p) \gtrsim 3.5 \times 10^{-12}$ pb at 95 % BC.

While we have not taken into account the recent LHC limits from direct SUSY searches, we have checked that our conclusions do not change when requiring gluino and squark masses above 1 TeV. The conclusions drawn from the Higgs sector are thus orthogonal to those from the SUSY searches. In particular, this makes our results directly comparable to the pMSSM interpretation of the CMS SUSY searches at 7–8 TeV [232, 233].

The 13–14 TeV run of the LHC will provide increased precision for Higgs measurements as well as a higher reach for SUSY particles. Particularly relevant in point of view of an interplay between Higgs and SUSY results is an improved sensitivity for higgsinos, gluinos and 3rd generation squarks. It will be interesting to see if a tension between Higgs results and SUSY limits arises or if there is a convergence as a result of the discovery of, i.e., light charginos and neutralinos. Last but not least, if the Higgs boson is found in the end to have an enhanced $h \rightarrow \gamma\gamma$ rate compared to the SM, implications for μ and M_2 are substantial, m_A is shifted to higher values and $\mu(Vh \rightarrow Vb\bar{b})$ is suppressed—allowing for some possibility of verifying consistency with or creating tension within the pMSSM.

2.9 Lilith: A New Public Tool for Constraining BSM Scenarios from Higgs Measurements

In the work presented in Sects. 2.5–2.8, the definition of the Higgs likelihood from the experimental results and its evaluation from a set of reduced couplings was done by a single FORTRAN code. As more and more Higgs results were released, we found it necessary to develop a new, modular program for evaluating the Higgs likelihood, where the user input—specifying the modifications to the properties of the 125 GeV Higgs boson—and the experimental input entering the likelihood are decoupled from the main code. Moreover, only measurements in the Gaussian approximation were taken into account in the FORTRAN code, while the full likelihood in the 2D plane ($\mu(\text{ggF} + \text{ttH}, Y)$, $\mu(\text{VBF} + \text{VH}, Y)$) recently became available for some final states Y ($\gamma\gamma$, WW^* and ZZ^* for ATLAS [57–59], $\gamma\gamma$ for CMS [43]). Finally, Higgs measurements are relevant for constraining a large variety of new physics models, while it is not trivial to define a good approximation to the Higgs likelihood.

This motivated us working on a public modular tool for applying the Higgs constraints on models of new physics. In collaboration with J  r  my Bernon, another PhD student at the LPSC Grenoble, the development of a Python program with this aim, called `Lilith`, started at the end of 2013. The public release of the program and of its associated manual is in preparation [263], but a beta version can already be found at [264]. In addition to being a seductive female demon, `Lilith` stands for “light likelihood fit for the Higgs”. It is designed as a light and user-friendly program, where user and experimental input are stored in XML files which are easy to modify. The experimental results shipped with the program consist mostly in signal strengths in the theory space, when available, as was used in Sects. 2.5–2.8. This can easily be extended with any experimental result given in terms of signal strengths. Below we briefly summarize the main features of `Lilith`.

`Lilith` works with two types of user inputs, provided in the form of XML files. A first possibility is to provide directly signal strengths in the theory space (i.e., in terms of $\mu(X, Y)$ with X and Y being production and decay modes of the SM Higgs). This is relevant if these are pre-calculated quantities, or if the user prefers to compute signal strengths himself/herself. Alternatively, the user can provide as input to `Lilith` a list of reduced couplings, again in XML format. This list may or may not contain reduced couplings to gluons and photons; if not provided, they will be internally calculated from the reduced couplings to SM particles. The set of reduced couplings is used by the program to compute signal strengths in the theory space, either using analytic formulas at leading order or using grids for the production cross sections and decay widths, as function of the reduced couplings, taking into account (N)NLO QCD corrections as obtained from `HIGLU` [29, 111, 112], `VBFNLO` [265] and `HDECAY` [29, 30]. In all cases (input in terms of signal strengths or reduced couplings), multi-particle labels are defined in order to simplify and improve readability of the input. For example, “VVH” is the shortcut for a common scaling of the WH, ZH and VBF production modes, and “ff” can be used to rescale all fermionic couplings or decays in the same way.

The experimental results are stored in a database consisting of XML files (one per measurement). When `LiliTh` is called, a list of experimental results to be considered (i.e., a list of XML files) should be given. The program was designed to handle a variety of experimental input given in terms of signal strengths in a transparent way. First, measurements can be provided in the Gaussian approximation, either in 1D or in 2D. For a 1D measurement, the central value and the uncertainty at 68 % CL should be provided, while for a 2D measurement the five parameters that appear in Eq. (2.14) should be provided. Second, measurements beyond the Gaussian approximation can be used as input to the program, again in 1D or in 2D. In the 1D case, a grid making the correspondence between signal strength and likelihood values should be given; the same thing can be done in the 2D case by provided a 2D grid of signal strengths and their associated likelihood values. This information is then interpolated internally by the program for evaluating the likelihood. Note that the experimental results given as input may or may not correspond to signal strengths in the theory plane. It is always possible to associate efficiencies for different production and/or decay modes to a measurement, making it possible to give as input any kind of measurement expressed in terms of signal strengths.

The primary output of the program is a likelihood value for the tested scenario. An evaluation of the p -value is also given from a naive estimate of the number of degrees of freedom. The functionalities of `LiliTh` can easily be integrated into any Python code by importing `LiliTh` as a library; examples are provided in the beta version [264]. The integration of `LiliTh` into a C and C++ code has also been developed and is used for integrating the program into `micrOMEGAS` [170]. Compared to system calls, calling `LiliTh` internally as a library has the advantage of being much lighter since the initialization of the program is only done once. This is particularly relevant in the case of large scans. For couplings fits, the use of minimization algorithms such as those present in MINUIT [127] is relevant for deriving constraints. This can easily be done in Python by using, i.e., `iminuit` [266] (a Python module that passes low-level MINUIT functionality to Python functions).

More details on the structure of `LiliTh` and instructions on how to use the program are given on the webpage [264]. It includes explicit examples for the two input modes and explanations for running `LiliTh` as a library in Python, for which examples are shipped with the beta version.

2.10 Some Thoughts on the Future of Higgs Measurements and Likelihoods

In this chapter, we derived an approximation to the Higgs likelihood based on signal strengths in the theory plane, most notably from the information given by the ATLAS and CMS collaborations in the $(\mu(\text{ggF} + \text{ttH}), \mu(\text{VBF} + \text{VH}))$ plane for $Y = \gamma\gamma, ZZ^*, WW^*, b\bar{b}$, and $\tau\tau$. This approach, presented in Sect. 2.4, was shown to provide a good approximation to the full likelihood in fits to reduced Higgs

couplings in Sect. 2.6, and was used to constrain new physics in Sects. 2.5–2.8 in the context of effective parameterizations or concrete extensions of the SM. The definition of the approximate Higgs likelihood was extended and refined in `Lilith`, a new public tool that evaluates the likelihood for modified properties of the 125 GeV Higgs boson using the latest information given by the experimental collaborations, as was presented in Sect. 2.9.

As we saw, the full likelihood in the 2D plane $(\mu(\text{ggF} + \text{ttH}, Y), \mu(\text{VBF} + \text{VH}, Y))$ has already been provided by the experimental collaborations for some final states. Hopefully, this information will be released systematically during Run II of the LHC and provided in a numerical form. There are however limitations when defining our approximation to the full Higgs likelihood from these 2D planes. It is therefore interesting to think of new ways of presenting the LHC Higgs results in the future. This was the motivation for the note “On the presentation of the LHC Higgs Results”, Ref. [267], to which I actively contributed. This note was submitted to arXiv on July 22, 2013, and originated from the workshops “Likelihoods for the LHC Searches”, 21–23 January 2013 at CERN, “Implications of the 125 GeV Higgs Boson”, 18–22 March 2013 at LPSC Grenoble, and from the 2013 Les Houches “Physics at TeV Colliders” workshop. This was built upon the recommendations given in the “Les Houches Recommendations for the Presentation of LHC Results” [128], which stressed the importance of providing all relevant information, including the best-fit signal strengths, on a channel-by-channel basis for the independent production and decay processes. In this section, some of the discussion present in Ref. [267] will be reproduced.

2.10.1 Signal Strengths

First, let us go back to the likelihoods presented in the $(\mu(\text{ggF} + \text{ttH}, Y), \mu(\text{VBF} + \text{VH}, Y))$ plane. In the future, production of the Higgs boson in association with a top quark pair will be probed with a much better precision, making it necessary to disentangle $\mu(\text{ggF}, Y)$ from $\mu(\text{ttH}, Y)$. Moreover, even if rescaling the VBF, WH and ZH production mechanisms by a common factor is theoretically justified in models with custodial symmetry, this might not exactly hold and one might want to check precisely the extent to which custodial symmetry can be tested in a global Higgs coupling fit. Eventually, we want to test ggF, ttH, VBF, ZH and WH separately, which means that we need a more detailed break down of the channels beyond the 2D plane.

The optimum would of course be to have the full statistical model available, and methods and tools are indeed being developed [268] to make this feasible, i.e., in the form of `ROOT` workspaces. However, it may still take a while until likelihoods will indeed be published in this way. We would therefore like to advocate as a compromise that the experiments give the likelihood for each final state Y as a function of a full set of production modes, that is to say, in the

$$(m_H, \mu_{\text{ggF}}, \mu_{\text{ttH}}, \mu_{\text{VBF}}, \mu_{\text{ZH}}, \mu_{\text{WH}}) \quad (2.99)$$

parameter space. By getting the likelihood function in this form for each decay mode, a significant step could be taken towards a more precise fit in the context of a given BSM theory. Note that the signal strengths' dependence on m_H is especially important for the high-resolution channels ($\gamma\gamma$ and ZZ , also $Z\gamma$ in the future). While the signal strengths seem to form a plateau in the case of $H \rightarrow \gamma\gamma$ (at least in ATLAS), there is a very sizable change in the $H \rightarrow ZZ$ channel if m_H is changed by 1 or 2 GeV. The likelihood could be communicated either as a standalone computer library or as a large grid data file. This choice is mostly meant to be an intermediate step between a full effective Lagrangian parameterization (which would be difficult to communicate) and simple 2D parameterizations which unfortunately do not cover all the theoretical possibilities.

Of course, approximations still have to be made in order to reconstruct a global Higgs likelihood from this six-dimensional information, even in the case of a simple scaling of the SM production cross sections and branching fractions. While all correlations are included for a given decay mode Y in a given experiment, the global likelihood is simply defined as the product of the individual 6D likelihoods (analogously to Eq. (2.15)), meaning that all experimental and theoretical correlations between different final states Y (or the same final state Y between ATLAS and CMS) are neglected. This is expected to become more and more problematic as measurements become limited by systematic uncertainties (see, i.e., Ref. [269]). This includes experimental correlations (for instance, from the jet energy scale and resolution) and theoretical uncertainties on the SM predictions of the cross sections and branching fractions (the dominant one being gluon fusion, for which the uncertainties are currently estimated by the LHC Higgs Cross Section Working Group to be $^{+7.2}_{-7.8}\%$ and $^{+7.5}_{-6.9}\%$ at $m_H = 125.5$ GeV, from the variation of the QCD scale and uncertainties on $\text{PDF}+\alpha_s$, respectively [22]). Moreover, searches are not completely independent. For instance, $H \rightarrow WW^*$ events contribute to the signal in the search for $H \rightarrow \tau\tau$ [45]; also, in the search for $H \rightarrow b\bar{b}$ produced in association with a top-quark pair, there can be significant contributions from other decay modes (see Appendix 3 in Ref. [49]), leading to correlations between the individual 6D likelihoods.

In the Gaussian approximation, the problem of missing correlations can be solved if the $n \times n$ covariance matrix V (see Eq. (2.10)) is provided by the experiments, either for the n individual measurements or, even better and simpler, in theory space for the $n = n_X n_Y$ different $\mu(X, Y)$. In order to have all correlations, this covariance matrix V should be published jointly by the ATLAS and CMS collaborations after combination of their results. In this simple and powerful approach, there are however limitations when constraining theories with the same coupling structure as the SM. First, the covariance matrix V would be given at a fixed Higgs mass. It is possible to overcome this problem simply by publishing several covariance matrices corresponding to different Higgs masses (with, i.e., a step of $\Delta m_H = 250$ MeV). Second, the Gaussian approximation might be well justified with a very large statistical sample but is not an extremely good approximation with the current data,

as already discussed in Sect. 2.4. Third, in this approach all correlations would be included in the covariance matrix and it is not straightforward, in particular, to change the theoretical uncertainties in a consistent way.

As was mentioned in Sect. 2.4, there is no universal agreement on the treatment of theoretical uncertainties at the LHC, and it is time-dependent (it depends in particular on the status of the calculation of higher-order corrections and on the data included in the PDF sets). It would therefore be very valuable to be able to change it. Recently, an interesting proposal was made in this direction in Ref. [270]. Provided experimental collaborations publish likelihoods that are not profiled over a set of theoretical nuisance parameters of interest, but instead given for a fixed scenario, it is possible to build a “recoupled” likelihood incorporating these uncertainties at the later stage. This has the advantage of not being restricted to the Gaussian approximation. It would certainly be of great interest if the information in the 2D plane ($\mu(\text{ggF} + \text{ttH}, Y)$, $\mu(\text{VBF} + \text{VH}, Y)$), or even better in the 6D plane discussed above, could be given without profiling over the theoretical uncertainties on the Higgs signal. From the method presented in Ref. [270], one could then fully correlate the theoretical uncertainties between the different channels and experiments, and modify these uncertainties compared to what is done in ATLAS and CMS if wanted.

2.10.2 *Fiducial Cross Sections*

As we saw in Sect. 2.7, a simple scaling of production cross sections and decay branching fractions (relative to the SM) is not sufficient in situations in which the kinematic distributions of the signal depend on model parameters. Specifically, one must account for the change in the signal selection efficiency. In order to address this broader class of theories, we advocate the measurement of fiducial cross sections for specific final states, i.e. cross sections, whether total or differential, for specific final states within the phase space defined by the experimental selection and acceptance cuts. This is meant in addition to, not instead of, fits for signal strength modifiers μ . Indeed, the (largely model-independent) fiducial cross sections and signal strengths w.r.t. SM are complementary to each other and both provide very valuable information in their own right.

With the full dataset of the LHC Run I, measurements of fiducial cross sections with a precision of 20 % or so already became feasible in a number of channels. In fact, ATLAS has already made the first attempt and released fiducial cross sections for $H \rightarrow \gamma\gamma$ [271] and $H \rightarrow ZZ^*$ [272] (preliminary). Fiducial cross section measurements require no model-dependent extrapolations to the full phase space, nor do they acquire additional theoretical uncertainty associated with such extrapolations. With carefully defined “fiducial volumes”, the model-dependence of signal efficiencies within such “fiducial volumes” can also be minimized so as to make it smaller than the overall experimental uncertainties. For example, cuts on lepton transverse momenta can be raised well above the knee of the efficiency plateau—this would minimize the impact of possible variations in leptons’ p_T -spectra on the

overall signal efficiency. Including isolation of leptons into the “fiducial volume” definition would help minimize the sensitivity of a measured fiducial cross section on assumptions about the jet activity in signal events. In some cases this is more difficult, for instance when the fiducial volume is defined by a cut on missing transverse energy, which often introduces sensitivity to the topology of the event. In situations where there is residual model-dependence in the fiducial efficiency, a service such as RECAST [273] provided by the collaborations for explicitly calculating the fiducial efficiency would be of great value.

Fiducial cross sections, both total and differential, are standard measurements in high energy physics and for some processes are the only experimental cross sections available. For example, J/ψ and Υ production cross section measurements at hadron colliders are always performed in some specified “fiducial volumes”. This has allowed for a variety of models, many of which appeared or were substantially updated *after* the measurements had been made, to be confronted with the fixed experimental results. In the context of Higgs boson physics, the fiducial cross sections can be categorized according to:

- “target” decay mode, i.e., $H \rightarrow ZZ \rightarrow 4\ell$, $H \rightarrow \gamma\gamma$, $H \rightarrow WW \rightarrow \ell\nu\ell\nu$, *etc.*;
- “target” production mechanism signatures, i.e., (VBF-like jj)+ H , $(\ell\ell) + H$, $(\ell + E_T^{\text{mis}}) + H$, $(E_T^{\text{mis}}) + H$, (V-like jj)+ H , *etc.*;
- and signal purity, i.e., 0-jet, 1-jet, high-mass VBF-like jj , low-mass VBF-like jj , *etc.*

Fiducial cross sections can be interpreted in the context of whatever theoretical model, provided it is possible to compute its predictions for the fiducial cross section at hand (i.e., if it is possible to include experimental selection/cuts into the model). Typically, if the cuts defining “fiducial volume” can be implemented in a MC generator, this is rather straightforward. Therefore, complicated “fiducial volume” criteria (i.e. MVA-based) are not well suited, unless the MVA function is provided and depends only on kinematic information available at the generator level. Some reduction in signal sensitivity due to simplifications in the event selection and due to possibly tighter cuts (to minimize the dependence of a signal efficiency on model assumptions as discussed above) is an acceptable price.

If these requirements for “fiducial volume” definitions are satisfied, then theoretical parameters of interest can be extracted from a fit to the measured cross sections. As more than one fiducial cross section become available, to make a proper fit for parameters of interest, it is important that experiments provide a complete covariance matrix of uncertainties between the measured fiducial cross sections.

The ultimate measurements of an “over-defined” set of fiducial cross sections σ_i^{fid} can be unravelled into total cross sections associated with specific production mechanisms σ_j^{tot} via a fit of the following set of linear equations:

$$\sigma_i^{\text{fid}} = \sum_j A_{ij}^{\text{th}} \times \sigma_j^{\text{tot}}, \quad (2.100)$$

where A_{ij}^{th} are theoretical acceptances of “fiducial volumes”, in which fiducial cross sections σ_i^{fid} are measured.

The beauty of the concept of fiducial cross sections is that *experimental* uncertainties associated with measurements of fiducial cross sections σ_i^{fid} and *theoretical* uncertainties associated with “fiducial volume” acceptances A_{ij}^{th} are nicely factorized. Therefore, updates of theoretical acceptances/uncertainties or a confrontation of emerging new models with experimental results do not require a re-analysis of experimental data. One can also treat the total cross sections σ_j^{tot} as nuisance parameters and fit data for theoretical acceptances A_{ij}^{th} (i.e., a 0-jet veto acceptance), if it is these quantities that one is primarily interested in.

Finally, we note that measurements of differential fiducial cross sections, when they become possible, will be even more powerful (in comparison to just total exclusive fiducial cross sections) for scrutinizing the SM Lagrangian structure of the Higgs boson interactions, including tests for new tensorial couplings, non-standard production modes, determination of effective form factors, *etc.*

References

1. G. Aad et al., ATLAS Collaboration, Observation of a new particle in the search for the standard model Higgs boson with the ATLAS detector at the LHC. Phys. Lett. B **716**, 1–29 (2012). [arXiv:1207.7214](https://arxiv.org/abs/1207.7214)
2. S. Chatrchyan et al., CMS Collaboration, Observation of a new boson at a mass of 125 GeV with the CMS experiment at the LHC. Phys. Lett. B **716**, 30–61 (2012). [arXiv:1207.7235](https://arxiv.org/abs/1207.7235)
3. F. Englert, R. Brout, Broken symmetry and the mass of gauge vector mesons. Phys. Rev. Lett. **13**, 321–323 (1964)
4. P.W. Higgs, Broken symmetries, massless particles and gauge fields. Phys. Lett. **12**, 132–133 (1964)
5. P.W. Higgs, Broken symmetries and the masses of gauge bosons. Phys. Rev. Lett. **13**, 508–509 (1964)
6. G. Guralnik, C. Hagen, T. Kibble, Global conservation laws and massless particles. Phys. Rev. Lett. **13**, 585–587 (1964)
7. P.W. Higgs, Spontaneous symmetry breakdown without massless bosons. Phys. Rev. **145**, 1156–1163 (1966)
8. T. Kibble, Symmetry breaking in nonAbelian gauge theories. Phys. Rev. **155**, 1554–1561 (1967)
9. M.S. Chanowitz, *Strong WW Scattering at the End of the 90’s: Theory and Experimental Prospects*. hep-ph/9812215
10. S. Schael et al., ALEPH, DELPHI, L3, OPAL, SLD, LEP Electroweak Working Group, SLD Electroweak Group, SLD Heavy Flavour Group Collaboration, Precision electroweak measurements on the Z resonance. Phys. Rep. **427** (2006) 257–454. hep-ex/0509008
11. The LEP Electroweak Working Group. <http://lepewwg.web.cern.ch/LEPEWWG/>
12. H. Flacher, M. Goebel, J. Haller, A. Hocker, K. Monig et al., Revisiting the global electroweak fit of the standard model and beyond with Gfit. Eur. Phys. J. C **60**, 543–583 (2009). [arXiv:0811.0009](https://arxiv.org/abs/0811.0009)
13. M. Baak, M. Goebel, J. Haller, A. Hoecker, D. Kennedy et al., The electroweak fit of the standard model after the discovery of a new boson at the LHC. Eur. Phys. J. C **72**, 2205 (2012). [arXiv:1209.2716](https://arxiv.org/abs/1209.2716)

14. M. Baak, J. Cuth, J. Haller, A. Hoecker, R. Kogler, et al., *The Global Electroweak Fit at NNLO and Prospects for the LHC and ILC*. [arXiv:1407.3792](#)
15. R. Barate et al., LEP Working Group for Higgs boson searches, ALEPH, DELPHI, L3, OPAL Collaboration, Search for the standard model Higgs boson at LEP. *Phys. Lett. B* **565** (2003) 61–75. [hep-ex/0306033](#)
16. T. Aaltonen et al., CDF, D0 Collaboration, Higgs boson studies at the Tevatron. *Phys. Rev. D* **88**, 052014 (2013). [arXiv:1303.6346](#)
17. T. Hambye, K. Riesselmann, Matching conditions and Higgs mass upper bounds revisited. *Phys. Rev. D* **55**, 7255–7262 (1997). [hep-ph/9610272](#)
18. G. Degrandi, S. Di Vita, J. Elias-Miro, J.R. Espinosa, G.F. Giudice et al., Higgs mass and vacuum stability in the standard model at NNLO. *JHEP* **1208**, 098 (2012). [arXiv:1205.6497](#)
19. D. Buttazzo, G. Degrandi, P.P. Giardinio, G.F. Giudice, F. Sala et al., Investigating the near-criticality of the Higgs boson. *JHEP* **1312**, 089 (2013). [arXiv:1307.3536](#)
20. S. Alekhin, A. Djouadi, S. Moch, The top quark and Higgs boson masses and the stability of the electroweak vacuum. *Phys. Lett. B* **716**, 214–219 (2012). [arXiv:1207.0980](#)
21. A. Djouadi, The anatomy of electro-weak symmetry breaking. I: the Higgs boson in the standard model. *Phys. Rep.* **457**, 1–216 (2008). [hep-ph/0503172](#)
22. S. Heinemeyer et al., LHC Higgs Cross Section Working Group Collaboration, *Handbook of LHC Higgs Cross Sections: 3. Higgs Properties*, [arXiv:1307.1347](#)
23. J. Baglio, A. Djouadi, Higgs production at the LHC. *JHEP* **1103**, 055 (2011). [arXiv:1012.0530](#)
24. C. Delaunay, T. Golling, G. Perez, Y. Soreq, *Charming the Higgs*, [arXiv:1310.7029](#)
25. ATLAS Collaboration, *Physics at a High-Luminosity LHC with ATLAS (Update)*, ATL-PHYS-PUB-2012-004
26. CMS Collaboration, *CMS at the High-Energy Frontier Contribution to the Update of the European Strategy for Particle Physics*, CMS-NOTE-2012-006
27. S. Chatrchyan et al., CMS Collaboration, Observation of a new boson with mass near 125 GeV in pp collisions at $\sqrt{s} = 7$ and 8 TeV. *JHEP* **1306**, 081 (2013). [arXiv:1303.4571](#)
28. J. Beringer et al., Particle Data Group Collaboration, Review of particle physics (RPP). *Phys. Rev. D* **86**, 010001 (2012)
29. M. Spira, HIGLU and HDECAY: programs for Higgs boson production at the LHC and Higgs boson decay widths. *Nucl. Instrum. Methods A* **389**, 357–360 (1997). [hep-ph/9610350](#)
30. A. Djouadi, J. Kalinowski, M. Spira, HDECAY: a program for Higgs boson decays in the standard model and its supersymmetric extension. *Comput. Phys. Commun.* **108**, 56–74 (1998). [hep-ph/9704448](#)
31. G. Aad et al., ATLAS Collaboration, *Measurement of the Higgs Boson Mass from the $H \rightarrow \gamma\gamma$ and $H \rightarrow ZZ^* \rightarrow 4\ell$ Channels with the ATLAS Detector Using 25 fb⁻¹ of pp Collision Data*, [arXiv:1406.3827](#)
32. CMS Collaboration, *Precise Determination of the Mass of the Higgs Boson and Studies of the Compatibility of Its Couplings with the Standard Model*, CMS-PAS-HIG-14-009
33. CMS Collaboration, *Measurements of the Properties of the New Boson with a Mass Near 125 GeV*, CMS-PAS-HIG-13-005
34. ATLAS Collaboration, *Combined Measurements of the Mass and Signal Strength of the Higgs-like Boson with the ATLAS Detector Using up to 25 fb⁻¹ of Proton–Proton Collision Data*, ATLAS-CONF-2013-014
35. G. Aad et al., ATLAS Collaboration, Search for Higgs boson decays to a photon and a Z boson in pp collisions at $\sqrt{s} = 7$ and 8 TeV with the ATLAS detector. *Phys. Lett. B* **732**, 8–27 (2014). [arXiv:1402.3051](#)
36. S. Chatrchyan et al., CMS Collaboration, Search for a Higgs boson decaying into a Z and a photon in pp collisions at $\sqrt{s} = 7$ and 8 TeV. *Phys. Lett. B* **726**, 587–609 (2013). [arXiv:1307.5515](#)
37. ATLAS Collaboration, *Updated Coupling Measurements of the Higgs Boson with the ATLAS Detector Using up to 25 fb⁻¹ of Proton–Proton Collision Data*, ATLAS-CONF-2014-009
38. G. Aad et al., ATLAS Collaboration, Evidence for the spin-0 nature of the Higgs boson using ATLAS data. *Phys. Lett. B* **726**, 120–144 (2013). [arXiv:1307.1432](#)

39. S. Chatrchyan et al., CMS Collaboration, Study of the mass and spin-parity of the Higgs boson candidate via its decays to Z boson pairs. Phys. Rev. Lett. **110**, 081803 (2013). [arXiv:1212.6639](#)
40. S. Chatrchyan et al., CMS Collaboration, *Measurement of the Properties of a Higgs Boson in the Four-Lepton Final State*. [arXiv:1312.5353](#)
41. S. Chatrchyan et al., CMS Collaboration, Measurement of Higgs boson production and properties in the WW decay channel with leptonic final states. JHEP **1401**, 096 (2014). [arXiv:1312.1129](#)
42. G. Aad et al., ATLAS Collaboration, Measurements of Higgs boson production and couplings in Diboson final states with the ATLAS detector at the LHC. Phys. Lett. B **726**, 88–119 (2013). [arXiv:1307.1427](#)
43. V. Khachatryan et al., CMS Collaboration, *Observation of the Diphoton Decay of the Higgs Boson and Measurement of Its Properties*. [arXiv:1407.0558](#)
44. ATLAS Collaboration, *Evidence for Higgs Boson Decays to the $\tau^+\tau^-$ Final State with the ATLAS Detector*, ATLAS-CONF-2013-108
45. S. Chatrchyan et al., CMS Collaboration, *Evidence for the 125 GeV Higgs Boson Decaying to a Pair of τ Leptons*. [arXiv:1401.5041](#)
46. ATLAS Collaboration, *Search for the $b\bar{b}$ Decay of the Standard Model Higgs Boson in Associated (W/Z)H Production with the ATLAS Detector*, ATLAS-CONF-2013-079
47. S. Chatrchyan et al., CMS Collaboration, Search for the standard model Higgs boson produced in association with a W or a Z boson and decaying to bottom quarks. Phys. Rev. D **89**, 012003 (2014). [arXiv:1310.3687](#)
48. T. Aaltonen et al., CDF, D0 Collaboration, Evidence for a particle produced in association with weak bosons and decaying to a bottom-antibottom quark pair in Higgs boson searches at the Tevatron. Phys. Rev. Lett. **109**, 071804 (2012). [arXiv:1207.6436](#)
49. ATLAS Collaboration, *Search for the Standard Model Higgs Boson Produced in Association with Top Quarks and Decaying Into $b\bar{b}$ in pp Collisions at $\sqrt{s} = 8$ TeV with the ATLAS Detector at the LHC*, ATLAS-CONF-2014-011
50. ATLAS Collaboration, *Search for $H \rightarrow \gamma\gamma$ Produced in Association with Top Quarks and Constraints on the Top Quark-Higgs Boson Yukawa Coupling Using Data taken at 7 TeV and 8 TeV with the ATLAS Detector*, ATLAS-CONF-2014-043
51. <https://twiki.cern.ch/twiki/bin/view/CMSPublic/tHCombinationTWiki>
52. ATLAS Collaboration, *Measurements of the Properties of the Higgs-like Boson in the Two Photon Decay Channel with the ATLAS Detector Using 25 fb^{-1} of Proton-Proton Collision Data*, ATLAS-CONF-2013-012
53. ATLAS Collaboration, *Measurements of the Properties of the Higgs-like Boson in the $WW^{(*)} \rightarrow \ell\nu\ell\nu$ Decay Channel with the ATLAS Detector Using 25 fb^{-1} of Proton-Proton Collision Data*, ATLAS-CONF-2013-030
54. ATLAS Collaboration, *Measurements of the Properties of the Higgs-like Boson in the Four Lepton Decay Channel with the ATLAS Detector Using 25 fb^{-1} of Proton-Proton Collision Data*, ATLAS-CONF-2013-013
55. M.E. Peskin, T. Takeuchi, A new constraint on a strongly interacting Higgs sector. Phys. Rev. Lett. **65**, 964–967 (1990)
56. M.E. Peskin, T. Takeuchi, Estimation of oblique electroweak corrections. Phys. Rev. D **46**, 381–409 (1992)
57. ATLAS full 2D likelihood for $H \rightarrow \gamma\gamma$. doi:[10.7484/INSPIREHEP.DATA.A78C.HK44](#)
58. ATLAS full 2D likelihood for $H \rightarrow ZZ^*$. doi:[10.7484/INSPIREHEP.DATA.RF5P.6M3K](#)
59. ATLAS full 2D likelihood for $H \rightarrow WW^*$. doi:[10.7484/INSPIREHEP.DATA.26B4.TY5F](#)
60. CMS Collaboration, *Updated Measurements of the Higgs Boson at 125 GeV in the Two Photon Decay Channel*, CMS-PAS-HIG-13-001
61. CMS Collaboration, *Properties of the Higgs-like Boson in the Decay $H \rightarrow ZZ \rightarrow 4\ell$ in pp Collisions at $\sqrt{s} = 7$ and 8 TeV*, CMS-PAS-HIG-13-002
62. ATLAS Collaboration, *Observation and Study of the Higgs Boson Candidate in the Two Photon Decay Channel with the ATLAS Detector at the LHC*, ATLAS-CONF-2012-168

63. Status of the LHC and Experiments, CERN seminars, 13 Dec 2012. <http://indico.cern.ch/conferenceDisplay.py?confId=219381>
64. CMS Collaboration, *Combination of Standard Model Higgs Boson Searches and Measurements of the Properties of the New Boson with a Mass Near 125 GeV*, CMS-PAS-HIG-12-045
65. Hadron Collider Physics Symposium 2012 (HCP 2012), 12–16 Nov 2012, Kyoto, Japan. <http://www.icepp.s.u-tokyo.ac.jp/hcp2012/>
66. CMS Collaboration, *Evidence for a New State Decaying into Two Photons in the Search for the Standard Model Higgs Boson in pp Collisions*, CMS-PAS-HIG-12-015
67. G. Belanger, B. Dumont, U. Ellwanger, J. Gunion, S. Kraml, Higgs couplings at the end of 2012. JHEP **1302**, 053 (2013). [arXiv:1212.5244](https://arxiv.org/abs/1212.5244)
68. D. Carmi, A. Falkowski, E. Kuflik, T. Volansky, Interpreting LHC Higgs results from natural new physics perspective. JHEP **1207**, 136 (2012). [arXiv:1202.3144](https://arxiv.org/abs/1202.3144)
69. A. Azatov, R. Contino, J. Galloway, Model-independent bounds on a light Higgs. JHEP **1204**, 127 (2012). [arXiv:1202.3415](https://arxiv.org/abs/1202.3415)
70. J. Espinosa, C. Grojean, M. Muhlleitner, M. Trott, Fingerprinting Higgs suspects at the LHC. JHEP **1205**, 097 (2012). [arXiv:1202.3697](https://arxiv.org/abs/1202.3697)
71. M. Klute, R. Lafaye, T. Plehn, M. Rauch, D. Zerwas, Measuring Higgs couplings from LHC data. Phys. Rev. Lett. **109**, 101801 (2012). [arXiv:1205.2699](https://arxiv.org/abs/1205.2699)
72. A. Azatov, S. Chang, N. Craig, J. Galloway, Higgs fits preference for suppressed down-type couplings: implications for supersymmetry. Phys. Rev. D **86**, 075033 (2012). [arXiv:1206.1058](https://arxiv.org/abs/1206.1058)
73. D. Carmi, A. Falkowski, E. Kuflik, T. Volansky, Interpreting the Higgs. Frascati. Phys. Ser. **57**, 315–322 (2013). [arXiv:1206.4201](https://arxiv.org/abs/1206.4201)
74. I. Low, J. Lykken, G. Shaughnessy, Have we observed the Higgs (Imposter)? Phys. Rev. D **86**, 093012 (2012). [arXiv:1207.1093](https://arxiv.org/abs/1207.1093)
75. T. Corbett, O. Eboli, J. Gonzalez-Fraile, M. Gonzalez-Garcia, Constraining anomalous Higgs interactions. Phys. Rev. D **86**, 075013 (2012). [arXiv:1207.1344](https://arxiv.org/abs/1207.1344)
76. P.P. Giardinò, K. Kannike, M. Raidal, A. Strumia, Is the resonance at 125 GeV the Higgs boson? Phys. Lett. B **718**, 469–474 (2012). [arXiv:1207.1347](https://arxiv.org/abs/1207.1347)
77. J. Ellis, T. You, Global analysis of the Higgs candidate with mass $\tilde{125}$ GeV. JHEP **1209**, 123 (2012). [arXiv:1207.1693](https://arxiv.org/abs/1207.1693)
78. M. Montull, F. Riva, Higgs discovery: the beginning or the end of natural EWSB? JHEP **1211**, 018 (2012). [arXiv:1207.1716](https://arxiv.org/abs/1207.1716)
79. J. Espinosa, C. Grojean, M. Muhlleitner, M. Trott, First Glimpses at Higgs’ face. JHEP **1212**, 045 (2012). [arXiv:1207.1717](https://arxiv.org/abs/1207.1717)
80. D. Carmi, A. Falkowski, E. Kuflik, T. Volansky, J. Zupan, Higgs after the discovery: a status report. JHEP **1210**, 196 (2012). [arXiv:1207.1718](https://arxiv.org/abs/1207.1718)
81. S. Banerjee, S. Mukhopadhyay, B. Mukhopadhyaya, New Higgs interactions and recent data from the LHC and the Tevatron. JHEP **1210**, 062 (2012). [arXiv:1207.3588](https://arxiv.org/abs/1207.3588)
82. F. Bonnet, T. Ota, M. Rauch, W. Winter, Interpretation of precision tests in the Higgs sector in terms of physics beyond the standard model. Phys. Rev. D **86**, 093014 (2012). [arXiv:1207.4599](https://arxiv.org/abs/1207.4599)
83. T. Plehn, M. Rauch, Higgs couplings after the discovery. Europhys. Lett. **100**, 11002 (2012). [arXiv:1207.6108](https://arxiv.org/abs/1207.6108)
84. J.R. Espinosa, C. Grojean, V. Sanz, M. Trott, NSUSY fits. JHEP **1212**, 077 (2012). [arXiv:1207.7355](https://arxiv.org/abs/1207.7355)
85. D. Elander, M. Piai, The decay constant of the holographic techni-dilaton and the 125 GeV boson. Nucl. Phys. B **867**, 779–809 (2013). [arXiv:1208.0546](https://arxiv.org/abs/1208.0546)
86. A. Djouadi, Precision Higgs coupling measurements at the LHC through ratios of production cross sections. Eur. Phys. J. C **73**, 2498 (2013). [arXiv:1208.3436](https://arxiv.org/abs/1208.3436)
87. W. Altmannshofer, S. Gori, G.D. Kribs, A minimal flavor violating 2HDM at the LHC. Phys. Rev. D **86**, 115009 (2012). [arXiv:1210.2465](https://arxiv.org/abs/1210.2465)
88. B.A. Dobrescu, J.D. Lykken, Coupling spans of the Higgs-like boson. JHEP **1302**, 073 (2013). [arXiv:1210.3342](https://arxiv.org/abs/1210.3342)
89. S. Chang, S.K. Kang, J.-P. Lee, K.Y. Lee, S.C. Park et al., Comprehensive study of two Higgs doublet model in light of the new boson with mass around 125 GeV. JHEP **1305**, 075 (2013). [arXiv:1210.3439](https://arxiv.org/abs/1210.3439)

90. G. Moreau, Constraining extra-fermion(s) from the Higgs boson data. *Phys. Rev. D* **87**, 015027 (2013). [arXiv:1210.3977](#)
91. G. Cacciapaglia, A. Deandrea, G.D. La Rochelle, J.-B. Flament, Higgs couplings beyond the standard model. *JHEP* **1303**, 029 (2013). [arXiv:1210.8120](#)
92. P. Bechtle, S. Heinemeyer, O. Stål, T. Stefaniak, G. Weiglein et al., MSSM interpretations of the LHC discovery: light or heavy Higgs? *Eur. Phys. J. C* **73**, 2354 (2013). [arXiv:1211.1955](#)
93. T. Corbett, O. Eboli, J. Gonzalez-Fraile, M. Gonzalez-Garcia, Robust determination of the Higgs couplings: power to the data. *Phys. Rev. D* **87**, 015022 (2013). [arXiv:1211.4580](#)
94. E. Masso, V. Sanz, Limits on anomalous couplings of the Higgs to electroweak gauge bosons from LEP and LHC. *Phys. Rev. D* **87**(3) (2013) 033001, [arXiv:1211.1320](#)
95. A. Azatov, J. Galloway, Electroweak symmetry breaking and the Higgs boson: confronting theories at colliders. *Int. J. Mod. Phys. A* **28**, 1330004 (2013). [arXiv:1212.1380](#)
96. P. P. Giardino, K. Kannike, I. Masina, M. Raidal, A. Strumia, *The Universal Higgs fit*. [arXiv:1303.3570](#)
97. A. Falkowski, F. Riva, A. Urbano, Higgs at last. *JHEP* **1311**, 111 (2013). [arXiv:1303.1812](#)
98. T. Alanne, S. Di Chiara, K. Tuominen, LHC data and aspects of new physics. *JHEP* **1401**, 041 (2014). [arXiv:1303.3615](#)
99. A. Djouadi, G. Moreau, *The Couplings of the Higgs Boson and Its CP Properties from its of the Signal Strengths and Their Ratios at the 7+8 TeV LHC*. [arXiv:1303.6591](#)
100. T. Corbett, O. Éboli, J. Gonzalez-Fraile, M. Gonzalez-Garcia, Determining triple gauge boson couplings from Higgs data. *Phys. Rev. Lett.* **111**(1) (2013), 011801, [arXiv:1304.1151](#)
101. G. Cacciapaglia, A. Deandrea, G. D. La Rochelle, J.-B. Flament, *Searching for a Lighter Higgs: Parametrisation and Sample Tests*. [arXiv:1311.5132](#)
102. P. Bechtle, S. Heinemeyer, O. Stål, T. Stefaniak, G. Weiglein, *Probing the Standard Model with Higgs Signal Rates from the Tevatron, the LHC and a future ILC*. [arXiv:1403.1582](#)
103. J. Baglio, A. Djouadi, R. Godbole, The apparent excess in the Higgs to di-photon rate at the LHC: new physics or QCD uncertainties? *Phys. Lett. B* **716**, 203–207 (2012). [arXiv:1207.1451](#)
104. ATLAS Collaboration, *Coupling Properties of the New Higgs-like Boson Observed with the ATLAS Detector at the LHC*, ATLAS-CONF-2012-127
105. J.R. Espinosa, M. Muhlleitner, C. Grojean, M. Trott, Probing for invisible Higgs decays with global Fits. *JHEP* **1209**, 126 (2012). [arXiv:1205.6790](#)
106. J.F. Gunion, Y. Jiang, S. Kraml, Could two NMSSM Higgs bosons be present near 125 GeV? *Phys. Rev. D* **86**, 071702 (2012). [arXiv:1207.1545](#)
107. P. Ferreira, R. Santos, H.E. Haber, J.P. Silva, Mass-degenerate Higgs bosons at 125 GeV in the two-Higgs-doublet model. *Phys. Rev. D* **87**(5), 055009 (2013). [arXiv:1211.3131](#)
108. J.F. Gunion, Y. Jiang, S. Kraml, Diagnosing degenerate Higgs bosons at 125 GeV. *Phys. Rev. Lett.* **110**, 051801 (2013). [arXiv:1208.1817](#)
109. CMS Collaboration, *Properties of the Observed Higgs-like Resonance Decaying into Two Photons*, CMS-PAS-HIG-13-016
110. A. David et al., LHC Higgs Cross Section Working Group Collaboration, *LHC HXSWG Interim Recommendations to Explore the Coupling Structure of a Higgs-like Particle*, [arXiv:1209.0040](#)
111. M. Spira, A. Djouadi, D. Graudenz, P. Zerwas, Higgs boson production at the LHC. *Nucl. Phys. B* **453**, 17–82 (1995). [hep-ph/9504378](#)
112. M. Spira, *HIGLU: A Program for the Calculation of the Total Higgs Production Cross-Section at Hadron Colliders Via Gluon Fusion Including QCD Corrections*. [hep-ph/9510347](#)
113. ATLAS Collaboration, *Updated Results and Measurements of Properties of the New Higgs-like Particle in the Four Lepton Decay Channel with the ATLAS Detector*, ATLAS-CONF-2012-169
114. ATLAS Collaboration, *An Update of Combined Measurements of the New Higgs-like Boson with High Mass Resolution Channels*, ATLAS-CONF-2012-170
115. ATLAS Collaboration, *Update of the $H \rightarrow WW^{(*)} \rightarrow e\nu\mu\nu$ Analysis with 13.0 fb^{-1} of $\sqrt{s} = 8\text{ TeV}$ Data Collected with the ATLAS Detector*, ATLAS-CONF-2012-158

116. ATLAS Collaboration, *Search for the Standard Model Higgs Boson Produced in Association with a Vector Boson and Decaying to Bottom Quarks with the ATLAS Detector*, ATLAS-CONF-2012-161
117. ATLAS Collaboration, *Search for the Standard Model Higgs Boson in $H \rightarrow \tau^+ \tau^-$ Decays in Proton–Proton Collisions with the ATLAS Detector*, ATLAS-CONF-2012-160
118. CMS Collaboration, *Updated Results on the New Boson Discovered in the Search for the Standard Model Higgs Boson in the $H \rightarrow WW \rightarrow 4\ell$ Channel in pp Collisions at $\sqrt{s} = 7$ and 8 TeV*, CMS-PAS-HIG-12-041
119. CMS Collaboration, *Search for SM Higgs in $WH \rightarrow WWW \rightarrow 3\ell 3\nu$* , CMS-PAS-HIG-12-039
120. CMS Collaboration, *Evidence for a Particle Decaying to $W^+ W^-$ in the Fully Leptonic Final State in a Standard Model Higgs Boson Search in pp Collisions at the LHC*, CMS-PAS-HIG-12-042
121. CMS Collaboration, *Search for the Standard Model Higgs Boson Produced in Association with W or Z Bosons, and Decaying to Bottom Quarks*, CMS-PAS-HIG-12-044
122. CMS Collaboration, *Search for Higgs Boson Production in Association with a Top Quark Pair in pp Collisions*, CMS-PAS-HIG-12-025
123. CMS Collaboration, *Search for the Standard Model Higgs Boson Decaying to Tau Pairs*, CMS-PAS-HIG-12-043
124. CMS Collaboration, *Search for the Standard Model Higgs Boson Decaying to Tau Pairs Produced in Association with a W or Z Boson*, CMS-PAS-HIG-12-051
125. A. Juste, *Standard Model Higgs boson searches at the Tevatron*, Talk at HCP2012, 15 Nov. 2012, Kyoto, Japan. <http://kds.kek.jp/conferenceDisplay.py?confId=9237>
126. Y. Enari, *$H \rightarrow b\bar{b}$ from Tevatron*, Talk at HCP2012, 14 Nov. 2012, Kyoto, Japan. <http://kds.kek.jp/conferenceDisplay.py?confId=10808>
127. F. James, M. Roos, Minuit: a system for function minimization and analysis of the parameter errors and correlations. *Comput. Phys. Commun.* **10**, 343–367 (1975)
128. S. Kraml, B. Allanach, M. Mangano, H. Prosper, S. Sekmen et al., Searches for new physics: Les Houches recommendations for the presentation of LHC results. *Eur. Phys. J. C* **72**, 1976 (2012). [arXiv:1203.2489](https://arxiv.org/abs/1203.2489)
129. <https://twiki.cern.ch/twiki/bin/view/LHCPhysics/CrossSections>
130. A. de Roeck, *Private Communication*
131. F.J. Petriello, Kaluza–Klein effects on Higgs physics in universal extra dimensions. *JHEP* **0205**, 003 (2002). [hep-ph/0204067](https://arxiv.org/abs/hep-ph/0204067)
132. G. Belanger, A. Belyaev, M. Brown, M. Kakizaki, A. Pukhov, Testing minimal universal extra dimensions using Higgs boson searches at the LHC. *Phys. Rev. D* **87**, 016008 (2013). [arXiv:1207.0798](https://arxiv.org/abs/1207.0798)
133. S. Biswas, E. Gabrielli, B. Mele, Single top and Higgs associated production as a probe of the Htt coupling sign at the LHC. *JHEP* **1301**, 088 (2013). [arXiv:1211.0499](https://arxiv.org/abs/1211.0499)
134. M. Farina, C. Grojean, F. Maltoni, E. Salvioni, A. Thamm, Lifting degeneracies in Higgs couplings using single top production in association with a Higgs boson. *JHEP* **1305**, 022 (2013). [arXiv:1211.3736](https://arxiv.org/abs/1211.3736)
135. A. Drozd, B. Grzadkowski, J.F. Gunion, Y. Jiang, Two-Higgs-doublet models and enhanced rates for a 125 GeV Higgs. *JHEP* **1305**, 072 (2013). [arXiv:1211.3580](https://arxiv.org/abs/1211.3580)
136. G. Branco, P. Ferreira, L. Lavoura, M. Rebelo, M. Sher et al., Theory and phenomenology of two-Higgs-doublet models. *Phys. Rept.* **516**, 1–102 (2012). [arXiv:1106.0034](https://arxiv.org/abs/1106.0034)
137. P. Teixeira-Dias, Higgs boson searches at LEP. *J. Phys. Conf. Ser.* **110**, 042030 (2008). [arXiv:0804.4146](https://arxiv.org/abs/0804.4146)
138. D. Choudhury, R. Islam, A. Kundu, Anomalous Higgs couplings as a window to new physics. *Phys. Rev. D* **88**(1) (2013), 013014, [arXiv:1212.4652](https://arxiv.org/abs/1212.4652)
139. G. Bhattacharyya, D. Das, P.B. Pal, Modified Higgs couplings and unitarity violation. *Phys. Rev. D* **87**, 011702 (2013). [arXiv:1212.4651](https://arxiv.org/abs/1212.4651)
140. G. Belanger, B. Dumont, U. Ellwanger, J. Gunion, S. Kraml, Status of invisible Higgs decays. *Phys. Lett. B* **723**, 340–347 (2013). [arXiv:1302.5694](https://arxiv.org/abs/1302.5694)

141. 48th Rencontres de Moriond, Electroweak Interactions and Unified Theories session, 2–9 Mar. 2012, La Thuile, Italy. <https://indico.in2p3.fr/conferenceDisplay.py?confId=7411>
142. 48th Rencontres de Moriond, QCD and High Energy Interactions Session, 9–16 Mar. 2013, La Thuile, Italy. <http://moriond.in2p3.fr/QCD/2013/MorQCD13Prog.html>
143. G. Belanger, B. Dumont, U. Ellwanger, J. Gunion, S. Kraml, Global fit to Higgs signal strengths and couplings and implications for extended Higgs sectors. *Phys. Rev. D* **88**, 075008 (2013). [arXiv:1306.2941](https://arxiv.org/abs/1306.2941)
144. B. Dumont, *Higgs Couplings after Moriond*. [arXiv:1305.4635](https://arxiv.org/abs/1305.4635)
145. P. Bechtle, S. Heinemeyer, O. Stål, T. Stefaniak, G. Weiglein, *HiggsSignals*: Confronting arbitrary Higgs sectors with measurements at the Tevatron and the LHC. *Eur. Phys. J. C* **74**, 2711 (2014). [arXiv:1305.1933](https://arxiv.org/abs/1305.1933)
146. ATLAS Collaboration, *Combined Coupling Measurements of the Higgs-like Boson with the ATLAS Detector Using up to 25 fb⁻¹ of Proton–Proton Collision Data*, ATLAS-CONF-2013-034
147. CMS Collaboration, *Search for $t\bar{t}H$ Production in Events with $H \rightarrow \gamma\gamma$ at $\sqrt{s} = 8$ TeV Collisions*, CMS-PAS-HIG-13-015
148. CMS Collaboration, *Update on the Search for the Standard Model Higgs Boson in pp Collisions at the LHC Decaying to W^+W^- in the Fully Leptonic Final State*, CMS-PAS-HIG-13-003
149. CMS Collaboration, *Search for the Standard Model Higgs Boson in $WH \rightarrow WWW \rightarrow 3\ell 3\nu$ Decays*, CMS-PAS-HIG-13-009
150. CMS Collaboration, *Search for the Standard Model Higgs Boson Produced in Association with W or Z Bosons, and Decaying to Bottom Quarks (LHCP 2013)*, CMS-PAS-HIG-13-012
151. CMS Collaboration, *Search for the Standard-Model Higgs Boson Decaying to Tau Pairs in Proton–Proton Collisions at $\sqrt{s} = 7$ and 8 TeV*, CMS-PAS-HIG-13-004
152. ATLAS Collaboration, *Search for Invisible Decays of a Higgs Boson produced in Association with a Z Boson in ATLAS*, ATLAS-CONF-2013-011
153. M.S. Carena, D. Garcia, U. Nierste, C.E. Wagner, Effective Lagrangian for the $\bar{t}bH^+$ interaction in the MSSM and charged Higgs phenomenology. *Nucl. Phys. B* **577**, 88–120 (2000). [hep-ph/9912516](https://arxiv.org/abs/hep-ph/9912516)
154. H. Eberl, K. Hidaka, S. Kraml, W. Majerotto, Y. Yamada, Improved SUSY QCD corrections to Higgs boson decays into quarks and squarks. *Phys. Rev. D* **62**, 055006 (2000). [hep-ph/9912463](https://arxiv.org/abs/hep-ph/9912463)
155. H.E. Logan, M.-A. Roy, Higgs couplings in a model with triplets. *Phys. Rev. D* **82**, 115011 (2010). [arXiv:1008.4869](https://arxiv.org/abs/1008.4869)
156. A. Falkowski, S. Rychkov, A. Urbano, What if the Higgs couplings to W and Z bosons are larger than in the standard model? *JHEP* **1204**, 073 (2012). [arXiv:1202.1532](https://arxiv.org/abs/1202.1532)
157. D. Zeppenfeld, R. Kinnunen, A. Nikitenko, E. Richter-Was, Measuring Higgs boson couplings at the CERN LHC. *Phys. Rev. D* **62**, 013009 (2000). [hep-ph/0002036](https://arxiv.org/abs/hep-ph/0002036)
158. A. Djouadi, R. Kinnunen, E. Richter-Was, H. Martyn, K. Assamagan, et al., *The Higgs Working Group: Summary Report*. [hep-ph/0002258](https://arxiv.org/abs/hep-ph/0002258)
159. M. Duhrssen, S. Heinemeyer, H. Logan, D. Rainwater, G. Weiglein et al., Extracting Higgs boson couplings from CERN LHC data. *Phys. Rev. D* **70**, 113009 (2004). [hep-ph/0406323](https://arxiv.org/abs/hep-ph/0406323)
160. C. Burgess, M. Pospelov, T. ter Veldhuis, The minimal model of nonbaryonic dark matter: a singlet scalar. *Nucl. Phys. B* **619**, 709–728 (2001). [hep-ph/0011335](https://arxiv.org/abs/hep-ph/0011335)
161. S. Kanemura, S. Matsumoto, T. Nabeshima, N. Okada, Can WIMP dark matter overcome the nightmare scenario? *Phys. Rev. D* **82**, 055026 (2010). [arXiv:1005.5651](https://arxiv.org/abs/1005.5651)
162. X.-G. He, J. Tandean, Hidden Higgs boson at the LHC and light dark matter searches. *Phys. Rev. D* **84**, 075018 (2011). [arXiv:1109.1277](https://arxiv.org/abs/1109.1277)
163. Y. Mambrini, Higgs searches and singlet scalar dark matter: combined constraints from XENON 100 and the LHC. *Phys. Rev. D* **84**, 115017 (2011). [arXiv:1108.0671](https://arxiv.org/abs/1108.0671)
164. P.J. Fox, R. Harnik, J. Kopp, Y. Tsai, Missing energy signatures of dark matter at the LHC. *Phys. Rev. D* **85**, 056011 (2012). [arXiv:1109.4398](https://arxiv.org/abs/1109.4398)
165. A. Djouadi, O. Lebedev, Y. Mambrini, J. Quevillon, Implications of LHC searches for Higgs-portal dark matter. *Phys. Lett. B* **709**, 65–69 (2012). [arXiv:1112.3299](https://arxiv.org/abs/1112.3299)

166. A. Djouadi, A. Falkowski, Y. Mambrini, J. Quevillon, Direct detection of Higgs-portal dark matter at the LHC. *Eur. Phys. J. C* **73**, 2455 (2013). [arXiv:1205.3169](#)
167. E. Aprile et al., XENON100 Collaboration, Dark matter results from 225 live days of XENON100 data. *Phys. Rev. Lett.* **109**, 181301 (2012). [arXiv:1207.5988](#)
168. D. Akerib et al. LUX Collaboration, *First Results from the LUX Dark Matter Experiment at the Sanford Underground Research Facility*. [arXiv:1310.8214](#)
169. P. Junnarkar, A. Walker-Loud, Scalar strange content of the nucleon from lattice QCD. *Phys. Rev. D* **87**(11) (2013), 114510, [arXiv:1301.1114](#)
170. G. Belanger, F. Boudjema, A. Pukhov, A. Semenov, micrOMEGAs_3: a program for calculating dark matter observables. *Comput. Phys. Commun.* **185**, 960–985 (2014). [arXiv:1305.0237](#)
171. G. Belanger, F. Boudjema, A. Pukhov, A. Semenov, Dark matter direct detection rate in a generic model with micrOMEGAs 2.2. *Comput. Phys. Commun.* **180**, 747–767 (2009). [arXiv:0803.2360](#)
172. C.-Y. Chen, S. Dawson, Exploring two Higgs doublet models through Higgs production. *Phys. Rev. D* **87**(5) (2013), 055016, [arXiv:1301.0309](#)
173. A. Celis, V. Ilisie, A. Pich, LHC constraints on two-Higgs doublet models. *JHEP* **1307**, 053 (2013). [arXiv:1302.4022](#)
174. B. Grinstein, P. Uttayarat, Carving out parameter space in type-II two Higgs doublets model. *JHEP* **1306**, 094 (2013). [arXiv:1304.0028](#)
175. B. Coleppa, F. Kling, S. Su, Constraining type II 2HDM in light of LHC Higgs searches. *JHEP* **1401**, 161 (2014). [arXiv:1305.0002](#)
176. C.-Y. Chen, S. Dawson, M. Sher, Heavy Higgs searches and constraints on two Higgs doublet models. *Phys. Rev. D* **88**, 015018 (2013). [arXiv:1305.1624](#)
177. O. Eberhardt, U. Nierste, M. Wiebusch, Status of the two-Higgs-doublet model of type II. *JHEP* **1307**, 118 (2013). [arXiv:1305.1649](#)
178. N. Craig, J. Galloway, S. Thomas, *Searching for Signs of the Second Higgs Doublet*, [arXiv:1305.2424](#)
179. L. Maiani, A. Polosa, V. Riquer, Bounds to the Higgs sector masses in minimal supersymmetry from LHC data. *Phys. Lett. B* **724**, 274–277 (2013). [arXiv:1305.2172](#)
180. G. Aad et al., ATLAS Collaboration, Search for the neutral Higgs bosons of the minimal supersymmetric standard model in pp collisions at $\sqrt{s} = 7$ TeV with the ATLAS detector. *JHEP* **1302**, 095 (2013). [arXiv:1211.6956](#)
181. B. Dumont, J. F. Guion, Y. Jiang, S. Kraml, *Constraints on and Future Prospects for Two-Higgs-Doublet Models in Light of the LHC Higgs Signal*. [arXiv:1405.3584](#)
182. N.G. Deshpande, E. Ma, Pattern of symmetry breaking with two Higgs doublets. *Phys. Rev. D* **18**, 2574 (1978)
183. E. Ma, Verifiable radiative seesaw mechanism of neutrino mass and dark matter. *Phys. Rev. D* **73**, 077301 (2006). [hep-ph/0601225](#)
184. R. Barbieri, L.J. Hall, V.S. Rychkov, Improved naturalness with a heavy Higgs: an alternative road to LHC physics. *Phys. Rev. D* **74**, 015007 (2006). [hep-ph/0603188](#)
185. L. Lopez Honorez, E. Nezri, J.F. Oliver, M.H. Tytgat, The inert doublet model: an archetype for dark matter. *JCAP* **0702** (2007) 028. [hep-ph/0612275](#)
186. M. Krawczyk, D. Sokolowska, P. Swaczyna, B. Swiezewska, Constraining inert dark matter by $R_{\gamma\gamma}$ and WMAP data. *JHEP* **1309**, 055 (2013). [arXiv:1305.6266](#)
187. B. Swiezewska, Yukawa independent constraints for 2HDMs with a 125 GeV Higgs boson. *Phys. Rev. D* **88**, 055027 (2013). [arXiv:1209.5725](#)
188. A. Pierce, J. Thaler, Natural dark matter from an unnatural Higgs boson and new colored particles at the TeV scale. *JHEP* **0708**, 026 (2007). [hep-ph/0703056](#)
189. E. Lundstrom, M. Gustafsson, J. Edsjo, The inert doublet model and LEP II limits. *Phys. Rev. D* **79**, 035013 (2009). [arXiv:0810.3924](#)
190. A. Goudelis, B. Herrmann, O. Stål, Dark matter in the inert doublet model after the discovery of a Higgs-like boson at the LHC. *JHEP* **1309**, 106 (2013). [arXiv:1303.3010](#)
191. A. Arhrib, R. Benbrik, N. Gaur, $H \rightarrow \gamma\gamma$ in inert Higgs doublet model. *Phys. Rev. D* **85**, 095021 (2012). [arXiv:1201.2644](#)

192. M. Gustafsson, S. Rydbeck, L. Lopez-Honorez, E. Lundstrom, Status of the inert doublet model and the role of Multileptons at the LHC. *Phys. Rev. D* **86**, 075019 (2012). [arXiv:1206.6316](#)
193. B. Swiezewska, M. Krawczyk, Diphoton rate in the inert doublet model with a 125 GeV Higgs boson. *Phys. Rev. D* **88**(3) (2013), 035019, [arXiv:1212.4100](#)
194. B. Dumont, S. Fichet, G. von Gersdorff, A Bayesian view of the Higgs sector with higher dimensional operators. *JHEP* **1307**, 065 (2013). [arXiv:1304.3369](#)
195. W. Buchmuller, D. Wyler, Effective Lagrangian analysis of new interactions and flavor conservation. *Nucl. Phys. B* **268**, 621–653 (1986)
196. B. Grzadkowski, M. Iskrzynski, M. Misiak, J. Rosiek, Dimension-six terms in the standard model Lagrangian. *JHEP* **1010**, 085 (2010). [arXiv:1008.4884](#)
197. H. Davoudiasl, S. Gopalakrishna, E. Ponton, J. Santiago, Warped 5-dimensional models: phenomenological status and experimental prospects. *New J. Phys.* **12**, 075011 (2010). [arXiv:0908.1968](#)
198. J.A. Cabrer, G. von Gersdorff, M. Quiros, Suppressing electroweak precision observables in 5D warped models. *JHEP* **1105**, 083 (2011). [arXiv:1103.1388](#)
199. C. Arzt, M. Einhorn, J. Wudka, Patterns of deviation from the standard model. *Nucl. Phys. B* **433**, 41–66 (1995). [hep-ph/9405214](#)
200. A.V. Manohar, M.B. Wise, Modifications to the properties of the Higgs boson. *Phys. Lett. B* **636**, 107–113 (2006). [hep-ph/0601212](#)
201. C. Grojean, E.E. Jenkins, A.V. Manohar, M. Trott, Renormalization group scaling of Higgs operators and $\Gamma(h \rightarrow \gamma\gamma)$. *JHEP* **1304**, 016 (2013). [arXiv:1301.2588](#)
202. J. Elias-Mirás, J. Espinosa, E. Masso, A. Pomarol, Renormalization of dimension-six operators relevant for the Higgs decays $h \rightarrow \gamma\gamma, \gamma Z$. *JHEP* **1308**, 033 (2013). [arXiv:1302.5661](#)
203. C. Burgess, S. Godfrey, H. Konig, D. London, I. Maksymyk, Model independent global constraints on new physics. *Phys. Rev. D* **49**, 6115–6147 (1994). [hep-ph/9312291](#)
204. K. Hagiwara, R. Peccei, D. Zeppenfeld, K. Hikasa, Probing the weak Boson sector in $e^+e^- \rightarrow W^+W^-$. *Nucl. Phys. B* **282**, 253 (1987)
205. Tevatron New Physics Higgs Working Group, CDF, D0 Collaboration, *Updated Combination of CDF and D0 Searches for Standard Model Higgs Boson Production with up to 10.0 fb⁻¹ of Data*. [arXiv:1207.0449](#)
206. CMS Collaboration, *Search for the Standard Model Higgs boson in the Z Boson Plus a Photon Channel in pp Collisions at $\sqrt{s} = 7$ and 8 TeV*, CMS-PAS-HIG-13-006
207. R. Barbieri, A. Pomarol, R. Rattazzi, A. Strumia, Electroweak symmetry breaking after LEP-1 and LEP-2. *Nucl. Phys. B* **703**, 127–146 (2004). [hep-ph/0405040](#)
208. LEPEWWG/TGC/2005-01, *A Combination of Results in Charged Triple Gauge Boson Couplings Measured by the LEP Experiments*. http://lepewwg.web.cern.ch/LEPEWWG/lepww/tgc/2005/gc_pdg05.ps
209. K. Hagiwara, Q. Li, K. Mawatari, Jet angular correlation in vector-boson fusion processes at hadron colliders. *JHEP* **0907**, 101 (2009). [arXiv:0905.4314](#)
210. Y. Gao, A.V. Gritsan, Z. Guo, K. Melnikov, M. Schulze et al., Spin determination of single-produced resonances at hadron colliders. *Phys. Rev. D* **81**, 075022 (2010). [arXiv:1001.3396](#)
211. D. Stolarski, R. Vega-Morales, Directly measuring the tensor structure of the scalar coupling to Gauge bosons. *Phys. Rev. D* **86**, 117504 (2012). [arXiv:1208.4840](#)
212. J.S. Gainer, K. Kumar, I. Low, R. Vega-Morales, Improving the sensitivity of Higgs boson searches in the golden channel. *JHEP* **1111**, 027 (2011). [arXiv:1108.2274](#)
213. G. Aad et al., ATLAS Collaboration, *Expected Performance of the ATLAS Experiment—Detector, Trigger and Physics*, [arXiv:0901.0512](#)
214. W. Kilian, M. Kramer, P. Zerwas, Anomalous couplings in the Higgsstrahlung process. *Phys. Lett. B* **381**, 243–247 (1996). [hep-ph/9603409](#)
215. M. Farina, C. Grojean, E. Salvioni, (Dys)Zphilia or a custodial breaking Higgs at the LHC. *JHEP* **1207**, 012 (2012). [arXiv:1205.0011](#)
216. S. Alam, S. Dawson, R. Szalapski, Low-energy constraints on new physics revisited. *Phys. Rev. D* **57**, 1577–1590 (1998). [hep-ph/9706542](#)

217. R. Trotta, Bayes in the sky: Bayesian inference and model selection in cosmology. *Contemp. Phys.* **49**, 71–104 (2008). [arXiv:0803.4089](#)
218. S. Fichtel, Quantified naturalness from Bayesian statistics. *Phys. Rev. D* **86**, 125029 (2012). [arXiv:1204.4940](#)
219. J. Press, *Subjective and Objective Bayesian Statistics: Principles, Models, and Applications*, 2nd edn. (Wiley Series in Probability and Statistics)
220. E.T. Jaynes, Prior probabilities. *IEEE Trans. Syst. Sci. Cybern.* **4**(3), 227–241 (1968)
221. B. Allanach, C. Lester, Multi-dimensional mSUGRA likelihood maps. *Phys. Rev. D* **73**, 015013 (2006). [hep-ph/0507283](#)
222. A. Gelman, D.B. Rubin, Inference from iterative simulation using multiple sequences. *Stat. Sci.* **7**, 457–472 (1992)
223. A. Djouadi, *Implications of the Higgs Discovery for the MSSM*. [arXiv:1311.0720](#)
224. F. Brummer, S. Kraml, S. Kulkarni, Anatomy of maximal stop mixing in the MSSM. *JHEP* **1208**, 089 (2012). [arXiv:1204.5977](#)
225. M. Carena, S. Gori, N.R. Shah, C.E. Wagner, L.-T. Wang, Light stau phenomenology and the Higgs $\gamma\gamma$ rate. *JHEP* **1207**, 175 (2012). [arXiv:1205.5842](#)
226. U. Ellwanger, A Higgs boson near 125 GeV with enhanced di-photon signal in the NMSSM. *JHEP* **1203**, 044 (2012). [arXiv:1112.3548](#)
227. J.F. Gunion, Y. Jiang, S. Kraml, The constrained NMSSM and Higgs near 125 GeV. *Phys. Lett. B* **710**, 454–459 (2012). [arXiv:1201.0982](#)
228. S. Kraml, Implications of LHC Higgs results for supersymmetry. *J. Phys. Conf. Ser.* **455**, 012053 (2013)
229. A. Arbey, M. Battaglia, A. Djouadi, F. Mahmoudi, An update on the constraints on the phenomenological MSSM from the new LHC Higgs results. *Phys. Lett. B* **720**, 153–160 (2013). [arXiv:1211.4004](#)
230. A. Djouadi, L. Maiani, G. Moreau, A. Polosa, J. Quevillon et al., The post-Higgs MSSM scenario: Habemus MSSM? *Eur. Phys. J. C* **73**, 2650 (2013). [arXiv:1307.5205](#)
231. M. Cahill-Rowley, J. Hewett, A. Ismail, T. Rizzo, *Constraints on Higgs Properties and SUSY Partners in the pMSSM*. [arXiv:1308.0297](#)
232. CMS Collaboration, *Phenomenological MSSM Interpretation of the CMS 2011 5 fb^{-1} Results*, CMS-PAS-SUS-12-030
233. CMS Collaboration, *Phenomenological MSSM Interpretation of the CMS 7 and 8 TeV Results*, CMS-PAS-SUS-13-020
234. B. Dumont, J.F. Gunion, S. Kraml, The phenomenological MSSM in view of the 125 GeV Higgs data. *Phys. Rev. D* **89**, 055018 (2014). [arXiv:1312.7027](#)
235. B. Dumont, Higgs coupling measurements and impact on the MSSM. *PoS DIS2014* (2014) 128, [arXiv:1407.0415](#)
236. MSSM Working Group Collaboration, A. Djouadi et al., *The Minimal Supersymmetric Standard Model: Group Summary Report*. [hep-ph/9901246](#)
237. J. Camargo-Molina, B. O’Leary, W. Porod, F. Staub, **Vevacious**: a tool for finding the global minima of one-loop effective potentials with many scalars. *Eur. Phys. J. C* **73**, 2588 (2013). [arXiv:1307.1477](#)
238. B. Allanach, SOFTSUSY: a program for calculating supersymmetric spectra. *Comput. Phys. Commun.* **143**, 305–331 (2002). [hep-ph/0104145](#)
239. F. Mahmoudi, SuperIso v2.3: a program for calculating flavor physics observables in Supersymmetry. *Comput. Phys. Commun.* **180**, 1579–1613 (2009). [arXiv:0808.3144](#)
240. G. Belanger, F. Boudjema, A. Pukhov, A. Semenov, MicrOMEGAs: a program for calculating the relic density in the MSSM. *Comput. Phys. Commun.* **149**, 103–120 (2002). [hep-ph/0112278](#)
241. M. Muhlleitner, A. Djouadi, Y. Mambrini, SDECAY: a Fortran code for the decays of the supersymmetric particles in the MSSM. *Comput. Phys. Commun.* **168**, 46–70 (2005). [hep-ph/0311167](#)
242. P.Z. Skands, B. Allanach, H. Baer, C. Balazs, G. Belanger et al., SUSY Les Houches accord: interfacing SUSY spectrum calculators, decay packages, and event generators. *JHEP* **0407**, 036 (2004). [hep-ph/0311123](#)

243. B. Allanach, C. Balazs, G. Belanger, M. Bernhardt, F. Boudjema et al., SUSY Les Houches Accord 2. Comput. Phys. Commun. **180**, 8–25 (2009). [arXiv:0801.0045](#)
244. Y. Amhis et al., Heavy Flavor Averaging Group Collaboration, *C-Hadron, and Tau-Lepton Properties as of Early Averages of B-Hadron*, (2012). [arXiv:1207.1158](#)
245. M. Misiak, H. Asatrian, K. Bieri, M. Czakon, A. Czarnecki et al., Estimate of $B(\bar{B} \rightarrow X_s \gamma)$ at $\mathcal{O}(\alpha_s^2)$. Phys. Rev. Lett. **98**, 022002 (2007). [hep-ph/0609232](#)
246. Y. Amhis et al., Heavy Flavor Averaging Group Collaboration, HFAG update, May 2013. <http://www.slac.stanford.edu/xorg/hfag/rare/2013/radll/OUTPUT/TABLES/radll.pdf>
247. ATLAS, CMS, LHCb Collaboration, *Search for the Rare Decays $B_{(s)}^0 \rightarrow \mu^+ \mu^-$ at the LHC with the ATLAS, CMS and LHCb Experiments*, ATLAS-COM-CONF-2012-090, CMS-PAS-BPH-12-009, LHCb-CONF-2012-017
248. A. Akeroyd, F. Mahmoudi, D.M. Santos, The decay $B_s \rightarrow \mu^+ \mu^-$: updated SUSY constraints and prospects. JHEP **1112**, 088 (2011). [arXiv:1108.3018](#)
249. CMS, LHCb Collaboration, *Combination of Results on the Rare Decays $B_{(s)}^0 \rightarrow \mu^+ \mu^-$ from the CMS and LHCb Experiments*
250. G. Bennett et al., Muon G-2 Collaboration, Final Report of the Muon E821 Anomalous Magnetic Moment Measurement at BNL. Phys. Rev. D **73** (2006) 072003. [hep-ex/0602035](#)
251. K. Hagiwara, R. Liao, A.D. Martin, D. Nomura, T. Teubner, $(g-2)_\mu$ and $\alpha(M_Z^2)$ re-evaluated using new precise data. J. Phys. **G38**, 085003 (2011). [arXiv:1105.3149](#)
252. D. Stockinger, The Muon magnetic moment and supersymmetry. J. Phys. **G34**, R45–R92 (2007). [hep-ph/0609168](#)
253. ATLAS, CMS Collaboration, *Combination of ATLAS and CMS Results on the Mass of the Top Quark Using up to 4.9 fb^{-1} of Data*, ATLAS-CONF-2012-095, CMS-PAS-TOP-12-001
254. M. Muehther et al., Tevatron Electroweak Working Group, CDF, D0 Collaboration, *Combination of CDF and D0 Results on the Mass of the Top Quark Using up to 8.7 fb^{-1} at the Tevatron*. [arXiv:1305.3929](#)
255. LEPSUSYWG, ALEPH, DELPHI, L3 and OPAL experiments. notes LEPSUSYWG/01-03.1, LEPSUSYWG/02-04.1, and LEPSUSYWG/04-01.1. <http://lepsusy.web.cern.ch/lepsusy/Welcome.html>
256. R. Aaij et al., LHCb Collaboration, First evidence for the decay $B_s^0 \rightarrow \mu^+ \mu^-$. Phys. Rev. Lett. **110**, 021801 (2013). [arXiv:1211.2674](#)
257. CMS Collaboration, *Search for MSSM Neutral Higgs Bosons Decaying to Tau Pairs in pp Collisions*, CMS-PAS-HIG-13-021
258. P. Planck Collaboration, Planck Ade et al., *results* (Cosmological parameters, XVI, 2013). [arXiv:1303.5076](#)
259. J.F. Gunion, H.E. Haber, Two-body decays of neutralinos and charginos. Phys. Rev. D **37**, 2515 (1988)
260. A. Djouadi, The anatomy of electro-weak symmetry breaking. II. The Higgs bosons in the minimal supersymmetric model. Phys. Rep. **459**, 1–241 (2008). [hep-ph/0503173](#)
261. C. Wymant, Optimising stop naturalness. Phys. Rev. D **86**, 115023 (2012). [arXiv:1208.1737](#)
262. R.V. Harlander, S. Liebler, H. Mantler, SusHi: a program for the calculation of Higgs production in gluon fusion and bottom-quark annihilation in the standard model and the MSSM. Comput. Phys. Commun. **184**, 1605–1617 (2013). [arXiv:1212.3249](#)
263. J. Bernon, B. Dumont, in preparation
264. <http://lpsc.in2p3.fr/projects-th/liilith/>
265. K. Arnold, M. Bahr, G. Bozzi, F. Campanario, C. Englert et al., VBFNLO: a parton Level Monte Carlo for processes with electroweak bosons. Comput. Phys. Commun. **180**, 1661–1670 (2009). [arXiv:0811.4559](#)
266. <http://iminuit.github.io/iminuit/>
267. F. Boudjema, G. Cacciapaglia, K. Cranmer, G. Dissertori, A. Deandrea, et al., *On the presentation of the LHC Higgs results*, [arXiv:1307.5865](#)
268. See the talks by Glen Cowan and Kyle Cranmer at the workshop on *Likelihoods for the LHC Searches*, CERN, 21–23 January 2013. <http://indico.cern.ch/conferenceDisplay.py?confId=218693>

- 269. S. Dawson, A. Gritsan, H. Logan, J. Qian, C. Tully, et al., *Working Group Report: Higgs Boson*. [arXiv:1310.8361](#)
- 270. K. Cranmer, S. Kreiss, D. Lopez-Val, T. Plehn, *A Novel Approach to Higgs Coupling Measurements*. [arXiv:1401.0080](#)
- 271. G. Aad et al., ATLAS Collaboration, *Measurements of Fiducial and Differential Cross Sections for Higgs Boson Production in the Diphoton Decay Channel at $\sqrt{s} = 8$ TeV with ATLAS*. [arXiv:1407.4222](#)
- 272. ATLAS Collaboration, *Inclusive and Differential Fiducial Cross Sections of Higgs Boson Production Measured in the $H \rightarrow ZZ^* \rightarrow 4\ell$ Decay Channel Using $\sqrt{s} = 8$ TeV pp Collision Data Recorded by the ATLAS Detector*, ATLAS-CONF-2014-044
- 273. K. Cranmer, I. Yavin, RECAST: extending the impact of existing analyses. JHEP **1104**, 038 (2011). [arXiv:1010.2506](#)

Higgs, Supersymmetry and Dark Matter After Run I of
the LHC

Dumont, B.

2017, XVII, 259 p. 95 illus., 50 illus. in color., Hardcover

ISBN: 978-3-319-44955-5